Deutsches Zentrum
für Luft- und Raumfahrt e.V.

Ref.: Proposal-No. 3005921

Hot Plume Testing Facilities for ELV Propulsion Characterization

May 24, 2013

Deutsches Zentrum
für Luft- und Raumfahrt e.V.
in der Helmholtz-Gemeinschaft

Contents

1 Introduction

ESA outlines the requirements for Hot Testing Facilities for ELV Propulsion Characterization in the appendix 1 of Ref. [3] given supplementary to the invitation to tender. The investigation is motivated by discrepancies between the wind tunnel simulations with cold jet-on conditions and actual in-flight measurements on the Ariane 5. Based on these experiences, ESA lists the requirements described hereafter for the future facility.

The facility is specified to

- □ operate in the transonic flight regime between Mach 0.8 and 1.3.
- □ allow geometric scaling.
- □ allow accurate Reynolds number scaling.
- □ allow similarity between the test plume and flight plume.
- □ similarity between plume and free stream.

Furthermore, it is desired to take future developments as described in Ref. into consideration, meaning the facility must include the possibility to simulate

- □ a single plume stage like VEGA and also
- □ multiple plumes stage similar to Ariane IV and Ariane V first stages.

ESA refers to the investigations of Ref. to express the

- □ need for investigations with hot plumes.

The goal is to provide accurate and flight representative data concerning

- □ the underestimated base pressure and the interrelated base drag,
- □ the heat loads,
- □ and the fluctuating loads on the nozzle

for a better understanding of the physics and particularly for

- □ the validation of CFD computations.

According to Ref., the desired outcome under consideration of the proposal of the DLR (Ref.) should be:

- □ A strong justification for a European hot plume facility.
- □ A definition of the required scaling parameters to ensure similarity between tests and flight.

- A complete design for a hot plume wind-tunnel.
- A complete design for the auxiliary facility and infrastructure.
- A cost analysis for construction and completion of the facility.
- Professional and technical drawings for the facility and wind tunnel developed in the frame of the contract.

DLR proposed to organize these objectives with the work structure presented in Ref. [15]. A list of the tasks with the number of the corresponding work packages, title and deliverable is given in Tab. 1. For a better readability, the work packages were reorganized according to the list given in Tab. 2.

Table 1: List regarding to the work structure as proposed in Ref. [15].

Work package	Task	Title	Deliverable
WP1	Task 1	Scope of Operation of Wind tunnel	TN2100
WP2	Task 2	Scaling Issues	TN2200
WP2	Task 4	Measurement Techniques	TN2300
WP2	Task 5	Design Trade-Off	TN2400
WP2	Task 6	Aerothermodynamic Design	TN2500
WP3	Task 7	Wind Tunnel Design	TN3100
WP3	Task 8	Facility Design	TN3200
WP4	Task 9	Cost Analysis	TN4100

Table 2: Reorganized work structure.

Title	Deliverable	Chapter
Scope of Operation	TN2100	2
Scaling Issues	TN2200	3
Measurement Techniques	TN2300	4
Aerothermodynamic Design	TN2500	4
Model and Facility Design	TN3132	6
Design Trade-Off and Cost Analysis	TN2441	8

In detail, chapter 2 evaluates the scope of operation of the future facility. The conditions during the ascend of representative space transportation systems are presented and it is discussed how these conditions can be duplicated in wind tunnel experiment. In

chapter 3, the influence of different mixture ratios and the turbine exhaust gas are discussed and investigated numerically. Chapter 4 then investigates the concept of an upstream supported wind tunnel model, which is refined in chapter 6. Chapter 5 goes into the details of the combustion chamber design. Then, the different wind tunnel concepts and wind tunnel model concepts are discussed in chapter 6. The measurement techniques under consideration are studied in chapter 7, and finally, the report concludes with the cost analysis in chapter 8.

Deutsches Zentrum
für Luft- und Raumfahrt e.V.

TN2100

Scope of Operation of Wind Tunnel

May 24, 2013

Dominik Saile, Ali Gülhan

Institute of Aerodynamics
and Flow Technology
Supersonic and Hypersonic Technology Department[1]

DLR **Deutsches Zentrum für Luft- und Raumfahrt** e.V.
in der Helmholtz-Gemeinschaft

ESA STUDY CONTRACT REPORT

No ESA Study Contract Report will be accepted unless this sheet is inserted after the coverpage of each volume of the Report.

ESA CONTRACT No.: AO/1-6731/ 11/NL/SFe	SUBJECT Hot Testing Facility for ELV Propulsion Characterization		CONTRACTOR DLR
* ESA CR( )No	* STAR CODE	No of TN 2100	

ABSTRACT:

This report presents the results from a study regarding to the scope of operation of the future hot plume facility in the framework of the ESA technology research project "Hot Testing Facilities for ELV Propulsion Characterization". Mission profiles of representative space transportation systems like from the European launcher family and from the international side are presented. Ariane 5 is then defined to serve as benchmark for the similarity study. Next, sensitivities are determined, which dominate the effects in the base region. As an outcome, the corresponding properties at the nozzle exit of the core stage and the boosters are calculated with respect to the ambient conditions during the ascend. In order to match these conditions in a simulation environment, an appropriate solid and hydrogen/oxygen rocket engine is found and characterized by taking the a typical transonic wind tunnel's operational range into account. Finally, the real and the simulation environment are opposed to each other and suggestions are given on how to reach partial similarity.

The work described in this report was done under ESA contract. Responsibility for the contents resides in the author or organization that prepared it.

Name of author: D. Saile, A. Gülhan (DLR, Cologne, Germany)

** NAME OF ESA STUDY MANAGER	** ESA BUDGET HEADING
N. Murray DIV: TEC-MPA DIRECTORATE: D\TEC	

* Sections to be completed by ESA

** Information to be provided by ESA Study Manager

2 Scope of Operation of Wind Tunnel - TN2100

Space transportation systems are exposed to high mechanical and thermal loads. Especially the base flow issue is very challenging. For the failure of flight 157 in 2002 of *Ariane 5* (Ref. [2]), the inquiry board found as one of the most probable reasons for failure the *non-exhaustive definition of the loads to which the Vulcain 2 engine is subjected during flight*. For the next generation launcher, this has to be avoided under all circumstances and is also of importance for the development of the current Ariane 5 system. Consequently, it is crucial to correctly predict and specify the loads on space transportation systems.

Ariane 5 uses an hydrogen/oxygen combustion that is exposed to a set of issues that differ from a pure solid propellant concept, like afterburning of the hydrogen rich fuel in the shear layer of the plume. This causes heat loads that have to be considered. Currently, there is no facility in Europe that offers the opportunity to study hot plume effects, not to mention with hydrogen/oxygen combustion. Consequently, there is a lack of data available with respect to prediction and specification, but also for numerical validation.

The *Ariane 6* concept is very likely to be what was named *PPH*-configuration, meaning a configuration with three stages, while the first and second stage use solid propellants and the upper stage uses oxygen/hydrogen as propellant. Additionally, the first stage is foreseen to feature two to three boosters in parallel.

The *Ariane 6* concept imposes challenges that differ from the ones encountered before. Now, two-phase flow and multiple nozzle effects have to be taken into account for the base loads due to the solid propellant and, obviously, the booster arrangement. Among other challenges, one has to deal with:

- Multiple-plumes interaction.
- Base heating resulting from flow circulation.
- Base heating resulting from radiation including solid particle radiation.

Fig. 1 from Ref. [32] is given to visualize the first two challenges on the list. It shows the recirculation region at various altitudes. It becomes apparent that the circulation region has to be investigated with care for different environmental conditions since the multiple-plumes interaction results in a transport of kinetic and thermal energy in the base region. Regions of high-temperature flow with hot spots is one of the known outcomes of the shock wave interaction of plumes. Thus, thermal protection systems have to be designed appropriately.

Further, most solid propellants contain finely ground aluminum powder to improve the specific impulse, which then react to aluminum oxide during the combustion process.

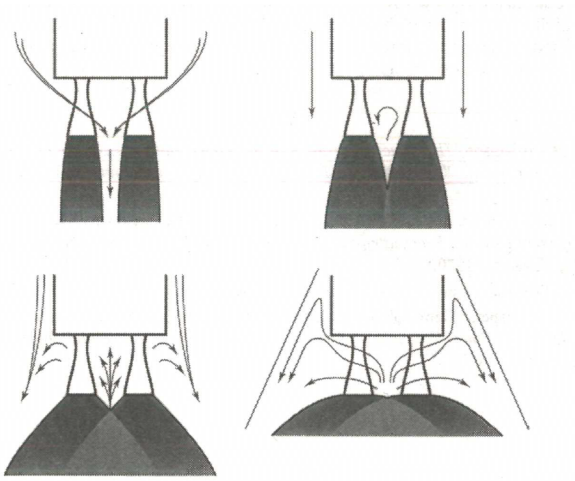

Figure 1: Recirculation regions at various altitudes (Ref. [32]).

Depending on the mass fraction, the particles may influence the structure of the plume due to the relative lag to gaseous flow. Additionally, it is found that the particles are arranged in the flow field according to their size, e.g. heavier particles resided in the core region. Lag and size distribution have a strong influence on the thermal emission from the plumes [32].

As one of the consequences of the *Ariane 5* flight 157, the responsible inquiry board requested an *assessment of possibilities for simulation during ground tests of loads observed during actual flight* (Ref. [2]). Despite the challenging nature, the paper at hand presents an advanced approach to simulate the occurring loads for the existing and future space transportation systems in Europe. It will provide high quality data for the validation of numerical results.

2.1 Mission Profile of Representative Launchers

One of the objectives for the hot testing facility is to be applicable to future ELV propulsion systems. In order to do so, the trajectories of several different space transportation is presented in this chapter. Then, the *International Standard Atmosphere* is used to develop the typical non-dimensional figures of merit. In a last step, a reference trajectory is chosen for the detailed analysis.

Fig. 2 and Fig. 3 shows the trajectory as it is given by most user's guides of the individual space transportation system. The space transportation systems here are the European representatives *Ariane 5*, *Vega*, *Ariane 4* and *Soyuz*, *LM-3A*, *Angara Proton*. The

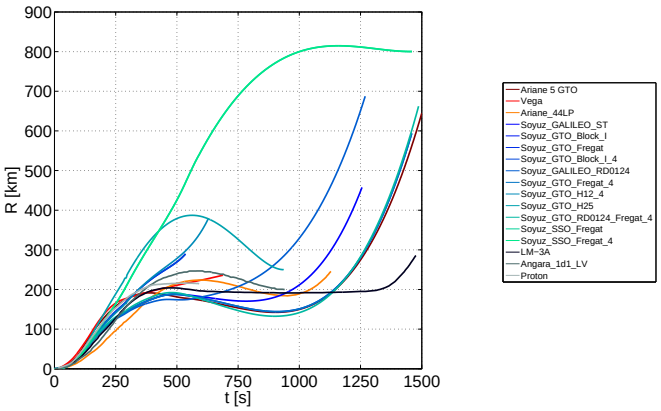

Figure 2: Altitude over time for various launchers

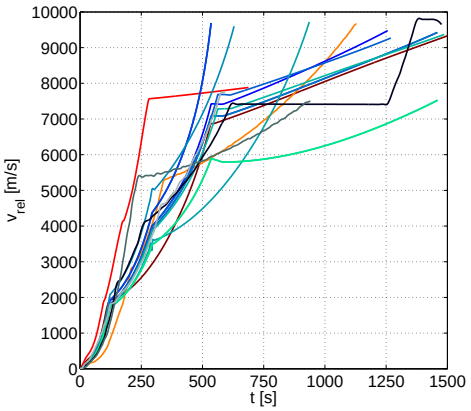

Figure 3: Velocity over time for various launchers

trajectories show that course of altitude or velocity over time of the various systems is relatively similar.

The ambient conditions are required for the determination of aforementioned figures of merit and the later introduced similarity ratios. Thus, they are plotted up to an altitude of 24 km in Figs. 4 to 6. The ambient temperature (Fig. 4) as influential parameter for the Mach number decreases constantly in the troposphere and is then assumed to be constant for altitudes beyond the tropopause. The speed of sound (Fig. 7) decreases correspondingly. The ambient pressure and density also decrease according to Fig. 5 and Fig. 6.

One of the main figures of merit, the Mach number is now plotted in Fig. 8 for the complete flight path. As it can be seen in the close up (Fig. 9), the transonic flight regime as region of interest is passed at the latest after about 100 s (*Ariane 4*, $Ma = 1.5$). With respect to the altitude, the Mach number is plotted in Fig. 10.

The second main figure of merit, namely the Reynolds number is plotted over the Mach number in Fig. 11. It is only shown here for Ariane 4, Ariane 5 and Vega. This is basically the operational range that has to be met for simulations. It can be seen that at first, the unit Reynolds number increases due to the increasing velocity of the space transportation system. In the transonic regime, the Reynolds number reaches a maximum and decreases afterwards. This is assigned to the decreasing density in higher altitudes.

Note, that the trajectories of the various space transportation systems are comparable. With respect to the shown ones, the parameters lay in a small corridor between the trajectory of *Ariane 4* and *Vega*. The trajectory of *Ariane 5* is located very closely to a

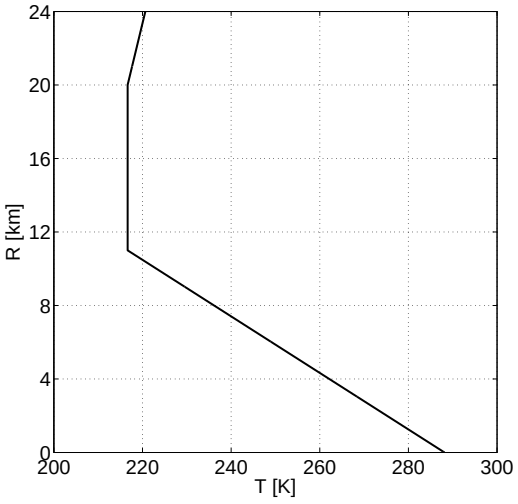

Figure 4: Temperature according to International Standard Atmosphere

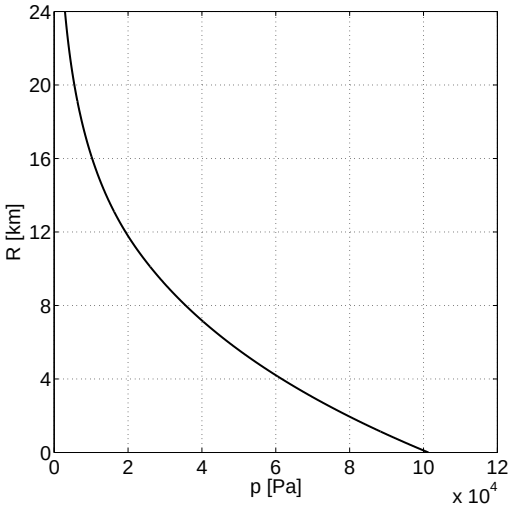

Figure 5: Pressure according to International Standard Atmosphere

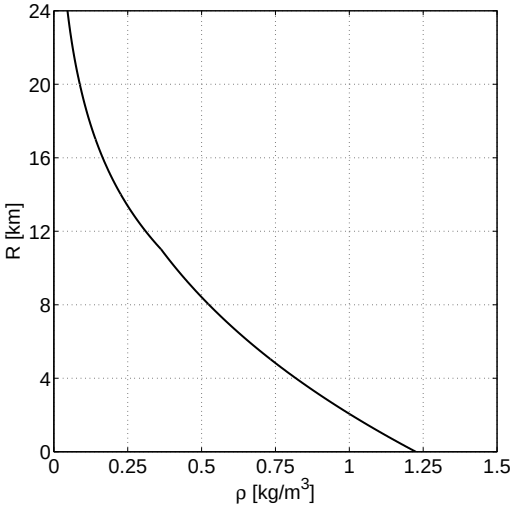

Figure 6: Density according to International Standard Atmosphere

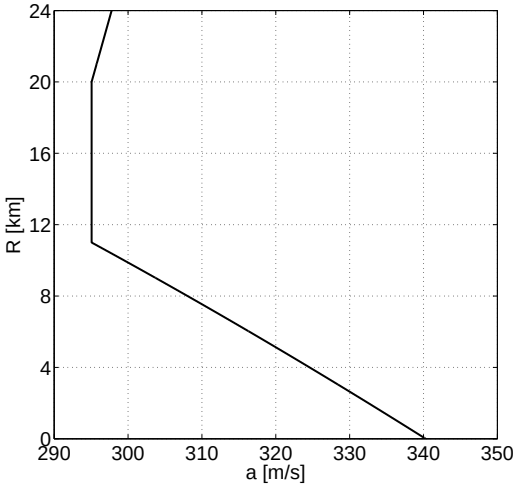

Figure 7: Speed of sound according to International Standard Atmosphere

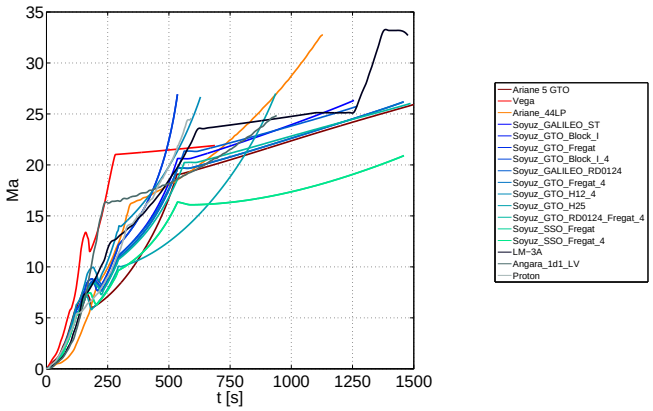

Figure 8: Mach number over time for various launchers

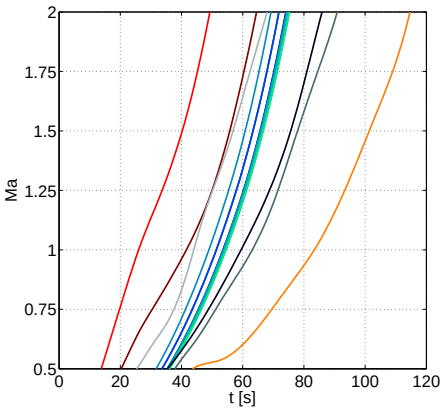

Figure 9: Mach over time for different launchers in the transonic regime

path in the middle of that corridor, it seems to be very similar to the others and since it is the main existing European space transportation system, it will be taken as reference trajectory for the later shown similarity studies.

The Mach numbers can easily be duplicated for transonic wind tunnel testing by simply using the appropriate expansion ratio of the wind tunnel nozzle. The unit Reynolds number as shown in Fig. 11 instead imposes serious difficulties. This becomes obvious when comparing the operational range of the two exemplary wind tunnel facilities VMK and TMK with the graph before. Fig. 12 and Fig. 13 return the potential unit Reynolds number as a function of the Mach number.

It can be seen that the unit Reynolds numbers are in the same range. Consequently, there is a discrepancy of the one to two magnitudes since it has to be multiplied with either the original characteristic length of the space transportation system or the length of the wind tunnel model. The wind tunnel model is usually scaled by a factor of ~ 50 to ~ 150.

This discrepancy can be solved by increasing the free stream unit Reynolds number in the wind tunnel, which can be done by increasing the reservoir pressure or decreasing the temperature. Both methods impose additional challenges leading to a string of consequences, like increased wall thicknesses of the new wind tunnel or cooling the ambient flow with liquid nitrogen. Finally, these efforts are mirrored in expenses for transonic wind tunnel testing. Another option is to have a closer look first at the sensitivities that dominate the mechanisms of base flows. This is done in the following.

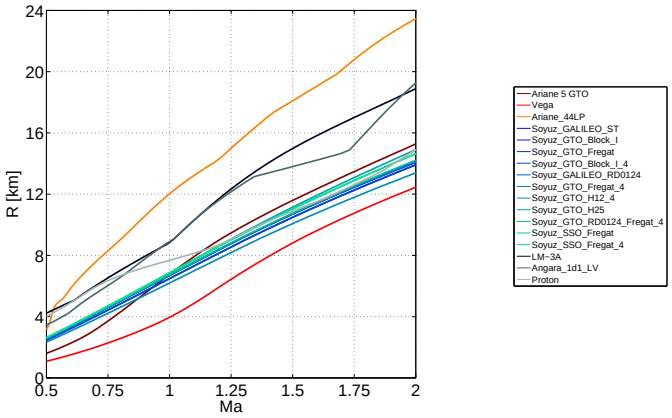

Figure 10: Altitude over Mach number various launchers in the transonic regime

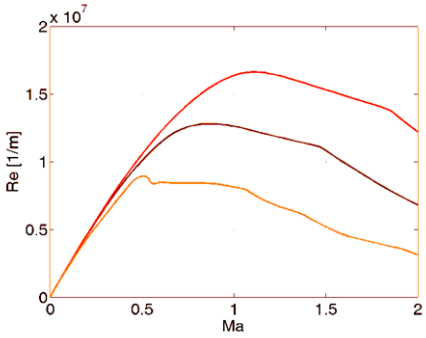

Figure 11: Unit Reynolds number over Mach number in the transonic regime for Ariane 4, Ariane 5 and Vega

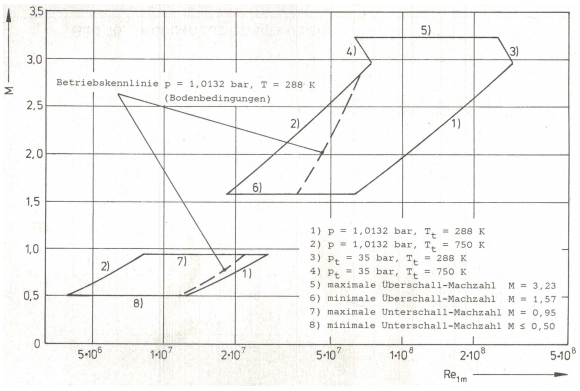

Figure 12: Operational range of VMK (Ref. [36]).

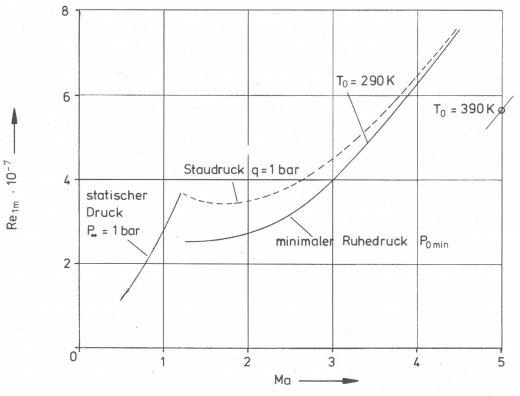

Figure 13: Operational range of TMK (Ref. [11]).

2.2 Sensitivities

The base pressure plays a major role in the development with respect to the imposed thermal and mechanical loads on the base. It is the driving parameter with respect to the plume shape, thus the parameter that influences mostly the effects of the ambient flow/plume flow interaction. Ref. [6] shows in his model that the location of the shear-layer of the ambient flow and the shear-layer of the supersonic nozzle flow is dependent on the ratio between the base pressure and the ambient pressure (Fig. 14).

Consequently, the base pressure has also an impact on buffet/buffeting. Ref. [38] transferred the idea of the flow over a cavity on the Ariane 5 base flow. As shown in Fig. 15, the recirculation region of the base of Ariane 5 is here considered to be similar to a cavity. Further, in that paper, it is described that "the main source that induces base-flow buffeting is assumed to be a the instability of the free shear-layer emanated from the edge of the central body...". "This kind of instability... interacts with the upstream propagating acoustic waves, generated by the impingement of the vortices associated with the shear layer, along the external surface of the ... nozzle downstream. This interaction amplifies the instability of the shear layer resulting in a shedding of new vortices or oscillatory waves, and possibly and amplitude increase in the shear layer excitation. In this way, the vortices or oscillary waves and the acoustic disturbances form a feedback loop."

In Ref. [27], several correlations can be found to calculate the base pressure for geometries similar to projectiles. The simplest correlation of Gabeaud or Kármán and Moore only consider the Mach number. More sophisticated correlations of Hill, Cope, Hoerner, Kurzweg identify further important parameters: the dynamic heat, the surface temperature and the boundary layer thickness increase the base pressure. The angle of attack obviously also impacts the base pressure. But, it is also stated for several correlations that base pressure is not strongly/not influenced by the model length or the Reynolds number (as long as it is turbulent/high enough).

This approach seems to be valid if compared to the experimental results shown in Fig. 16 and Fig. 17. The two different graphs represent the results of investigations with two different jet Mach numbers, two different pylon/nozzle lengths and different Reynolds numbers. For both, several pressure tabs arranged in the azimuthal direction on the base do not detect an influence when the Reynolds number is changed. Thus, these experiments and the correlations, which are also partially based on experiments, indicate strongly that the Reynolds number similarity between wind tunnel tests and flight is not required as long as the boundary layer on the wind tunnel model is turbulent.

As it can be seen in the previously presented graphs, other parameters like the pylon/nozzle length or the jet Mach number are influential. It shows that a shorter nozzle length decreases the base pressure due to different reattachment mechanisms, which are

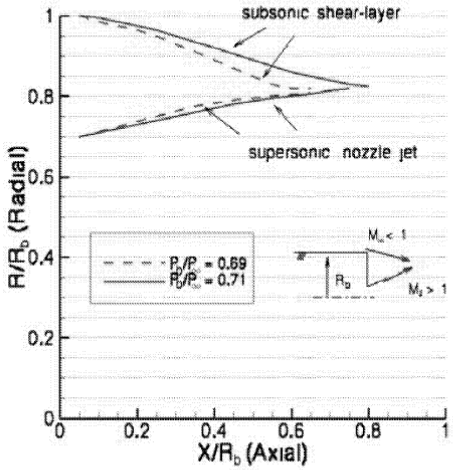

Figure 3 : Base Pressure Influence to Jet and Shear-Layer Envelope (Baik and Zumwalt)

Figure 14: Base pressure influence to jet and shear-layer envelope (Ref. [6]).

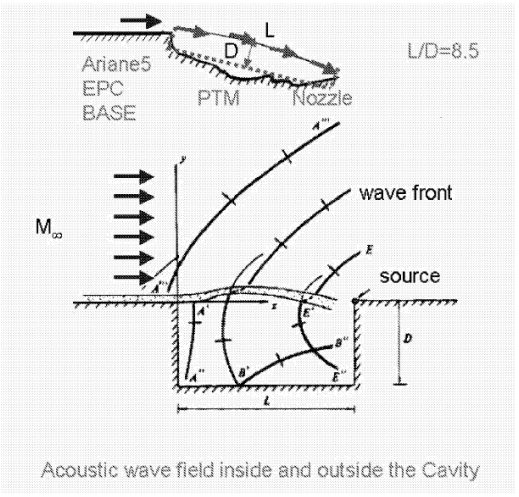

Figure 4 : Ariane 5 Base-Flow Buffeting Model

Figure 15: Ariane 5 base buffeting model (Graph from Ref. [38]).

sketched in Fig. 18 for a free reattachment and in Fig. 19 for a reattachment on the nozzle. In this case without nozzle flow.

A higher jet Mach number decreases the base pressure and so does the increasing ambient flow Mach number as shown in Fig. 20. A higher stagnation temperature, higher nozzle deflection angle and larger boundary layer thickness leads according to Fig. 21, Fig. 22 and Fig. 23 to higher base pressures.

A more complex behavior can be found for an increase of the reservoir pressure in the wind tunnel model. As it is shown in Fig. 24 and Fig. 25, the base pressure first decreases with increasing pressure to a certain point, and then increases again. According to Ref. [31], the decreasing branch is attributed a nozzle flow that is detached from the nozzle contour. The ejector effect causes a decrease of the base pressure as long as the nozzle flow is detached. For higher pressure ratios, the displacement effects of the nozzle flow causes an increase again.

Most studies in the past have been conducted with cold nozzle flows and do not take temperature effects into account. During the ascend of Ariane 5, higher base pressures have been observed though, which have an influence on the flight performance. In experiment, this was found as well as it can be seen in Fig. 27 and Fig. 26. An increase of the temperature in the jet causes an increase of the base pressure. The temperatures shown

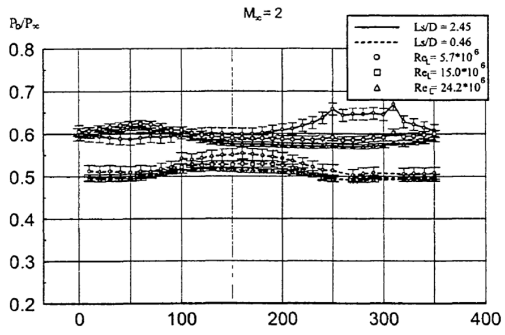

Figure 16: Effect of Reynolds number and flow reattachment on nozzle for Mach 2.0. The x-axis describes the azimuthal location of the individual pressure tab (Ref. [39]).

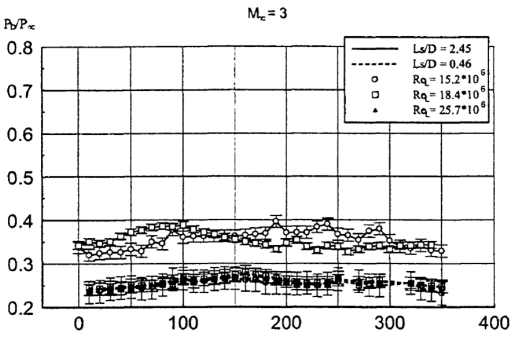

Figure 17: Effect of Reynolds number and flow reattachment on nozzle for Mach 3.0. The x-axis describes the azimuthal location of the individual pressure tab (Ref. [39]).

though are still too low in comparison to realistic exhaust plumes. Future investigations are recommended to goal for higher temperatures to capture the real temperature effects.

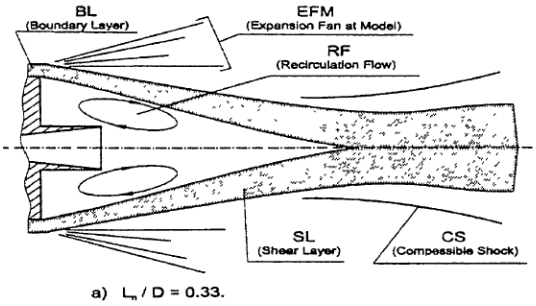

Figure 18: Free flow reattachment (Ref. [39]).

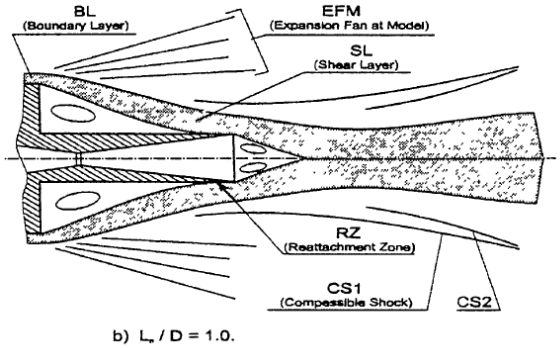

Figure 19: Reattachment of the flow on the nozzle contour (Ref. [39]).

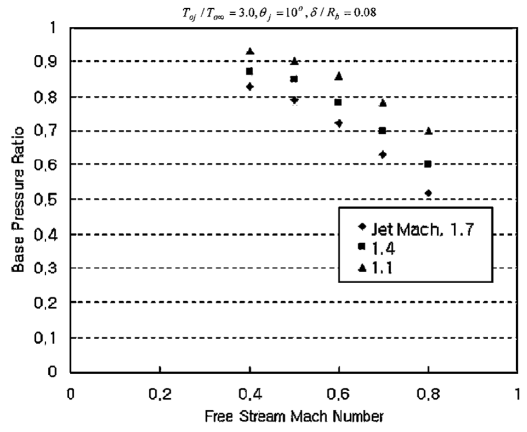

Figure 20: Effect of free stream Mach number (Ref. [39]).

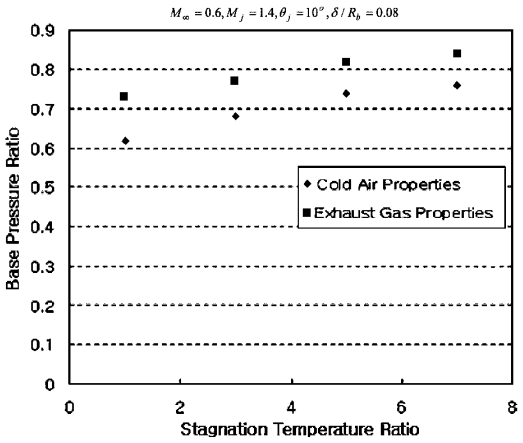

Figure 21: Effect of stagnation temperature (Ref. [39]).

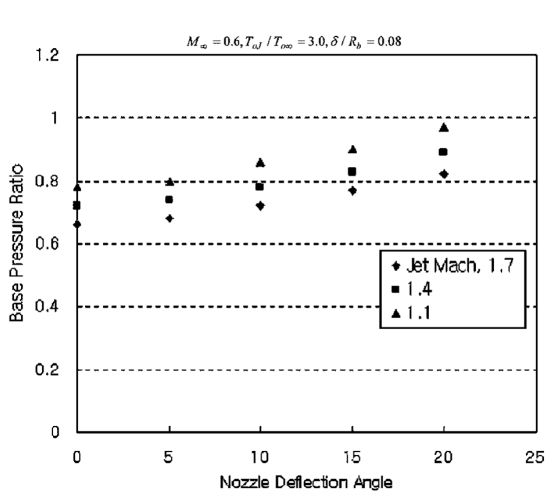

Figure 22: Effect of nozzle deflection angle (Ref. [39]).

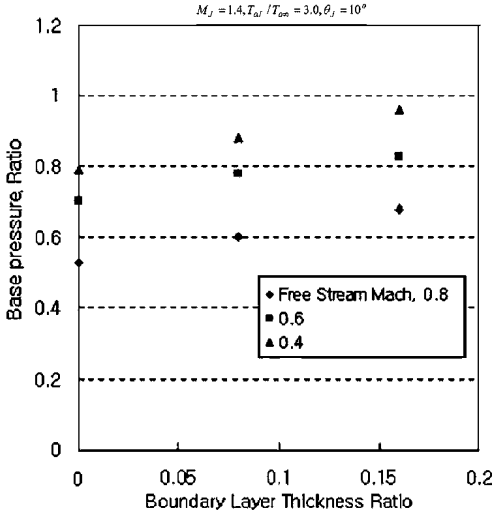

Figure 23: Effect of boundary layer thickness (Ref. [39]).

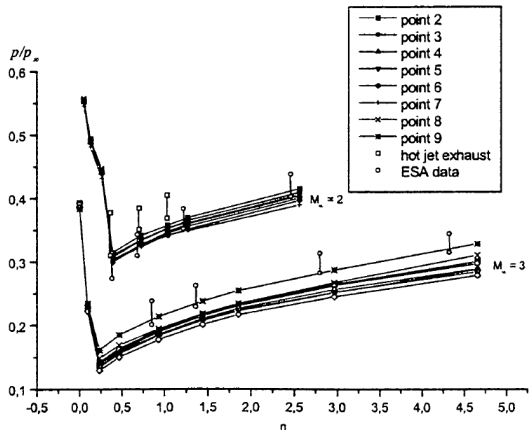

Figure 24: Effect of "combustion" chamber pressure for a short pylon length (Ref. [39]).

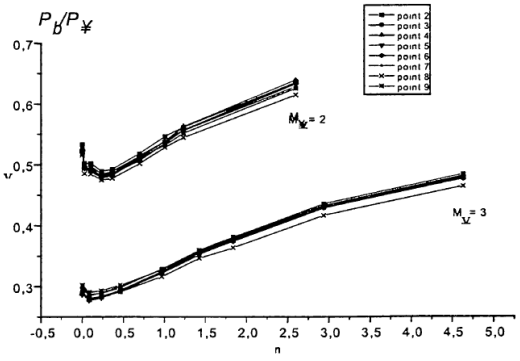

Figure 25: Effect of "combustion" chamber pressure for a long pylon length (Ref. [39]).

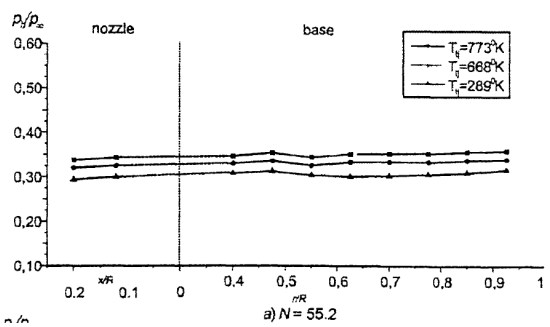

Figure 26: Effect of jet temperature (Ref. [39]).

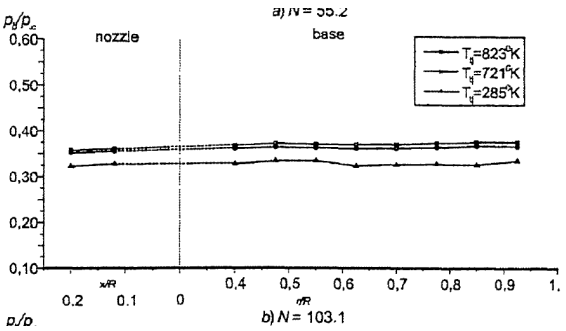

Figure 27: Effect of jet temperature (Ref. [39]).

2.3 Ariane 5 Ascend Conditions

2.3.1 Physical Properties at the Core Stage

Fig. 28 depicts the ascend of the Ariane 5 space transportation system in terms of altitude and Mach number. The ascend is a result of a simulation conducted within the department of *Supersonic and Hypersonic Technology Department* of the *German Aerospace Center*. The simulation tool was extensively tested in the past and double checked for the work here against the distinctive points along the ascend listed in the section *Flight sequence* released after every Ariane 5 launch (e.g. [20]).

The graph shows that the region of interest, namely the transonic flow region, is located in the troposphere between a height of 2 and 9 km. The troposphere exhibits a decreasing pressure, density and temperature with increasing altitude, which explains the course of the graphs following later. In these graphs, thermodynamic ratio are plotted over the Mach number since it is, as shown in Fig. 28, interlinked with the altitude and makes more sense for comparison with experiments or wind tunnel parameters.

Since this study is motivated by aft flow issues, which is influenced by the interaction between the exterior/ambient flow around the space transportation system and the plume from the nozzle, the physical properties exiting the nozzle need to be estimated. By using a program called the *Rocket Propulsion Analysis* [28], the physical properties at the nozzle exit can easily be calculated with a one-dimensional approach. The Vulcain 2 design parameters according to [16] are listed in Tab. 3 and are used as input parameters for before mentioned tool. The output is summed up in Tab. 4. Since the two operational modi of the Vulcain 2 are used during the Ariane 5 ascend and since these to modes do not differ by much, the exit conditions are considered to be constant. The one-dimensional approach is justified because it can be used without further ado and is sufficient to describe the driving mechanisms.

Table 3: Vehicle design parameters of H173 Ariane 5E [16].

Engine designation		Vulcain 2	
Propellant		LOX/H2	
Chamber pressure	p_{CC}	11.5	MPa
Nozzle expansion ratio	ϵ	58.5	
Mixture ratio	O/F	6.1:1	

Table 4: Physical properties at the nozzle exit of Vulcain 2 calculated with [28].

Nozzle exit pressure	p_e	0.0153	MPa
Nozzle exit density	ρ_e	0.0198	kg/m^3
Nozzle exit temperature	T_e	1330.3	K
Nozzle exit velocity	v_e	4322.6	m/s
Nozzle exit Mach number	Ma_e	4.41	

The ratio between of the driving physical parameters is used to describe the relation between the ambient flow (subscripted with $_\infty$) and the nozzle flow at the exit (subscripted with $_e$). One of the most important parameters with respect to the plume shape is the *Nozzle Pressure Ratio* (NPR) shown in Fig. 29. The blue curve represents the results with an exit pressure as given by an one-dimensional isentropic expansion, the pink curve uses the nozzle exit pressure from a two-dimensional numerical simulation with a truncated ideal contour (TIC) nozzle comparable to Vinci 2 nozzle ([7]). The exit pressure of the latter is taken at the exit in the boundary layer along the contour.

The NPR determines if the nozzle flow is overexpanded ($NPR < 1$), adapted ($NPR = 1$) or underexpanded ($NPR > 1$). Fig. 29 reveals that the nozzle flow is overexpanded in the whole transonic regime. The TIC nozzle indicates an adapted state at Mach 1.2. But, this is only valid for the pressure at the contour. In the core though, flow still features a lower static pressure since this is where the nozzle reaches first high Mach numbers.

The NPR is also, besides the Mach number of the nozzle, an influencing parameter for flow separation within the nozzle. The higher the ambient pressure is, the lower is the NPR and the more likely is the flow to separate in the nozzle. A separated nozzle flow is, due to high side loads, an undesired state, and thus kept small by an appropriate design in the nominal case.

Since the one-dimensional analysis (blue curve) indicates a flow separation in the nozzle due to the low NPR (see [13]), the two-dimensional approach with a higher exit pressure

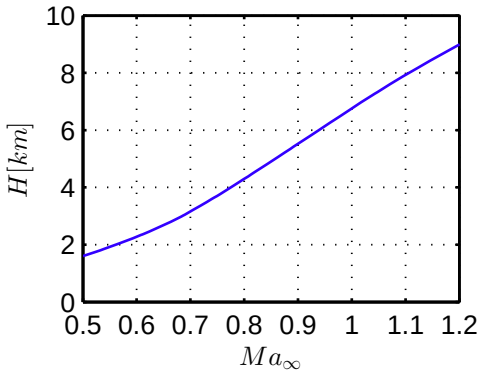

Figure 28: Altitude over ambient Mach number for Ariane 5 for the transonic flow regime.

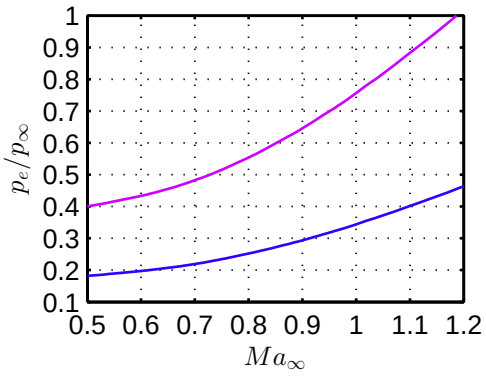

Figure 29: Nozzle pressure ratio (NPR) over Mach number for the ascend of Ariane 5. Blue for 1D (Tab.4), pink for 2D approach (numerical simulation of D. Banuti).

(higher NPR) due to the truncated geometry is plotted in the same graph to show that the flow actually does not separate in the nominal case. Note again, that one of the objectives of the one-dimensional investigation is to identify sensitivities and to study similarities between flight and experiment.

The NPR is increasing with higher Mach numbers, which is due to the decreasing ambient pressure at higher altitudes. The risk of flow separation reduces correspondingly. Similar courses can be found for the density ratio and the temperature ratio according to Fig. 30 and Fig. 31, respectively. The rocket engine parameters at the exit stay constant, while the ambient temperature and the density decrease with altitude in the troposphere. The temperature ratio was chosen since it plays an important role with respect to viscosity effects.

Further, the space transportation gains obviously speed, which is reflected in the decreasing velocity ratio in Fig. 32. The counteracting course of the velocity ratio and the density ratio result in an turning pint in the impulse density course in Fig. 33. Velocity and density gradients play an important role in the formation of Kelvin-Helmholtz vortices. Interesting here is that buffeting was found to be highest at about Mach 0.8 [8].

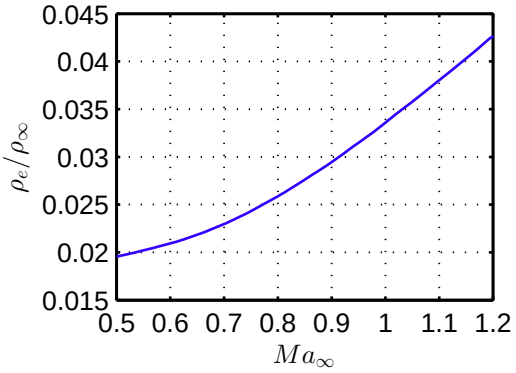

Figure 30: Density ratio over Mach number for the ascend of Ariane 5.

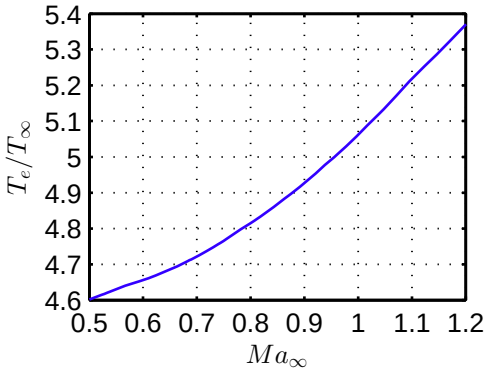

Figure 31: Temperature ratio over Mach number for the ascend of Ariane 5.

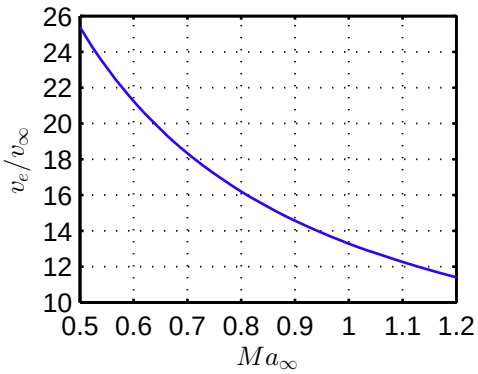

Figure 32: Velocity ratio over Mach number for the ascend of Ariane 5.

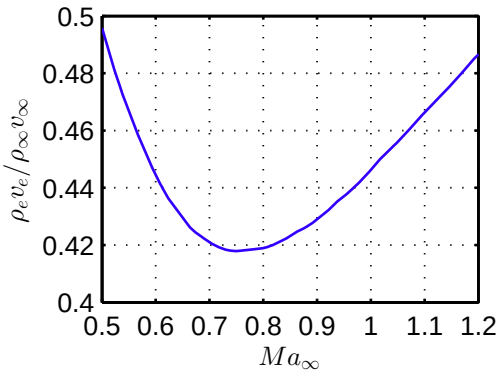

Figure 33: Impulse density ratio over Mach number for the ascend of Ariane 5.

2.3.2 Physical Properties at the Boosters

The conditions at the exit of the booster nozzle and the accompanying similarity ratios during the ascend are determined correspondingly. Tab. 5 shows the main engine parameters of the *P240* booster of *Ariane 5*. These engine parameters define the conditions at the exit of the nozzle, which are shown in Tab. 6.

Table 5: Vehicle design parameters of P240 booster of Ariane 5E [16].

Engine designation		P240 Ariane 5E	
Propellant		HTPB1814	
Chamber pressure	p_{CC}	6.13	MPa
Nozzle expansion ratio	ϵ	10.36	

Obviously, the conditions at the boosters change during the ascend as well. Fig. 34 to **??** reflect the similarity ratios again for the pressure, density, temperature, velocity and impulse density. Note, that the pressure ratio for the booster is higher, which is due to the adaption of the nozzle flow to lower altitudes. Consequently, the nozzle flow is less sensitive to flow separation.

Table 6: Physical properties at the nozzle exit of P240 booster calculated with [28].

Nozzle exit pressure	p_e	0.0896	MPa
Nozzle exit density	ρ_e	0.1465	kg/m^3
Nozzle exit temperature	T_e	2137.7	K
Nozzle exit velocity	v_e	2569.5	m/s
Nozzle exit Mach number	Ma_e	3.0	

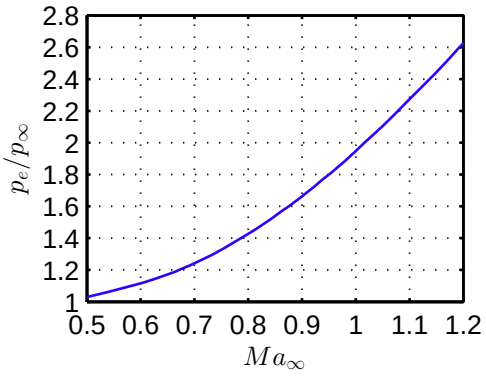

Figure 34: Pressure ratio over Mach number for the boosters during Ariane 5 ascend.

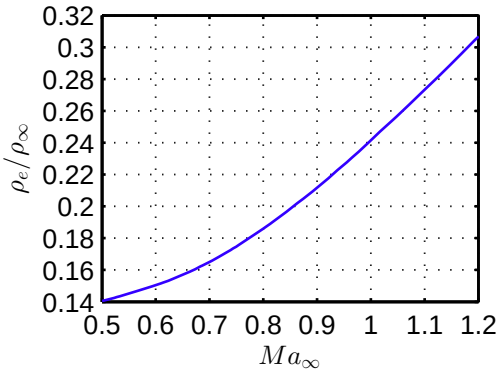

Figure 35: Density ratio over Mach number for the boosters during Ariane 5 ascend.

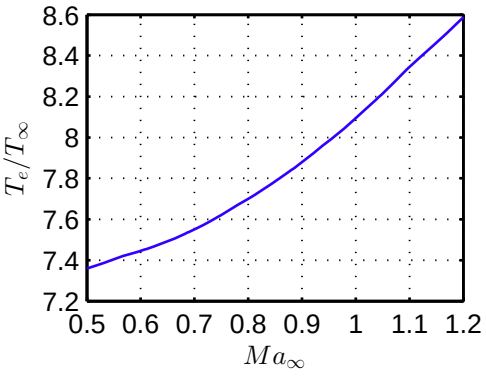

Figure 36: Temperature ratio over Mach number for the boosters during Ariane 5 ascend.

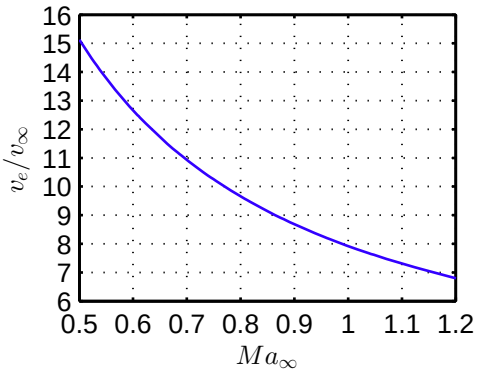

Figure 37: Velocity ratio over Mach number for the boosters during Ariane 5 ascend.

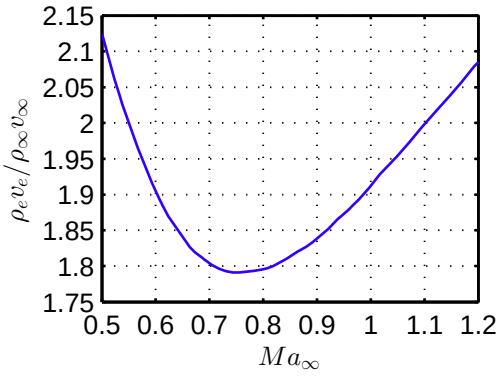

Figure 38: Impulse density ratio over Mach number for the boosters during Ariane 5 ascend.

2.4 Experimental Simulation of Ariane 5 Ascend

In the following section, it is discussed how space transportation systems can be simulated in experiments. As baseline, the *Ariane 5* is chosen with the core stage and the boosters. Consequently, it is studied how a hot plume can be realized with hydrogen/oxygen combustion and also with solid propellants. The latter also applies on the newest member of the European space transportation system, the *Vega*. If desired, a similar investigation can also be done with methane/oxygen combustion, which has been in consideration for future systems as well [19].

2.4.1 Rocket Engine Model Definition - Core Stage

In the next step, the objective is to determine the mass flow for the rocket engine model with hydrogen/oxygen combustion. A figure of merit to measure the performance of the combustion chamber independently from the nozzle characteristics is the characteristic velocity given in Eqn. 1 [35]. The second version of the equation is dependent on the gas properties like the isentropic exponent κ, the intrinsic in the specific gas constant R on the molecular mass and the temperature in the combustion chamber. The mass flux $\frac{\dot{m}}{A_t}$ can now be determined easily for a given combustion chamber pressure p_{CC}.

$$c^\star = \frac{p_{CC} A_t}{\dot{m}} = \frac{\sqrt{\kappa R T_{CC}}}{\kappa \sqrt{[2/(\kappa+1)]^{(\kappa+1)/(\kappa-1)}}} \tag{1}$$

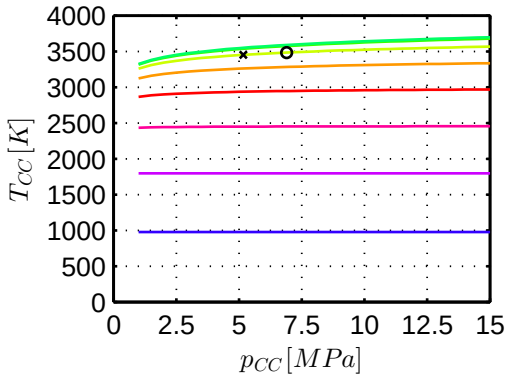

Figure 39: Combustion chamber temperature as function of mixture ratio and combustion chamber pressure.

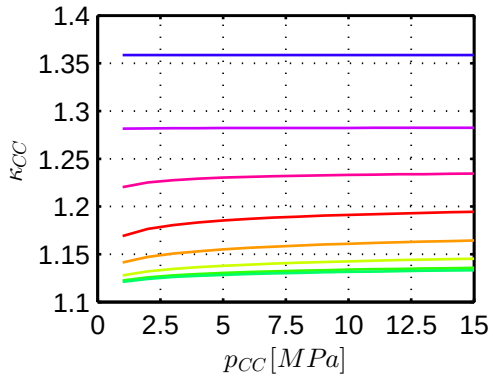

Figure 40: Isentropic exponent as function of mixture ratio and combustion chamber pressure.

The calculation is being done with the before mentioned *Rocket Propulsion Analysis* tool [28]. It uses a method based on minimizing Gibbs free energy to find a stable equilibrium for the gas composition and temperature in the combustion chamber. Some of the results are plotted in Fig. 39 to Fig. 41.

Fig. 39 shows that the combustion chamber temperature is independent from the combustion chamber pressure for mixture ratios far from the stoichiometric ratio. Mixture ratios closer or with the stoichiometric ratio reveal that a dependency of the combustion chamber temperature on the pressure. The amount of heat released is related to the equilibrium of the gas composition, which is a function of pressure for higher temperatures. This is where the method of minimization of the Gibbs free energy, also called chemical potential, comes into play. The cross and the circle refer to properties related to the reference combustion chamber introduced later.

The change of the gas composition is also reflected in the isentropic exponent shown in Fig. 40. The relation (Eqn. 1) explains why the characteristic velocity depicted in Fig. 41 increases for an increasing mixture ratio and decreases again. The increase is due to the higher temperature and the decrease is the results of the decreasing isentropic exponent. As it can be seen in Fig. 42, the mass flux then just linearly scales with desired combustion chamber pressure.

The mass flux is now determined for any rocket engine burning hydrogen and oxygen. Selecting an appropriate throat diameter delivers the total mass flow and the hydrogen and oxygen mass flow for the desired combustion chamber pressure. Scaling studies before revealed that a throat diameter of approximately 8 mm is applicable to simulate Ariane 5-like conditions while taking into account an expansion ratio of about $A_e/A_t = 58.5$. The corresponding exit diameter of the nozzle contour is 61.2 mm and the corresponding outer diameter of the main body results in 158 mm, which refers to the generic Ariane 5

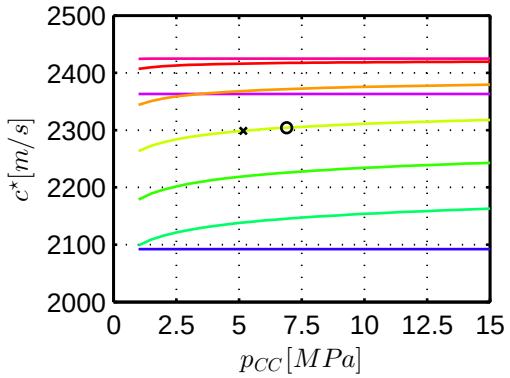

Figure 41: Characteristic velocity as function of mixture ratio and combustion chamber pressure.

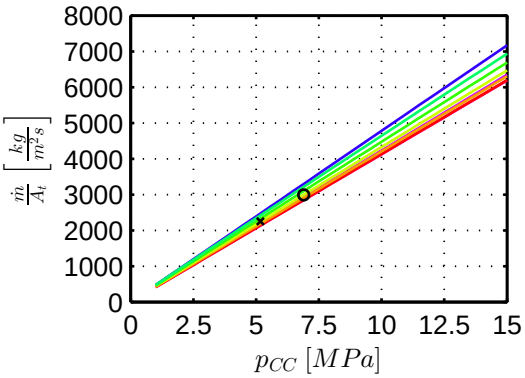

Figure 42: Mass flux as function of mixture ratio and combustion chamber pressure.

dimensions where the nozzle exit diameter is approximately 0.4 times the diameter of the main body. The results are presented in Fig. 43 to Fig. 45.

For a better overview, the design parameters are listed again in Tab. 7. The first two lines represent the required mass flow for scaled Ariane 5-like conditions, the second two lines denote the recommended design parameters for the hot plume facility, which takes a smaller expansion ratios into account. Consequently, the feeding system is designed with a margin for higher mass flow rates. This can be assigned again to a corresponding throat diameter.

Table 7: Mass flow for a mixture ratio of $O/F = 6$.

Combustion chamber pressure p_{CC}	Expansion ratio ϵ	Mass flux $\frac{\dot{m}}{A_t}$	Throat diameter d_t	Mass flow $\dot{m}$	
11.5 MPa	58.5	4971.0 $\frac{\text{kg}}{\text{m}^2\text{s}}$	8 mm	hydrogen oxygen	36 g/s 214 g/s
6.89 MPa	20	2990.1 $\frac{\text{kg}}{\text{m}^2\text{s}}$	13.7 mm	hydrogen oxygen	63 g/s 378 g/s

The combustion chamber is now defined with respect to the physical properties and the mass flow required. In the following, the properties at the end of the nozzle are calculated to compare the similarity parameters. Usually, the flow is considered to be frozen with respect to the gas composition downstream from the nozzle throat. Thus, the isentropic exponent in the throat region (Fig. 46) and the corresponding gas constant (Fig. 47)

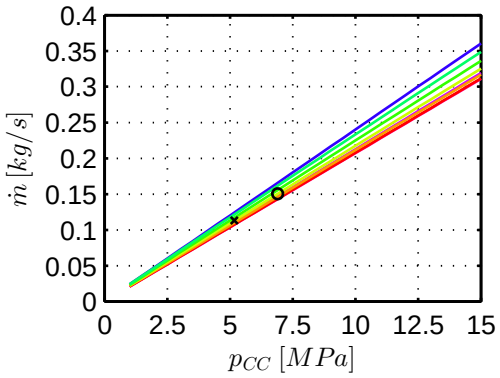

Figure 43: Total mass flow as a function of mixture ratio and combustion chamber pressure.

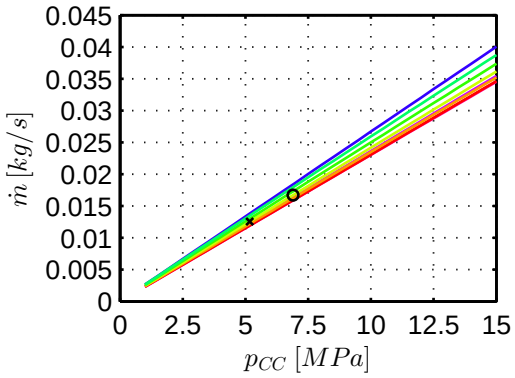

Figure 44: Hydrogen mass flow as a function of mixture ratio and combustion chamber pressure.

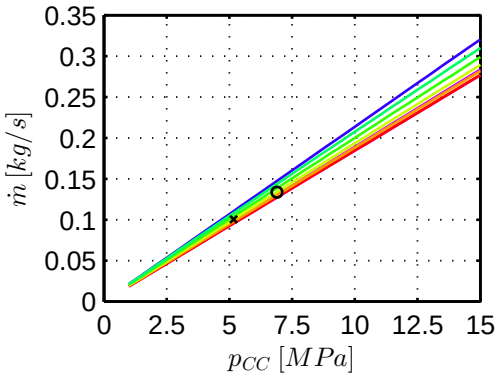

Figure 45: Oxygen mass flow as a function of mixture ratio and combustion chamber pressure.

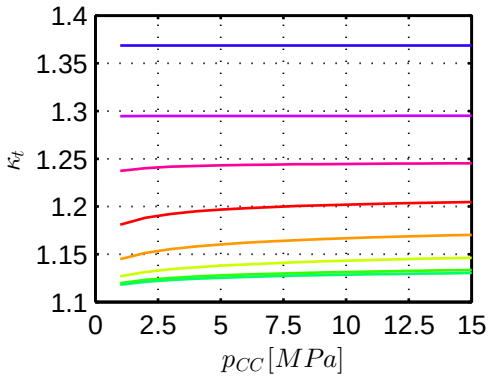

Figure 46: Isentropic exponent in the throat area for as function of mixture ratio and combustion chamber pressure.

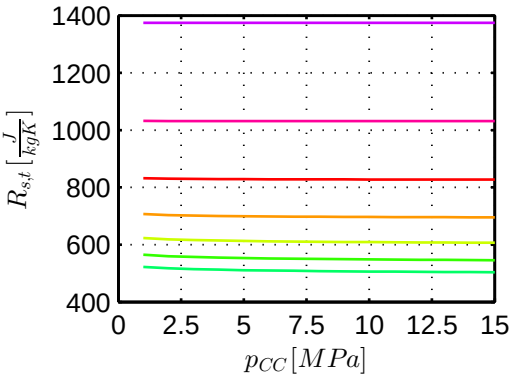

Figure 47: Gas constant in the throat area for as function of mixture ratio and combustion chamber pressure.

can be used to calculate properties at the nozzle exit assuming an isentropic expansion. But these values here are only given for completeness. The *Rocket Propulsion Analysis* tool allows to to take a shifting equilibrium into account in the nozzle expansion. These values are used here since they are somewhat more accurate.

The physical properties like the exit pressure, temperature, density, velocity, impulse density and Mach number as function of the initial combustion chamber pressure and the mixture ratio are given in Fig. 48 to Fig. 53 for the Ariane 5-like expansion ratio of 58.5. Fig. 48 shows that the exit pressure is obviously higher for higher combustion chamber pressures, and also for higher mixture ratio, ergo combustion chamber temperatures. The exit temperature is mainly a function of the mixture ratio (Fig. 49). This again defines the exit velocity (Fig. 51) according to Eqn. 2 (one-dimensional, ideal nozzle), and thus the exit Mach number (Fig. 53). The exit density is bound to the behavior of the exit pressure (Fig. 50) and consequently, the course of the impulse density is accordingly (Fig. 52).

$$v_e = \sqrt{\frac{2\kappa}{\kappa - 1} R T_{CC} \left[1 - (\frac{p_{CC}}{p_e})^{(\kappa-1)/\kappa}\right]} \tag{2}$$

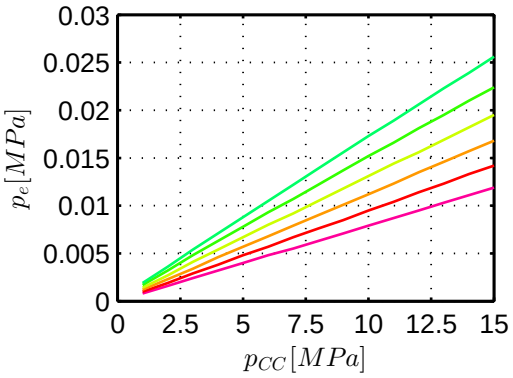

Figure 48: Exit pressure as a function of mixture ratio and combustion chamber pressure.

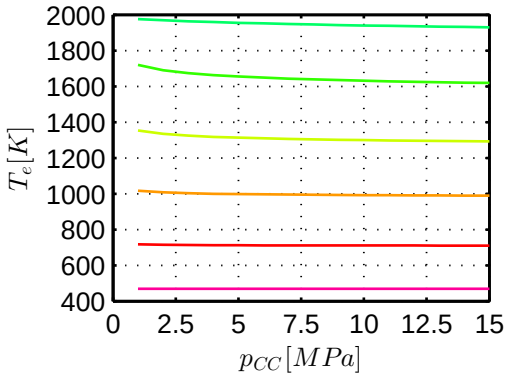

Figure 49: Exit temperature as a function of mixture ratio and combustion chamber pressure.

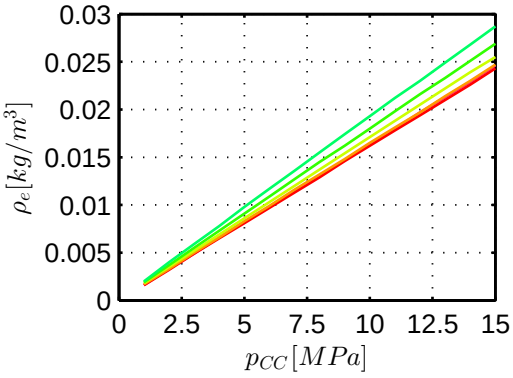

Figure 50: Exit density as a function of mixture ratio and combustion chamber pressure.

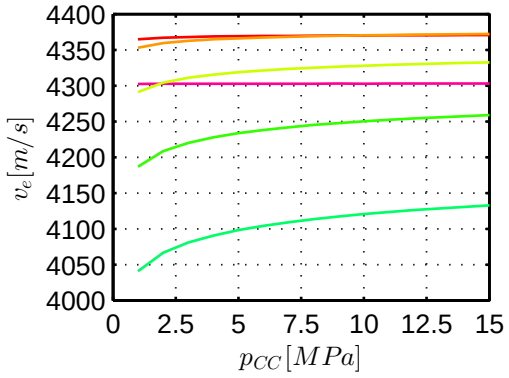

Figure 51: Exit velocity as a function of mixture ratio and combustion chamber pressure.

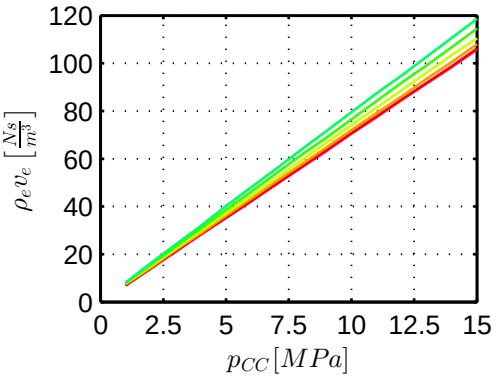

Figure 52: Exit impulse density as a function of mixture ratio and combustion chamber pressure.

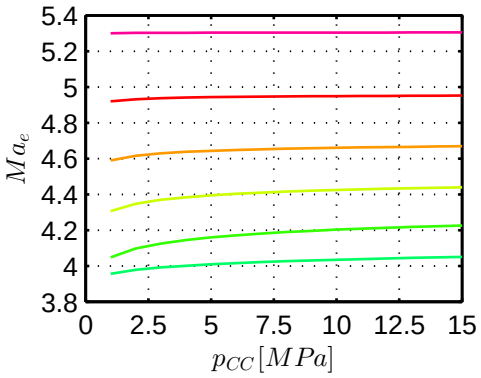

Figure 53: Exit Mach number as a function of mixture ratio and combustion chamber pressure.

2.4.2 Rocket Engine Model Definition - Boosters

The previous section described the circumstances of how to mirror the conditions for the core stage of the Ariane 5 ascend with hydrogen/oxygen combustion. Solid propellants, as they are used today for the Ariane 5 boosters, can now be used to simulate exactly the same in the wind tunnel model, meaning the nozzle flow from the booster.

Future concepts of Ariane 6 consider rocket engines with solid propellants as first stages and second stage. Thus, rocket plumes which are similar with respect to most aspects of the Ariane 6 configuration can be tested by wind tunnel models using solid propellants.

Additionally, if the chemical composition of the plume is not taken into account for plume-interaction investigations, it can be used to simulate the flow from the core stage of Ariane 5. The advantage here lays on the simplicity of the self-contained system, the high combustion chamber pressure supply and the nozzle exit velocities that are comparable to flight conditions.

For the design of solid rocket engine, the *Klemmung* is required to determine the throat diameter of the nozzle for a given combustion chamber pressure. *Klemmung* reflects the ratio between the burning surface area A_b and the throat diameter A_t as shown in Eqn. 3. For a given burn rate at a desired combustion chamber pressure p_{CC} and a given characteristic velocity $c^\star$ and density of the solid propellant ρ_P, the *Klemmung* can be calculated according to Eqn. 4.

$$K = A_b/A_t \tag{3}$$

$$p_{CC} = K\rho_P c^\star r \tag{4}$$

Fig. 54 and Fig. 55 show the aforementioned dependency for two representatives, for a double-base solid propellant and a composite propellant based on AP+AN (ammonium perchlorate + ammonium nitrate), HTPB (hydroxyl-terminated polybutadiene), and aluminum, respectively. The latter curve describes an exponential behavior as given by the *Saint Robert*'s law (a.k.a. *Vieille*'s law). The corresponding coefficients for a formulation with 20% nanometric powder of the total aluminum powers of and an oxidizer ratio between AN and AP of 0.6/0.4 are extracted from Ref. [9]. Note that double-base propellant do not follow the St. Robert's law and are determined through experiments.

These two solid propellants were exemplarily selected for wind tunnel testing for the reasons described hereafter. Double-base propellants do not develop toxic and corrosive plumes like composite solid propellants with AP. It can be used without considerations of the toxic and corrosive effects on humans or the wind tunnel, respectively. At the *Supersonic and Hypersonic Technology Department* exists a longterm experience with the handling and usage of double-base propellants (e.g. Ref. [33], Ref. [34]).

The latter choice reflects ongoing research activities towards 'green propellants' involving the desire to find a less toxic/corrosive formulation (e.g. Ref. [5], Ref. [9]). Formulations, as currently used for the Ariane 5 boosters or Vega with pure AP as oxidizer were already tested in VMK. The proposed ecologically safer propellant can be tested in VMK without imposing any additional constraints. The 'green propellants' incorporates a certain percentage of AN to reduce the environmental impact due to hydrochloric contents in the plume and uses nanometric aluminum powders to compensate to a certain degree the diminished specific impulse.

The essential statement of the graphs is, that solid propellants can be used to simulate realistic nozzle flows since very high combustion chamber pressures and comparably high combustion chamber temperatures can be reached. Comparably here refers to hydrogen/oxygen combustion. The pressure can be adjusted and the conditions at the nozzle exit adapt correspondingly with an appropriate expansion ratio, meaning desired and realistic exit conditions can be met. The influence of the expansion ratio on the Mach number for a double-base solid propellant is given in Fig. 56. The temperature is an influential parameter for the potential velocity, which is mentioned to be relatively high ($\sim 2300\,\mathrm{K}$). Further, it shall be emphasized that solid propellant stages like the Ariane 6 configuration can be duplicated.

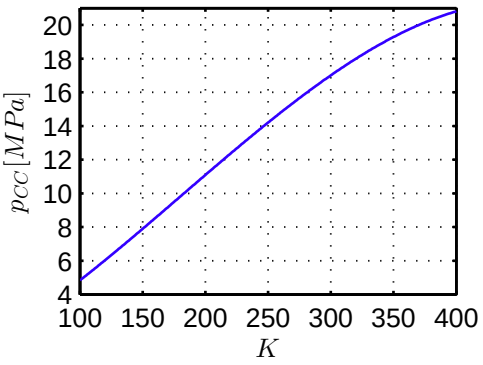

Figure 54: Combustion chamber pressure as function of Klemmung for a typical double-based solid propellant.

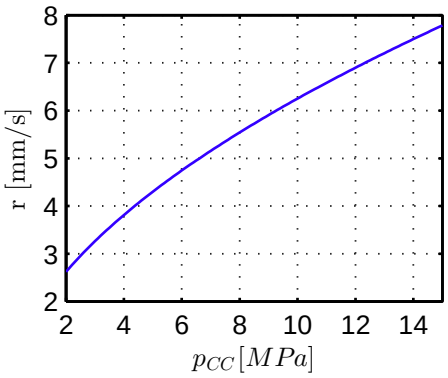

Figure 55: Burn rate as a function of combustion chamber pressure for a composite solid propellant with AP, HTPB, aluminum.

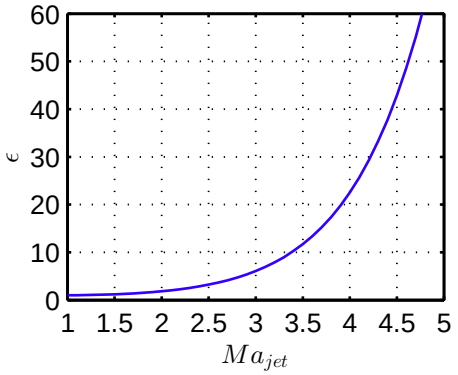

Figure 56: Expansion ratio over Mach number for $\kappa = 1.235$.

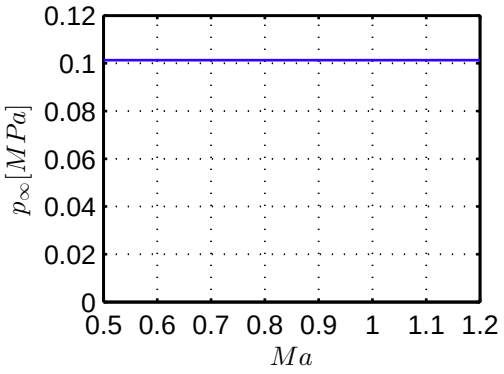

Figure 57: Free stream pressure in the wind tunnel as a function of the Mach number.

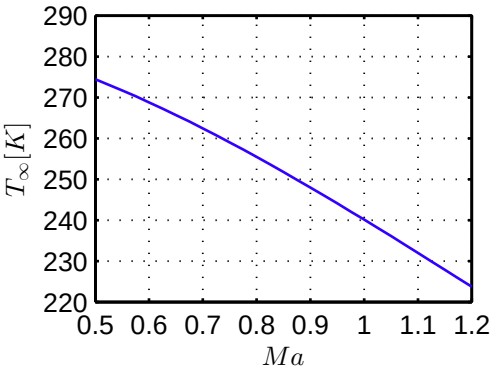

Figure 58: Free stream temperature in the wind tunnel as a function of the Mach number.

2.4.3 Simulation Environment - Wind Tunnel Conditions

The exterior flow can be simulated with wind tunnels with either open or closed measurement sections. The flow in an open measurement section like the VMK is expanded to the atmospheric pressure, meaning the ambient pressure is imposed to the flow field. TMK features a transonic measurement section with perforated walls, which is, at its current state, calibrated the free stream pressure of 0.1 MPa. The reservoir temperature could be also be varied, which would lead to an increased velocity for a constant Mach number. This is usually not done. Thus, for similarity studies later, the free stream flow condition are given in the following for an ambient pressure of 0.1 MPa and for a reservoir temperature of 288.15 K as a function of the Mach number.

Fig. 57 shows the imposed ambient pressure imposed on the free stream for the complete transonic Mach number range. The isentropic expansion causes the temperature to drop according to Fig. 58, which consequently causes an increase of the the density in the flow field Fig. 59. The expanding air then reaches velocities dependent on the Mach number according to Fig. 60. The impulse density increases correspondingly as depicted in Fig. 61.

For completeness, the mass flow is given exemplarily for Mach 0.8 and 1.2. A cylindrical nozzle of 600 mm delivers for the conditions mentioned previously a mass flow rate of $\sim$ 104 and $\sim$ 160kg/s, respectively. In comparison to supersonic tests, this is a rather high mass flow rate, which explains why transonic tests are more costly.

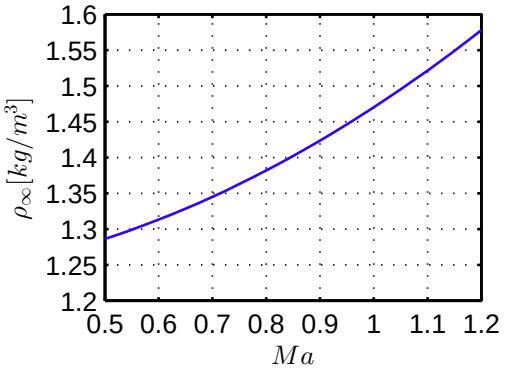

Figure 59: Free stream density in the wind tunnel as a function of the Mach number.

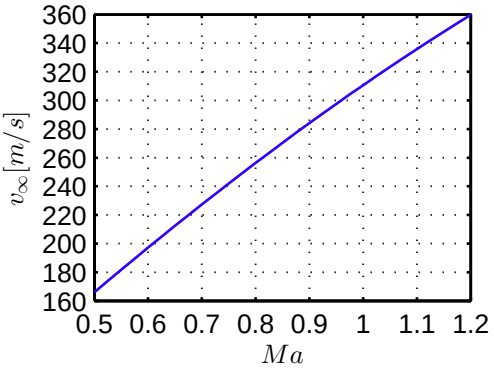

Figure 60: Free stream velocity in the wind tunnel as a function of the Mach number.

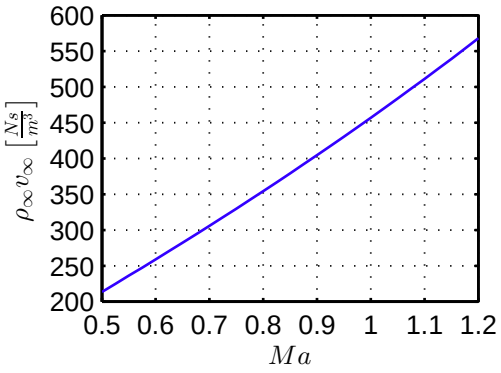

Figure 61: Free stream impulse density in the wind tunnel as a function of the Mach number.

2.5 Similarity: Ariane 5 Flight vs. Wind Tunnel Simulation

In this section, the Ariane 5 flight is opposed to the wind tunnel simulation for a fixed condition of the wind tunnel model combustion chamber. As baseline for the comparisons between flight and experiment, a combustion chamber pressure of 6.89 MPa, equal to 1000 psi, a mixture ratio of 6.0 and an expansion rate of 58.5 is used. These reference conditions have been marked with a circle in the graphs from Fig. 39 to Fig. 45. The cross represents the combustion chamber pressure used in [24].

The first parameter above is chosen since the later introduced combustor is rated for a combustion chamber pressure of 1000 psi, and is one of the standard pressures investigated for a variety combustion chambers [35]. The second is at about a mixture ratio found for most oxygen/hydrogen based rocket engines [16], and the last refers to an expansion ratio found for the Vinci 2 rocket engine. In this section, the curves of reference case are always marked in red.

The methodology to judge the similarity is to simply divide the physical properties resulting from the experiments by the ones from the flight. This is no similarity in a classical sense where non-dimensional numbers, mainly the Reynolds number and the Mach number, are kept equal. For the planned investigations, the Mach number of the ambient flow is similar to flight by simply imposing as operational condition for the wind tunnel. It is shown in Fig. 53 that the Mach number at the nozzle exit of the wind tunnel model indeed reach Mach numbers comparable to flight. But, this involves sufficient combustion chamber pressures to prevent flow separation in the nozzle.

Similarity with respect to the Reynolds number is not possible since the difference of the dimensions can not be compensated by adjusting the kinematic viscosity or the velocity without taking extreme measures for a complete new wind tunnel facility. The pressure in the measurement section would need be very high. Additionally, it was shown in several previous studies presented in [27] that the effect of the Reynolds number on the base pressure is negligible as long as the boundary layer is turbulent.

The physical properties have been provided before for the flight and the planned simulations. As a result, a good similarity of a certain property is 1. As before, the pressure, density, temperature, velocity and impulse densities are investigated over for the whole Mach number range. In order to reveal the sensitivities and to show the direction in which the system can be moved, the comparisons are done for different expansion ratios (ϵ = 10, 20, 40, 58.5), mixture ratios (O/F = 4, 6, 8) and combustion chamber pressures (p_{CC} = 1.0, 6.89, 15.0 MPa). The relatively high mixture ratio 4 was added to the list since the thermodynamic library used in the *Rocket Propulsion Analysis* tool does not deliver results for the high expansion ratio of 58.5, meaning low temperatures at the exit of the nozzle for mixture ratios at about 1. Lower mixture ratios are very interesting because moderate combustion chamber temperatures still lead to high and

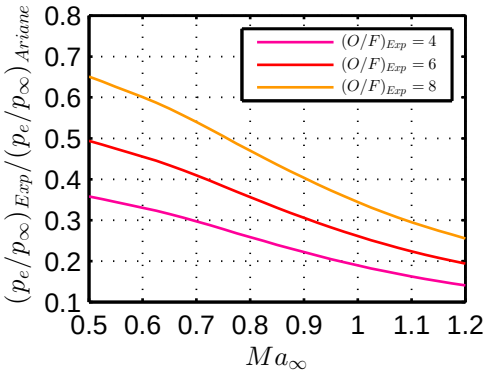

Figure 62: Pressure ratios between experiment and flight for different mixture ratios over Mach number.

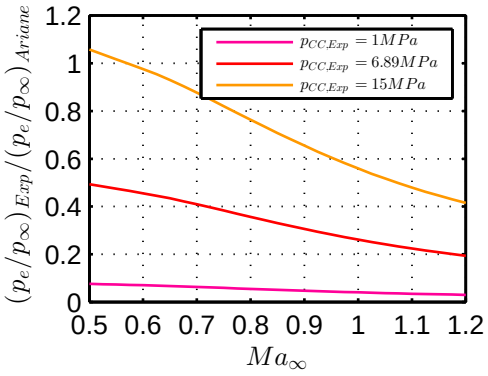

Figure 63: Pressure ratios between experiment and flight for different combustion chamber pressures over Mach number.

comparable exit velocities. Thus, this mixture ratio is used to show the tendency of the system.

It should be kept in mind that these influencing parameters come with a cost. For example, higher mixture ratios come with higher combustion chamber temperatures, ergo higher thermal loads. An increase of the combustion chamber pressure is equivalent to an increase concerning the mass flow, but also a higher risk for combustion instabilities. A higher mass flow is also the consequence for lower expansion ratios if the exit diameter is kept constant.

As it can be seen in Fig. 62 to Fig. 64, the pressure ratio is smaller in the experiment then in flight. This is the result of a decreasing ambient pressure with altitude in the troposphere. A change to higher the mixture ratio has only a small influence (Fig. 62). Increasing the combustion chamber pressure actually results in comparable conditions at least in the low Mach number range (Fig. 63). The third approach of decreasing the expansion ratio seems to be promising in order to achieve comparable pressure ratios (Fig.64).

It is not surprising to notice, that the course of the density ratio shown in Fig. 65 to Fig. 67 is comparable to the pressure ratio. An additional, but negligible factor comes into play due to the fact that the density at the exit of the wind tunnel nozzle becomes higher with increasing Mach numbers. Generally, it can be stated that the similarity with respect to the density between flight and experiment deviates stronger for higher Mach numbers. As adjusting screw, the expansion ratio again seems to be the preferred parameter as shown in Fig. 67. The mixture ratio (Fig. 65) and the combustion chamber pressure (Fig. 66) have the same effects as for the pressure. The higher the combustion chamber pressure or the closer to stoichiometric, the closer to the flight conditions.

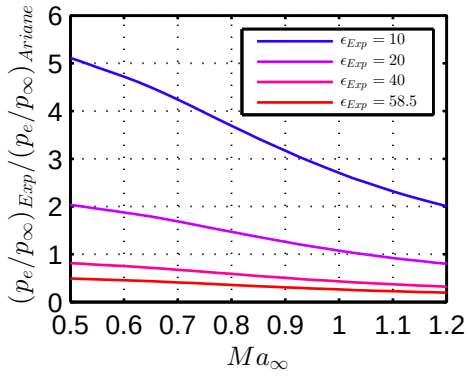

Figure 64: Pressure ratios between experiment and flight for expansion ratios over Mach number.

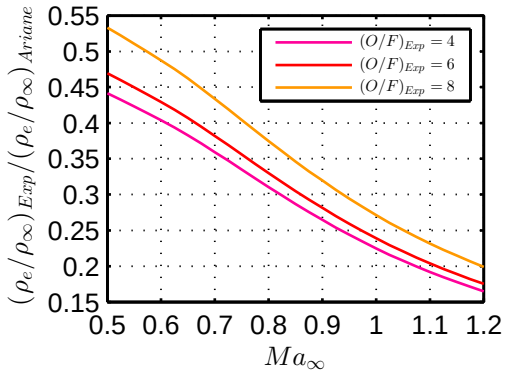

Figure 65: Density ratios between experiment and flight for different mixture ratios over Mach number.

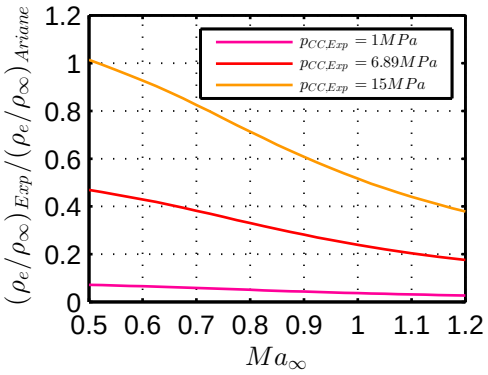

Figure 66: Density ratios between experiment and flight for different combustion chamber pressures over Mach number.

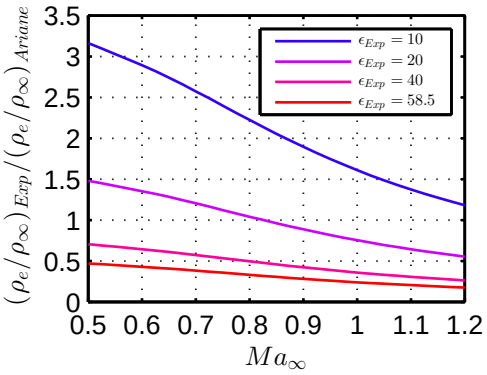

Figure 67: Density ratios between experiment and flight for expansion ratios over Mach number.

The temperature ratio depicted in Fig. 68 to Fig. 70 shows that the experiments meet the flight conditions almost perfectly for the reference combustion chamber. Obviously this is due to the similar mixture ratio and expansion ratio. In this case, there is no need for an adjustment of the mixture ratio (Fig. 68), but it shows the spectrum that can be covered. A pressure change in the combustion chamber model (Fig. 69) does not influence the temperature ratio by much. The slight variation results from the shift in the equilibrium of the gas composition. It is good to see that a different expansion ratio only changes modestly the temperature ratio Fig. 70 since, as discussed before, the expansion is considered as one of the screws to adjust the similarity parameters.

The closely to the temperature ratio related velocity ratio consequently meets the similarity with this respect as well as it can be seen in Fig. 71 to Fig. 73. The mixture

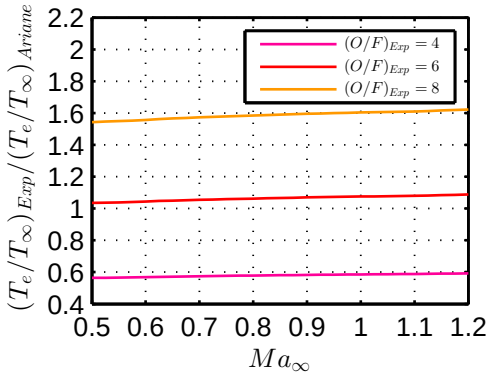

Figure 68: Temperature ratios between experiment and flight for different mixture ratios over Mach number.

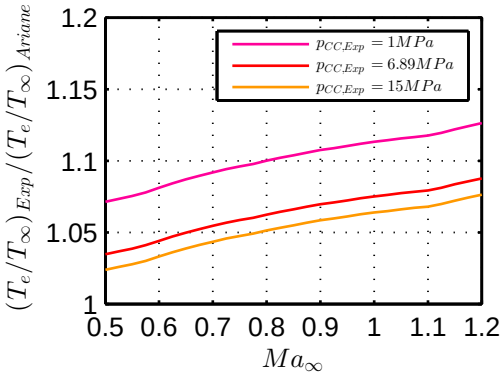

Figure 69: Velocity ratios between experiment and flight for different combustion chamber pressures over Mach number.

ratio itself does not impact the velocity ratio as much as it can be observed for the temperature ratio (Fig. 68). This aspect was discussed before and is interesting in a sense that high exit velocities are reached for moderate combustion chamber temperatures. Another interesting aspect is shown in Fig. 73: The difference between experiment and flight conditions even for an expansion ratio of 20 is only about 5%, meaning the pressure ratio can be increased by adjusting the expansion ratio without a major difference with respect to the velocity ratio. This behavior can be explained with the lower molar mass, ergo a higher gas constant for lower mixture ratios (see Eqn. 2). As expected, combustion chamber pressure exhibits a minor influence (Fig. 72).

The impulse density ratio as a result of the multiplication of the density and velocity ratio resembles the course of the density ratio (Fig. 74 to Fig. 77). The decreasing density with altitude in the troposphere is notable in impulse density ratio. As before, the most promising approach to compensate for that seems to be a smaller expansion ratio, which is depicted in Fig. 77.

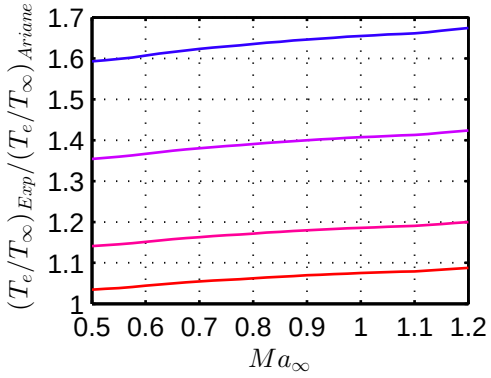

Figure 70: Temperature ratios between experiment and flight for expansion ratios over Mach number.

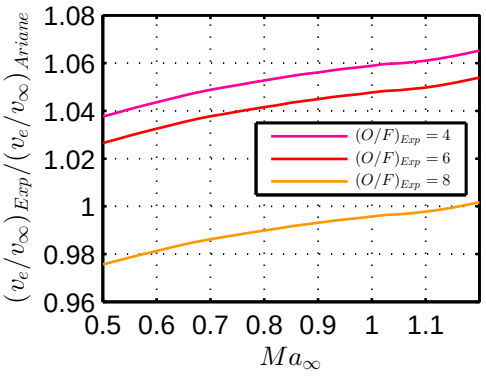

Figure 71: Velocity ratios between experiment and flight for different mixture ratios over Mach number.

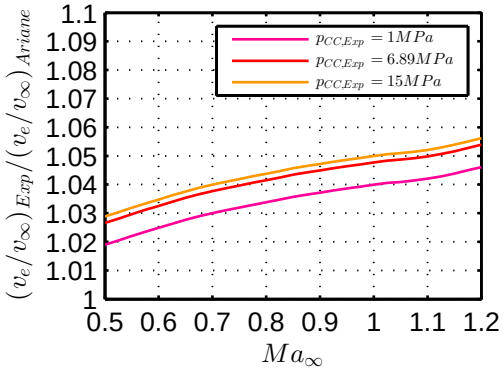

Figure 72: Velocity ratios between experiment and flight for different combustion chamber pressures over Mach number.

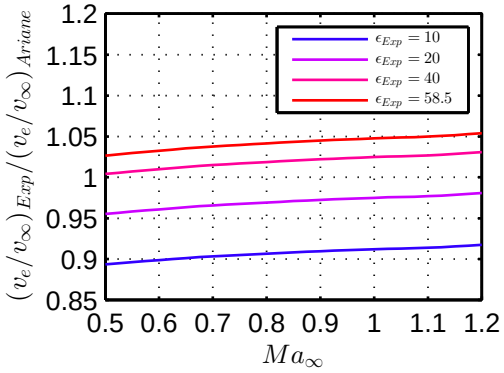

Figure 73: Velocity ratios between experiment and flight for expansion ratios over Mach number.

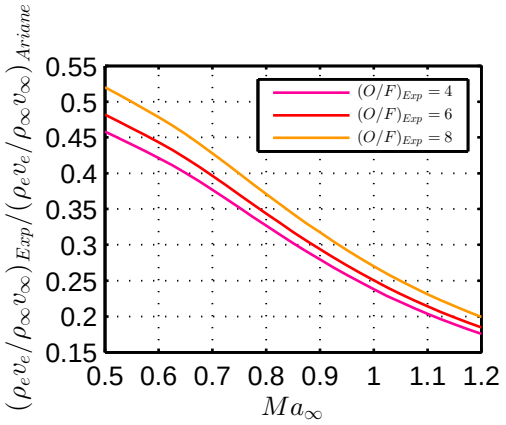

Figure 74: Impulse density ratios between experiment and flight for different mixture ratios over Mach number.

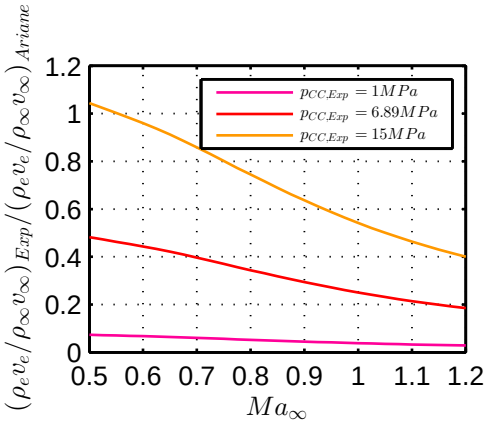

Figure 75: Impulse density ratios between experiment and flight for different combustion chamber pressures over Mach number.

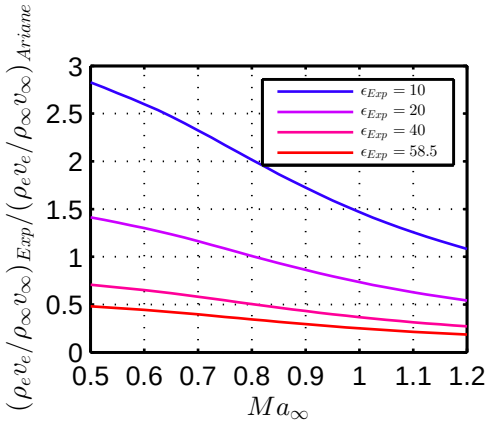

Figure 76: Impulse density ratios between experiment and flight for expansion ratios over Mach number.

Deutsches Zentrum
für Luft- und Raumfahrt e.V.

TN2200

Scaling Issues

May 24, 2013

Daniel Banuti

Institute of Aerodynamics
and Flow Technology
Department Spacecraft

DLR **Deutsches Zentrum
für Luft- und Raumfahrt** e.V.
in der Helmholtz-Gemeinschaft

ESA STUDY CONTRACT REPORT

No ESA Study Contract Report will be accepted unless this sheet is inserted after the coverpage of each volume of the Report.

ESA CONTRACT No.: AO/1-6731/ 11/NL/SFe	SUBJECT Hot Testing Facility for ELV Propulsion Characterization		CONTRACTOR DLR
* ESA CR( )No	* STAR CODE	No of TN 2200	

ABSTRACT:

This report identifies relevant scaling parameters as output of the work performed in the framework of the ESA technology research project "Hot Testing Facilities for ELV Propulsion Characterization". First, an overview is given to the results of previous studies. Then, the effect of the TEG and H_2 dump and an lower mixture ratios is investigated numerically in detail. The first issue is driven by the question if the TEG dump is required to be resolved in experiments and the second issue is motivated by the desire to conduct experiments at lower combustion chamber temperatures due to constraints imposed on the wind tunnel model. The numerical simulations are executed for two distinct points of the Ariane 5 ascend, which are at Mach 0.86 and 1.2. It has been found that the TEG and H_2 dump can be neglected in the simulations without significantly influence thee shear layer. The fuel rich operation point simulation revealed a very good agreement with realistic conditions.

The work described in this report was done under ESA contract. Responsibility for the contents resides in the author or organization that prepared it.

Name of author: D. Banuti (DLR, Goettingen, Germany)

** NAME OF ESA STUDY MANAGER	** ESA BUDGET HEADING
N. Murray DIV: TEC-MPA DIRECTORATE: D\TEC	

* Sections to be completed by ESA

** Information to be provided by ESA Study Manager

3 Scaling Issues - TN2200

CONTENT

1 Introduction

Aiming for the development of the next generation of launch vehicles, basic research is still necessary to understand contributing physical phenomena. Interaction of the nozzle exhaust with the surrounding gas is one of these topics which is at the same time also highly relevant from the technical point of view. As such, it has been investigated previously, e.g. as part of the work on buffeting reduction (see Lüdeke and Calvo [4]). While this elaborate numerical work has been supported by experiments, one major shortcoming has not been improved upon so far: up to this point, no technical facility is capable of simulating a hot exhaust gas with realistic physical properties. A positive theoretical feasibility study has been carried out by Frey [5]. Today, this topic is still of immediate relevance, e.g. concerning launcher stage separation [1][3].

Thus, it is the goal of the TRP “Hot testing facilities for ELV propulsion characterization” [2] to investigate conditions and ultimately install a hot plume test facility.

In order to support the design of the facility and suitable models, it is the purpose of this report to give an overview of relevant nondimensional parameters and of flow phenomena in the vicinity of rocket nozzles. Computational Fluid Dynamics (CFD) simulations will be employed to serve this purpose. Special attention will be given to the reachable exit velocity when using a model operating point of the combustion chamber.

2 Identification of relevant similarity rules

While scaling and similarity rules are topics well treated in the aerospace literature, plume scaling in particular has not been treated much. This has been pointed out by Frey who carried out a feasibility study on plume simulations in wind tunnels as part of the ESA TRP on buffeting reduction [5]. In inviscid supersonic flow, similarity is reached for similarity in Mach number and isentropic exponent γ, as can be found in any gas dynamics textbook, such as Liepmann and Roshko [11] . Pure geometrical scaling is hence sufficient if suitable adjustment of γ is possible. This, however, is not sufficient in the cases regarded in this report.

The reasoning of Frey, whose report is mainly concerned with the development of a scaling law and the investigation of the role of axial velocity scaling, is as follows: the subsonic wake flow at the rocket base is determined by its interaction with the nozzle or nozzle plume. The nozzle plume can only communicate with the surrounding flow via the shear layer separating the plume from the environment. Two means can be identified, first the shape of the plume, second entrainment of surrounding fluid. While the plume shape is mainly determined by inviscid scaling laws, the shear layer clearly is not. Furthermore, classical Goethert scaling [6] has also been found to be inappropriate for launcher wake flow as it is mainly concerned with clustered nozzle plume interaction and neglects effects of Mach number and exit velocity.

Being mainly concerned with the development of the plume in the vicinity of the nozzle exit when regarded at a single point of the trajectory, Frey proposes six similarity parameters which should ensure similarity between original and simulated plume. They are visualized in Figure 1 which depicts the top cut through a nozzle lip with flow discharging to the right.

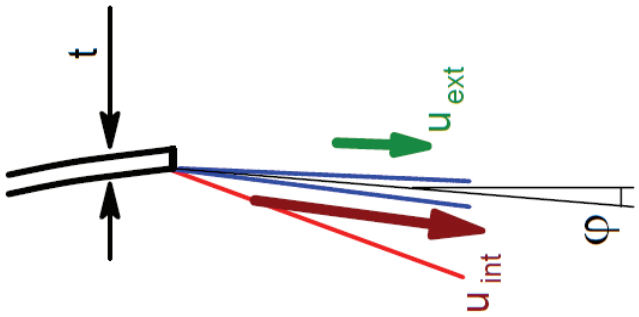

Figure 1: Similarity parameters at nozzle lip (from Frey [5])

- u_{int} plume velocity after adaption to ambient pressure
- u_{ext} surrounding flow velocity
- ρ_{int}/ρ_{ext} density ratio of adapted plume and ambient flow
- Tu degree of turbulence
- φ angle between shear layer direction and nozzle axis
- t nozzle lip thickness

Frey concludes that “the most important parameters for turbulent shear layer growth are the velocities on both sides of the shear layer – either as velocity ratio or as velocity difference – and the respective density ratio.” He furthermore stresses that the most difficult parameter to

achieve is the exit velocity, and in fact devotes large parts of his report to the treatment of this problem. Figure 2 illustrates nozzle exit velocities estimated with a simplified inviscid 1D treatment of optimal expansion into vacuum using the classical Eq. (1) from [11]

$$u_{\max} = \sqrt{\frac{2\gamma}{\gamma - 1}\frac{\Re T_0}{\mathrm{M_{mol}}}} \tag{1}$$

where u_{max} , γ , T_0, R, M_{mol} are exit velocity, ratio of specific heats, total temperature, ideal gas constant and molecular weight, respectively.

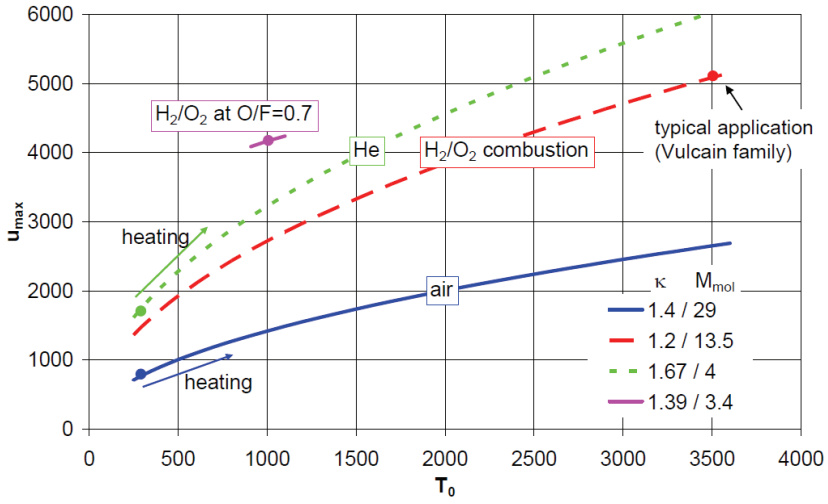

Figure 2: Exhaust velocity of different nozzle operation points (from Frey [5])

It becomes evident that a reduction of T_0, while desirable from an operational point of view in the experimental facility, greatly increases the difficulty of attaining a sufficiently high exit velocity in order to achieve similarity. Frey suggests an alternative point of operation of the combustion chamber, i.e. an oxidizer mass to fuel mass mixture ratio of 0.7 instead of 7.1 in order to yield high exit velocities.

Thus, in this work, the focus will be set on an investigation of exit velocities at the two operating points.

CFD

2.1 Computational Method and Model

Computations are carried out using the DLR TAU Code. It is discussed in detail in the literature see e.g. [7][8]. TAU is a hybrid grid, finite volume second order accuracy flow solver. It has been validated for a variety of steady and unsteady flow cases, ranging from sub- to hypersonic Mach numbers.
As the investigated geometries are essentially axisymmetric in this work, all computations are carried out in two dimensions under assumption of axisymmetry. For this initial study, the involved gases are treated as a mixture of nonreacting ideal gases. Regarded species are H_2, H, O_2, O, H_2O, OH, HO_2, H_2O_2, N_2.
The reservoir composition inside the combustion chamber is computed with NASA's "Chemical Equilibrium and Applications" (CEA) code by Gordon and McBride [9][10].

2.2 Geometry and Grid

The Vulcain2 nozzle configuration is chosen for this investigation due to prior experience with the geometry. A rendering with a 90° cut out can be seen in Figure 3. The combustion chamber is seen on the left, flow direction is left to right. The structure seen in the middle of the nozzle is characteristic for the Vulcain2 configuration: the turbine exhaust gas (TEG) created in the gas generator cycle as well as the hydrogen of the combustion chamber wall dump (H_2 dump) cooling are introduced into the flow to act as film cooling downstream and provide additional thrust (a blow up of the grid in this region can be seen in Figure 7).

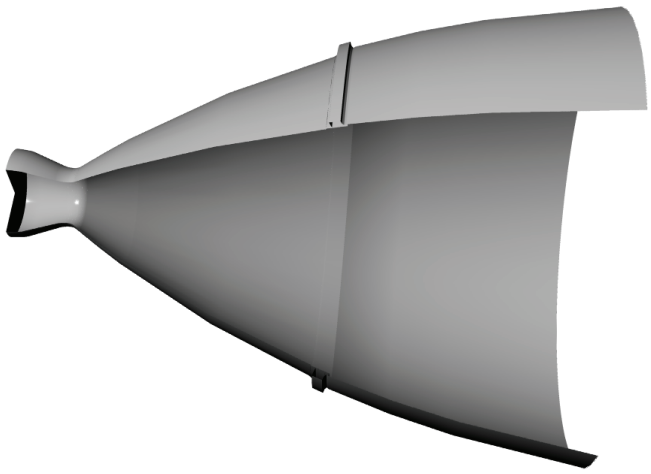

Figure 3: Vulcain2 nozzle rendered with cutaway

The nozzle can be treated as 2D axisymmetric. A small initial grid is shown in Figure 4, for cases where the supersonic wake region is of prime importance. The outer dimensions of the farfield are ten by ten nozzle exit diameters D, the grid is refined only in the wake region.

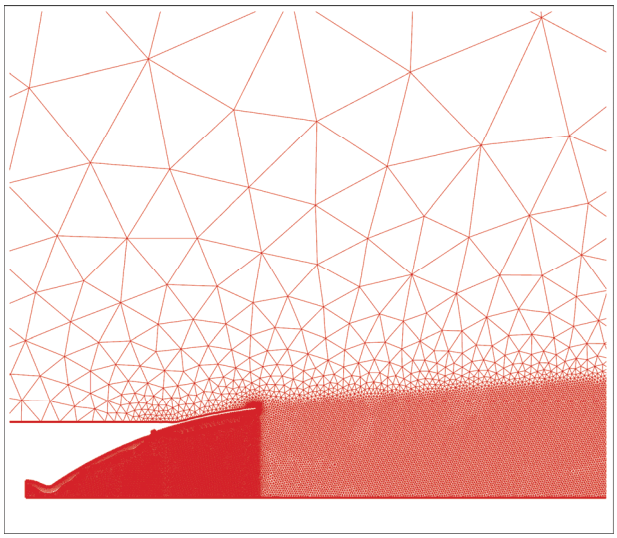

Figure 4: Cut out of original grid, 10D x 10D

However, for this work, the shear layer and its interaction with surrounding flow is important. Thus, an improved grid had to be created. Figure 5 shows the complete new grid, its outer dimensions are 100 times 100 the nozzle exit diameter to account for the influence of boundary conditions in subsonic flow. Left, right, and top sides are treated numerically as farfield boundary conditions (BC).

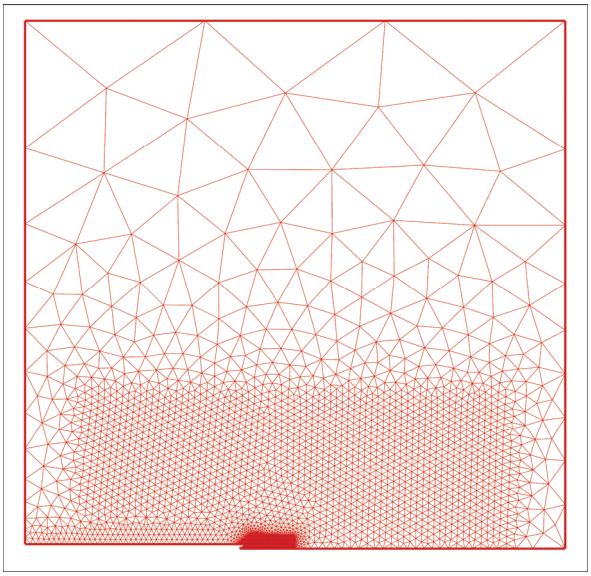

Figure 5: Grid total 100D

Figure 6 shows the nozzle and wake region. It can be seen that the refined region is extended to the outer nozzle side and includes a prism layer to account for shock formation and boundary layer buildup, respectively. The nozzle walls, inside and outside, are treated numerically as viscous walls. The bottom edge is assumed to be an axisymmetry axis. The generic “rocket body” is modeled as an inviscid wall to minimize influence of this arbitrary

structure. The outer side of the nozzle protruding from this cylinder is modeled as viscous wall.

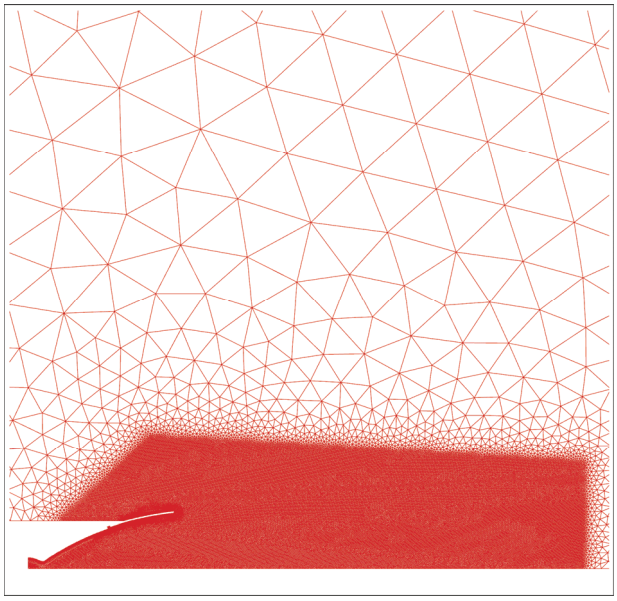

Figure 6: Blow up of nozzle and wake region

As a specialty of the Vulcain2 engine, TEG and H_2 dump act as inlet boundaries. A detail of this region is depicted in Figure 7. The TEG expands through a throat and enters the nozzle supersonically. Numerically, the top wall of the TEG is modeled as a reservoir boundary condition, the H_2-dump is treated as a Dirichlet boundary condition.

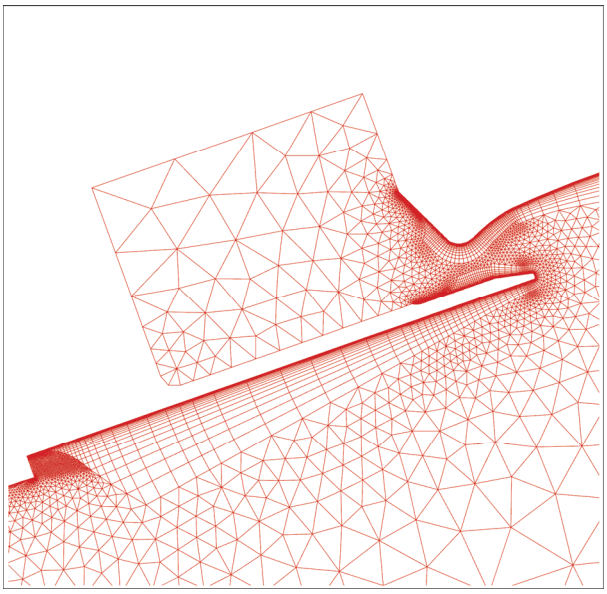

Figure 7: Grid detail of H2 dump and TEG

2.3 Flow conditions

The realistic Vulcain2 engine conditions, as used in the Buffeting TRP, are compiled in Table 1. Boundary type refers to the numerical model used for the respective inlet: reservoir assumes an isentropic expansion from total conditions, Dirichlet boundary conditions (BC) prescribe the mentioned values at the inlet. Thus, velocity is not a prescribed value of a reservoir boundary condition, just as total values are not set for the Dirichlet BC. Gas composition is listed in terms of mass fraction.

		Main chamber	TEG	H_2 dump
Boundary type		Reservoir	Reservoir	Dirichlet
Mass flow	kg/s	313.23	8.5	2.67
Mass flow fraction		0.965567201	0.026202219	0.00823058
Temperature	K	3668.55	628.562	352.0
Total density	kg/m^3	5.8944	0.36922	-
Total Pressure	Pa	1.19E+07	5.03E+05	-
Density	kg/m^3	5.641	0.027	2.0
Velocity		-	-	644.13
H_2 (mass fract.)		0.01973	0.46529	1.0
H		0.00206	0	0
O_2		0.0349	0	0
O		0.00951	0	0
H_2O		0.84927	0.53471	0
OH		0.08453	0	0
HO_2		0	0	0
H_2O_2		0	0	0
N_2		0	0	0

Table 1: Vulcain2 engine conditions

It can be seen that these conditions impose severe mechanical and thermal loads on involved structures. In order to reduce these stresses on experimental facilities, Frey [5] suggests an alternative mixture ratio of O/F = 0.7. This amounts to an adiabatic flame temperature of 1008K at still somewhat comparable exit velocities, as determined by Eq. (1). See Table 2 for a comparison of both conditions.

Name		**Chamber O/F 7.1**	**Chamber O/F 0.7**
Type		Reservoir	Reservoir
Mass flow	kg/s	313.23	313.23
Total Pressure	Pa	1.19E+07	1.19E+07
Temperature	K	3668.55	1008.2
Density	kg/m3	5.8944	4.8546
Molecular weight	g/mol	13.496	3.428
γ		1.141	1.363
H_2 (mass fract.)		0.01973	0.53609
H		0.00206	0
O_2		0.0349	0
O		0.00951	0
H_2O		0.84927	0.464
OH		0.08453	0
HO_2		0	0
H_2O_2		0	0
N_2		0	0
$u_{max, theor}$	m/s	6047.81	4285.17

Table 2: Adapted conditions; w/o TEG, H_2-dump / low T mixture ratio

Finally, Table 3 summarizes the test cases to be investigated in this study. Initially, the influence of TEG and H_2 dump needs to be investigated in order to decide whether it needs to be accounted for in further computations.[1] The remaining four cases are comprised of two mixture ratios at two trajectory points, respectively.

Case	**I**	**II**	**III**	**IV**	**V**	**VI**
Name	**TEG on**	**TEG off**	**M0.86 OF7.1**	**M0.86 OF0.7**	**M1.2 OF7.1**	**M1.2 OF0.7**
Grid	10D	10D	100D	100D	100D	100D
Type	Vulcain 2	Vulcain 2	Vulcain 2	Vulcain 2	Vulcain 2	Vulcain 2
H	n/a	n/a	5.07 km	5.07 km	8.99 km	8.99 km
Ma	0.7	0.7	0.86	0.86	1.2	1.2
p	0.697e5 Pa	0.697e5 Pa	0.551e5 Pa	0.551e5 Pa	0.330e5 Pa	0.330e5 Pa
T	300 K	300 K	273 K	273 K	244.3 K	244.3 K
O/F	7.1	7.1	7.1	0.7	7.1	0.7
TEG/H_2dump	on	off	on/off	on/off	on/off	on/off
Chemistry	frozen	frozen	frozen	frozen	frozen	frozen

Table 3: Test cases and external flow conditions

[1] As merely the difference between on and off is of interest, the smaller grid will be used for its computational efficiency.

3 Main Results

3.1 Grid independency

A grid independency study has been carried out to see whether the computational results vary with the discretization. Figure 8 to Figure 13 show the progression of grids and results. The internal flow and the shear layer are established rather quickly. The position of the Mach stem changes with different grids, however differences are negligible after the 4th adaptation. As the main interest of this study is the shear layer, grid convergence can be regarded as achieved.

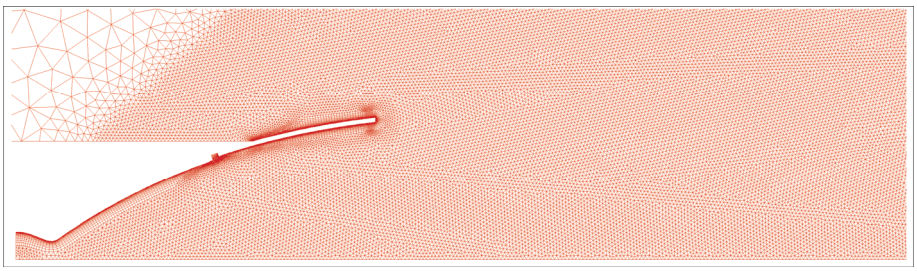

Figure 8: Original grid

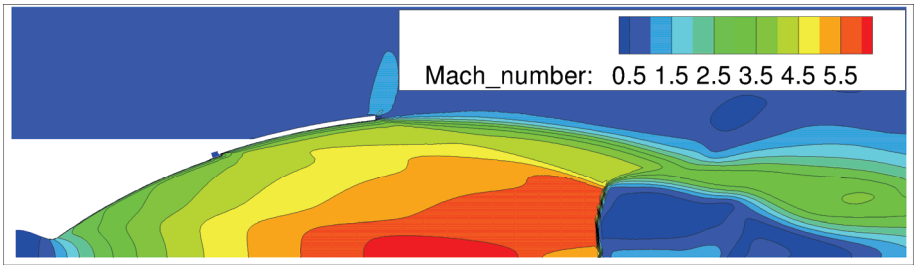

Figure 9: Result on unrefined grid

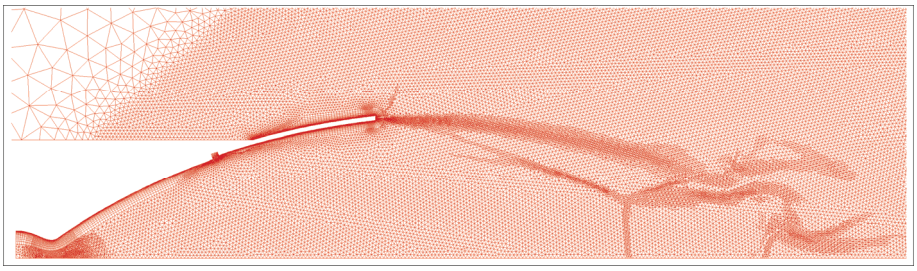

Figure 10: Grid after 2nd adaptation

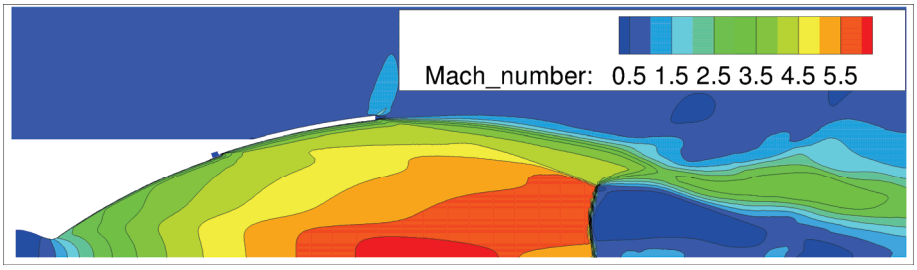

Figure 11: Result after 2nd adaptation

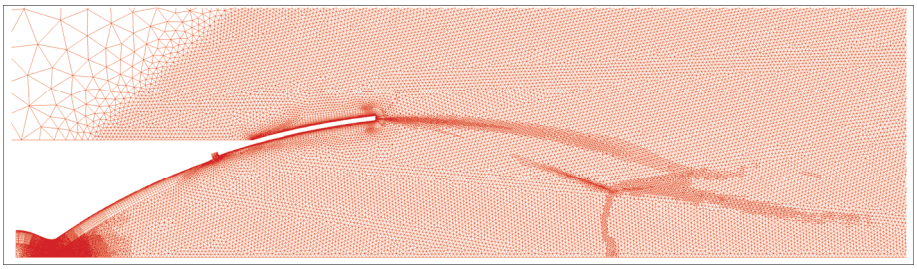

Figure 12: Grid after 5th and final adaptation

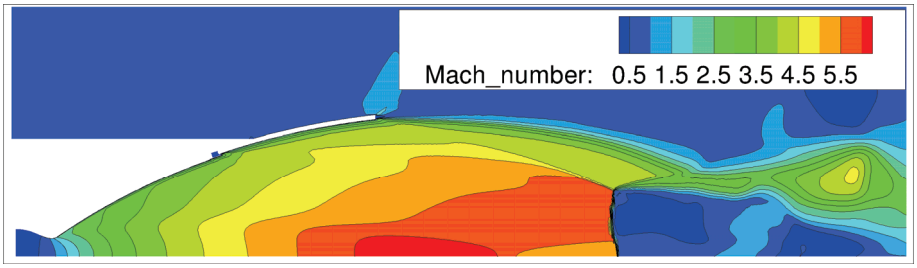

Figure 13: Result after 5th and final adaptation

3.2 Visualization

Results are shown either as contour plots or as profiles, extracted from the flowfield. The positions of these profiles are shown in Figure 14.

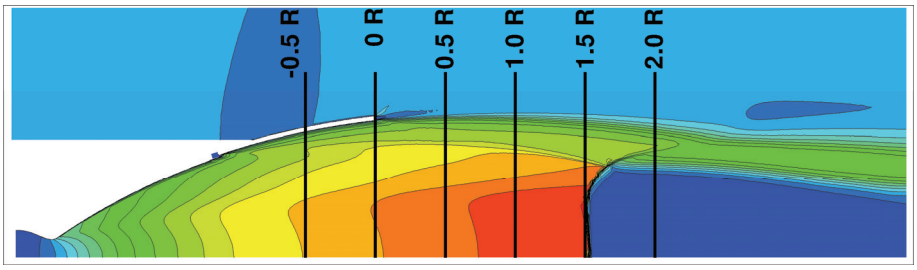

Figure 14: Positions of extracted profiles. R is the exit radius of the Vulcain2 nozzle. Reference plane (0 R) is the exit plane.

3.3 Influence of TEG and H_2 dump on overall nozzle flow

As discussed in 2.2, the Vulcain2 engine is equipped with a hydrogen dump and a turbine exhaust gas inlet that both feed into the nozzle. The nozzle has been chosen because of prior experience with the geometry as well as its relevance in European space flight. However, integration of these injection systems into a model complicates matters significantly for both experiment and computation. It is thus of prime importance to evaluate the contribution to the overall plume structure to decide whether it can be neglected.

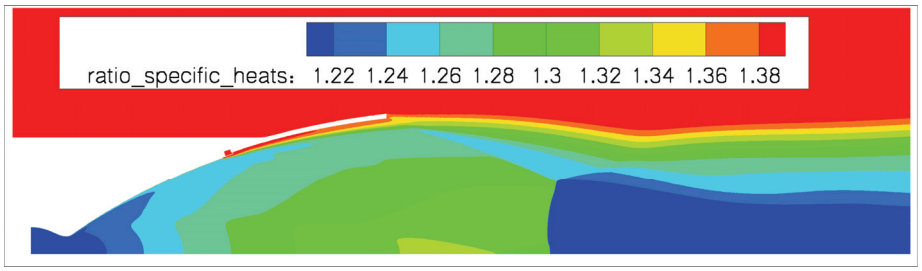

Figure 15: Case I: Ratio of specific heats γ with TEG/H_2 dump

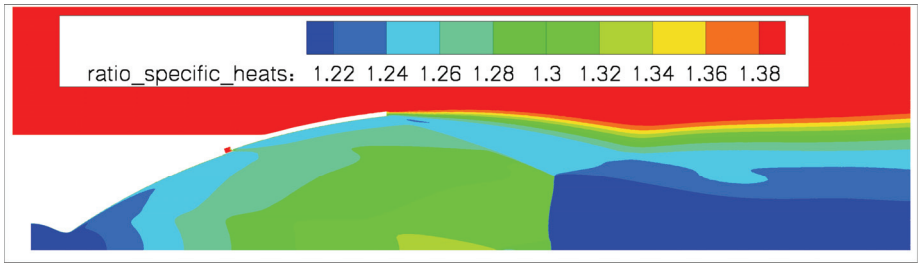

Figure 16: Case I: Ratio of specific heats γ w/o TEG/H_2 dump

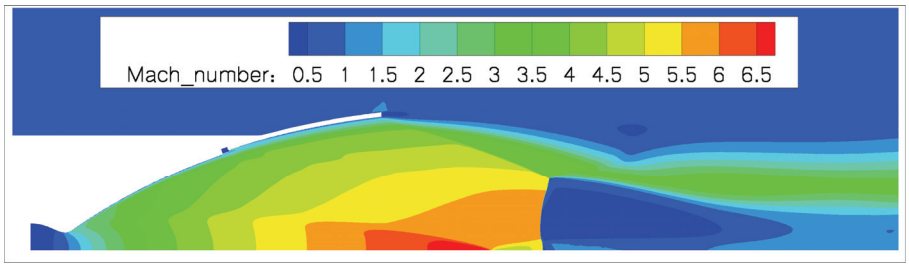

Figure 17: Case II: Mach number distribution with TEG/H_2 dump

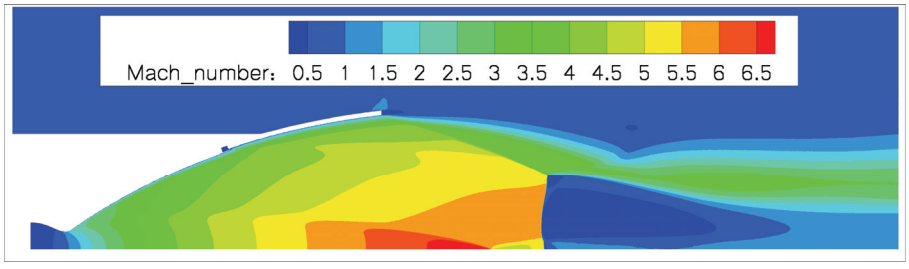

Figure 18: Case II: Mach number distribution w/o TEG/H_2 dump

Figure 15 to Figure 18 show results of computations which contrast the effect of TEG and H_2 dump. The difference in gas composition of the plume can best be seen in its effect on the ratio of specific heats, see Figure 15 and Figure 16. As compiled in Table 1: Vulcain2 engine conditions, a very hydrogen dominant[2] flow is injected through TEG and H_2 dump which is responsible for the layer of gas of approximately $\gamma = 1.4$.
However, as can be seen in Figure 17 and Figure 18, the effect on the overall plume structure is negligible. Key flow characteristics, such as shear layer angle or Mach stem position, are identical in both cases.

For the remainder of the study a simplified flow field without TEG and H_2 dump contribution will be regarded, i.e. cases III to VI of Table 3 will be carried out with TEG and H_2 dump off. Numerically this is taken into account be replacing the inflow boundary conditions with a wall boundary condition.

3.4 Subsonic trajectory point: Mach 0.86

The subsonic operation point corresponds to a flight altitude of 5 km at which a Mach number of 0.86 is reached, static pressure reaches 0.551e5 Pa. The flow accelerates to supersonic velocities at the nozzle tip. The plume is overexpanded and contracts after leaving the nozzle. Both cases depicted in Figure 19 and Figure 20 form a Mach reflection with a subsonic region behind the normal shock Mach stem. The shear layer can be seen to roll up behind the Mach disc where the velocity gradient between outer flow and subsonic wake is large. The influence on the shear layer development can be neglected. The different shock paths and Mach numbers reached can be attributed to the difference in the ratio of specific heats γ for cases III and IV, respectively.

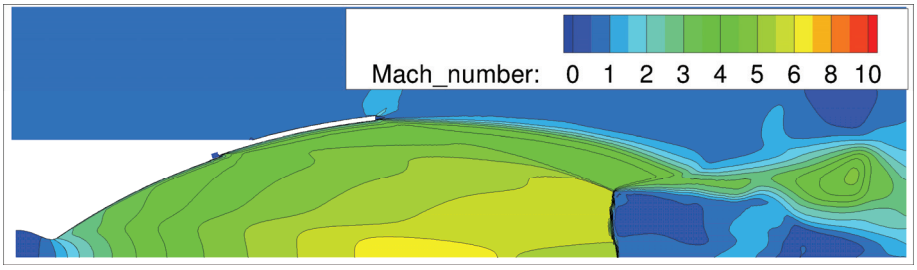

Figure 19: Case III: Ma = 0.86, O/F = 7.1; Mach number contours

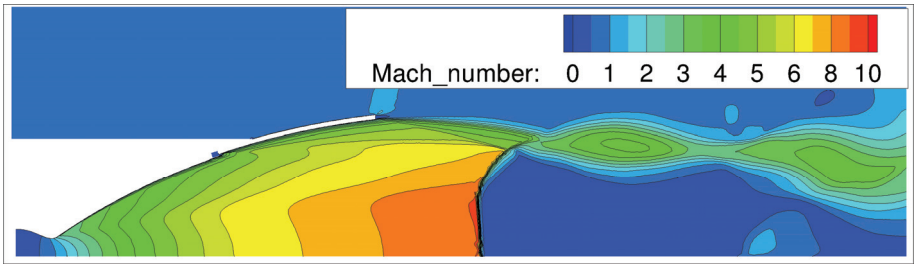

Figure 20: Case IV: Ma = 0.86, O/F = 0.7; Mach number contours

[2] Values are compiled in mass fractions, hydrogen mole (and thus volume) fractions hence are much larger.

Extracted profiles of Mach number and x-velocity showing more detail can be seen in Figure 21 and Figure 22.

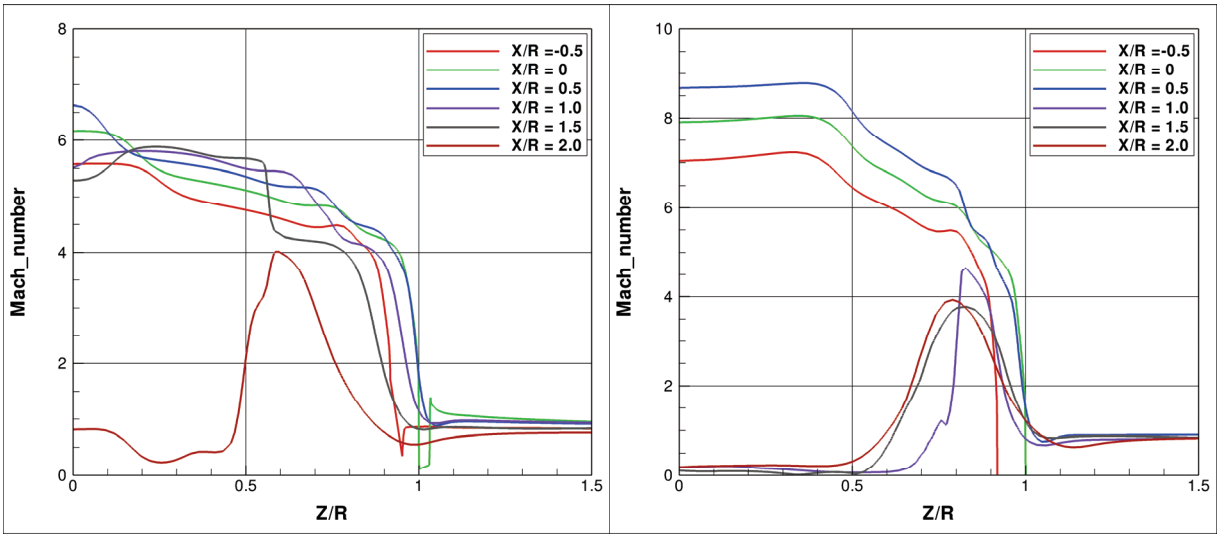

Figure 21: Case III (left) and Case IV (right) Mach number profiles (different scales)

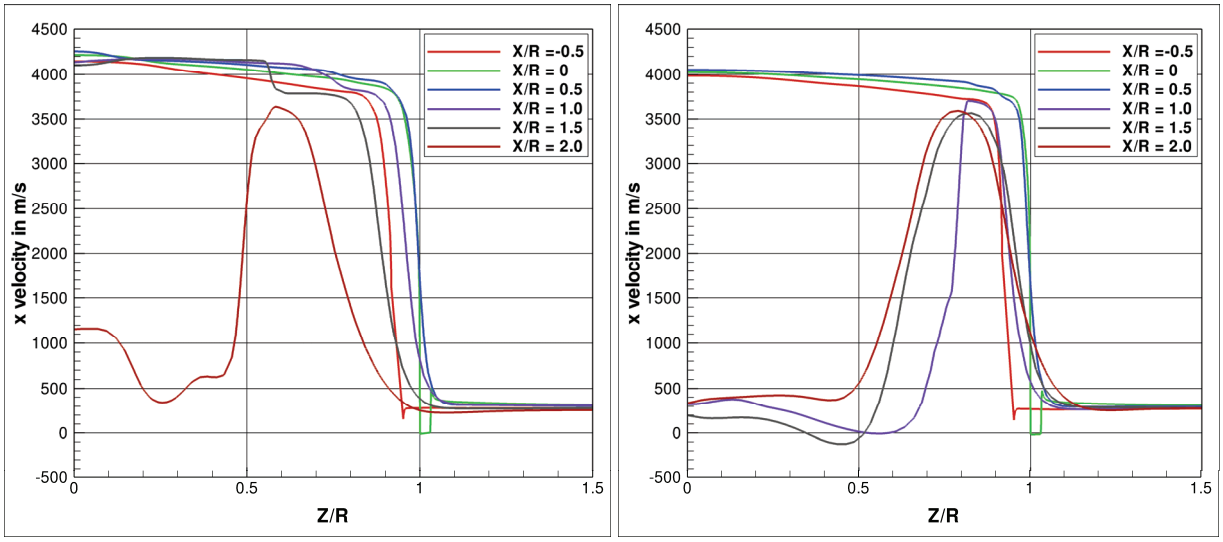

Figure 22: Case III (left) and Case IV (right) x-velocity profiles

3.5 Supersonic trajectory point: Mach 1.2

The supersonic operation point corresponds to a flight altitude of 9 km at which a Mach number of 1.2 is reached, static pressure reaches 0.330e5 Pa. Mach number contours for two mixture ratios can be seen in Figure 23: Case V: Ma = 1.2, O/F = 7.1; Mach number contours and Figure 24: Case VI Ma = 1.2, O/F = 0.7: Mach number contours. A detached shock can be seen on the base of the nozzle skirt, the flow accelerates to supersonic velocities before it passes the nozzle exit plane.

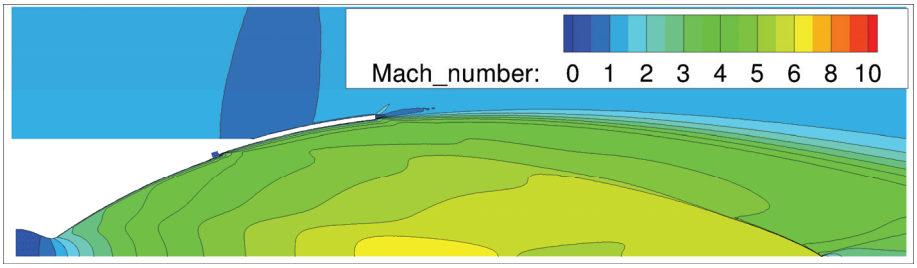

Figure 23: Case V: Ma = 1.2, O/F = 7.1; Mach number contours

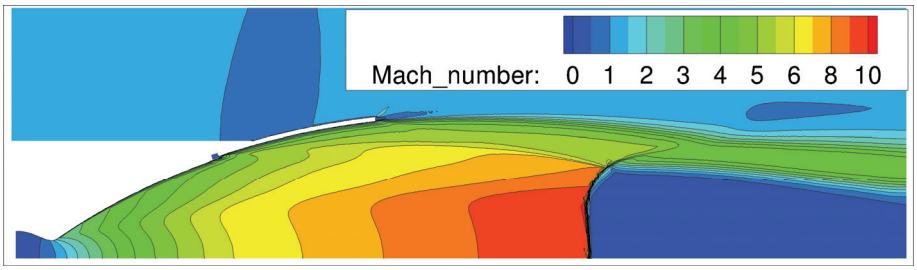

Figure 24: Case VI Ma = 1.2, O/F = 0.7: Mach number contours

Extracted profiles of Mach number and axial velocity can be seen in Figure 25 and Figure 26. Note the irregular shape of the X/R=1.5 profile in case VI where the Mach disc is cut.

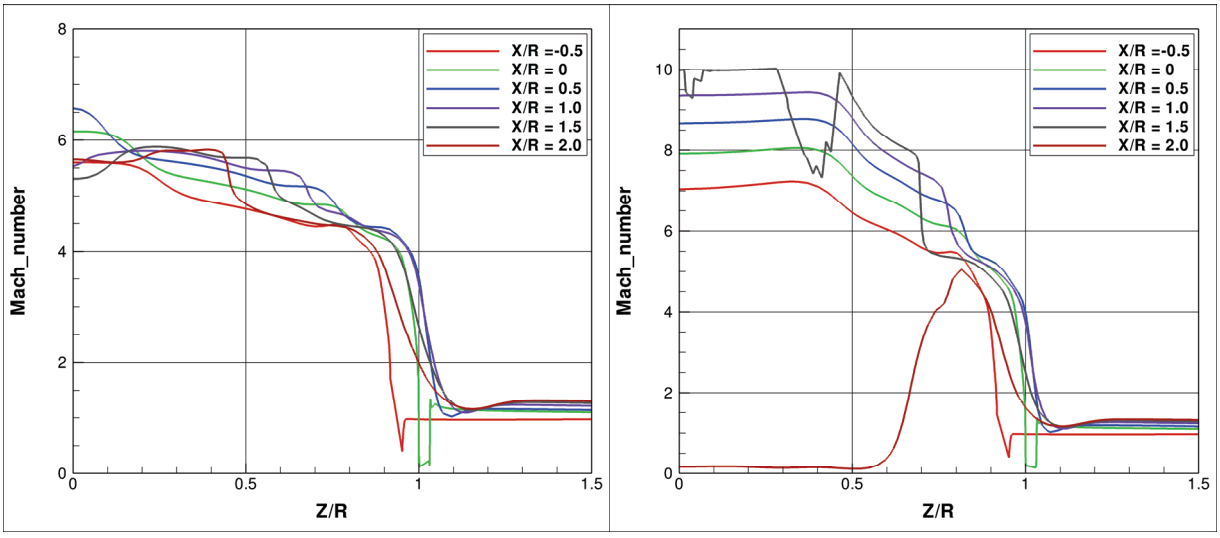

Figure 25: Case V (left) and Case VI (right) Mach number profiles

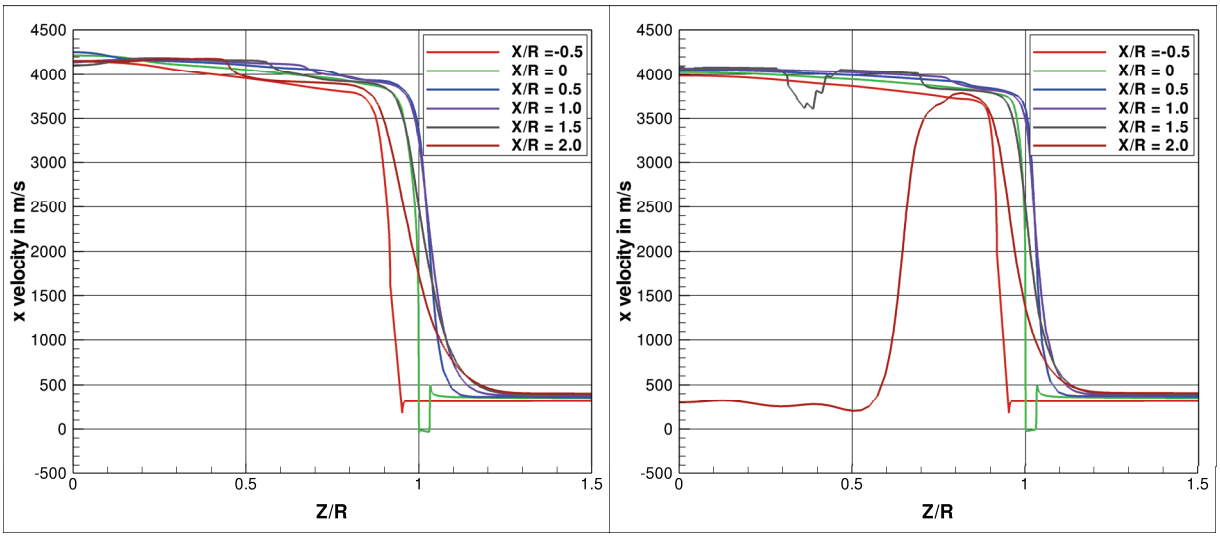

Figure 26: Case V (left) and Case VI (right) x-velocity profiles

3.6 Effect of mixture ratio variation

Figure 27 shows radial profiles of axial velocity in the vicinity of the nozzle exit, i.e. 0.5 and 1.0 radii downstream of the exit plane. These positions have been chosen because they appear most relevant to the development of the shear layer immediately behind the nozzle. In the subsonic case the plume contracts downstream, in the supersonic case, the plume appears to be of almost constant dimensions. The similarity of the velocity distribution in the shear layer between the different mixture ratios is striking in either case. Furthermore, the difference in maximum velocity reached is merely of an order of 10 % in most profiles. However, in the higher pressure subsonic case, the a Mach disc occurs earlier in the low mixture ratio case than in the original case, causing a substantial velocity difference.

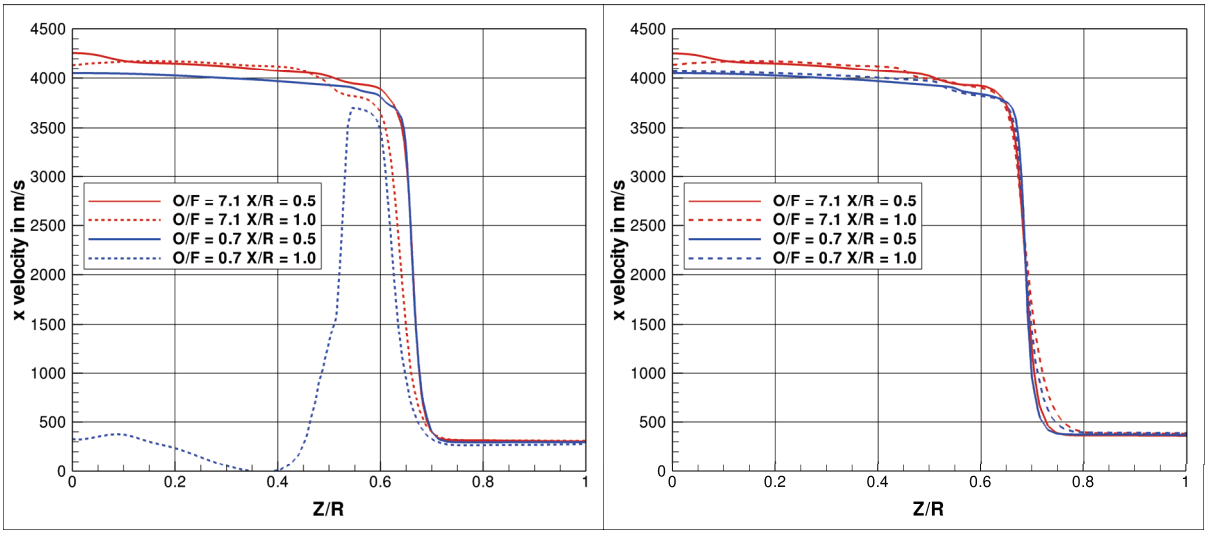

Figure 27: Axial velocity in m/s for sub- (left) and supersonic (right) case

3.7 Interpretation of similarity in velocity profiles

So far it could be seen that the reduced mixture ratio cases reach higher Mach numbers than the original cases. This seems somewhat counterintuitive given the estimated maximum exhaust velocity being dependant on the total temperature which is much higher in the regular mixture ratio case, see Table 2. However, as the reached temperatures are also lower, the resulting exit velocity is reduced compared to the original case. Furthermore, Table 2 predicts higher exit velocities for the O/F = 7.1 case than reached, and a large exit velocity difference between both mixture ratios. Note that this difference is higher than the one shown in Figure 2 because of the different γ used in each estimation. When looking at actual computed velocity profiles, Figure 27, it can be seen that the velocity difference is not nearly as big.

The reason can be found in the dependency of the exit velocity on the ratio of specific heats, γ. In fact, contrary to the simplified view of Eq. (1), γ is not constant throughout expansion of the gas inside the nozzle. As the gas expands, its temperature decreases which in turn effects γ. Figure 28 shows this variation in a contour plot.

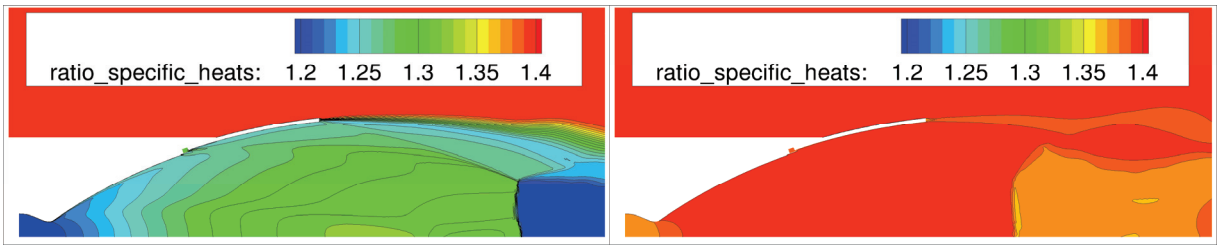

Figure 28: Ratio of specific heats for O/F = 7.1 (left) and O/F = 0.7 (right)

In the O/F = 7.1 case, γ can be seen to vary between 1.2 and 1.32. For O/F = 0.7, the picture looks different. The ratio of specific heats rises from 1.36 to 1.39 in the nozzle throat and stays constant afterwards. The variation is hence much smaller and does not proceed throughout the expansion. Table 4 summarizes the effect of γ on the theoretical maximum exit velocity, again as estimated using Eq. (1), i.e. under assumption of a constant γ. Variation is accounted for by using maximum and minimum occurring γ (and intermediate values for O/F=7.1).

γ		1.14	1.20	1.26	1.32	1.36	1.39
O/F		7.1	7.1	7.1	7.1	0.7	0.7
Temperature	K	3668.55	3668.55	3668.55	3668.55	1008.2	1008.2
Mol.weight	g/mol	13.496	13.496	13.496	13.496	3.428	3.428
u max	m/s	6047.81	5207.63	4680.19	4317.94	4285.17	4174.92

Table 4: Exit velocity and isentropic exponent γ

The effect of γ variation is most pronounced in the high mixture ratio case. The calculated exit velocity varies from 6000 m/s to 4300 m/s where the lowest value is most consistent with the results plotted in Figure 27. For O/F = 0.7, both the variation of γ in itself is smaller and its effect on the exit velocity is almost negligible when compared to the fuel rich case. This also explains why the theoretical estimation agrees very well with the numerical computation.

4 Summary, conclusions and recommendations for future activities

It is desirable to be able to simulate realistic nozzle plumes in an experimental facility. In order to support the design of such a facility and associated models, nozzle expansion flows have been simulated numerically for two Mach numbers 0.86 and 1.2, corresponding to distinct points in the ascent trajectory of the Ariane5 launcher. An alternative combustion chamber operation point with a mixture ratio O/F of 0.7 has been compared to the regular operation point of 7.1. Main advantage is the substantially reduced adiabatic flame temperature of ~1000K compared to the original ~3500K with an associated theoretical maximum exit velocity of ~4000 m/s. It is expected that this benefits design and operation of the experimental facility.

Relevant similarity parameters have been compiled which might allow for a scaled experiment of nozzle plume flow. The axial velocity has been found to be of major importance and has hence received special attention in this report.

It has been found that TEG and H_2 dump can be neglected in the simulations without significant influence on the shear layer. The author hence suggests that the model nozzle will be designed in a simplified manner, i.e without these additional injection ports, in order to reduce manufacturing, operational and numerical simulation difficulties which may arise due to small scales.

The alternative fuel rich operation point has been found to lead to higher exit Mach numbers compared to the original mixture ratio. However, exit velocities have been found to be in more than satisfactory agreement. The lower total temperature has less influence than the advantageously reduced molecular weight. The theoretical limit velocity has been found to agree better with the fuel rich operation point. This could be attributed to the difference of variation of the isentropic exponent between both cases. Simplified 1D theory thus overestimates the difference between the realistic and the model operation point exit velocity.

The author suggests that the promising approach of alternative operation points is more systematically investigated.

5 References

[1] ESA ITT, Statement of Work, Launcher stage separation and plume interaction validation, T417-004MP, 27.04.2010. ESA Directorate of Technical and Quality Management, Appendix to ITT 1-6468/10/NL/NA.

[2] A. Gülhan, K. Hannemann, C. Willert, A. Henckels, D. Saile (2011) „Hot testing facilities for ELV propulsion characterization“, Technical/Management Proposal, T418-303MP

[3] DLR Proposal 3004690, Launcher stage separation and plume interaction validation, 10.09.2010.

[4] H. Lüdeke, J. Bartolome Calvo (2011) “A fluid structure coupling of the Ariane-5 nozzle section during start phase by detached eddy simulation”, CEAS Space Journal 1: 33-44

[5] M. Frey (2009) “TRP on buffeting reduction, WP3200: Feasibility study for the plume simulation”, ESA TP24-TN122/2009

[6] B.H Goethert (1961) “Base flow characteristics of missiles with cluster-rocket exhausts”, Aerospace Engineering

[7] T. Gerhold, M. Galle, O. Friedrich, and J. Evans (1997) “Calculation of complex three dimensional configurations employing the DLR-TAU-code”. In Proceedings of the 35th Aerospace Sciences Meeting and Exhibit, number AIAA-1997-167, Reno, USA

[8] A. Mack and V. Hannemann (2002) “Validation of the unstructured DLR-TAU-code for hypersonic flows”. In Proceedings of the 32nd AIAA Fluid Dynamics Conference and Exhibit, AIAA-2002-3111

[9] S. Gordon, B.J. McBride (1994) “Computer Program for Calculation of Complex Chemical Equilibrium Compositions and Applications I. Analysis”, NASA RP-1311-P1

[10] B.J. McBride, S. Gordon (1996) “Computer Program for Calculation of Complex Chemical Equilibrium Compositions and Applications II. User's Manual and Program Description”, NASA RP-1311-P2

[11] H.W. Liepmann, A. Roshko (2002) “Elements of Gasdynamics”, Dover Publishing

Deutsches Zentrum
für Luft- und Raumfahrt e.V.

TN2500

Aerothermodynamic Design

July 18, 2013

Daniel Banuti

Institute of Aerodynamics
and Flow Technology
Department Spacecraft

DLR **Deutsches Zentrum
für Luft- und Raumfahrt** e.V.
in der Helmholtz-Gemeinschaft

ESA STUDY CONTRACT REPORT

No ESA Study Contract Report will be accepted unless this sheet is inserted after the coverpage of each volume of the Report.

ESA CONTRACT No.: AO/1-6731/ 11/NL/SFe	SUBJECT Hot Testing Facility for ELV Propulsion Characterization		CONTRACTOR DLR
* ESA CR( )No	* STAR CODE	No of TN 2500	

ABSTRACT:

This report presents the results from numerical simulations performed in the framework of the ESA technology research project "Hot Testing Facilities for ELV Propulsion Characterization". The intention of this report is to validate the suggested concept to test space transportation systems with realistic nozzle plumes in an experimental facility. An upstream supported wind tunnel model is opposed to a sought free-flight wind tunnel model without support at Mach 0.86. In CFD simulations, this concept is found to be valid for the facility layout.

The work described in this report was done under ESA contract. Responsibility for the contents resides in the author or organization that prepared it.

Name of author: D. Banuti (DLR, Goettingen, Germany)

** NAME OF ESA STUDY MANAGER	** ESA BUDGET HEADING
N. Murray DIV: TEC-MPA DIRECTORATE: D\TEC	

* Sections to be completed by ESA

** Information to be provided by ESA Study Manager

4 Aerothermodynamic Design - TN2500

CONTENT

1 Introduction

1.1 Overview

Aiming for the development of the next generation of launch vehicles, basic research is still necessary to understand contributing physical phenomena. Interaction of the nozzle exhaust with the surrounding gas is one of these topics which is at the same time also highly relevant from the technical point of view. As such, it has been investigated previously, e.g. as part of the work on buffeting reduction (see Lüdeke and Calvo [6]). While this elaborate numerical work has been supported by experiments, one major shortcoming has not been improved upon so far: up to this point, no technical facility is capable of simulating a hot exhaust gas with realistic physical properties. A positive theoretical feasibility study has been carried out by Frey [7]. Today, this topic is still of immediate relevance, e.g. concerning launcher stage separation [1][5].

1.2 Goal

Thus, it is the goal of the TRP “Hot testing facilities for ELV propulsion characterization” [2] to investigate conditions and ultimately install a hot plume test facility.

In order to support the design of the facility and suitable models, it is the purpose of this report to compare flow conditions around the rocket base model in free flight and in the facility. Computational Fluid Dynamics (CFD) simulations using the DLR TAU code will be employed.

1.3 Problems

No problems have been encountered during the work on this work package.

2 CFD Methodology

2.1 Computational Method and Model

Computations are carried out using the DLR TAU Code. It is discussed in detail in the literature see e.g. [8][9]. TAU is a hybrid grid, finite volume second order accuracy flow solver. It has been validated for a variety of steady and unsteady flow cases, ranging from sub- to hypersonic Mach numbers.
As the investigated geometries are essentially axisymmetric in this work, all computations are carried out in two dimensions under assumption of axisymmetry. For this initial study, the involved gases are treated as a mixture of nonreacting ideal gases. Species accounted for are H_2, H, O_2, O, H_2O, OH, HO_2, H_2O_2, and N_2.
The reservoir composition inside the combustion chamber is computed with NASA's "Chemical Equilibrium and Applications" (CEA) code by Gordon and McBride [10][11].

2.2 Generic Rocket Base Configuration

Initial computations within this project have been carried out using the Vulcain2 nozzle configuration, see TN2200 [3]. A newly designed configuration base has been supplied for the subsequent investigation in TN2400 [4]. This generic rocket base is shown in Figure 1.

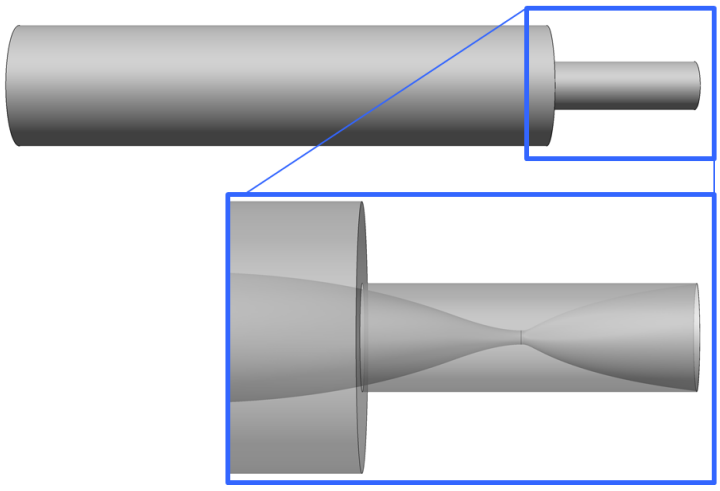

Figure 1: Rocket model base with nozzle contour

Combustion chamber reservoir conditions correspond to the Vulacain2 main chamber conditions, not taking into account mass flow through the H2 dump or turbine exhaust gas. Thermodynamic state and gas composition is compiled in Table 1.

		Chamber O/F 7.1
Total Pressure	Pa	1.19E+07
Temperature	K	3668.55
Density	kg/m3	5.8944
Molecular weight	g/mol	13.496
γ		1.141
H_2 *(mass fract.)*		0.01973
H		0.00206
O_2		0.0349
O		0.00951
H_2O		0.84927
OH		0.08453
HO_2		0
H_2O_2		0
N_2		0

Table 1: Vulcain2 like chamber conditions

Grids and numerical setup need to be specified in order to answer the question, whether free flight flow conditions can be reproduced in the suggested facility. As a first step, a flight Mach number of 0.86 at ambient pressure is chosen.

2.3 Free Flight Flow field

The complete computational grid of the free flight case is depicted in Figure 2, a detail of the region marked in blue, i.e. the rocket model base, is shown in Figure 3. The outer grid boundaries are marked as farfield boundary conditions. These boundaries are placed at a distance exceeding 1000 rocket nozzle radii to ensure a pressure decoupling of the solution from the boundary condition. To ensure a clean inflow, the rocket body is extended all the way to the inlet boundary. This part is treated as an inviscid Euler wall. It is changed to a viscous wall for the same length as the rocket model length provided for the wind tunnel case (Figure 3). The combustion chamber reservoir is set according to Table 1. The grid is refined in the rocket base region.

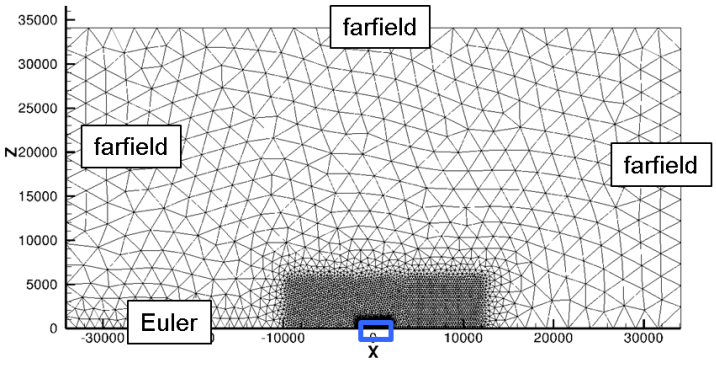

Figure 2: Free flight computational grid

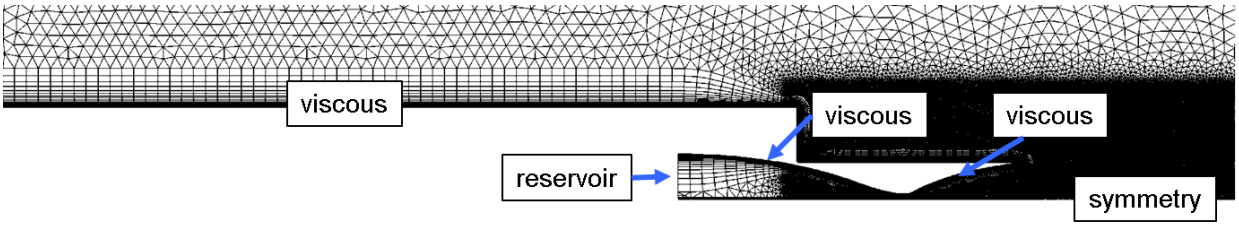

Figure 3: Free flight base detail

2.4 Facility Flow field

The facility concept avoids a potentially flow-disturbing sting to hold the model by placing it coaxially inside the wind tunnel nozzle. A 3D rendering can be seen in Figure 4.

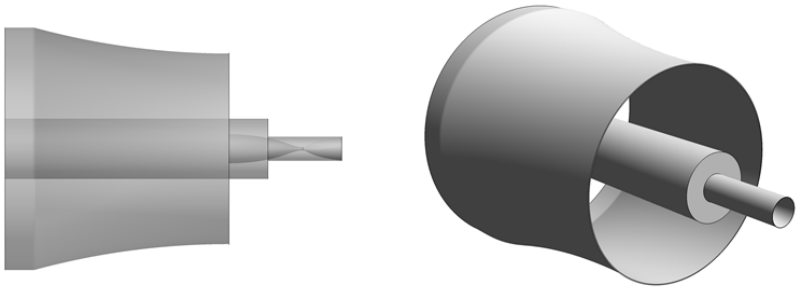

Figure 4: Model in nozzle concept

The view of the whole computational domain is shown in Figure 5. The detail of the wind tunnel nozzle with the rocket base is depicted in Figure 6.

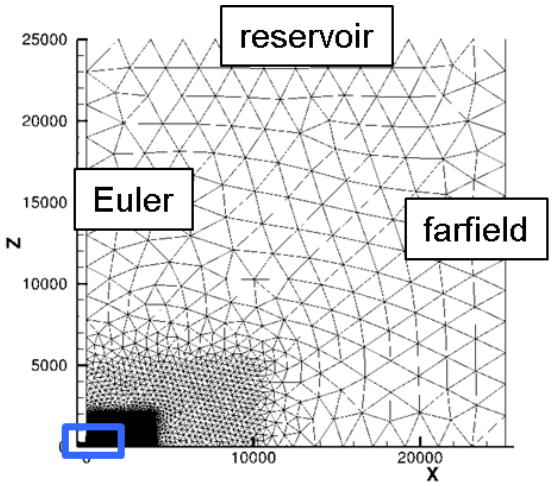

Figure 5: Facility computational grid

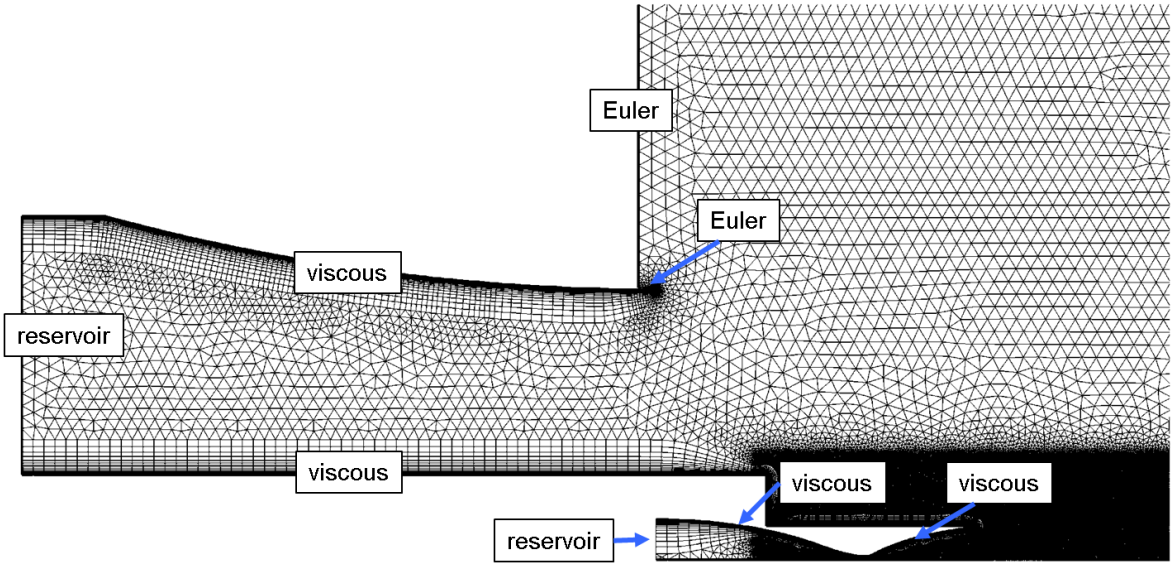

Figure 6: Facility computational grid base detail

The numerical modelling of this case is more involved than for the free stream case. While in the latter the actual flow condition can be prescribed in sufficient distance, effectively directly modelling the investigated case, it is well beyond the scope of this study to model a whole facility. Instead, a sufficient representation is sought for the present calculation. Key points clearly are the wind tunnel nozzle and the rocket model base, both of which can be assumed to be axisymmetric. Now, the ambient pressure boundary conditions need to be placed in sufficient distance to the investigated region in order to not influence the result. This is realized by placing the top and right domain boundary at a distance of more than 800 nozzle radii away from the rocket base. Clearly, this is not possible with the left vertical domain boundary, as it would intersect with the wind tunnel nozzle. Furthermore, it can be expected that the primary interaction mechanism at the open section of the wind tunnel is not a parallel stream but instead entrainment from the stagnant environment. Thus, the left vertical boundary has been modelled as an inviscid wall. The right outflow domain boundary is modelled as farfield, while the top boundary is modelled as a reservoir with a slightly (<1%) higher pressure than the farfield. This helps convergence acceleration, as a clear pressure gradient establishes a flow of nonetheless negligible influence. The grid is refined in the rocket base region.
Boundary parameters are summarized in Table 2.

Type	Description		Remarks	
Symmetry axis	Symmetry			
Farfield	Outflow	p	1.01325E+05	Pa
Reservoir	Top inflow	p0	1.02E+05	Pa
Euler wall	Faceplate			
Euler wall	Tunnel nozzle outer lid			
Viscous wall	Tunnel nozzle wall	T	288.15	K
Reservoir	Nozzle reservoir	p0	1.64E+05	Pa
		rho0	1.83E+00	kg/m3
Viscous wall	Rocket base	T	288.15	K
Reservoir	Chamber reservoir	p0	1.19E+07	Pa
		rho0	5.89E+00	kg/m3
Viscous wall	Chamber wall		adiabatic	
Viscous wall	Nozzle wall	T	700	K

Table 2: Facility boundary conditions

3 Results

The Mach number contours of the resulting flow fields are compared in Figure 7 and Figure 8.

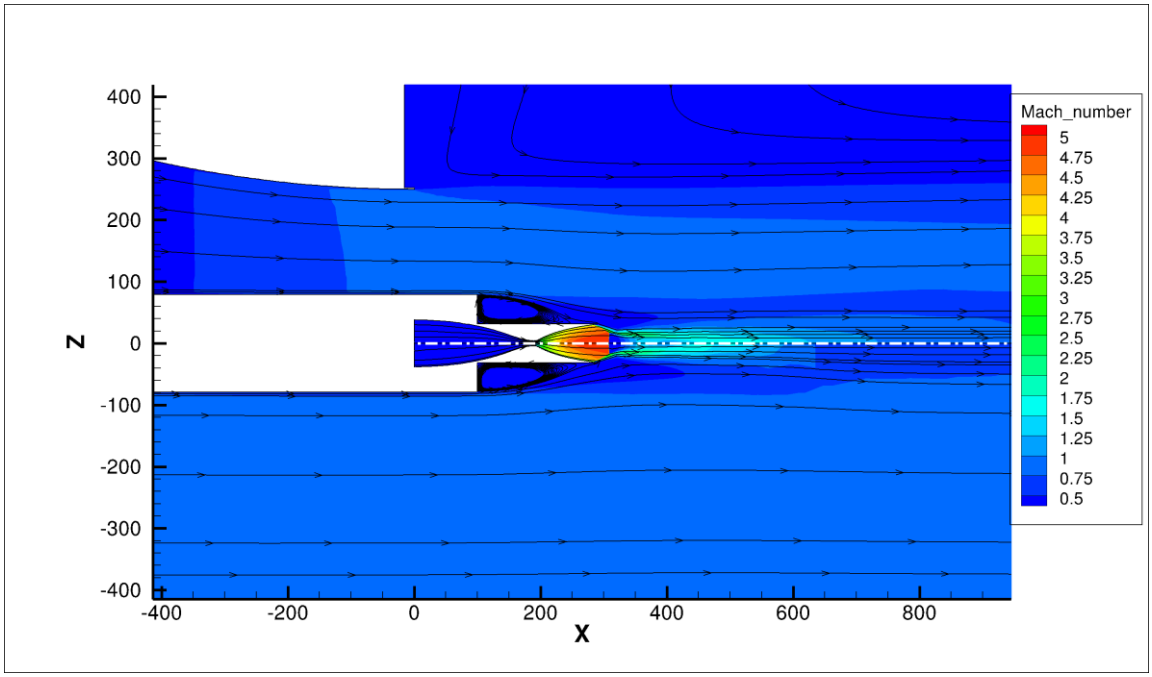

Figure 7: Comparison of Mach number contours of facility (top) and free flight (bottom) case.

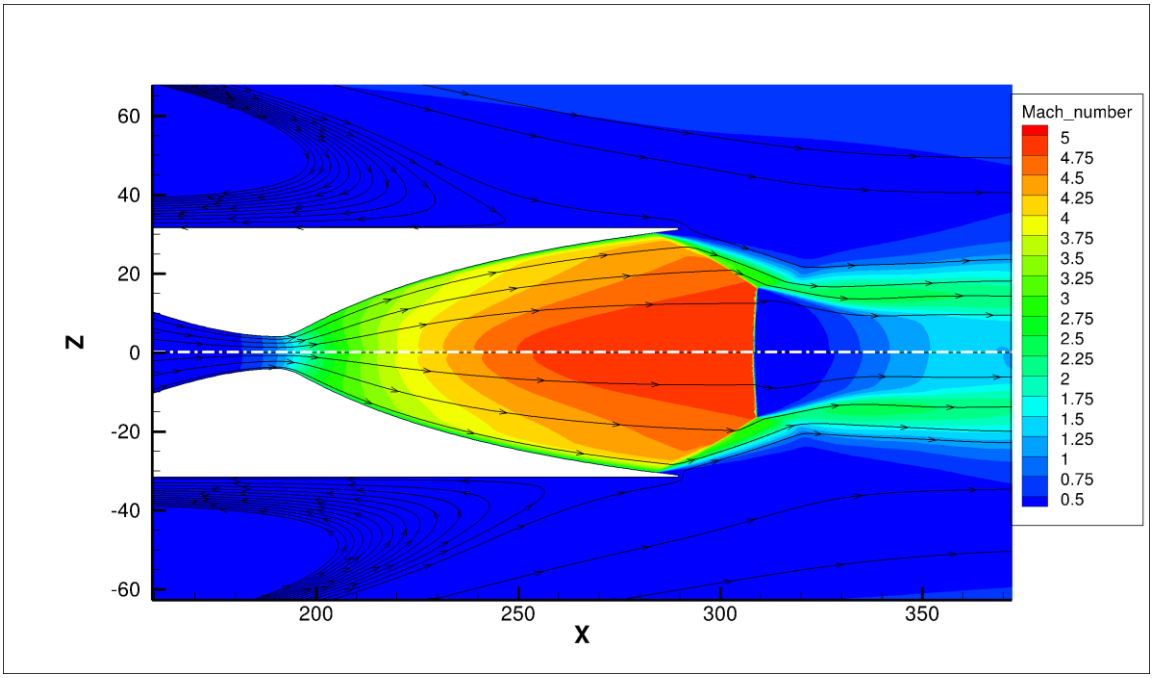

Figure 8: Comparison of Mach number contours of facility (top) and free flight (bottom) case, detail of rocket plume.

Figure 7 demonstrates how the fundamentally different flow fields nonetheless lead to practically indistinguishable flow conditions at the rocket base. It can be seen in Figure 8 that the base recirculation, the nozzle separation, and the position of the Mach disc are practically identical in both cases.

In order to allow a qualitative comparison, profiles are extracted in radial direction at three positions: at the wind tunnel nozzle exit and at both 0.5R and R behind the rocket nozzle, where R is the rocket nozzle radius.

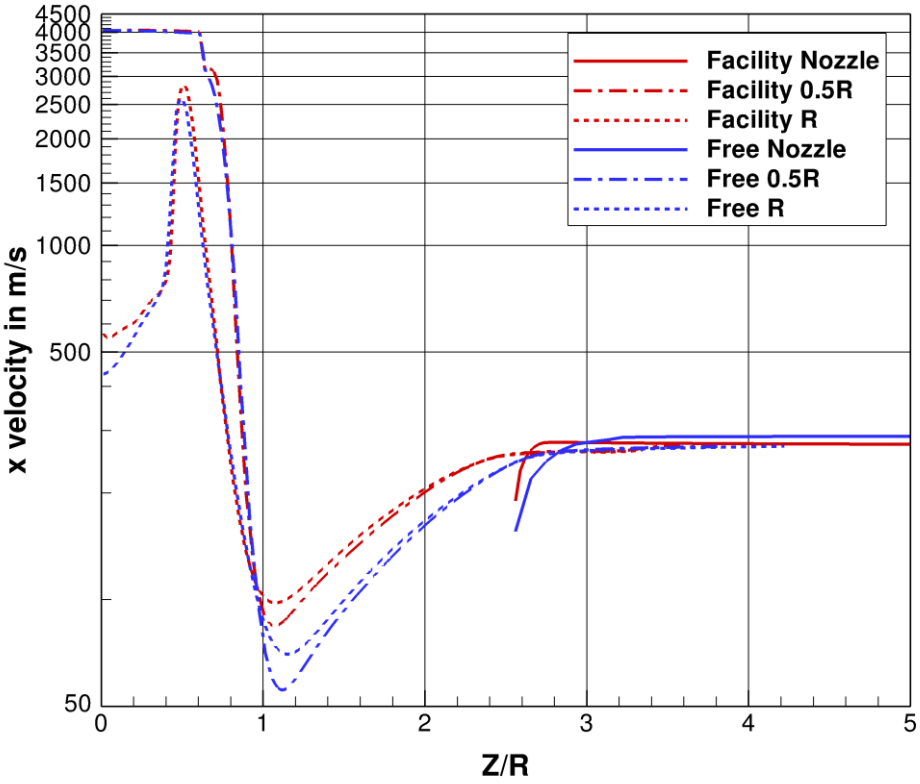

Figure 9: Radial profiles of axial velocity of free flight (Free) and facility (Facility) case.

It can be seen that the wind tunnel nozzle has been well designed. The boundary layer profile stopping to early is a data extraction artefact, the velocity reduces to zero at a no-slip boundary. The boundary layer profiles differ slightly. This might be due to the free flight case having a homogeneous build-up in a constant pressure environment, whereas the flow is accelerated through the wind tunnel nozzle. The difference in velocity at the nozzle exit is negligible, the shear layer develops slightly differently, possibly due to the difference in boundary layer profile. Overall agreement between both cases is in terms of density is satisfactory as well. This can be seen in Figure 10.

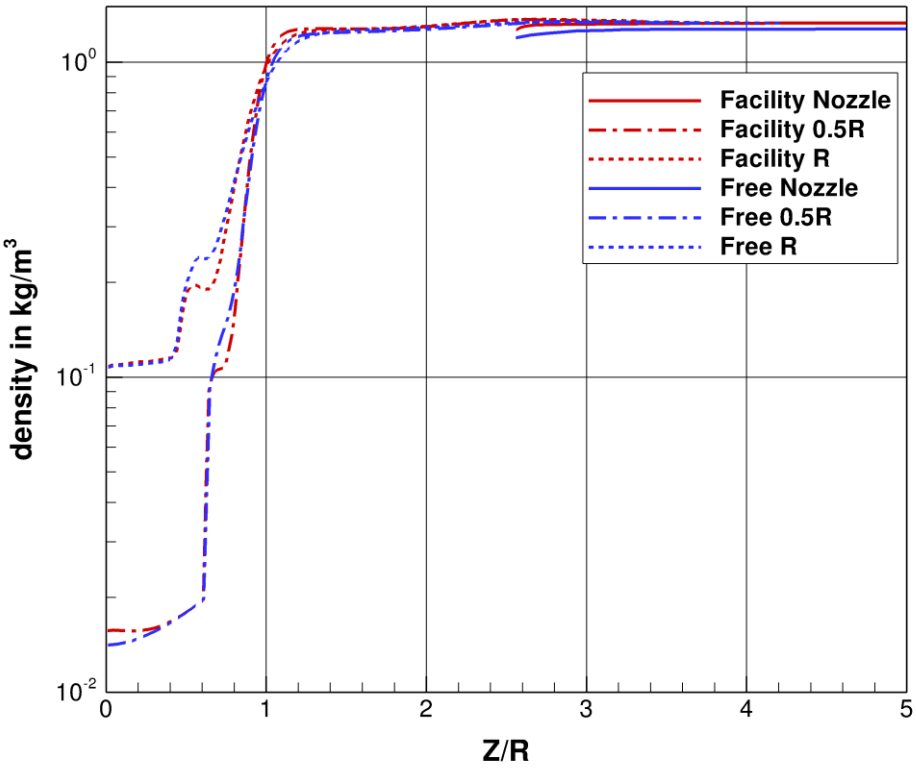

Figure 10: Radial profiles of density of free flight (Free) and facility (Facility) case.

4 Summary, conclusions and recommendations for future activities

It is desirable to be able to simulate realistic nozzle plumes in an experimental facility. In order to support the design of such a facility and associated models, nozzle expansion flows have been simulated numerically in order to compare a free flight condition with a wind tunnel condition at M=0.86.

The difficulties in designing a representative numerical model of the facility flow have been discussed in detail.

Data have been provided which show overall good agreement between the sought free flight and the wind tunnel condition. CFD has successfully contributed in the proof of concept of the facility layout.

5 References

[1] ESA ITT, Statement of Work, Launcher stage separation and plume interaction validation, T417-004MP, 27.04.2010. ESA Directorate of Technical and Quality Management, Appendix to ITT 1-6468/10/NL/NA.

[2] A. Gülhan, K. Hannemann, C. Willert, A. Henckels, D. Saile (2011) „Hot testing facilities for ELV propulsion characterization“, Technical/Management Proposal, T418-303MP

[3] D. Banuti (2012) “Definition of scaling parameters”, ESA TRP-HOTP-DTN2200

[4] D. Saile (2012) “Design trade-off and final design point selection”, ESA TRP-HOTP-DTN2400

[5] DLR Proposal 3004690, Launcher stage separation and plume interaction validation, 10.09.2010.

[6] H. Lüdeke, J. Bartolome Calvo (2011) “A fluid structure coupling of the Ariane-5 nozzle section during start phase by detached eddy simulation”, CEAS Space Journal 1: 33-44

[7] M. Frey (2009) “TRP on buffeting reduction, WP3200: Feasibility study for the plume simulation”, ESA TP24-TN122/2009

[8] T. Gerhold, M. Galle, O. Friedrich, and J. Evans (1997) “Calculation of complex three dimensional configurations employing the DLR-TAU-code”. In Proceedings of the 35th Aerospace Sciences Meeting and Exhibit, number AIAA-1997-167, Reno, USA

[9] A. Mack and V. Hannemann (2002) “Validation of the unstructured DLR-TAU-code for hypersonic flows”. In Proceedings of the 32nd AIAA Fluid Dynamics Conference and Exhibit, AIAA-2002-3111

[10] S. Gordon, B.J. McBride (1994) “Computer Program for Calculation of Complex Chemical Equilibrium Compositions and Applications I. Analysis”, NASA RP-1311-P1

[11] B.J. McBride, S. Gordon (1996) “Computer Program for Calculation of Complex Chemical Equilibrium Compositions and Applications II. User's Manual and Program Description”, NASA RP-1311-P2

Deutsches Zentrum
für Luft- und Raumfahrt e.V.

TN3300

Combustion Chamber Design

May 24, 2013

Dominik Saile[1]
Wolfgang Kitsche[2]

Institute of Aerodynamics
and Flow Technology
Supersonic and Hypersonic
Technology Department[1]

Institute of Space Propulsion
Test Facilities[2]

DLR **Deutsches Zentrum**
für Luft- und Raumfahrt e.V.
in der Helmholtz-Gemeinschaft

ESA STUDY CONTRACT REPORT

No ESA Study Contract Report will be accepted unless this sheet is inserted after the coverpage of each volume of the Report.

ESA CONTRACT No.: AO/1-6731/ 11/NL/SFe	SUBJECT Hot Testing Facility for ELV Propulsion Characterization		CONTRACTOR DLR
* ESA CR( )No	* STAR CODE	No of TN 3300	

ABSTRACT:

This report presents the results from a study regarding to the combustion chamber design of the future hot plume facility in the framework of the ESA technology research project "Hot Testing Facilities for ELV Propulsion Characterization". A set of reference conditions are determined for which a combustion chamber design is found. Consecutively, the dimensions and materials of the injector head, the combustion chamber and the nozzle are presented and discussed. Additionally, a thermal analysis is conducted to approximate the run time of the combustion chamber. Technical drawings of the combustion chambers are provided.

Name of author: D. Saile, W. Kitsche (DLR, Cologne/Lampoldshausen, Germany)

** NAME OF ESA STUDY MANAGER	** ESA BUDGET HEADING
N. Murray DIV: TEC-MPA DIRECTORATE: D\TEC	

* Sections to be completed by ESA

** Information to be provided by ESA Study Manager

5 Combustion Chamber Design - TN3300

5.1 Definition of Reference Load Steps

The main output of the study before is the mass flow for the rocket engine model and the comparison of the future experiments with the conditions during the ascend of the Ariane 5. In the following, reference load steps shall be defined to design or to find an appropriate combustion chamber/nozzle configuration that satisfy the requirements and to design the corresponding feeding system. Before, one shortcoming needs to be discussed: flow separation in the nozzle can not be taken into account with the applied one-dimensional approach used for the similarity study.

If only small deviation occur between the experimental and flight conditions (see spectrum of variation in Fig. 62 to Fig. 77), it might be possible to extrapolate tendencies from the variation of the corresponding parameter. Though, in case of the pressure ratio, the one-dimensional approach completely neglects the fact that the nozzle flow can separates inside the nozzle since the boundary layer at the nozzle exit has to overcome the ambient pressure.

The effect of flow separation inside the nozzle was intensively investigated in the past and published. Among others, it was researched in Ref. [13], where the graph shown in Fig. 77 can be found. It depicts the nozzle pressure ratio of several correlations and experiments over the Mach number. The flow in the nozzle basically separates if the nozzle pressure ratio is found in the lower half at low nozzle pressure ratios. One has to be aware that this range has a massive impact on the flow topology.

Consequently, an appropriate pressure ratio needs to be kept in experiments. This was kept in the back of the head while investigating the similarity of the physical properties. Thus, the screws for increasing the pressure ratio at the nozzle exit like a close to stoichiometric mixture ratio, increased combustion chamber pressure and a lower expansion were opposed to each other.

To continue the design, reference load steps need to be defined. The reference conditions for the similarity study are used as basis to find a set of the reference load steps. These load steps are based on a combustion chamber design [24] of the *Pennsylvania State University* in the *Cryogenic Combustion Laboratorys (CCL)*, the design parameters of which are given later in Tab. 11.

This combustion chamber withstands a maximum chamber pressure of 6.89 MPa and can work up to near stoichiometric mixture ratios. For the case here, a mixture ratio of 6.0 is chosen due to its relevance to flight conditions. As shown in Chap. 5.2, these conditions are extremely challenging for a small combustion chamber.

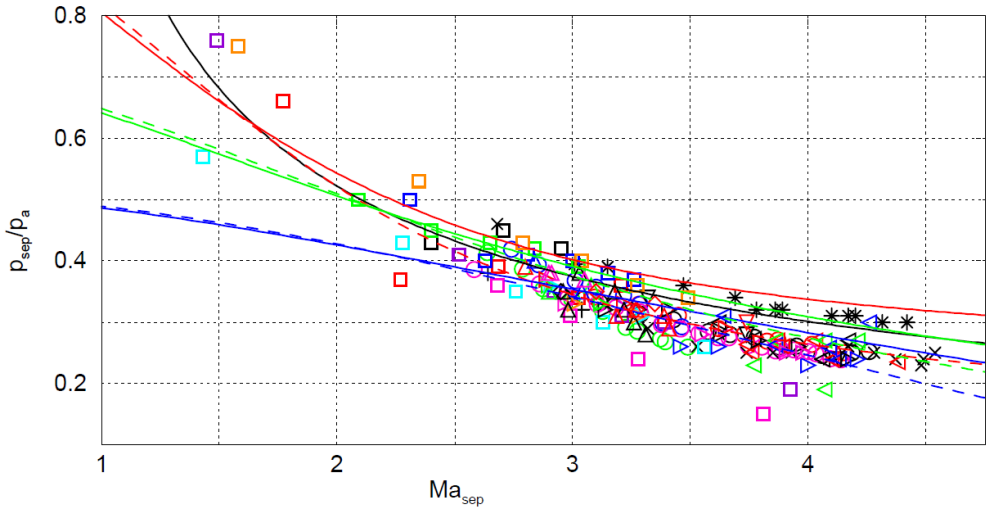

Figure 77: Separation nozzle pressure ratio for different separation criteria and experiments plotted as a function of the nozzle design Mach number [13].

Then, the nozzle throat diameter is defined to calculate the mass flow through the whole system. A throat diameter of 8.0 mm is used as starting point. It is very close to the throat diameter of the Penn State combustor, and, as shown later, it results in an acceptable outer diameter if the geometric of Ariane 5 is used.

The ambient reference flow is defined to be at Mach 0.8 and 1.2 to have a subsonic and supersonic representative. According to flight measurements (Ref. [8]) during the ascend of Ariane 5 and corresponding experiments, the highest loads with respect to pressure fluctuations occur actually at about 0.8.

The curves depicted in Fig. 78 and Fig. 79 reflect that finding. It shows the root mean square value of the pressure coefficient c_{Prms} as a function of the Mach number and the spectral content of the pressure fluctuations as power spectral density function over the non-dimensional frequency Str at Mach 0.8, respectively. The highest c_{Prms}-values can be found at Mach 0.8, which also features high pressure fluctuations in the spectrum in comparison to other Mach numbers shown in Ref. [8].

The results for the combustor for the defined input parameters, called test case C1, are presented along with further test cases in Tab. 8 with respect to the similarity properties at reference Mach numbers 0.8 and 1.2, and additionally at 1.5. In opposition to the studies before, the issue of flow separation and the various measures to encounter this effect is discussed in detail. As before, the wind tunnel is set to standard transonic setting for transonic investigations (test case C1 to C4), meaning the free stream pressure is

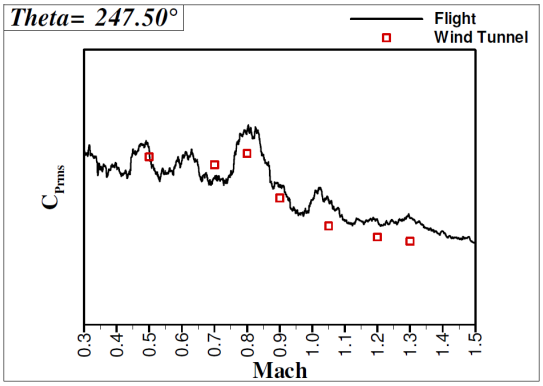

Figure 78: RMS pressure coefficient for flight and wind tunnel experiments [8].

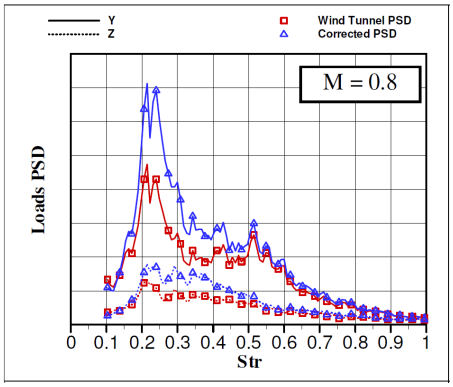

Figure 79: Loads PSD on the nozzle and engine thermal protection (PTM) [8].

$\sim$ 0.1MPa and the reservoir temperature is at 288.15 K. Additionally, Tab. 9 explains the reasoning of the selected load steps.

The test case C1 occurred in the studies above. The issue here becomes obvious if the exit pressure ratio of 0.09 is compared to Fig. 77, which reveals a separated nozzle flow. Test case C2 encounters that issue by decreasing the expansion ratio. As a consequence, the mass flow is kept constant, but the geometrical similarity to Ariane 5 is violated because the ratio between outer nozzle diameter and the main body is not comparable anymore. An increase of the combustion chamber pressure, as suggested in test case C3, solves the issue of flow separation. But, it comes with the cost of an increased heat transfer in the combustion chamber, which is not known to the author to have been tested for the Penn State combustor. Test case C4 instead ensures geometrical similarity of the diameter ratio and prevents the nozzle flow separation by increasing the nozzle throat diameter.

For the cases C1 and C2, the combustion chamber could most likely be integrated in the wind tunnel environment without major modification since the combustion chamber was designed for these conditions. Nevertheless, it is recommended to execute an independent thermal and stress analysis. For case of C3 and C4, the thermal and mechanical loads might exceed safety requirements due to the increased combustion pressure and the mass flux, ergo heat flux.

Note, that Fig. 77 also indicates a clear flow separation for the one-dimensionally calculated nozzle pressure ratio in test case C3. These parameters are identical to Vulcain 2 conditions where only a slight flow separation is observed, which is due to the nature of a Vulcain 2 nozzle. There, a truncated nozzle is used, which features a higher exit pressure at the nozzle wall.

Generally, the similarity ratios of test case C1 to C4 exhibit a good agreement to flight if the temperature and the velocity is observed. The latter property is held responsible

Table 8: Selected load steps of the rocket model engine and corresponding similarity to flight conditions.

Case			C1	C2	C3	C4	C5	C6
	Mach number	Ma	0.8‖1.2	0.8‖1.2	0.8‖1.2	0.8‖1.2	1.5	1.5
Combust. chamber	Pressure	p_{CC} in [MPa]	6.89	6.89	11.5	6.89	6.89	6.89
	Mixture ratio	O/F	6.0	6.0	6.0	6.0	6.0	6.0
	Mass flux (throat)	$\dot{m}/A_t$ in [kgm^{-2}s^{-1}]	2990.1	2990.1	4971.0	2990.1	2990.1	2990.1
	Total mass flow	$\dot{m}$ in [gs^{-1}]	150.3	150.3	249.9	440.8	150.3	-
Nozzle	Expansion ratio	ϵ	58.5	20	58.5	20	20	58.5
	Throat diameter	d_t in [mm]	8.0	8.0	8.0	13.7	8.0	-
	Exit diameter	d_e in [mm]	61.2	35.8	61.2	61.2	35.8	-
	Exit pressure ratio	$(p_e/p_\infty)_{Exp}$	0.09	0.37	0.15	0.37	5.51	1.34
	Exit Mach number	M_e	4.41	3.62	4.43	3.62	3.62	4.41
Similarity ratio	Pressure	$\frac{(p_e/p_\infty)_{Exp}}{(p_e/p_\infty)_{Ariane}}$	0.36‖0.19	1.47‖0.80	0.59‖0.32	1.47‖0.80	8.18	1.99
	Density	$\frac{(\rho_e/\rho_\infty)_{Exp}}{(\rho_e/\rho_\infty)_{Ariane}}$	0.33‖0.18	1.04‖0.55	0.55‖0.29	1.04‖0.55	5.51	1.75
	Temperature	$\frac{(T_e/T_\infty)_{Exp}}{(T_e/T_\infty)_{Ariane}}$	1.06‖1.09	1.40‖1.42	1.06‖1.08	1.40‖1.42	1.47	1.12
	Velocity	$\frac{(v_e/v_\infty)_{Exp}}{(v_e/v_\infty)_{Ariane}}$	1.04‖1.05	0.97‖0.98	1.04‖1.06	0.97‖0.98	0.99	1.07
	Impulse denstity	$\frac{(\rho_e v_e/\rho_\infty v_\infty)_{Exp}}{(\rho_e v_e/\rho_\infty v_\infty)_{Ariane}}$	0.34‖0.18	1.01‖0.54	0.57‖0.31	1.01‖0.54	5.45	1.87

Table 9: Explanation to selected load steps for combustion chamber.

Case	C1	C2	C3
Approach	Penn State combustor cond. Ariane 5-like nozzle transonic	Penn State combustor cond. decreased expansion ratio transonic	increased comb. ch. pressure Ariane 5-like nozzle transonic
Advantage	tested system (appl. for VMK) geometric similarity	tested system (appl. for VMK) increased exit pressure → no nozzle flow separation	geometric & flow similarity increased exit pressure → no nozzle flow separation
Disadvantage	nozzle flow separation	no geometric similarity w.r.t diameter ratio	increased pressure/heat flux increased instability risk
Case	**C4**	**C5**	**C6**
Approach	increased throat diameter decreased expansion ratio transonic	Penn State combustor cond. decreased expansion ratio supersonic with ejector	Penn State combustor cond. Ariane 5-like nozzle supersonic with ejector
Advantage	increased exit pressure → no nozzle flow separation outer geometry is kept → geometric similarity	adjustable free-stream pressure → no nozzle flow separation → geometric & flow similarity → altitude simulation	adjustable free-stream pressure → no nozzle flow separation → geometric & flow similarity →altitude simulation
Disadvantage	increased mass flux → increased heat flux	not transonic	not transonic

for triggering the shear layer instabilities. Decreasing the extension ratio shows to be an appropriate measure to increase the pressure ratio in order to avoid separation and to keep similarity especially at Mach 0.8. This measure also improves the similarity with respect to density and impulse density. An unusual approach for transonic testing to push the density/impulse density to even higher ratios could be a higher reservoir temperature resulting in a higher density ratio $(\rho_e/\rho_\infty)_{Exp}$. Obviously, the velocity ratio and the temperature ratio itself is changing then too, but not as strongly.

Test case C5 is investigated separately since it is for Mach 1.5. For this case, it was taken full advantage of the ejector system of TMK, which offers the capability to decrease the free stream pressure p_∞ in the measurement section by a factor of almost 15 for Mach 1.5. Consequently, as it can be seen in Tab. 8, the pressure ratios $(p_e/p_\infty)_{Exp}$ and $(p_e/p_\infty)_{Exp}/(p_e/p_\infty)_{Ariane}$ can be increased substantially.

This case is very interesting because it shows the capability of TMK for conducting of altitude simulations independently of the Mach number. Basically, the pressure ratio $(p_e/p_\infty) = 5.51$ corresponds to an altitude of 24.5 km or a Mach number of 3.0 if Ariane 5 is taken as reference. It shall be emphasized again: At Mach 1.5, TMK offers the opportunity to adjust the pressure ratio (p_e/p_∞) from ground conditions to an altitude of 24.5 km for a combustion chamber pressure of 6.81 MPa and an expansion ratio of 20. For an Ariane 5-like expansion ratio of 58.5 and the same combustion chamber pressure, this would correspond to an altitude of 15.8 km and a Mach number of 2.1.

For the transonic flight regime, a full altitude simulation in TMK is also imaginable if an additional ejector system is installed. The perforated walls in the transonic measurement section enable a pressure adjustment along the wall in such a manner that the streamlines are not squeezed when surpassing the wind tunnel model, meaning the streamline curvature, therefore the centrifugal forces and the pressure gradients are represented like under free-flight conditions. If necessary, excessive mass flow that could cause wall interferences is removed from the perforated measurement section through a pipe. This pipe is connected to through a control valve with the atmosphere.

If the main ejector system is running now, the pressure in the measurement section decreases. In the current set-up, this would cause a mass flux through the pipe to the measurement section. In order to prevent that, an additional controlled ejector system could be installed, which controls the mass flow through the perforated wall. This new altitude simulation system would need to be developed and require testing in order to be calibrated.

Reference conditions from the previous studies are defined now for conceptual phase. As outcome of Tab. 8 and Tab. 9, it shall be concluded that partial similarity can be achieved for most of the test cases. In particular, the temperature and velocity ratio a well-matched. Adjustments to receive the desired pressure ratios/prevent nozzle flow separation (C1) can be made by changing the expansion ratio (C2, C4, C5), increasing

the combustion chamber pressure (C3) or by using the ejector system of TMK (C5, C6) for supersonic investigations. Note, that an additional ejector system can massively extend the performance range of TMK with respect to pressure ratio adjustments/altitude simulations for transonic testing.

Although showing higher loads for full flow similarity like in C3 or C4, the test cases also indicate that the mass flow rate is not out of reach at least for the feeding system. For this reason, two different load steps shall be defined: the first being a design point for the combustion chamber, which leans on the Penn State combustor [24] providing similarity according to C1, C2, C5 and C6; the second representing the potential of the feeding system to realize the similarity presented in case C3 and C4, meaning the current combustion chamber is not designed to withstand these conditions, but future combustion chambers can be supplied accordingly. Both reference conditions are listed in Tab. 10 and referred to as RC 1 and RC2, respectively.

Table 10: Defintion of reference conditions.

Reference condition			RC 1	RC 2
Cases			C1, C2, C5 and C6	C3, C4
Combustion chamber pressure	p_{CC}	MPa	6.89	11.5(15)
Mixture ratio	O/F		6.0	-
Total mass flow	$\dot{m}$	g/s	150.3	440.8
Mass flow oxygen	$\dot{m}_{O_2}$	g/s	128.8	377.8
Mass flow hydrogen	$\dot{m}_{H_2}$	g/s	21.5	63.0

5.2 Thrust Chamber

The maximum mass flow to be expected for a given thrust chamber was defined in the Chap. 5.1. This before mentioned thrust chamber developed by the Pennsylvania State University in *Pennsylvania State University* in the *Cryogenic Combustion Laboratorys (CCL)* is now discussed in detail followed by the modifications that are required in order to be used for a wind tunnel model. This is done for all compononents of a thrust chamber: it starts with injector, then continues with the combustion chamber, and concludes with the nozzle.

The main properties of the Penn State 1.5 in thrust chamber with no preburner are given in Tab. 11. It can be seen that the proposed thrust chamber meets the requirements with respect to the desired characteristics and dimensions. In detail, the Penn State thrust chamber was selected for the future experiments due to the reasons listed in Tab. 12. To sum these observations up, it is basically due to the prove of concept, the high readiness level, the high similarity to reproduce flight conditions, the flexibility to study scaling effects and the availability of benchmark data and geometry.

It is also imaginable to connect the combustion chamber with the Penn State preburners as described in Ref. [17], [18], [37], [24]. The preburners would be installed outside of the measurement section and not directly at the wind tunnel model. Details to this configuration is given in Ref. [24].

For the case without a preburner, the characteristic chamber length as figure of merit is $L^\star = 5.7\,\mathrm{m}$. This results from a combustion chamber volume of $V_{CC} \approx 3.4{\cdot}10^{-4}\,\mathrm{m}^3$ and a throat diameter of 8.67 mm (Tab. 13). Compared to typical values found in literature of between 0.8 and 3.0 [35], this is very long. The stay time is about $\sim 0.0063\,\mathrm{s}$. In literature, this value is found to be between 0.001 and 0.04 s for different types of propellants and thrust chambers.

More recently, the Penn State Universtiy group investigates a thrust chamber with a chamber diameter $D_{CC} = 1.0\,\mathrm{in}$ [17], [18]. The smaller diameter might be advantageous with respect to the cross-section blocked by the model, and thus will be kept in mind. The injector (Fig. 81 and Fig. 82) itself is identical concerning the diameter of the coaxial shear injector. But, it additionally features a multiple-hole injector plate to eliminate the recirculation zone which forms close to the exit of the injector face. For the moment, the 1.5 in thrust chamber is preferred due to the high quality of numerical and experimental data. Future iterations including stress analyses will reveal if this thrust chamber should be preferred instead. Tab. 13 gives an overview to main parameter like combustion chamber pressure, mixture ratio, injector type and dimensions, chamber geometry and throat diameter of the different combustion chambers investigated at Penn State University. Additionally, the input parameters for the numerical simulations published in Ref. [37] in the same table.

Table 11: Design parameters of Penn State thrust chamber[24]. Mass flow rate for a throat diameter $d_t = 8.68\,\text{mm}$ and a mixture ratio of $O/F = 6$.

Propellant		GO_2/GH_2
Mixture ratio	O/F	up to near stoichiometric
Combustion chamber pressure	$p_{CC,max}$	6.89 MPa
Combustion chamber temp.	$T_{CC,max}$	3555 K
Mass flow (measured [24])	$\dot{m}(p_{CC} = 5.17\,\text{MPa})$	122-131 g/s
Mass flow (calculated [28])	$\dot{m}(p_{CC} = 6.89\,\text{MPa})$	177 g/s
Cooling of combustion chamber		heat sink cooling using OHFC
Cooling of nozzle		water cooled

An overview to the system concept is given in Tab. 15. As listed, the configuration consists of a single shear-coaxial injector element, a cylindrical combustion chamber and a conical nozzle. The materials in consideration are based on the recommendations given in Ref. [10]. The materials denoted in bold font are selected for the individual component. As preferred thermal protection methods, printed in bold again, is absorption and ablative heat sink cooling. The combustion chamber is ignited with a pyrotechnic element. More details to the individual elements are given hereafter.

5.2.1 Injector Element

A single shear coaxial injector element is used, which is almost identical to the geometry of the *Rocketdyne* injector (US Patent 6,253,539). This injector was studied in the frame of investigations for the full-flow staged-combustion (FFSC) cycle engine as part of the NASA Reusable Launch Vehicle (RLV). The main geometrical dimensions are listed in Tab. 14 and are used as basis for the design of the injector for the thrust chamber integrated in the wind tunnel model. The corresponding technical drawing is given in Fig. 80.

It shows a close-up of the injector environment used for the wind tunnel models. Hydrogen and oxygen is supplied through the feeding tubes integrated in the strut support (1) and (2). The hydrogen and oxygen feeding tube is connect to a chamber (3) and an annular chamber (4), which feed the coaxial injector. The injector head is equipped with radial drill holes (5) that supply an additional chamber (6) to accommodate the option of film cooling. The film exits through the gap (7) between the wall the ring at the front end of the injector side. In this case, the front ring is equipped with an O-ring, thus film cooling is not applied. Instead, the technical drawing shows the second option for

Table 12: Opposition of the main features of the thrust chamber [24] and the outcome for the application at hand.

Feature	Advantage
extensively tested	→ high ready to use level
gaseous	→ better handling than cryogenic
oxygen/hydrogen combustion	part of the requirement → similar to Ariane 5
heat flux	→ run time can be determined → thermal protection system can be adapted
heat flux scaling law is known	→ flexible w.r.t. run time/combustion chamber pressure
combustion chamber pressures up to 6.89 MPa	→ high similarity → opportunity to study pressure scaling effects
comparably small dimensions	→ suitable to be integrated with little modifications in a wind tunnel model and installed in an appropriate wind tunnel
coaxial injector	almost identical *Rocketdyne* injector similar to the ones used in Vulcain 2 → high similarity
dimensions injector geometry are available	→ high ready to use level
data is available for a mixture ratio of 6.0	→ similar to mixture ratio of the Vulcain 2 rocket engine
works up to near stoichometric mixture ratios	→ high chamber temperatures → high similarity → opportunity to study temperature scaling effects

Table 13: Overview to experiments with gaseous hydrogen/oxygen combustion chambers executed at Pennsylvania State University plus a selected numerical investigation.

Paper	type	preburner	combustion chamber				injector diameters					nozzle
Ref.	exp./num.	no/yes	pressure p_{CC} MPa	mixture ratio O/F	length L_{CC} mm	width diameter D_{CC} mm	type[a]	post, inner $d_{ip,i}$ mm	post, outer $d_{ip,o}$ mm	sleeve d_{is} mm	recess r_{ip} mm	throat d_t mm
[24]	exp.	no/yes	2.07 to 5.17	6.0/6.6[b]	285.75	38.1	C	5.26	6.27	7.49	1.52	8.67/8.18
[29]	exp.	yes	5.42	161/1.13[c]	285.75	38.1	C	5.26	6.30	7.49	0.43[d]	8.166
[25]	exp.	no	1.31	4.0	245.6	50.8	C	7.75	9.56	12.7	0	11.36
[26]	exp.	no	1.31	4.0	245.6	50.8	C	7.75	9.53	12.7/10.74	0	11.36
[21]	exp.	no	1.37	3.8	245.6	50.8	C	7.75	9.53	12.7	0	11.35
[22]	exp.	no	1.28 to 6.89	4.0	246	50.8	C+SC	7.75	9.53	12.7	0	-
[12]	exp./num.	no	1.29	4.0	245.6	50.8	C	7.75	9.53	12.7	0	11.35
[23]	exp.	no	1.31	4.0	-	50.8	C	7.87	12.7	15.24	-	-
[17]	exp.	yes	0.34 to 1.38	6.0	-	25.4	CM	5.26	6.27	7.49	-	12.42
[18]	exp.	yes	0.79	6.0/4.25[e]	320.675	25.4	CM	5.26	6.27	7.49	-	8.05
[37][f]	num.	yes	5.5	6.7	285.75	38.1	C	5.26	6.30	7.49	0.43	8.17

[a] C: coaxial, SC: swirl coaxial, CM: coaxial injector surrounded by a multi-hole injector plate
[b] Mixture with/without preburner
[c] Oxidizer/fuel preburner mixture ratios
[d] For CFD modeling: most likely takes post growth due to thermal expansion already into account
[e] In total 4 mixture ratios: both ratios undiluted and diluted with Helium
[f] based on [29]

Table 14: Dimensions of Penn State thrust chamber [24].

Outer diameter of thrust chamber	$D_{CC,O}$	$\sim 148\,\text{mm}$
Combustion chamber length to nozzle entrance	L_{CC}	$285.75\,\text{mm}$
Combustion chamber diameter	D_{CC}	$38.1\,\text{mm}$
Injector: post inner diam.	$d_{ip,i}$	$5.26\,\text{mm}$
Injector: post, outer diam.	$d_{ip,o}$	$6.27\,\text{mm}$
Injector: sleeve diam.	d_{is}	$7.49\,\text{mm}$
Injector: post recess	r_{ip}	$1.52\,\text{mm}$
Throat diameter	d_t	$8.68\,\text{mm}$

cooling, which is an ablative layer (8). The drill hole (9) is used to measure the combustion chamber pressure by connecting a pressure sensor to the other side of tube (10). Except for the radial drill holes (5), the inner geometry of the injector is identical to the injector of Ref. [29] downstream from about the location described with (3) and (4). Identical with respect to the interior flow.

For the study here, the injector head is used for a mixture ratio of 6.0. The general setup though is modular to provide the opportunity to investigate different injector geometries. For instance, the variation of the mixture ratio by keeping the shear between the components constant. Ref. [24] points out the necessity of the injector's compatibility to oxygen. For this reason, Monel is used for the inner post and is planned for the injector here as well. High requirements are posed to the production accuracy, which is emphasized to be smaller than 0.025 mm due to its sensitive influence. This recommendation is taken as a reference for the wind tunnel model injector.

The mixing of the propellants in a coaxial injector is caused by the shear due to the velocity difference. In oxygen/hydrogen comustors, the the post typically supplies the oxygen, while hydrogen runs through space between the post and the outer sleeve. The mass flow rates and the velocities for the different load steps at the exit of the injector, which is again used as baseline for the current thrust chamber, is listed in Tab. 16.

5.2.2 Combustion Chamber

First, an overview to the Penn State thrust chamber given, then heat flux measurements shown in Ref. [24] are used as input to conduct a thermal analysis for two different loads steps and the results are then presented. Further, the thermal protection concept and ignition method is discussed. Technical drawings of the injector and combustion chamber close to readiness are provided.

Table 15: System concept.

Configuration	
Injector	single shear-coaxial element
Combustion chamber	cylindrical
Nozzle	cylindrical
	conical, ideal, TIC, TOC, ...
Materials	
Injector	**Monel**
	copper alloy
	Hastelloy C
	Haynes 25
Combustion chamber	**OHFC**
	copper alloy
	stainless steel/347 CRES
	Hastelloy C
	Haynes 25
Nozzle	Nobium
	pyrolytic graphite
	molded graphite
	Carbon-carbon
	Tungsten
	Molybdenum
Thermal protection	
Injector	not critical
Combustion chamber	*heat sink cooling*
	absorption using OHFC
	film cooling with hydrogen
	ablative inner C-C lining
Nozzle	absorption/ablative
Seals	Metall seals (K-/U-type)
Igniter	pyrotechnic

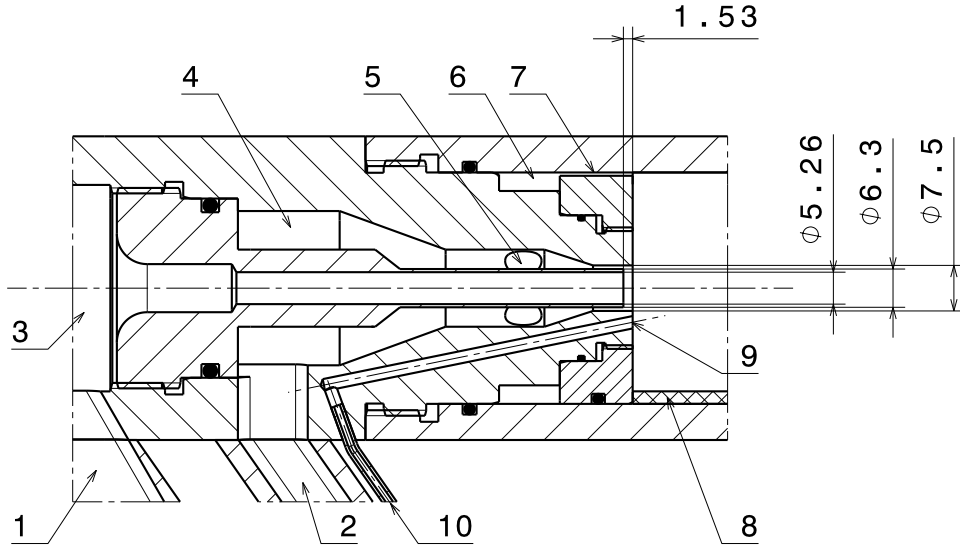

Figure 80: Cross-sectional view on the injector head.

Table 16: Flow conditions for various combustion chamber pressures and a mixture ratio of 6.0 according [24].

Mass flow rate	GH_2	g/s	7.4	12.0	14.9	18.6
	GO_2	g/s	44.6	67.0	89.3	111.6
Mixture ratio	O/F	6.0	6.0	6.0	6.0	6.0
Chamb. pressure	p_{CC}	MPa	2.07	3.10	4.14	5.17
Injector						
Ox. Velocity	v_O	m/s	77.4	77.4	77.4	77.4
Fuel Velocity	v_F	m/s	343.2	343.2	343.2	343.2
Velocity ratio	v_F/v_O		4.43	4.43	4.43	4.43
Mom. flux ratio	$\frac{\rho_F v_F^2}{\rho_O v_O^2}$		1.24	1.24	1.24	1.24
Mom. ratio	$\frac{\rho_F v_F^2}{\rho_O v_O^2} \cdot \frac{A_F}{A_O}$		0.74	0.74	0.74	0.74

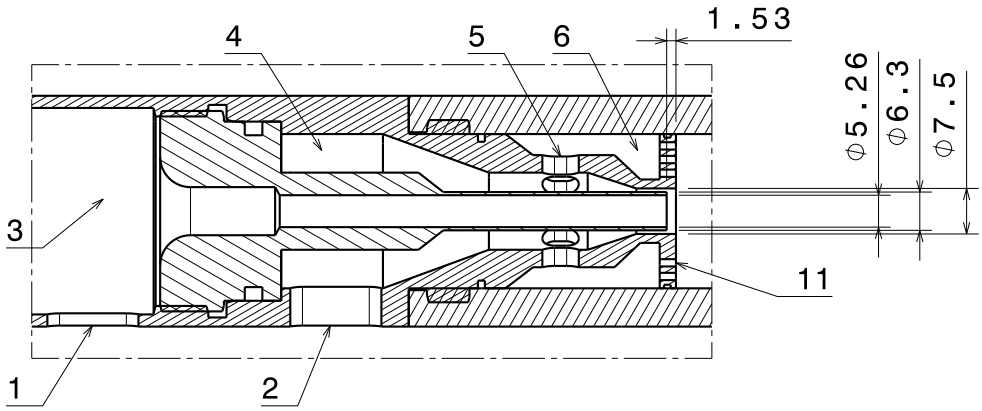

Figure 81: Sketch of a cross-sectional view on the injector head of the 1 in-combustion chamber.

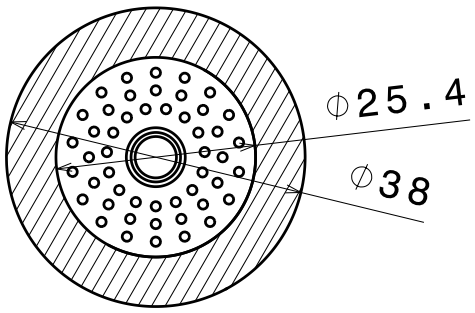

Figure 82: Front view on the injector head of the 1 in-combustion chamber.

One of the main challenges for the integration of the thrust chamber in a wind tunnel model concerns the handling of the thermal energy release in the thrust chamber while keeping the dimensions that are still acceptable for transonic testing. For the future model, one of the two cooling methods in use today has to be selected for the wind tunnel model at hand, namely *steady state* and *transient heat transfer/heat sink cooling* method. A steady state cooling is impractical and not necessary for the short duration runs of mostly 60 s.

Thus, the concept for the future thrust chambers rely on heat sink cooling. As it is shown later, three different models are planned, which take advantage of the different experimental environment of VMK and TMK. Due to the spatial restrictions in TMK, the heat sink concept based on the high conductivity of the thrust chamber material copper can not simply be transferred. But, the Penn State thrust chamber can be directly integrated in the VMK wind tunnel model.

In order to get some more insight into this thrust chamber, like the run time or the temperature distribution at a certain run time, a thermal analysis is presented hereafter based on the heat flux as given in Fig. 84.

The Penn State thrust chamber reaches for all combustion chamber pressures a scaled maximum heat flux of $\sim 2.3\,\mathrm{BTU/in^2/s}$, which corresponds to $3760\,\mathrm{kW/m^2}$, at about 2 in (51 mm) downstream from the injector. Here, scaled refers to the finding that the heat flux scales with respect to the chamber pressure to the power 0.8. The maximum combustion chamber pressure in these experiments is set to 750 psi ($\sim 5.17\,\mathrm{MPa}$) for which a maximum heat flux of $7826\,\mathrm{kW/m^2}$ was found. Extrapolating the power of 0.8 finding to a combustion chamber pressure of 6.89MPa results in an expected maximum heat flux of $9469\,\mathrm{kW/m^2}$.

The heat flux profile in the axial direction (Fig. 84) is now imposed on a cylindrical segment of a combustion chamber made of copper for a chamber pressure of 2.07 MPa (300 psi) and 6.89 MPa (1000 psi). The results are shown for the time step when the surface temperature of the combustion chamber exceeds 1080 °C, which is approximately the melting point of copper. The outer wall is defined to be radiation-adiabatic.

Fig. 85 depicts the temperature distribution for the 2.07 MPa case after 47.4 s. Obviously, the location where the highest temperature can be found corresponds to the location with the highest heat flux. The melting temperature is reached after 47.4 s, which is more than sufficient for testing with currently available measurement techniques.

The temperature profiles in radial direction of the thrust chamber for different times steps at the location with the highest heat flux (51 mm downstream from the injector) is given in Fig. 87. As expected, the wall absorbs and transports the heat towards the outer region. The energy transfer is fast enough to keep the surface wall temperature below the melting point of copper for a sufficient testing time.

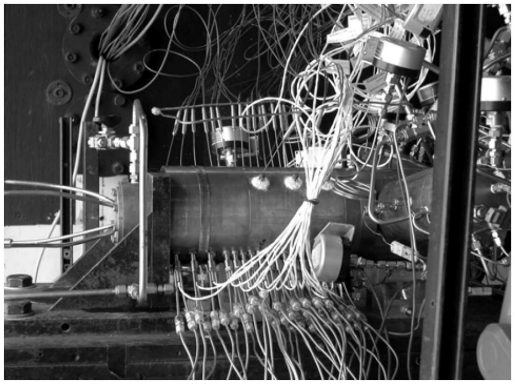

Figure 83: Picture of the combustion chamber Ref. [24].

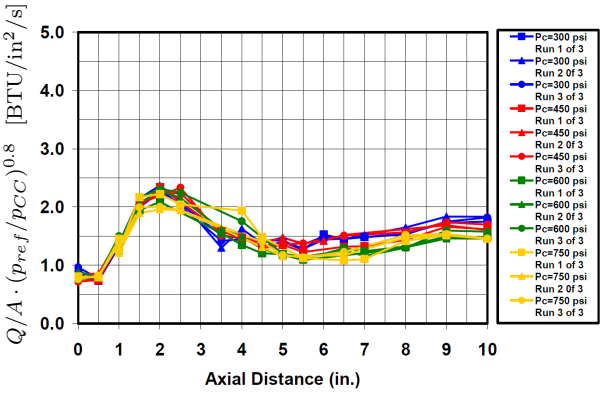

Figure 84: Heat flux (scaled with respect to $(300\,\text{pisa}/p_{CC})^{0.8}$) versus axial distance for a four combustion chamber pressures Ref. [24].

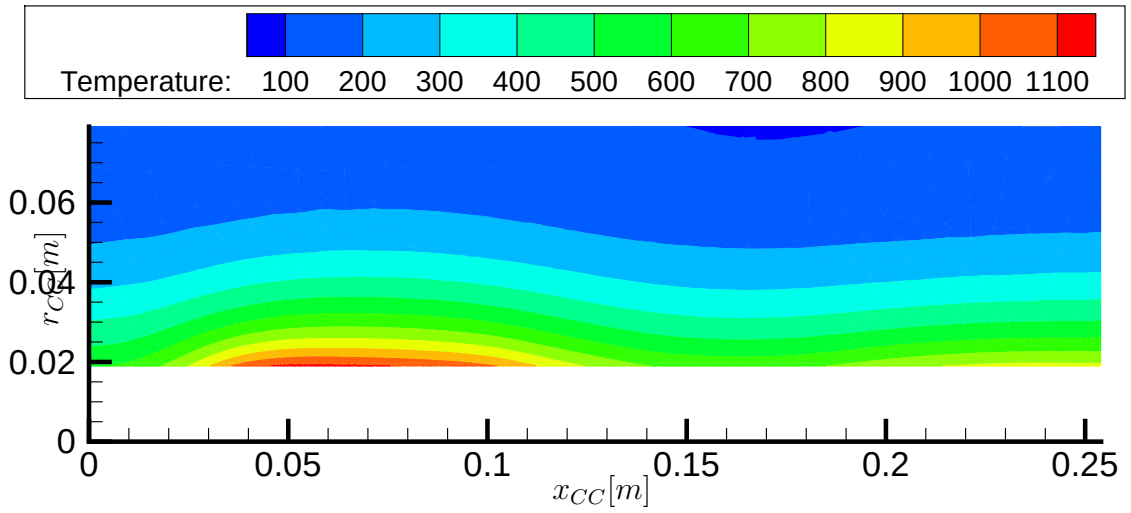

Figure 85: Temperature distribution of a copper thrust chamber after $t \approx 47.4$s for a heat flux rate corresponding to a chamber pressure of 2.07 MPa $=$ 300 psi.

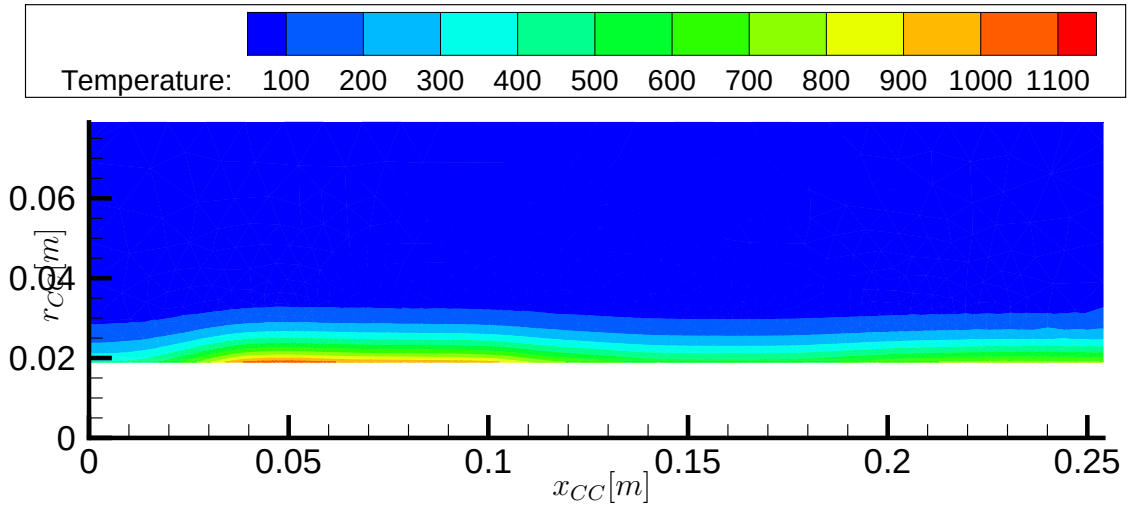

Figure 86: Temperature distribution of a copper thrust chamber after $t \approx 2.6$s for a heat flux rate corresponding to a chamber pressure of 6.89 MPa = 1000 psi.

This is more challenging for the 6.89 MPa case. The temperature distribution and temperature profiles in Fig. 86 and Fig. 88 reveal that the surface can only cope with that heat flux for about 2.6 s before the melting point of copper is reached. Heat transfer in the radial direction is not fast enough to allow a longer longer time.

The conductivity based heat sink cooling method can only be applied on the VMK model since the blockage due to the model is not as grave for the later suggested upstream supported wind tunnel model concept. The aspect of blockage becomes more dominant for the classical wind tunnel model with strut support as planned for testing in TMK. And due to spatial restrictions to the outer dimensions, other thermal protection concepts are required.

According to [35], ablative cooling is effective in small thrust chambers. Strong, orientated fibers of Kevlar or carbon engulfed in a matrix of plastics, epoxy or phenolic resins are used as ablative material. The cooling method is based on the endothermic degradation of the ablative material resulting in a cool film that seeps through matrix. The heat is absorbed through various energy conversion processes, namely surface melting, sublimation, charring, evaporation, decomposition, and finally causing a cooling film. The preferred ablative material is made of carbon fibres in a matrix of amorphous carbon, which features an erosion ratio of about erosion rate 0.0127 to 0.0254 mms^{-1} (0.0005 to 0.001 ins^{-1}). Consequently, it takes roughly 80 s for the worst case until a protective layer of carbon fibers in a carbon matrix of 2 mm is degraded.

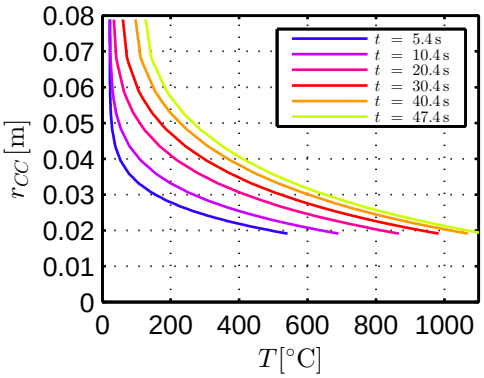

Figure 87: Temperature profiles at $x_{CC} = 51$ mm of a copper thrust chamber for a heat flux rate corresponding to a chamber pressure 2.07 MPa.

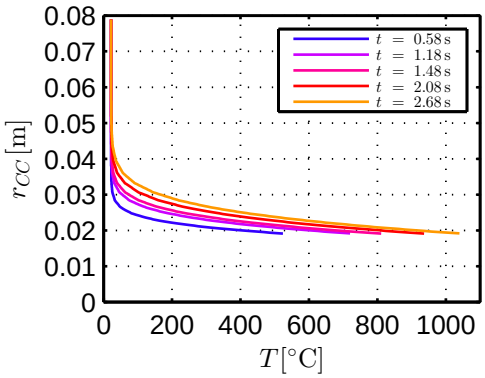

Figure 88: Temperature profiles at $x_{CC} = 51$ mm of a copper thrust chamber for a heat flux rate corresponding to a chamber pressure 6.89 MPa.

An ablative insert is considered as an appropriate approach to cope with high heat flux for the TMK model. In Fig. 80, this ablative insert is marked with 8. In this technical drawing, the thickness of the insert corresponds to the 2 mm as suggested before.

Additionally, it can be seen that the injector features the option protecting the walls with film cooling. The section upstream of the annular ring of the coaxial injector, which provides the mass flow of the gaseous hydrogen, exhibits drill holes. The mass flow through these drill holes exits through a gap between the front side where the injector is integrated and the surface walls of the combustion chamber supplying the wall with a cool hydrogen film. Different rings allow different gap sizes to adapt the mass flow. This method might help to reduce the heat flux at the location where it is maximal if the film persists. For the application at hand, a quantification of this method with respect to its efficiency requires an in-depth analysis or testing later. But, it seems to be a good-to-have option.

Several groups overseas and in Europe use the data of Ref. [24] as benchmark for the validation of their CFD codes. This is interesting to keep the investigations of the base flow effects focused on its actual purpose instead of investing time and money into calibration and investigation of the combustion chamber characteristics itself.

An example is given in Fig. 89, which is extracted from Ref. [37]. It shows the benchmark heat flux measurement with preburner of Ref. [24] versus numerical simulations for the load step of 5.17 MPa. Similar experimental results without preburner were shown before in Fig. 84. A whole spectrum of simulations, namely with steady Reynolds-Average Navier Stokes (RANS), unsteady Reynolds-Average Navier-Stokes (URANS) and three different Large Eddy Simualtions (LES), were executed by the NASA Marshal Space

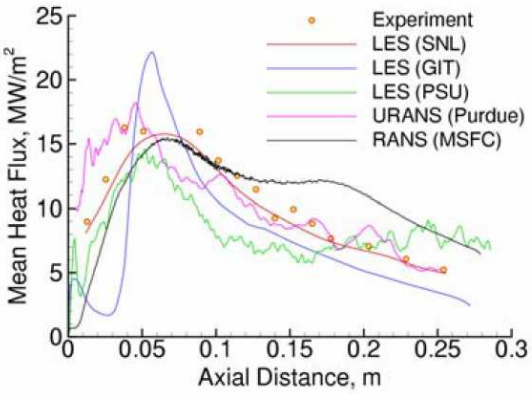

Figure 89: Heat flux prediction from different CFD calculations compared with corresponding experimental data [37].

Flight Center (MSFC), Purdue University, Pennsylvania State University, Georgia Institute of Technology and Sandia National Laboraties, respectively. Generally, it shows that the LES (SNL) from *Sandia National Laboratories* with the highest fidelity simulation accomplishes to match the data quite well over the whole course, while the other models achieve that only partially.

Another example is given in Fig. 90. It shows the time-averaged OH mass fraction distribution. Although, it can be seen that the results differ quantitatively and qualitatively, it shall be stated that the investigation of combustion mechanisms is an ongoing research topic and choosing a benchmark thrust chamber for numerical investigation keeps up the expectation of more data to come that would not be available otherwise.

This way, the characteristics of the thrust chamber are going to be more and more specified. For instance, the OH radical concentration or the temperature distribution is important with respect to the lifetime of the components. Further, data to the oxygen/hydrogen concentration distribution return a certain knowledge about the completeness of the reaction a deliver input conditions for the expansion through the nozzle for the base flow interaction investigation.

5.2.3 Nozzle

At this early stage of development, the nozzle is not defined in detail since it is not that relevant yet and can be designed according to the requirements given by ESA. One of the aspect set of the nozzle concerns the axisymmetric configuration. Further, a throat diameter of 8 mm was set to narrow down the reference parameters. But, the

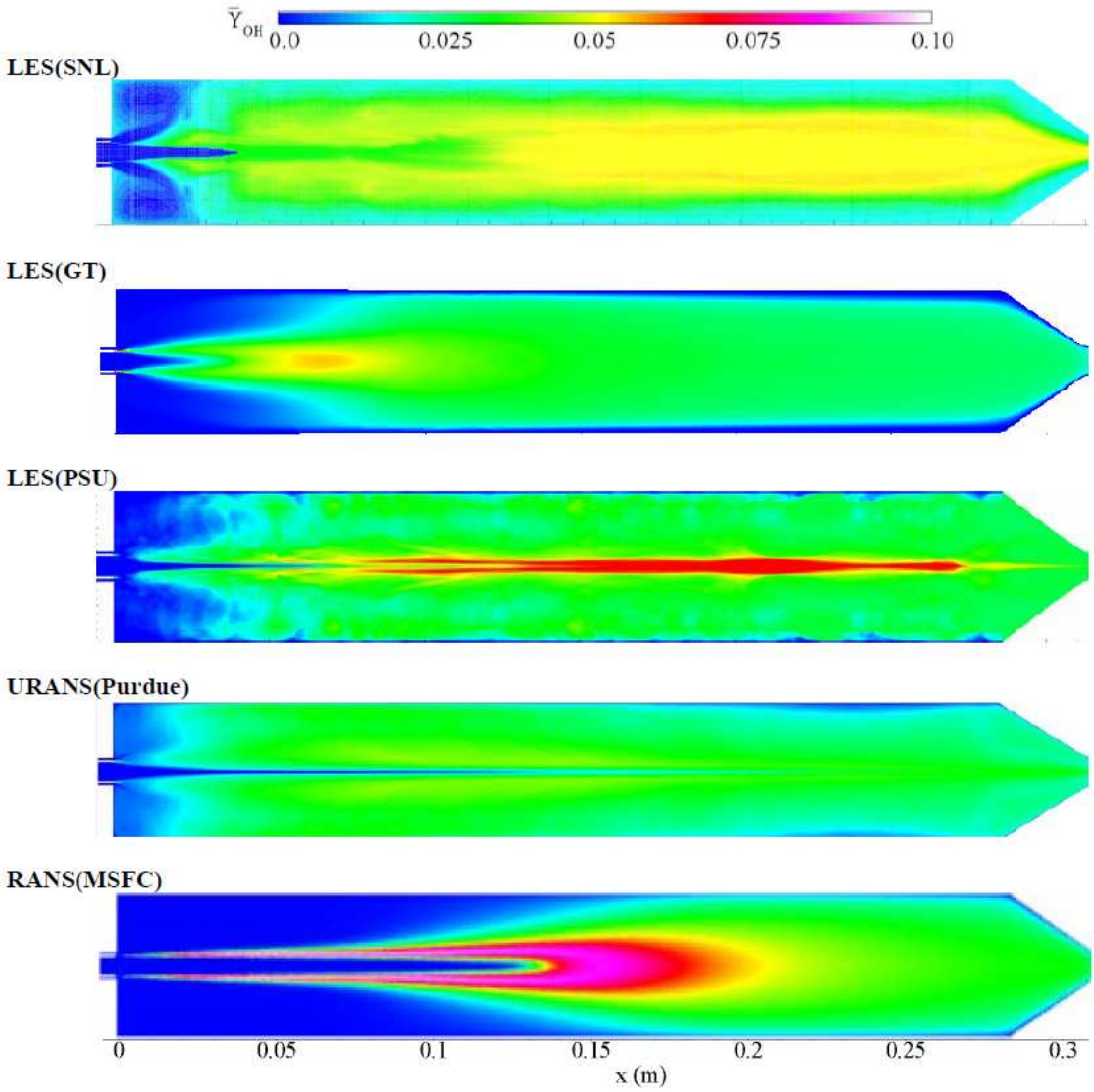

Figure 90: Time-averaged distribution of OH mass fraction [37].

contour itself manufactured as conical, ideal, truncated ideal contoured (TIC), truncated optimized contoured (TOC), etc. nozzle.

A water cooled nozzle configuration seems to be too complex at least for the TMK wind tunnel model due to the spatial restrictions. It could be realized for the VMK model, but is not intended. So far, it is planned to protect the the nozzle throat from high heat loads with an insert of pyrolytic graphite or with molybdenum. Both materials can withstand very high temperatures. Since it is expected that the nozzle throat erodes during testing, it is recommended to replaced the insert after hot tests.

Deutsches Zentrum
für Luft- und Raumfahrt e.V.

TN3132

Model and Facility Design

May 24, 2013

Dominik Saile
Andreas Henckels
Dieter Wyborny

Institute of Aerodynamics
and Flow Technology
Supersonic and Hypersonic
Technology Department

Deutsches Zentrum
für Luft- und Raumfahrt e.V.
in der Helmholtz-Gemeinschaft

ESA STUDY CONTRACT REPORT

No ESA Study Contract Report will be accepted unless this sheet is inserted after the coverpage of each volume of the Report.

ESA CONTRACT No.: AO/1-6731/ 11/NL/SFe	SUBJECT Hot Testing Facility for ELV Propulsion Characterization		CONTRACTOR DLR
* ESA CR( )No	* STAR CODE	No of TN 3132	

ABSTRACT:

This report presents the results from a study regarding to the wind tunnel model and facility design in the framework of the ESA technology research project "Hot Testing Facilities for ELV Propulsion Characterization". The concepts of wind tunnels with an open, closed and partially open measurement section are presented and opposed to each other. Results of blockage tests with in TMK as representative of a wind tunnel with a partially open measurement section are discussed. A test concept is provided involving an upstream supported and a strut supported wind tunnel model with and without boosters for tests in VMK and TMK. This concept meets the given requirements with respect to flight similarity by providing testing capabilities concerning altitude variation, variation of angle of attacks, dynamic pressure response, thermal analysis, influence of mixture ratio, of total temperature, of strut support, of single and multiple plumes, of oxygen/hydrogen and solid propellant combustion. The infrastructure for the feeding system of the hydrogen/oxygen combustion chamber is shown and how it will be realized on the site in Cologne.

The work described in this report was done under ESA contract. Responsibility for the contents resides in the author or organization that prepared it.

Name of author: D. Saile, A. Henckels, D. Wyborny (DLR, Cologne, Germany)

** NAME OF ESA STUDY MANAGER	** ESA BUDGET HEADING
N. Murray DIV: TEC-MPA DIRECTORATE: D\TEC	

* Sections to be completed by ESA

** Information to be provided by ESA Study Manager

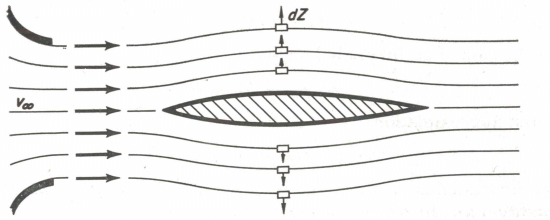

Figure 91: Streamline distortion in open test section [14].

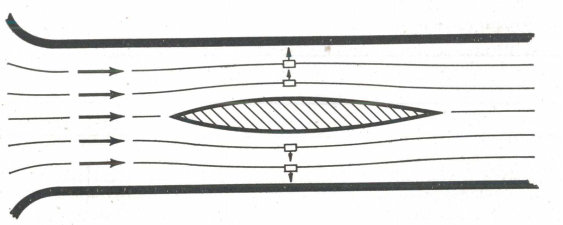

Figure 92: Streamline distortion in closed test section [14].

6 Model and Facility Design - TN3132

6.1 Wind Tunnel Design Selection

6.1.1 Opposition of Different Wind Tunnel Types

A short introduction to the different wind tunnel types under consideration is given in the following section to explain some inherent issues. The wind tunnels for the application at hand mainly differ with respect to the test section, which can be open, closed or partially open. Fig. 91 and Fig. 92 visualize the flow by means of streamlines around an exemplary wind tunnel model for a wind tunnel with an open and with a closed test section, respectively.

It can be noticed, that the streamlines for the open test section bulge out, while they are straightened and squeezed around the model for the closed measurement section. Obviously, this is a result of the different boundary conditions that are imposed on the flow. Fig. 93 gives an overview of the consequences with respect to free flight conditions.

For subsonic test in an open test section wind tunnel, the bulging of the streamlines due to the blockage of the model is causing a change of the interrelated physical parameters: the stream density and the velocity is smaller in comparison to free flight. The pressure gradient adapts faster in the lateral direction with respect of the flow due to the imposed ambient pressure at the wind tunnel nozzle exit. Also, a larger curvature of the streamlines larger and centrifugal forces is found. With increasing Mach number, this tendency continues even close to Mach 1. No peculiar effect is expected at that point for a wind tunnel model in the flow field since there is space for the streamlines to bulge farther.

In the supersonic regime, the most dominant effect with regard to the erroneous influences on the model is caused by wave reflections. Pressure waves that emanate from the tip of the model are reflected as expansion waves at the shear layer of the free jet.

An impingement of the expansion waves in the region of interest is consequently to be avoided. Note, that expansion waves are reflected as pressure waves.

The squeezing of the streamlines found in subsonic investigation using a closed test section consequences opposite effects. The stream density increases and leads to an increased velocity field between the model and the wall. Further consequences are a smaller pressure gradient, a smaller curvature of the streamlines and smaller centrifugal forces.

At higher Mach numbers, the well-known effect of 'choking' occurs. In this case, the narrowest section in the wind tunnel is given by the model. Thus, the flow accelerates and reaches Mach 1. Choking for instance is reached at Mach 0.8 and 0.9 for blockage ratios of 3.7% and 0.88%, respectively.

In the supersonic case, the situation is comparable to tests with an open test section. The wave reflections pose the limits on the wind tunnel length. Here at the solid wall though, shocks get reflected at shocks and expansion waves as expansion waves. The cross-sectional area of the wind tunnel model loses of importance.

It can be seen that the open test section leads to smaller velocities around the model and the opposite is the case for a closed test section. This is also depicted in Fig. 93. In the past, correction methods have been developed to encounter that problem. Though, the distortion of the streamlines still prevail with this method and are found to be impractical for general wind tunnel testing [14]. This graph already includes a solution to the opposing velocity tendencies of the two wind tunnel concepts, which is a partially open tunnel. If the flow disturbance around the model do not reach the vicinity of the wind tunnel walls, it can be expected that the velocity correction remains zero in subsonic tests.

Table 17: Opposition of wind tunnel with open and closed test section.

Effects at	Wind tunnel with	open test section	closed test section
	system interface	shear layer with ambient pressure imposed	solid wall
$Ma < 1$	streamlines	bulge out	straightened/ squeezed
	stream density	$\rightarrow$ smaller	$\rightarrow$ larger
	pressure gradient	$\rightarrow$ larger	$\rightarrow$ smaller
	curvature of streamlines	$\rightarrow$ larger	$\rightarrow$ smaller
	centrifugal forces	$\rightarrow$ larger	$\rightarrow$ smaller
	velocity	$\rightarrow$ smaller	$\rightarrow$ larger
$Ma \approx 1$	effects	no peculiar effect / streamlines can freely bulge out	choking
$Ma > 1$	wave reflection	pressure $\rightarrow$ exp. exp. $\rightarrow$ pressure	pressure $\rightarrow$ pressure exp. $\rightarrow$ exp.

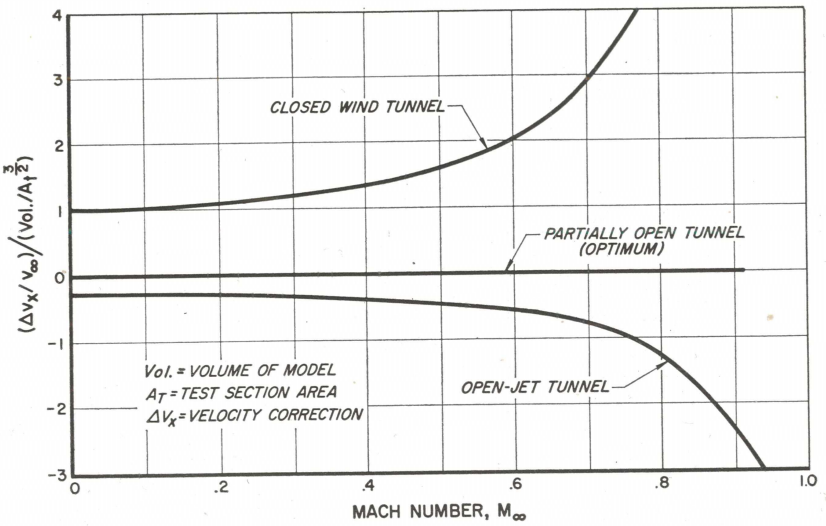

Figure 93: Velocity corrections in open, closed and partially open wind tunnels as function of Mach number [14].

6.1.2 Opposition of TMK and VMK

The cost-benefit analysis presented in the trade-off in Ref. [30] revealed that an update of the *Vertikale Messtrecke Köln* (VMK) and *Trisonische Messtrecke Köln* (TMK) is definitely to be preferred. Combined measurement campaigns in VMK and TMK with complementary wind tunnel models as presented in Chap. 6.2 offer a wide range for investigations and cope with the requirements listed in Ref. [4]. In the following, both wind tunnels are opposed to each other to find a concept for future wind tunnel models. Information that is relevant for the comparison is given in Tab. 18.

VMK is a 'blow-down'-type wind tunnel with a vertical free jet test section for the simulation of the flow in the Mach number range from 0.5 to 3.2 by using contoured axial-symmetrical nozzles, which is directly mounted on a platform on the floor. The measurement section is integrated in a concrete tower with overpressure protection. By means of its heater capacity for total temperatures up to 700 K, VMK allows to simulate sea level flight conditions up to a Mach number of 2.8 with a correct duplication of the corresponding pressure and temperature. On average, up to 10 tests a day are carried out at this facility, with a typical run time of approx. 60 seconds.

The aspects involving the design of the wind tunnel model can be exploited in such a way that an upstream supported wind tunnel model can be used for testing. If the model is held upstream in the center of the wind tunnel model and the flow has to pass through straighteners further downstream, the model is exposed to a flow that is not disturbed by any nearby sting or strut support. This fact is advantageous by itself, but it can further be used to extract information about the influence of the strut from the measurements in TMK.

Further, it is known that the streamlines in open test section bulge out in comparison to free flight [14] . The concept of an upstream held wind tunnel model though, as also shown in numerical simulations [7], does not result in an displacement of the flow in the region of interest, and thus avoids this effects making VMK, in contrast to the models in TMK, basically independent of the diameter with regard to blockage.

Not to underestimate is the accessibility of VMK due to the nature of featuring an open test section with room to the walls and its vertical orientation. Various and joined measurement techniques can be set up simultaneously delivering time-correlating measurement results. Setting them up is easy and convenient for the same reason.

Also on the plus side of VMK stands the concrete tower with overpressure protection. Even in the worst case scenario like an explosion of a rocket engine or fire, VMK isolates the test section from the stuff and the rest of the facility, meaning the level of safety is very high. After the careful development of the rocket engine, it can be tested in VMK without hesitation. This wind tunnel is unique with respect to this is feature in Europe.

The TMK is also a 'blow-down'-type wind tunnel with a closed test section of $600 \times 600\,\mathrm{mm}^2$. It is equipped with a flexible, continuously adjustable nozzle. The simulation range of this wind tunnel varies from subsonic (Mach 0.5) to transonic and the higher supersonic range of Mach 5.7. In the transonic setting, a test chamber with perforated walls is used. A storage heating allows to vary the total temperature from ambient temperature up to 550 K in the supersonic range. TMK is equipped with an ejector to decrease the ambient pressure or to adjust the Reynolds number. Depending on the Mach number, approx. 10 tests per day can be carried out. The typical duration of a test is between 30 and 60 seconds.

For clarity, some of the features are again discussed in more depth. It shall be emphasized that TMK enables continuous testing in the transonic flow regime due to continuously adjustable nozzle, while compensating for blockage or shock reflections due to the perforated walls in the transonic test section. If interested, the tests can be extended to higher Mach numbers if the transonic test section is removed.

In the supersonic setting at Mach $Ma > 1.5$, the usage of the ejector offers in combination with a combustion chamber the opportunity to conduct altitude simulations without actually varying the combustion chamber pressure. The pressure ratio, called the nozzle pressure ratio NPR, is adjusted by simply lowering the ambient pressure while keeping the Mach number constant. If no combustion chamber is integrated in the wind tunnel, this is comparable to a Reynolds number variation at a constant Mach number.

Note that the quality of the free stream is very high for TMK. It provides a very low turbulence level. This is the outcome of a careful design of TMK including straighteners and a settling chamber.

Summing these observations up, TMK is planned to be used for high flow quality transonic testing with a strut supported model. The blockage ratio has to be kept in mind. For this reason, after having defined the different wind tunnel model concepts, the dimensions of them are defined in the next section. A detailed list of the focus of the investigations for VMK and TMK is listed later in Chap. 6.2 where the wind tunnel models are discussed.

Table 18: Opposition of VMK and TMK.

Wind tunnel		**VMK**	**TMK**
Nozzle		*cylindrical*	*rectangular & adjustable*
	+	→ upstream supported → no strut induced disturbances	→ continous for Mach number range $0.5 < Ma < 5.7$
	-	→ Mach number not adjust. in supersonic range	→ strut support required → strut induced dist.
Test section		*open*	*perforated walls*
	+	→ very good accessibility w.r.t. optics & maintenance	→ designed especially for transonic testing w.r.t shock reflections and blockage
	-	→ potential bulging of streamlines (not for upstream supported model)	→ accessibility
		vertical	*horizontal*
	+	→ very good accessibility	→ no upstream deviation of flow before the nozzle entrance
	-	→ upstream deviation of flow before the nozzle entrance	n.a.
Ejector		*n.a.*	*can be used for* $Ma > 1.5$
	+	n.a.	→ pressure adjustments → Reynolds number variations → altitude simulation
Safety		*concrete tower*	*no special measures*
	+	→ with overpressure protection	n.a.
Settling chamber		*not installed*	*installed*
	+	n.a.	→ low turbulence
Straighteners		*installed*	*installed*
	+	→ planned for upstream supported model	→ low turbulence

ESA TRP Study

TRP Hot Testing Facilities for ELV Propulsion Characterization

Title: TMK blockage tests

Document Number: ESA TRP-HOTP-DXX
Issue: 1.0
Date: 09.11.2012

Author(s): Dominik Saile, Ali Gülhan
Organization: Supersonic and Hypersonic Technology Department
German Aerospace Centre (DLR)

CONTENT

1. Introduction

In the telephone conference with Neil Murray, Ali Gülhan and Dominik Saile on 08.08.2012, it was discussed to conduct a limited series of blockage tests to receive some preliminary results with respect to the influence of the blockage ratio between wind tunnel model and wind tunnel. It shall be emphasized that these measurements are additional to the deliverables described in the framework of the TRP contract [1,2,3]. Thus, limited and preliminary data mirror the fact that only limited time and resources were available for the tests.

Nevertheless, the pressure coefficient along the wall of the wind tunnel and on the sting downstream from the wind tunnel model are presented for a self-similar wind tunnel model at representative subsonic and supersonic Mach numbers, at 0.85 and at 1.1, respectively. The focus of this paper does not lay on a detailed aerodynamic interpretation of the flow effects.

2. Methods

The blockage tests are executed in the transonic setting of the TMK (Figure 1). The TMK is a „Blow-Down“ wind tunnel with a closed test section of 0.6 x 0.6 m². It is equipped with a flexible, continuously adjustable nozzle. The simulation range of this wind tunnel varies from subsonic (Mach 0.5) to transonic and the higher supersonic range of Mach 5.7. A view from the inside of the transonic test section is given in Figure 2. Tests are run at Mach 0.85 and 1.1.

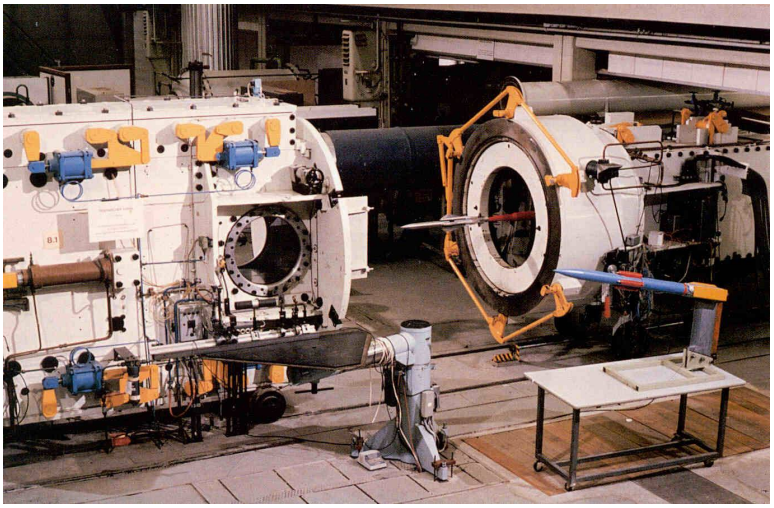

Figure 1: Picture of the TMK

Figure 2: Picture of the transonic measurement section of the TMK with embedded static pressure tabs

The blockage tests are conducted with a self-similar model shown Figure 3. The model is a cone with an aperture angle of 40.53°. With various segments, a blockage of 0.5%, 0.75%, 1%, 2%, 3%, 4%, 5%, 6%, 8%, 10% and 12% can be tested. A technical drawing of the cone is shown in Figure 4. The paper at hand presents tests with 1%, 2%, 3% and no wind tunnel model at all.

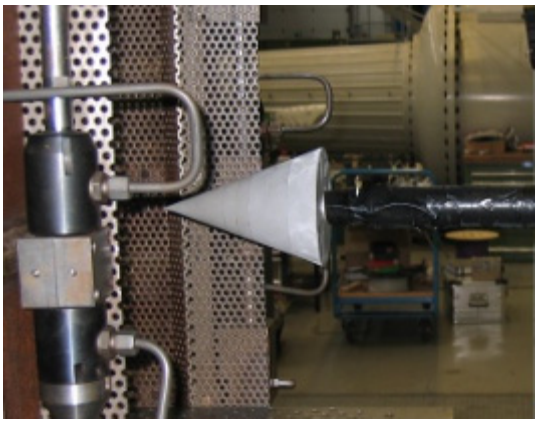

Figure 3: Picture of blockage model in the TMK

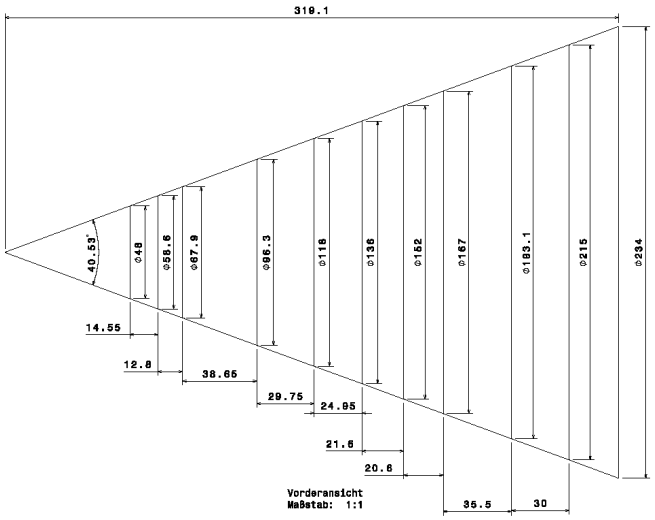

Figure 4: Technical drawing of blockage model

The influence of the model size is measured with pressure tabs on the sting of the wind tunnel model and along the wind tunnel wall. The pressure tabs on the sting are taped 0cm, 1cm, 2cm and 3cm downstream from the base. The wind tunnel wall is equipped with a strip of pressure tabs, which is shown on the left side of the picture in Figure 2. In total, 16 measurement tabs are used on a length of 45cm. Two tabs take the pressure at the height upstream from the model tip, the rest downstream.

The pressure tabs are connected with tubes to the following pressure transducers: Statham PDCR 22 (±10, ±25 psid), Statham PM856±15 (±15 psid), PM856±25 (±25 psid), PM131TC±10-350 (±10 psid), Statham PA208TC 50-350 (50 psia) pressure transducers. The measurement range is mentioned in brackets. The data acquisition system consists of a strain gage input module NI SCXI-1520 for signal conditioning and a NI PXI-6284 data acquisition module.

3. Measurement Results and Discussion

The Mach numbers of the runs with the various blockage models are depicted in Figure 5 and Figure 6 for the Mach 0.85 and 1.1 investigations, respectively. It is an outcome of the static pressure in the transonic measurement section and the reservoir pressure. The Mach number is plotted over the number of samples N, which is equivalent to a time interval of $\Delta t = 0.01s$. Note, that these runs are executed back-to-back, meaning no iterations are done to decrease the bounds of the Mach number courses.

With respect to the circumstances, it shows that the Mach number varies only slightly over the course of one run and that the transonic settings are repeatable. For the Mach 0.85 case, the difference of the various runs and within one run is less than 1%. Within one run, this statement can also be made for the Mach 1.1 case. With 2%, the difference between the runs is slightly higher for the run with no wind tunnel model. Generally, it shows that the Mach

number is kept constant over the course of one run and over the various runs, thus, the pressure coefficients presented hereafter are comparable within limits with each other.

The variations in the Mach number course is due to the fact that in transonic testing it is influenced by the model size. In the TMK, it can be adjusted to the model size by adapting the wind tunnel nozzle setting and the corresponding reservoir pressure, and additionally, by controlling the flow through the perforated wall in order to adjust the static pressure in the transonic measurement section. Depending on further conditions for a parallel wind tunnel flow, the latter offers the possibility to adjust the Mach number over a range of almost $\Delta Ma = 0.1$. As mentioned in Ref. [3], with these measures, the Mach number can be fine-tuned to reach an accuracy of $\Delta Ma = \pm 0.5\%$.

The pressure and pressure coefficient distribution on the sting is shown in Figure 7, Figure 8 and Figure 9, Figure 10 for Mach 0.85 and 1.1, respectively. The pressure and pressure coefficient distribution along the wind tunnel wall is shown in Figure 11 and Figure 12 for Mach 0.85. No data along the wind tunnel wall is available for the Mach 1.1 case, and also, for the case with no model at Mach 0.85. As mentioned before, in the frame of these investigations, no aerodynamic interpretation of the flow effects is given here. A simple approach is taken where the pressure coefficient is taken as reference for the influence on the blockage ratio. For a self-similar wind tunnel model, the pressure coefficient is expected to be independent of the model size if the influence of the wind tunnel is negligible.

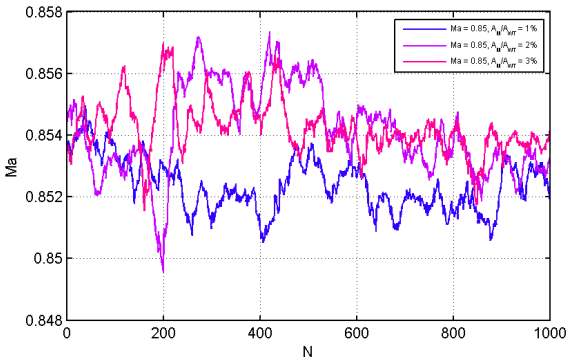

Figure 5: Mach number during experiments at Mach 0.85

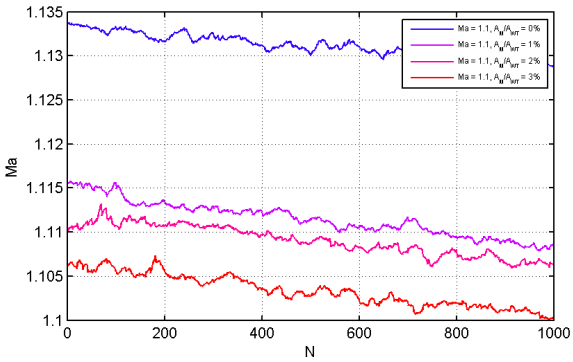

Figure 6: Mach number during experiments at Mach 1.1

For the Mach 0.85 case (Figure 8), it can be seen that the base pressure coefficient features an increase at all the locations downstream from the base if the wind tunnel model size is doubled from 1% blockage ratio. The maximum deviation of the pressure coefficient at 3 cm downstream from the base is about 13% to 14%. Consequently, tripling the model size results in even higher deviations.

The same statement holds true for the Mach 1.1 case (Figure 10). An overall increase of the pressure level can be observed if the model size is increased. No explanation is found for the major change in course of the pressure distribution in the frame of these quick investigations. As a result of the pressure measurements along the sting, it is strongly recommended to keep the blockage ratio of the model size below the 1%.

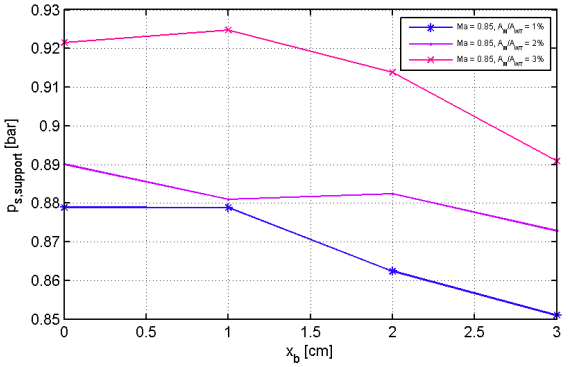

Figure 7: Pressure distribution on the sting downstream of the wind tunnel model at Mach 0.85

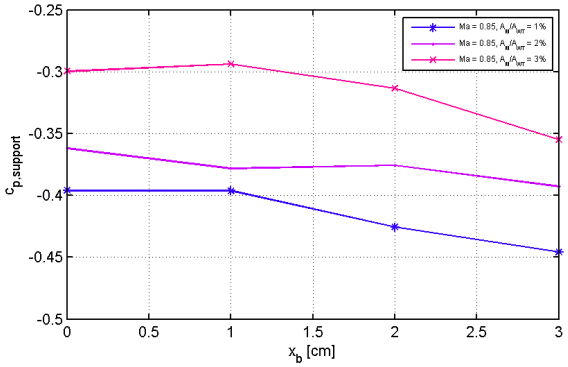

Figure 8: Pressure coefficient distribution on the sting downstream of the wind tunnel model at Mach 0.85

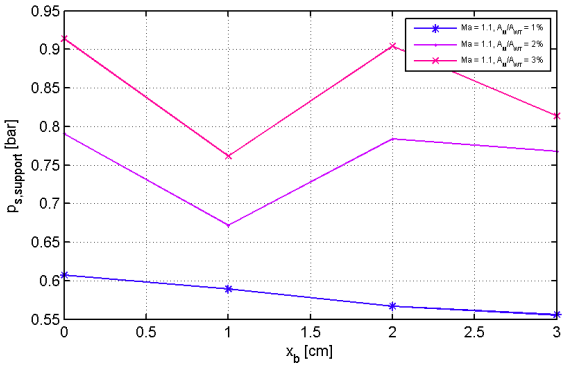

Figure 9: Pressure distribution on the sting downstream of the wind tunnel model at Mach 1.1

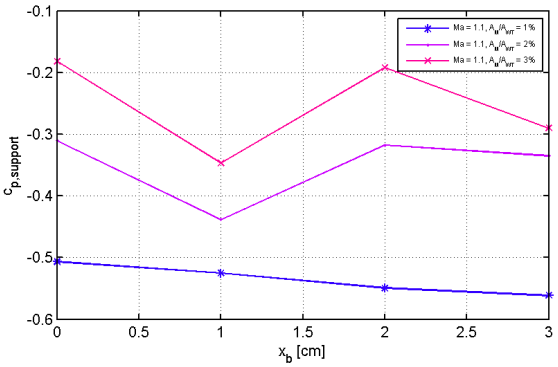

Figure 10: Pressure coefficient distribution on the sting downstream of the wind tunnel model at Mach 1.1

The wall pressure and wall pressure coefficient distribution is shown in Figure 11 and Figure 12. The tip of the model is located at the height of 0 cm. A flow field that is not influenced by the wall features a wall pressure coefficient of $c_P = 0$. For a blockage ratio of 1%, the pressure coefficient along the wind tunnel wall stays approximately at a constant level and indicates a negligible influence of the wind tunnel model to the flow. Higher blockage ratios impose a slight change on this course, consequently lead to the conclusion that the pressure coefficient is influenced by the model size.

4. Conclusion

A short additional study based on the ESA request has been carried out. The objective of the investigations here was to gain insights into the blockage effects in the transonic flow regime of TMK with very limited resources. The pressure coefficient distribution of a self-similar wind tunnel model was measured on the sting and along the wind tunnel wall at Mach 0.85 and 1.1, while varying the model size. It was shown that an increase of the model size causes a deviation from the pressure coefficient distribution compared to the blockage ratio of 1%. The wall pressure coefficient is also affected by the model size. Thus, a maximal model size of 1% is highly recommended, which is used as a rule of thumb for transonic testing in literature.

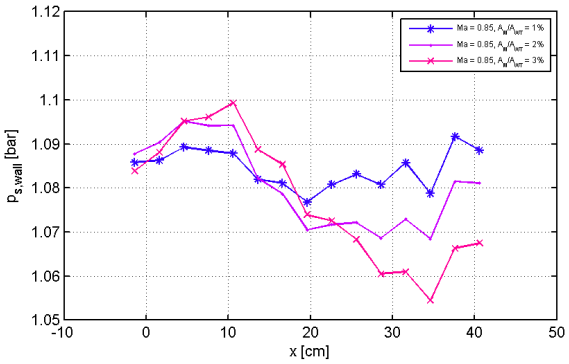

Figure 11: Pressure distribution along wind tunnel wall at Mach 0.85

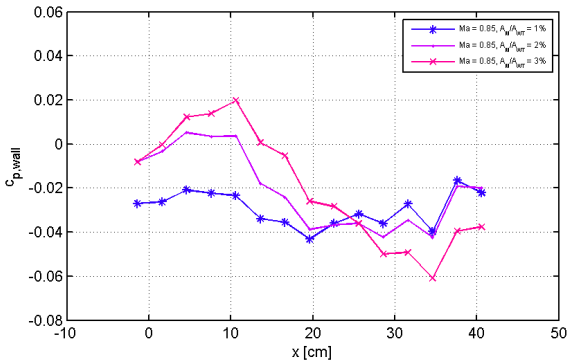

Figure 12: Pressure coefficient distribution along wind tunnel wall at Mach 0.85

In the frame of this project, no extensive testing was possible. Data for a blockage ratio below 1% are missing for comparisons. Additionally, no wall pressure is provided for the Mach 1.1 case. Hence, a test series for a detailed specification of the expected blockage effects is desirable.

5. References

[1] "ESA ITT, A0/1-6731/11/NL/SFe, Hot Testing Facilities for ELV Propulsion Characterization", pp. 1-3, 2011.

[2] "ESA ITT, Statement of Work, Hot Testing Facilities for ELV Propulsion Characterization, Appendix 1 to A0/1-6731/11/NL/SFe," vol. T418-303MP, pp. 1-13, 2011.

[3] A. Gülhan, K. Hannemann, C. Willert, A. Henckels, and D. Saile, "DLR Proposal-No.: 3005921/Hot Testing Facilities for ELV Propulsion Characterization," 2011.

6.2 Wind Tunnel Model Concept

In the following section, considerations to the 'outer shape' the future wind tunnel model are presented. The term 'outer shape' is supposed to describe the geometry that is exposed to the exterior flow. The specifications here are dominated by the requirements for transonic testing. The 'inner features' take considerations about the combustion chamber like the thermal protection concept or the dimensions into account and is described in Chap. 5.

The various effects that have to be considered in transonic testing are described in Chap. 6.1.1 and listed for a better overview in Tab. 17. Now, this knowledge is applied to narrow down the design of appropriate wind tunnel models.

Mainly two different effects have to be considered in order to avoid falsified measurement results. In the subsonic range, the first, being the blockage effect, and second, being wall interactions.

The blockage effect with regard to the geometry of the model is more restrictive. It reflects the effect of an erroneous flow field in compared to free flight due to 'squeezed' streamlines. If compared to flight, this results in reduced centrifugal forces and pressure gradients in the region between the wind tunnel model and the walls. The blockage ratio is given by the ratio between the cross-sectional area of the wind tunnel and the cross section of the measurement section. For a wind tunnel with a closed measurement section, this ultimately leads to choking of the flow since the narrowest section is then located on the wind tunnel model.

Transonic wind tunnels avoid this situation due to an arrangement of open and closed wall elements like the perforated wall in TMK. Experiments have shown that the blockage ratio can then be up to 1%. This is a commonly accepted rule of thumb as it is used in many transonic wind tunnel facilities like TMK [11], HSWT [1] (High Speed Wind Tunnel) of Lockheed Martin in Dallas, Texas, U.S.A., or ETW (European Transonic Windtunnel), in Cologne Germany. For TMK with a measurement section of $600\,\text{mm} \times 600\,\text{mm}$, this results in a cross-sectional area that corresponds to a model diameter of 67 mm (support not included). The cross-section of a strut support (if chosen as support system) also counts as part of the cross-sectional area.

To investigate the base flow effects, three different model concepts are suggested. The details of which are all listed in Tab. 19. The main feature of *Model 1* concerns the upstream supported strut that basically offers the opportunity to investigate the base flow without a disturbing strut in VMK. *Model 2* takes advantage of the fact that it can be investigated in VMK and TMK. The cross-section of this wind tunnel model is too large for being investigated with additional boosters. This is where *Model 3* comes into place. *Model 3* is designed to study plume interaction phenomena in TMK by using

solid propellants for the core and the booster stages. Solid propellant engines can easily be manufactured in a very compact fashion.

Some more details of *Model 1* can be seen in the image in Fig. 94 and the technical drawing in Fig. 95. It can be seen that the wind tunnel model is integrated in the wind tunnel nozzle and supported upstream. To minimize disturbances, two straighteners are implemented downstream of the support.

The technical drawing provides insights into the feeding system to the combustion chamber. Hydrogen is supplied in the upper pipes running horizontally in Fig. 95 and oxygen is supplied in the lower pipes. The two lines are kept separate until they reach the *PennState* injector head. Adjacent to the injector head is the combustion chamber, which exhibits exactly the dimensions of the *PennState* combustor. Obviously, the flow exits through the nozzle on top of the wind tunnel model.

This configuration was numerically investigated in the frame of *TN2500* due to the large diameter of 158 mm and concerns with respect to transonic effects. This diameter corresponds to a scaling of 35 : 1 for Ariane 5, which is pretty large.

Thus, this exact configuration with nozzle flow was first exposed to an ambient flow coming from the wind tunnel nozzle, then to a free ambient flow. No major differences in the flow field were detected. The flow field and some exemplarily extracted profiles were considered identical, and thus, the differences were considered to be negligible. Therefore, concerns with respect to the nominal blockage ratio higher than 1% could be solved and it was proven to be a valid concept.

This concept has far progressed. Even the equipment of *Kulites* was defined, which are located on the base and wired through one blind feeding pipe. The combustion chamber is identical to the *PennState* combustor with respect to the main dimensions, meaning it is a proven concept as well. The concept of the upstream supported wind tunnel model was tested in the past as well. Thus, this wind tunnel model could be manufactured in the near future.

Fig. 96 and Fig. 97 show *Model 1* with additional boosters. The boosters are attached to the feeding pipes and, correspondingly are upstream supported. The boosters supply plumes from solid propellants for a realistic simulation of the Ariane 5 configuration. This concept has not been numerically investigated yet to check potential interactions with the shear layer or other transonic effects.

As mentioned before, *Model 2* is planned for investigations in both wind tunnels. The hydrogen/oxygen combustion chamber itself is based on the inner geometry of the *PennState* combustor (see Chap. 5). The outer geometry is adapted to meet the requirements for wind tunnel testing, meaning it exhibits exactly a blockage ratio of 1%. In detail, this refers to the diameter of 50 mm corresponding to a scaling of 110 : 1 with respect to Ariane 5. The maximum overall length is 500 mm. Since *Model 1* and *Model 2*

Table 19: Wind tunnel model concepts.

	Model 1	*Model 2*	*Model 3*
Support	upstream	strut	strut
Wind tunnel	VMK	VMK + TMK	VMK + TMK
Mach number range	subsonic	sub-/trans-/supersonic	sub-/trans-/supersonic
	0.5 − 0.95 at low alt.	0.6 − 2.0 (Ma_{max} = 5.7)	0.6 − 2.0 (Ma_{max} = 5.7)
		altitude var. ($Ma >$ 1.5)	altitude var. ($Ma >$ 1.5)
Test environment	free-jet	free-jet + perforated wall	free-jet + perforated wall
Propellant	GO_2/GH_2	GO_2/GH_2	DB
Mixture ratio O/F	1 to 8	$\sim 1 - TBD$	n.a.
Boosters/multiple plumes	yes, with DB	pot. after eval. blockage tests	yes, with DB
Focus of investigations	influence of mixture ratio	altitude simulation	altitude simulation
	influence of temperature grad.	angle of attack	angle of attack
	influence of strut support	dynamic pressure response	dynamic pressure response
	plume interaction		plume interaction
	thermal analysis	thermal analysis	thermal analysis
Diameter of main body	158 mm	50 mm, (max.: 67 mm)	38 mm
Scaling Ariane 5:Model	$\sim 35 : 1$	$\sim 110 : 1$ (max.: $\sim 82 : 1$)	$\sim 144 : 1$
Ignition	pyrotechnic	pyrotechnic	pyrotechnic
Cooling of thrust ch.	transient heat transfer/	transient heat transfer/	transient heat transfer/
	heat sink cooling	heat sink cooling	heat sink cooling
	OFHC copper	ablative material	
Cooling of nozzle	heat sink cooling	heat sink cooling	heat sink cooling
	pyrolitic graphite	pyrolitic graphite	pyrolitic graphite
	molybdenum	molybdenum	molybdenum

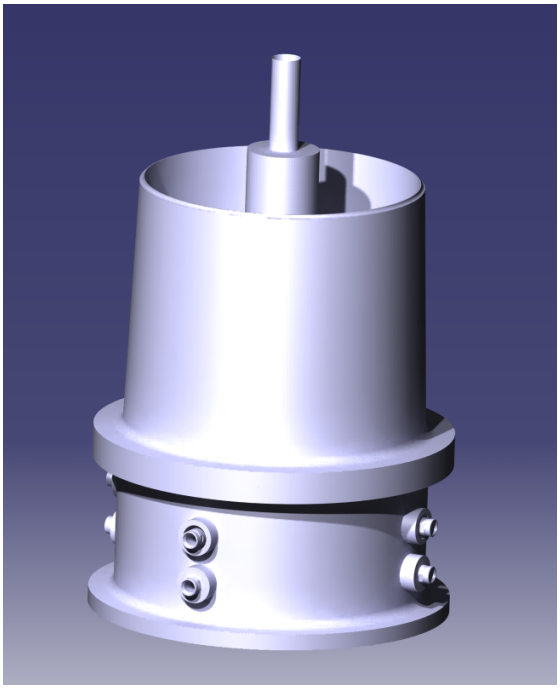

Figure 94: Image of model 1 for tests in VMK.

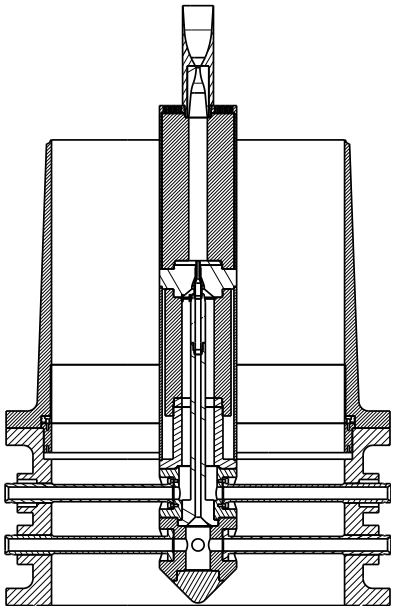

Figure 95: Technical drawing of model 1 for tests in VMK.

are based on the same combustion chamber geometry, this wind tunnel model features a high readiness level. An FEM analysis is still required to calculated the stability of the strut support.

A back-up solution was provided in Chap. 5 for the case that the support is required to be far wider than 6 mm, and consequently, the wind tunnel model runs the risk to cause blockage. The back-up solution refers to the 1.0 in instead of the 1.5 mm combustion chamber of the *Pennsylvania State University*. For the cost of a smaller scaling and smaller region of interest, this combustion chamber could also offer investigations with higher angle of attack.

Fig. 100 and Fig. 101 shows a design for *Model 3*. The concept requires some more detail-oriented work, like the routing of the pressure measurement tab inside of the model. Nevertheless, it contains the main components of a wind tunnel model with solid core and two booster stages. The core stage and the boosters here feature a diameter of 38 mm and 19.5mm, which results in a scale of 144 : 1.

Very high combustion chamber pressures can still be reached by using solid propellants. Fig. 102 and Fig. 103 show exemplarily, which combustion chamber pressures can be reached dependent on the throat diameter for an combustion chamber diameter of 30 mm (core model) and 11.5 mm (booster model), respectively. But, these values can only be used as an orientation since the diameters are very small and the influence of the displacement layer of the boundary layer might increase the pressure substantially. The testing time of such a configuration is up to 10 s.

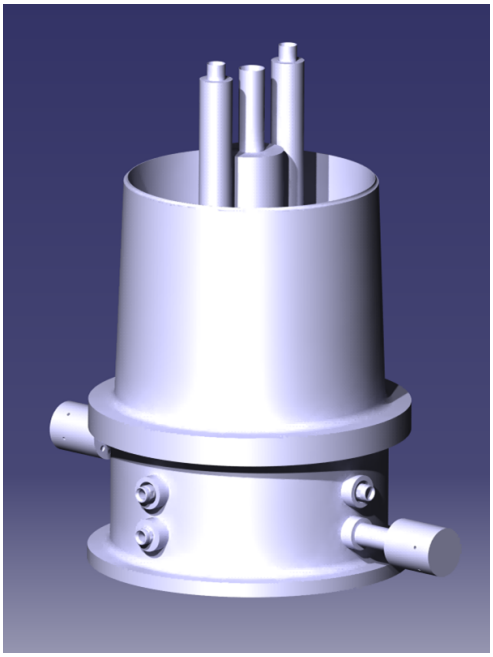

Figure 96: Image of model 1 with boosters for tests in VMK.

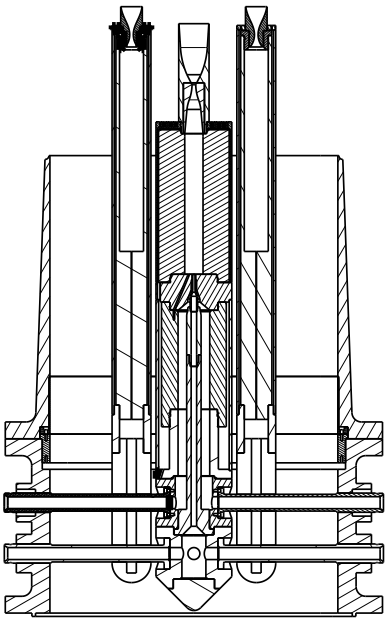

Figure 97: Technical drawing of model 1 with boosters for tests in VMK.

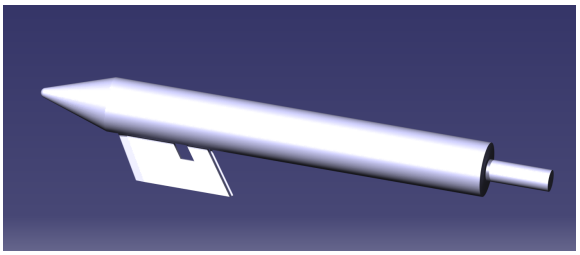

Figure 98: Image of model 2 with a hydrogen/oxygen combustion chamber.

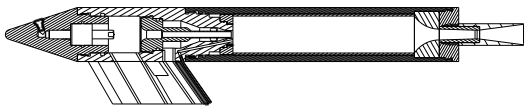

Figure 99: Technical drawing of model 2 with a hydrogen/oxygen combustion chamber.

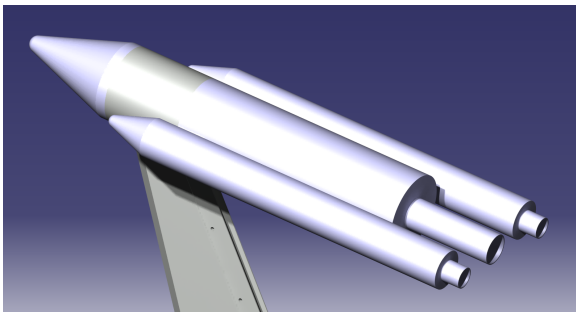

Figure 100: Image of model 3 with a solid propellant main stage and solid propellant boosters.

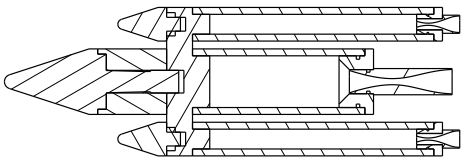

Figure 101: Technical drawing of model 3 with a solid propellant main stage and solid propellant boosters.

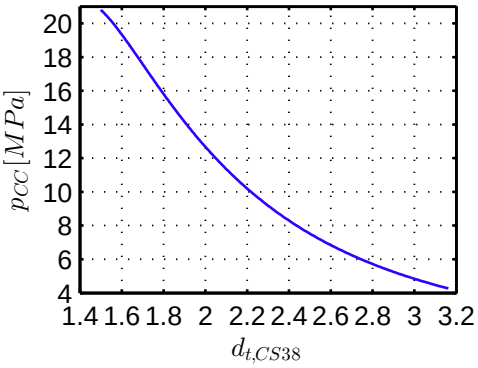

Figure 102: Combustion chamber pressure as a function of throat diameter for a double-base solid propellant with a front surface of 707 mm^2.

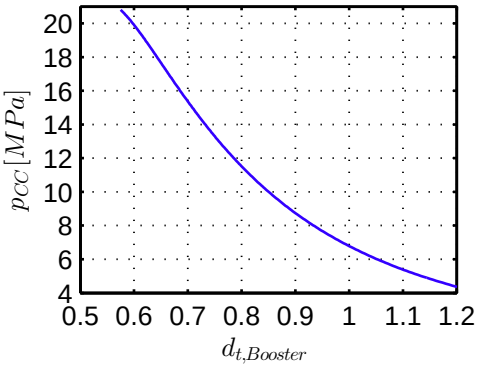

Figure 103: Combustion chamber pressure as a function of throat diameter for a double-base solid propellant with a front surface of 104 mm^2.

6.3 Feeding System

In the frame of this work, the *Supersonic and Hypersonic Technology Department* contacted various companies to get support for the tasks to tackle. *ANLEG GmbH* was addressed for the design of the hydrogen/oxygen feeding system. The flow chart provided in Fig. 104 gives an overview of the required components.

This feedings system is intended to be built up identically for TMK and VMK. Synergies, like a common buffer tank, still have to be evaluated. The hydrogen and oxygen lines themselves are identical as well with respect to the functionality of the components. The oxygen and hydrogen line are both equipped with a nitrogen flushing system. The whole system is divided spatially in three sections: an external section, a section close to the test area and the interface to the wind tunnel model. A short overview is given in the following.

Both lines start from a gas storage, which is in this case a gas bottle. It can be imagined to connect the future facility to the already existing hydrogen/oxygen supply system of the *Institute of Propulsion Technology* in Cologne. This has already been discussed as one option on the phone. From the buffer tank, the gas is led through a shut-off valve, filter, electromagnetic valve, pressure control valve towards the test area.

In the test area, the gas flow is controlled by a flow meter before going through a flow control valve towards the main valve. The last valve after the main valve and before the wind tunnel model is back-pressure. Downstream from there is where the feeding system is connected to the wind tunnel model with an appropriate interface.

In order to stop the combustion safely and to purge the lines from residual hydrogen and oxygen gas, a purging line is coupled into the main supply line. One purging line is connected to to both supply lines, the oxygen and hydrogen line right downstream from the back-pressure valve.

Fig. 105 to Fig. 111 show footprints of the infrastructure in Cologne to given an indication of where the feeding system is planned to be established. Fig. 105 and Fig. 106 show the first and second floor footprints, respectively. The location of VMK and TMK are clearly marked

For VMK, more details are given in Fig. 107 and Fig. 108 for the first and second floor. The area marked in red describes the location where the external, meaning the components surrounding gas storage, is placed. This corresponds to the picture given in Fig. 109. The test area is marked in pink Fig. 111 and the corresponding image is given Fig. 110. Both sections are connected through pipes, which are marked in brown on the footprint.

The same color code is applied for the TMK feeding system. Fig. 111 shows the detailed footprint of TMK. The external components are placed outside (Fig. 112) at the location marked in red and connected to the test area (Fig. 113) marked in pink.

It can be seen that for the feeding system can be established in both facilities, VMK and TMK. The gas can be stored externally and, the required components can be set-up in the near vicinity of each measurement section. For now, a common storage system seems not to be favorable.

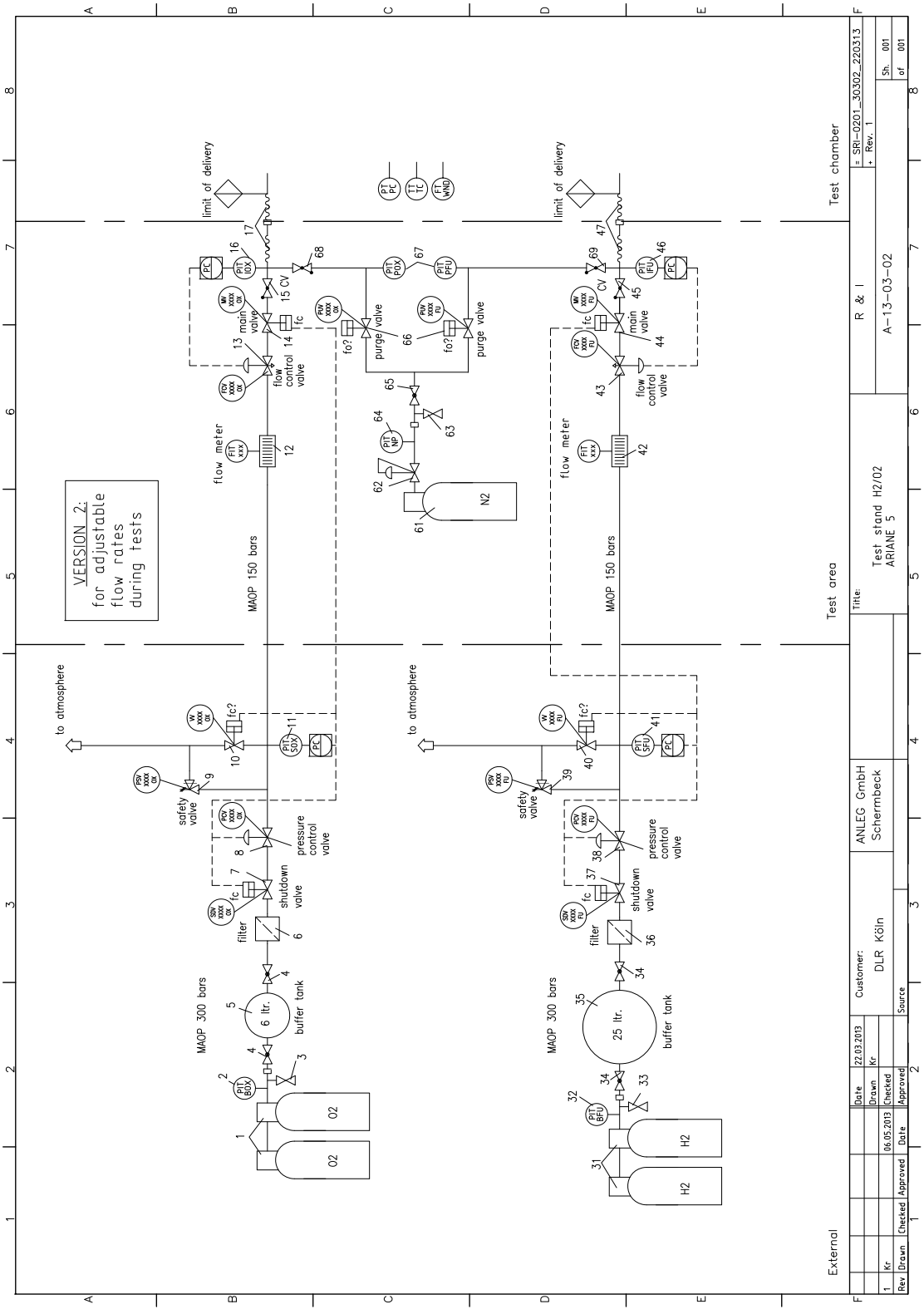

Figure 104: Flow chart H2/O2-feeding system.

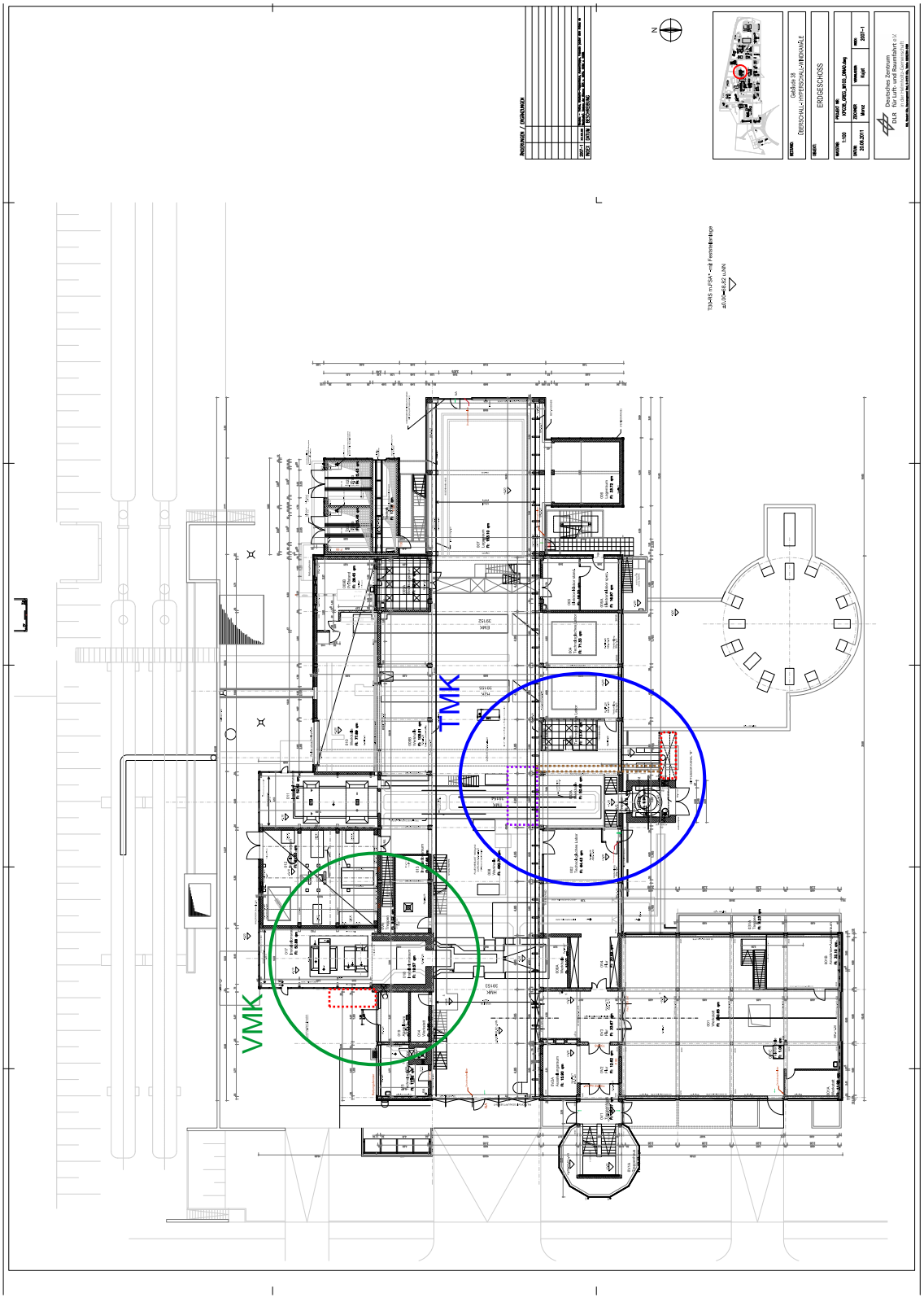

Figure 105: First floor footprint of the infrastructure in Cologne.

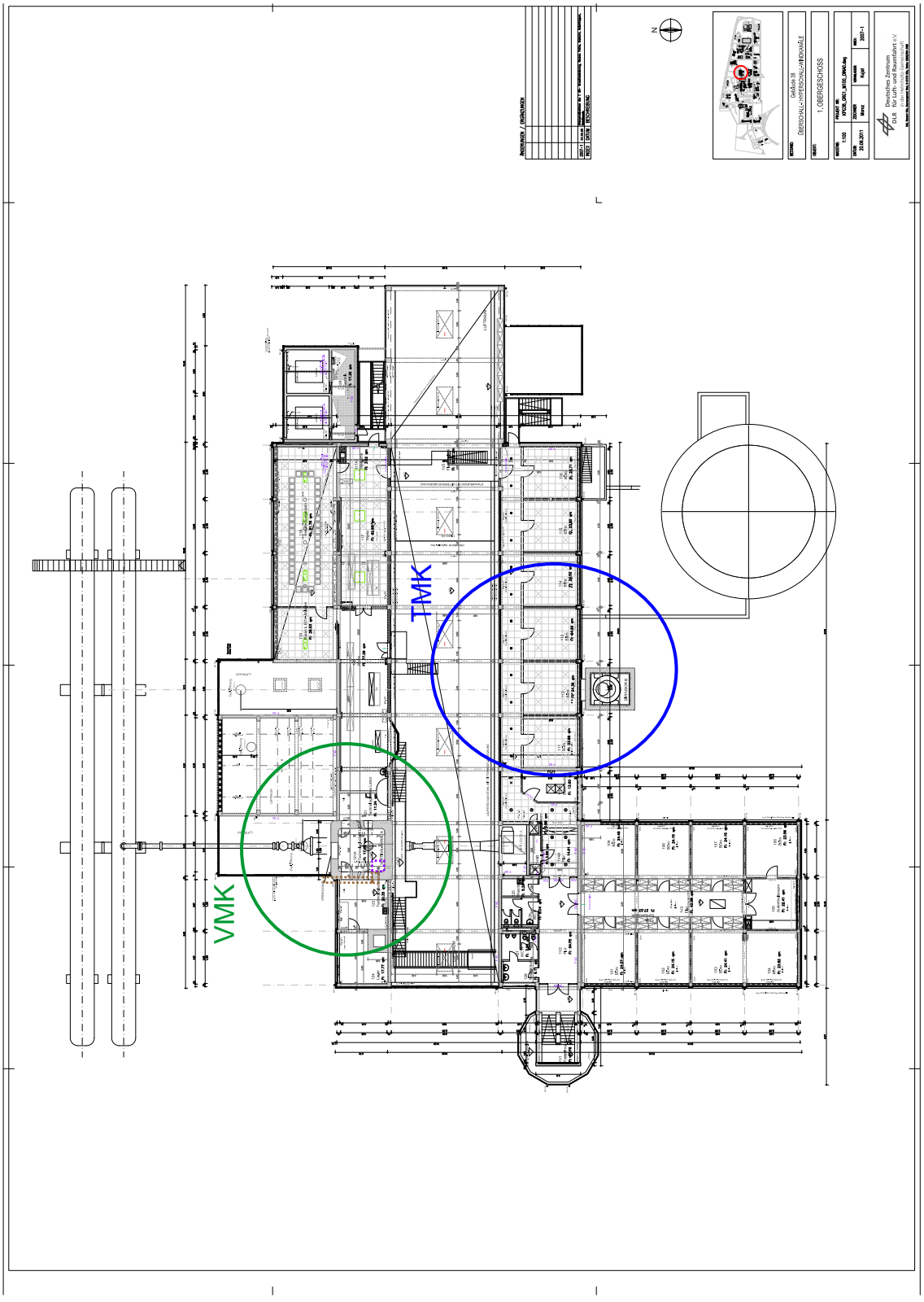

Figure 106: Second floor footprint of the infrastructure in Cologne.

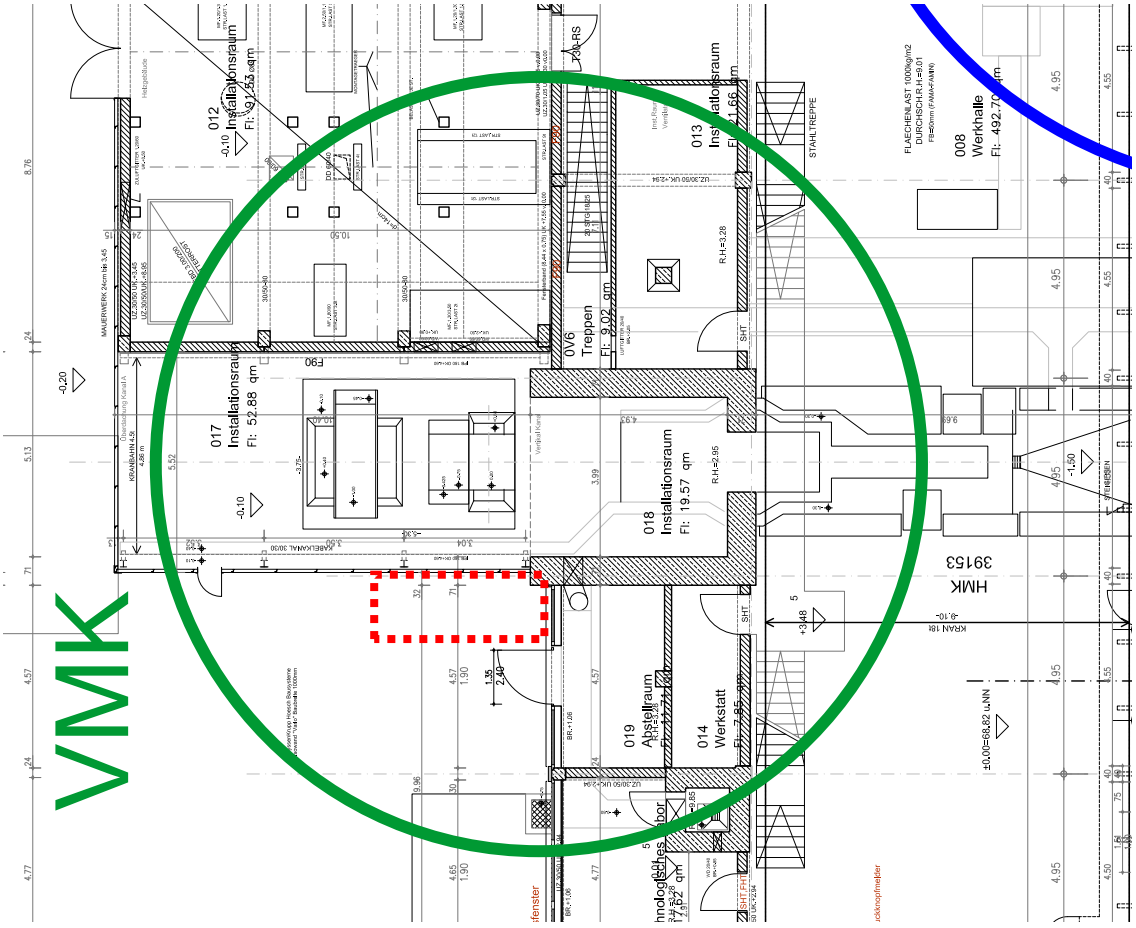

Figure 107: First floor footprint showing the VMK infrastructure.

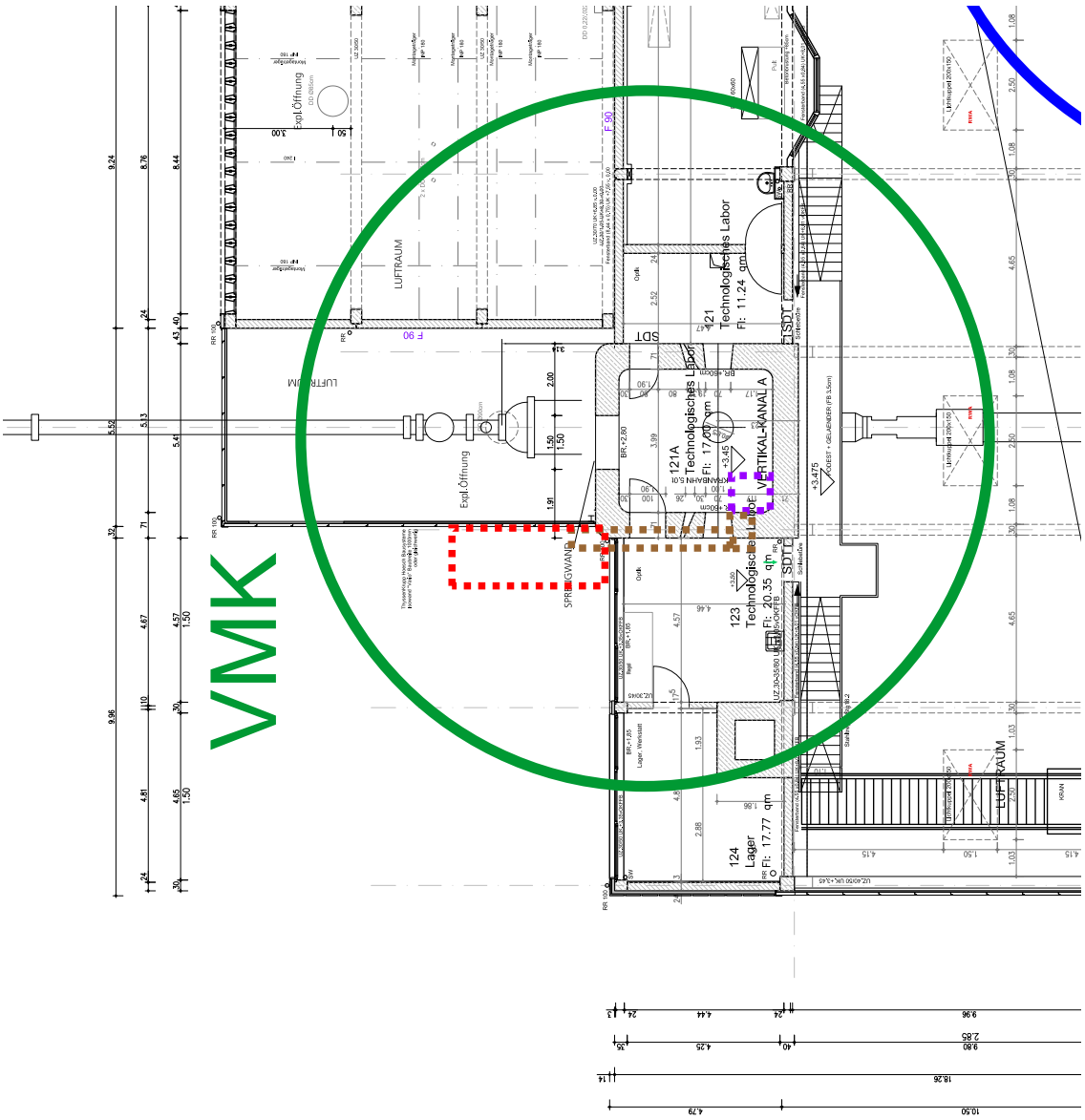
VMK
LUFTRAUM
Expl.Öffnung
F 90
SDT
121
Technologisches Labor
Fl: 11.24 qm
121A
Technologisches Labor
Fl: 17.40 qm
123
Technologische Labore
Fl: 20.35 qm
124
Lager
Fl: 17.77 qm
VERTIKAL-KANAL A
SPRINGWAND
LUFTRAUM

Figure 109: Picture showing the location of the external components for the gas supply system for VMK.

Figure 110: Picture showing the location of the components in the test area for the gas supply system for VMK.

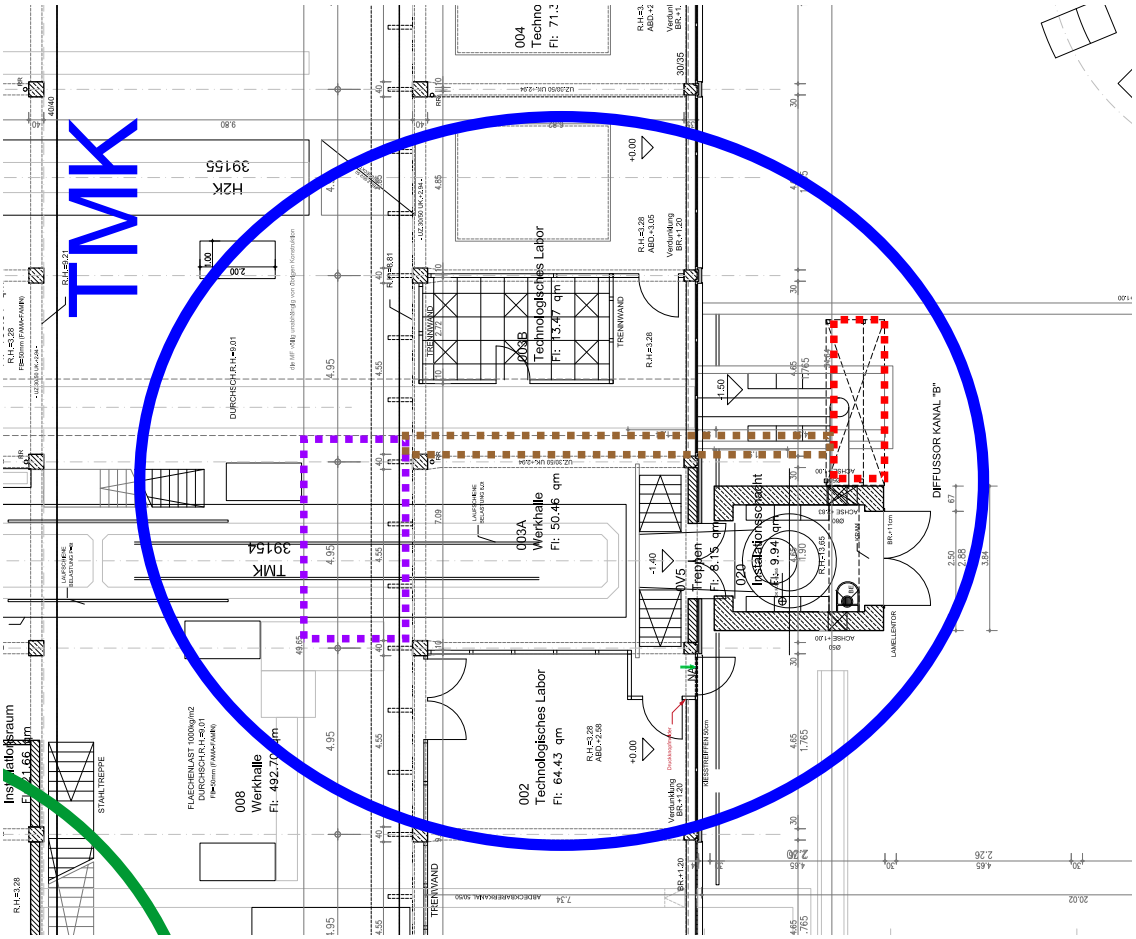

Figure 111: First floor footprint showing the TMK infrastructure.

Figure 112: Picture showing the location of the external components for the gas supply system for TMK.

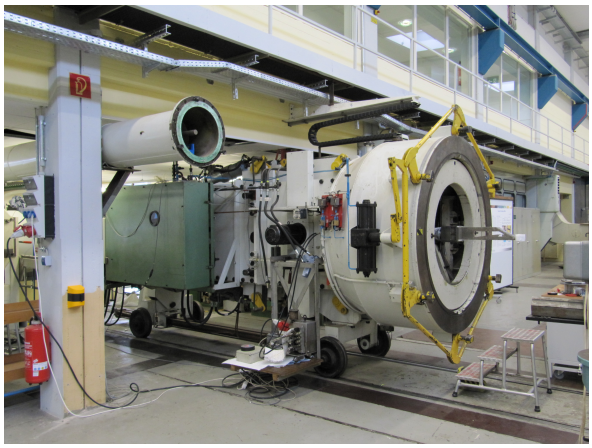

Figure 113: Picture showing the location of the components in the test area for the gas supply system for TMK.

Deutsches Zentrum
für Luft- und Raumfahrt e.V.

TN2300

Measurement Techniques

May 24, 2013

Chris Willert
Michael Fischer
Johannes Heinze
M. Voges
Institute of
Propulsion Technology
Engine Measurement Systems

DLR **Deutsches Zentrum
für Luft- und Raumfahrt** e.V.
in der Helmholtz-Gemeinschaft

ESA STUDY CONTRACT REPORT

No ESA Study Contract Report will be accepted unless this sheet is inserted after the coverpage of each volume of the Report.

ESA CONTRACT No.: AO/1-6731/ 11/NL/SFe	SUBJECT Hot Testing Facility for ELV Propulsion Characterization		CONTRACTOR DLR
* ESA CR( )No	* STAR CODE	No of TN 3300	

ABSTRACT:

This report presents the results from a study regarding to the applicable measurement techniques of the future hot plume facility in the framework of the ESA technology research project "Hot Testing Facilities for ELV Propulsion Characterization". The objective of this survey is the evaluation of the applicability of optical, image based techniques to capture the unsteady base flow phenomena. The survey concludes that an adequate optical access of the region of interest is required at best from all four sides. Finally, it presents a possible approach for LIF and PIV measurements.

Name of author: C. Willert, M. Fischer, J. Heinze, M. Voges (DLR, Cologne, Germany)

** NAME OF ESA STUDY MANAGER	** ESA BUDGET HEADING
N. Murray DIV: TEC-MPA DIRECTORATE: D\TEC	

* Sections to be completed by ESA

** Information to be provided by ESA Study Manager

7 Measurement Techniques - TN2300

CONTENT

1 Introduction

This survey of measurement techniques is part of a feasibility study for a new hot plume testing facility which is aimed at reproducing flow phenomena in the vicinity of launcher nozzles [1]. The need for such a test facility is motivated by the fact that the base pressure of cryogenic propulsion stages cannot be predicted accurately neither through theory, experiment or numerical simulation. Actual flight data has shown that the base pressure is higher than predicted through windtunnel experiments which has direct influence on vehicle drag and hence its flight performance [2,3]. The main reason for the difference is the fact that up to date windtunnel experiments do not duplicate the hot exhaust plume issuing from the nozzle [4].

The design of possible hot testing facilities is not only governed by properly replicating the aerodynamics (see c.f. Figure 1) but also by the capability of providing accurate measurement data. In terms of classical probe measurement techniques this is mainly an issue of adequate port and rake positions. Enabling optical measurement and visualization at the same time requires considerably more design effort and often involves a certain amount of trade-off between accessibility, operational reliability and cost. The focus of this survey is on optical, image based techniques because the whole field nature of the acquired data is of great importance in describing the base flow unsteady phenomena. Recommendations regarding optical access are made on the basis of the measurement technique found most suitable for this application.

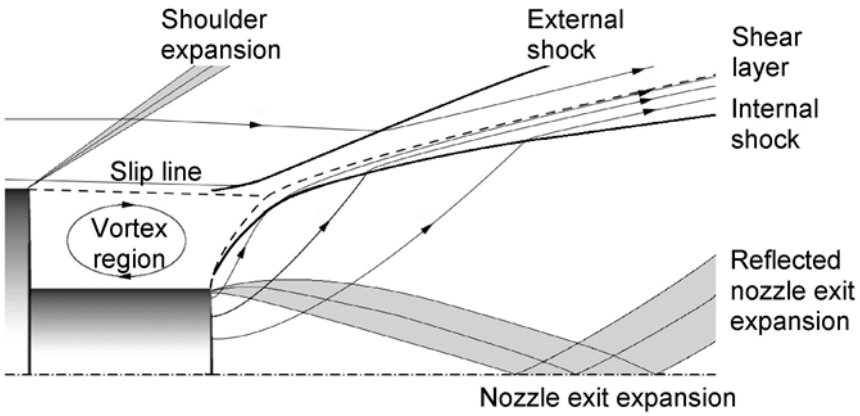

Figure 1: Base flow geometry on an idealized rocket model

1.1 Task description (from Proposal)

The measurement techniques that are required to properly capture the relevant flow phenomenon for extrapolation to flight and also for validation of CFD should be defined. Their relevant requirements in terms of accessibility and implementation should be assessed such that the tunnel design is consistent and capable for their inclusion. Steady and unsteady as well as intrusive and non-intrusive measurement techniques shall be considered.

Aside from particle image velocimetry (PIV) and planar laser induced fluorescence (OH-PLIF) a wide variety of alternative technologies are at the disposal of the Dept. of Engine Measurement Techniques (AT-TM). Among these are Doppler global velocimetry (DGV) for flow field measurement, filtered Rayleigh scattering (FRS) and coherent anti-Stokes Raman scattering (CARS) for temperature measurement, NO-PLIF and acetone PLIF for concentration measurement. The suitability of each of these methods for application in the proposed Hot-Plume facility will be subject of the study.

1.2 Overview of Requirements

The proposed Transonic Hot-Plume Facility will feature adequate optical access to allow the application of optical diagnostic techniques relying on non-intrusive image based methods. This technology will be provided by DLR's Institute of Propulsion Technology which is strongly engaged in the improvement of gas turbines in aviation and electric power generation by medium- to long-term exploitation of the inherent technical potentials. The Institute is located on-site in Cologne in the immediate vicinity of the proposed Transonic Hot-Plume Facility at AS-WK.

The choice of suitable optical techniques and along with it the required optical access depends both on the flow properties to be investigated as well as operational aspects such as the expected facility run times. Some of the relevant properties of the proposed facility are summarized in Table 1.

Table 1: Estimated physical parameters of the hot plume testing facility

Quantity	**Symbol**	
Test section width / diameter		600 mm
Test section length	L	600 mm
Facility run time (typical)		2 - 50 seconds
Free stream velocity, Mach number	V_{inf}, M_{inf}	160 – 360 m/s, 0.5-1.2
Free stream static pressure	P	1 bar
Free stream static temperature	T_{inf}	220 – 280 K
Launcher model diameter	D	50 – 158 mm
Nozzle diameter	D	0.4 D
Exhaust jet velocity, Mach number	V_{jet}, M_{jet}	3000 – 4400 m/s, 3.1 – 5.4
Exhaust jet static temperature	T_{jet}	340 – 2000 K

2 Overview of Relevant Optical Measurement Techniques

Within the scope of the proposed Transonic Hot-Plume Facility two measurement techniques are of particular significance: Particle Image Velocimetry (PIV) and planar laser induced fluorescence (PLIF) to provide instantaneous 2-D maps of velocity and temperature distribution, respectively.

2.1 Flow Field Diagnostics

2.1.1 Schlieren Methods, Line-of-Sight Methods

2.1.2 Particle Image Velocimetry

Since its introduction in the mid-1980's particle image velocimetry (PIV) has evolved to a mature measurement technique that nowadays finds widespread application in academic and industrial research. In its basic form the technique relies on capturing two images of particles that are illuminated in a defined plane using a double pulsed light source (typically a pulsed laser). Through correlation processing the displacement field of the particles between the two exposures can be estimated and, through division of the time separation of the light pulses, provides a first order estimate of the velocity field within the imaged plane. Numerous variants of the technique exist, allowing even the fully time- or volume resolved estimations of the investigated flow field. A considerable body of literature including several books describes many details of the technique and its applications [5], [6], [7].

At the Institute of Propulsion Technology, the PIV technique has a long history of development and application [8]. Today it is the most frequently used technique for velocity field measurement, especially for high-speed reactive flows found in pressurized combustion. First PIV measurements in a pressurized combustor featuring an air-blast atomized kerosene burner were performed in 2000 [9] and since has been used in numerous projects (e.g. [10], [11]).

The underlying PIV technology has found further application for the investigation of the supersonic flow of air-bag gas ejectors in the H2K facility of AS-HY. Figure 2 shows the flow field in the immediate proximity of a gas ejector model operated at a plenum pressure and temperature of 20 bar and 350K, respectively. The tracer material consisted of sub-micron porous silicon oxide spheres that were dispersed via a high pressure fluidized bed seeding device and introduced upstream of the ejector model. The small particle size and low specific weight ensured that the supersonic velocities exceeding 550 m/s could be measured reliably.

Figure 3 below shows an example of a PIV result obtained in the reacting flow downstream of a gas turbine combustor (EU project FUELCHIEF, [8]). The field of view is approximately 200 x 170 mm2 and is sampled on a grid of 1.5 x 1.5 mm^2 to provide about 5700 individual velocity vectors. Here the tracer material consisted of sub-micron aluminium oxide powder that was first dispersed via a pressurized fluidized bed aeration device and then introduced upstream into plenum immediately upstream of the gas turbine combustor.

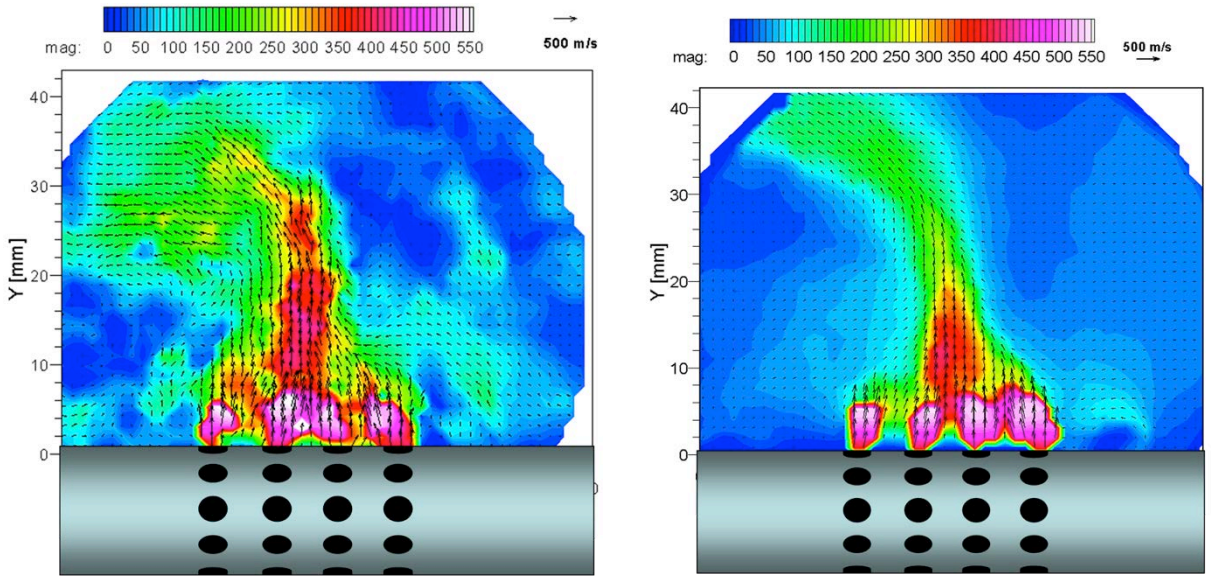

Figure 2: Instantaneous velocity field (left) and ensemble-average of 340 velocity fields (right) of compressed air jets issuing into a confined volume simulating air bag inflation (only 1/4th of vectors are shown).

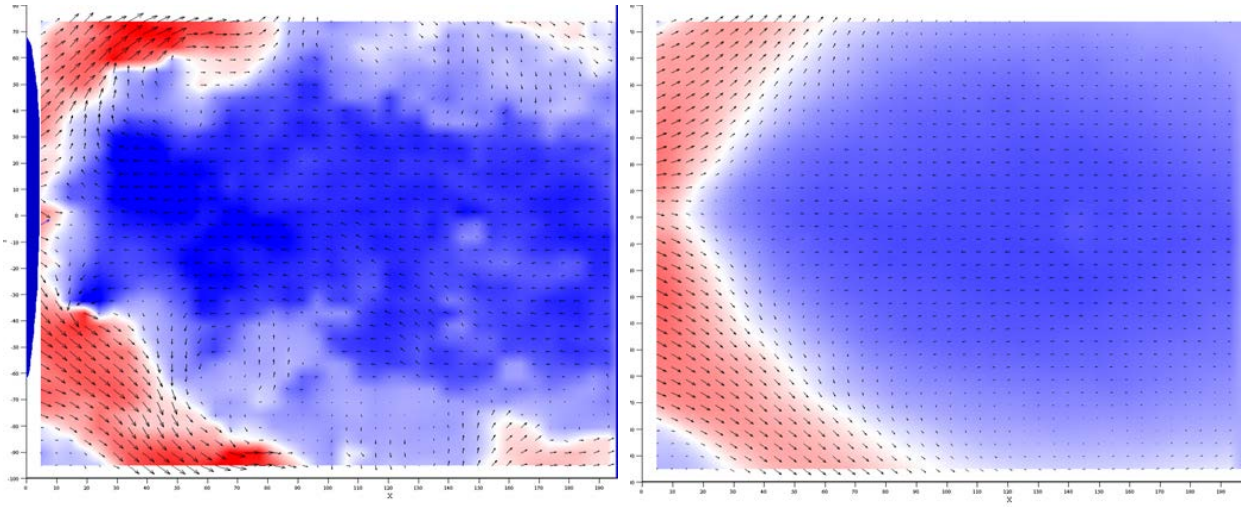

Figure 3: Velocity maps obtained with PIV of the flow downstream of a gas turbine combustor (EU-FP5 Project FUELCHIEF). Left: instantaneous velocity map, right: average velocity map from 200 recordings. Color coding shows horizontal velocity component, mean flow is left to right.

An actual example of a burner application with high spatial resolution under laboratory conditions is demonstrated in Figure 4 [12,13]. Here the PIV light sheet was arranged vertical to the effusive cooling plate of the burner housing. Nevertheless it was demonstrated under isothermal conditions, that wall near measurements were possible with high spatial resolution (about 100 px / mm). Depending on the good realized particle density a vector distance of dx = 0.15 mm was achieved. Validated measurements vertical to the wall were possible up to a minimum distance of x = 0.5 mm to the wall.

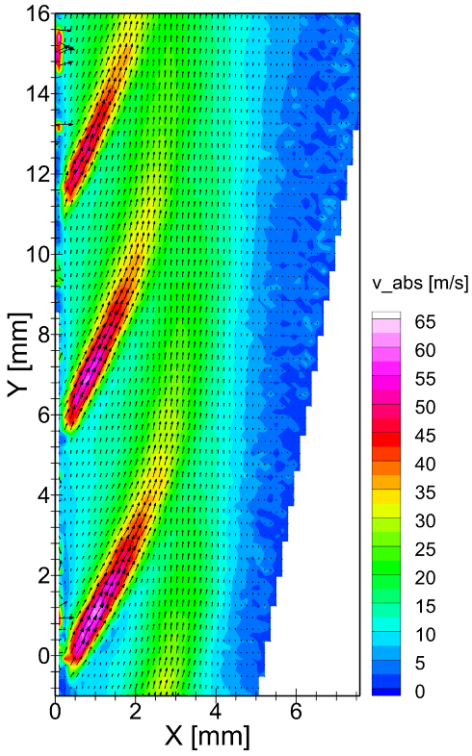

Figure 4: PIV measurement with high spatial resolution near to effusive cooled wall of a laboratory burner [13]. Camera objective f = 100 mm, working distance (camera objective – Laser light sheet) about 200 mm, diameter of the holes for the effusive air cooling 0.5 mm (on the left).

2.1.3 Doppler Global Velocimetry (DGV)

2.1.3.1 Introduction

For decades laser Doppler anemometry (LDA) and phase Doppler anemometry (PDA) were used to deliver data for code validation and to give an overview on the flow field to enhance the understanding of the burner and to identify flow phenomena. LDA and PDA are both point techniques and therefore quite time-consuming to apply. Planar light sheet techniques like particle image velocimetry (PIV) and Doppler global velocimetry (DGV) offer much higher data rates.
Today there is high interest to use planar velocimetry techniques in flames. One further reason, why especially DGV might be the favourable technique for this purpose is, that LDA, PDA and also PIV are very sensitive against strong fluctuations of the index of refraction, especially at high pressures at which they often fail. DGV in contrast has not to image single particles and therefore is less affected by fluctuations of the index of refraction. In addition to this, DGV also does not require windows with brilliant optical qualities. Furthermore, DGV can –to a certain extend- distinguish between the velocity of the kerosene particles and the gas velocity, an important feature in optical diagnostics for combustion.

Despite these advantages of DGV, the technique was not used for combustion research. Measurements in flames were hindered by the fact that the scattering signal has to overcome the background luminosity of the flame and the incandescence of solid particles (soot as well as tracers). The light intensity of cw Ar^+ lasers, which were often used for DGV, is normally not sufficient for this purpose, especially at high temperatures and high pressures.
To overcome this problem, pulsed Nd:YAG lasers can be used in combination with gated CCD-cameras. However, commercially available, pulsed Nd:YAG lasers had a rather wide bandwidth of about 100 MHz, or even more, due to their short pulse duration. This large bandwidth may result in a serious reduction of the measurement sensitivity. These lasers also tend to show an uneven frequency distribution over the light sheet height [14,15], reducing the measurement accuracy even more.
Therefore a new kind of narrow band frequency stabilized, tuneable, long pulse Nd:YAG laser was developed in the frame of a co-operation between the German Aerospace Center (DLR) and the Laser Center Hannover (LZH). The new laser is capable to fulfil the requirements for a successful DGV application. In [16] set-up and performance of this laser is described, with special emphasis on its frequency stabilization. Furthermore the DGV camera system with its intensified cameras is presented and the special aspects of the image processing are discussed. First successful DGV measurements in a kerosene combustion experiment demonstrated the capability of DGV and opened a new field of applicability.
Two remaining disadvantages of this laser concept were the sensitivity of the long laser resonator to vibrations and the limited pulse energy of about 1.5 mJ, which is not sufficient to perform single pulse measurements. Therefore at DLR-AT we acquired a so called macro pulse laser with a tuneable long pulse length and 200 mJ pulse energy, for future single pulse velocity measurements.
Flows in technical environments often show a periodic behaviour, for example the flow inside a piston engine or the flow in the compressor or in the turbine of a turbo engine. Sometimes flows also show periodic structures due to pure fluid mechanical reasons. An example for this is the von Karmann vortex street or the phenomenon of a precedating vortex core. If a trigger signal can be derived from such a flow, for example the signal of a pressure sensor or - in the case of a rotating machine – a trigger signal from the rotating axis, one can trigger the data acquisition to perform a phase averaged DGV measurement. Such a -successful- measurement is described in the paper of Willert et al [17], who used a cw Ar laser and a bragg cell to strobe the laser light. The applicability of this technique is limited by the fact, that most of the laser light is lost, because the bragg cell blocks the laser most of the time. Therefore in future applications it is planned to use the pulsed Nd:YAG laser phase locked to the

experiment. New insights in the flow physics of periodic flows are expected from time resolved measurements in, e.g. compressors, turbines and piston engines.
Pulsed DGV with the long-pulse Nd:YAG laser shows a high potential also for combustion research. The technique is able to provide large quantities of velocity-information in a short time, which makes new –quasi-evolutionary- parameter studies possible at reduced costs [18,19,20]. The coupling of 3-component velocity information with high measurement point density to temperature measurements (by e.g. CARS, LIF) is expected to enhance the understanding of reacting flows. Further activities will be aimed to apply this technique to combustion under high pressure. This is of particular importance because this light sheet technique is less sensitive to beam steering effects than point measurement methods.

More information on DGV can be found on our homepage: **www.dlr.de/en-at/tm**

2.1.3.2 Principle of Doppler Global Velocimetry

Like LDA or PIV, DGV also measures the velocity of tracer particles which need to be added to the flow. With one orientation of the laser light sheet and one direction of observation, one component of the flow velocity is measured. DGV takes advantage of the fact, that the frequency of the scattered light is shifted due to the Doppler effect:

$$\Delta\nu=\nu-\nu_0 \qquad (1)$$

ν_0 : Laser frequency
ν : Scattered light frequency
$\Delta\nu$: Doppler shift

This shift depends on the particle velocity $\vec{v}$, the light sheet direction $\vec{l}$ and the direction of observation $\vec{o}$:

$$\Delta\nu = \nu_o \frac{\left(\vec{o}-\vec{l}\right)}{c}\vec{v} \qquad (2)$$

The basic idea of DGV is to measure the scattered light frequency ν by transmitting the scattered light through an iodine cell (Figure 5). Iodine has strong absorption lines, which are used as a frequency to transmission converter. These lines interfere with the 514 nm line of the Ar^+ laser as well as the 532 nm line of the frequency doubled Nd:YAG laser. Assuming the frequency ν to be on the slope of one absorption line, then ν can be determined by measuring the iodine cell transmission of the scattered light. Therefore, two detectors are required to measure the light intensity before and after the cell. To correlate ν and T, the transmission profile $T(\nu)$ of the iodine cell must be known.
The laser frequency ν_0 has to be known and precisely stabilized, so that the Doppler shift $\Delta\nu$ can be calculated according to equation (1). With equation (2), one component of the vector $\vec{v}$ can be calculated. It is the component in the direction of $\vec{o}-\vec{l}$, the bisector of the angle formed by the direction of the laser light and the direction of observation (Figure 5). At a scattering angle of 90° a velocity of 1 m/s corresponds to a frequency shift of 2.7 MHz. Since the frequency width of the slope of the absorption line is between 300 to 600 MHz (depending on the operation conditions of the gas cell), the dynamic range of velocity measurement is between 100 and 200 m/s.

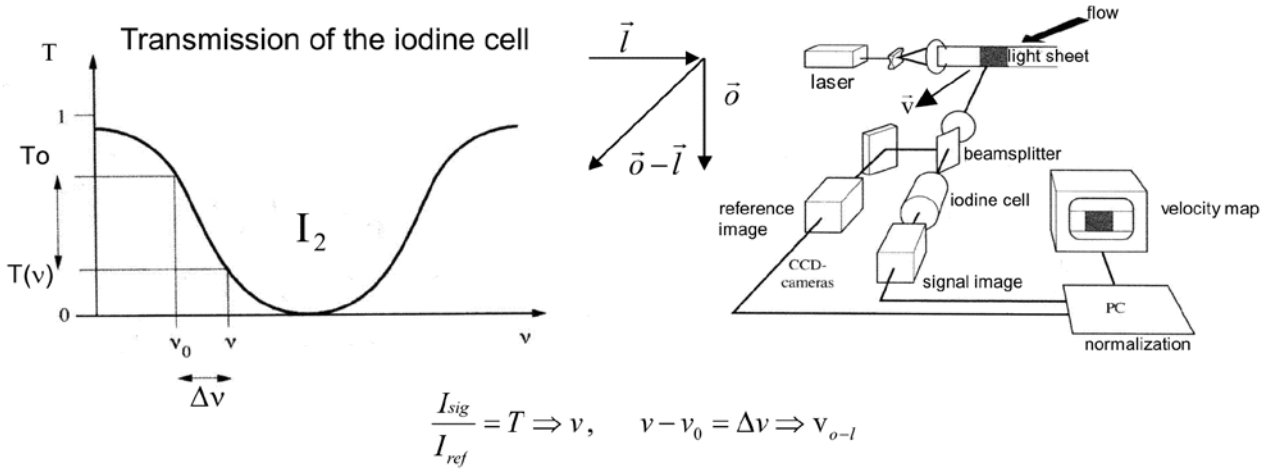

Figure 5: Doppler Global Velocimetry set-up and transmission profile of the iodine cell. Direction of the measured velocity component depending on the direction of laser light propagation and the direction of observation.

Another basic idea of DGV is to use two CCD-cameras as detectors, both watching the same section of a laser light sheet. By pixel wise division of the two pictures and further post processing a map of one velocity component in the light sheet is obtained. Depending on the type of laser (cw or pulsed), the result is either a time averaged or a frozen velocity image.

The second and the third velocity components can be measured by changing the arrangement of the optical set-up. There are two alternative ways to accomplish this:

- With one light sheet direction and three synchronized camera systems in different positions which simultaneously capture momentary pictures, the momentary 3D-velocity distribution can be obtained. Such a configuration is needed to investigate non-steady 3D-flow structures [18,19,20].
  Another DGV-configuration to measure three velocity components simultaneously using three viewing directions, a fiber bundle and one camera and one laser light sheet is presented in Figure 6.
- The second alternative is to use only one camera system in a fixed position and three light sheets with different orientations. The three pictures of the three light sheets have to be taken one after the other, with the consequence that this method is restricted to stationary flows only.

A summary on the possible imaging configurations is given in [18].
The second method is simpler than a set-up with three camera systems. It is well suited to measure mean velocities by long camera exposure times. When a pulsed laser is used a long exposure means that the cameras perform a so called “on chip integration” of a larger number of single-pulse images adding up the generated photoelectrons per pixel of each image. In this way, the turbulent velocity fluctuations are averaged and therefore the result is an image of the mean velocity distribution. Since the exposure times are typically in the order of several seconds, a weak seeding gives a sufficient amount of scattered light. Because of these reasons, a set-up with three light sheets and one camera system was chosen for the experiments presented in Chapter 2.1.3.5.

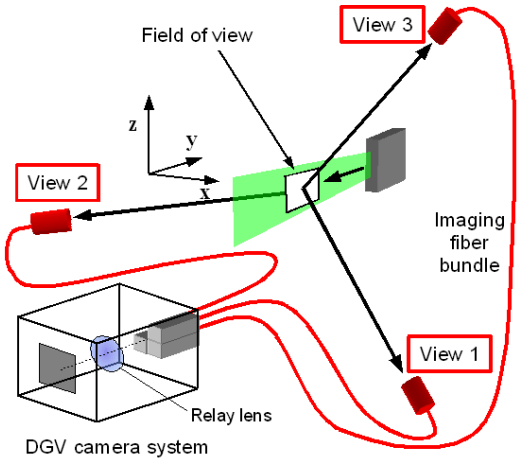

Figure 6: DGV-configuration to measure three velocity components using three viewing directions, a fiber bundle and one camera and one laser light sheet [Willert2007].

2.1.3.3 Data evaluation

The cold flow and the laser are switched on and the so called back ground images are taken for each camera and each light sheet direction. These images should contain the complete ambient light and reflexes of the laser light sheet, but no light scattered by particles. Then the combustor is ignited and a further set of images is acquired.
In the next step tracer particles are added to the flow and another set of images is acquired. These images contain several different kinds of light: The background light (laser light, flame emission, ambient light) and the light scattered by the tracer particles.

The first post processing step to determine the velocity of the tracers is therefore, to subtract the images of the flame (before background correction) from the flame images measured with tracer particles. The result is a pure tracer image.
Then these images undergo a standard post processing:

- Dewarping of the images
- Division of the content of each image pair
- Pixel specific sensitivity correction
- The mapping $T \rightarrow \nu$ (T) using a look up table
- The mapping $\nu \rightarrow \nu$ (ν) : Equation (2)
- Combination of three one component measurements to one 3-component-measurement, according to the direction of illumination and observation.
- Vector or false colour representation of the results
- Generation of structured ASCII-files for processing with further software

Aside of these procedures, there is of course another possible way to process the acquired data, which is to subtract the background images from the individual images of the flame and tracers and then continue with the post processing mentioned above.

2.1.3.4 Special aspects of DGV in combustion environments

The DGV technique was invented by Komine [21]. Doppler global velocimetry has been widely used in different environments, e.g. wind tunnels [22,23] and also in combustion chambers operated with air under isothermal conditions [24]. Up to now, DGV-measurements were restricted to cold flows, because the application in flames is hindered by the reduction of the signal to noise ratio due to background light originating from flame luminosity and incandescence of solid particles (soot as well as tracers). Under these conditions the light intensity of cw Ar^+ lasers, which are usually used for DGV, is not sufficient. It is well known from previous experiments in kerosene combustion chambers, that the problem of flame luminosity and particle incandescence increases dramatically with pressure and temperature in the combustion chamber. This is especially true when preheated air is used. To overcome this problem, pulsed lasers can be used in combination with gated CCD-cameras. During the laser pulse the intensity of the scattered light is much higher than the mentioned background radiation intensity Figure 7. In the time between the pulses, the camera intensifiers are switched off, so that the cameras are not sensitive to light. This principle which is usually used for spectroscopic measurements in flames (e.g. laser induced fluorescence (LIF) and coherent anti-Stokes Raman scattering (CARS)) is here applied to DGV.
In [16] we presented an extension of the technique to flame applications using a selfmade long pulse Nd:YAG-laser especially designed for mean velocity measurements in flames. The laser system was described in detail together with the complete DGV system.

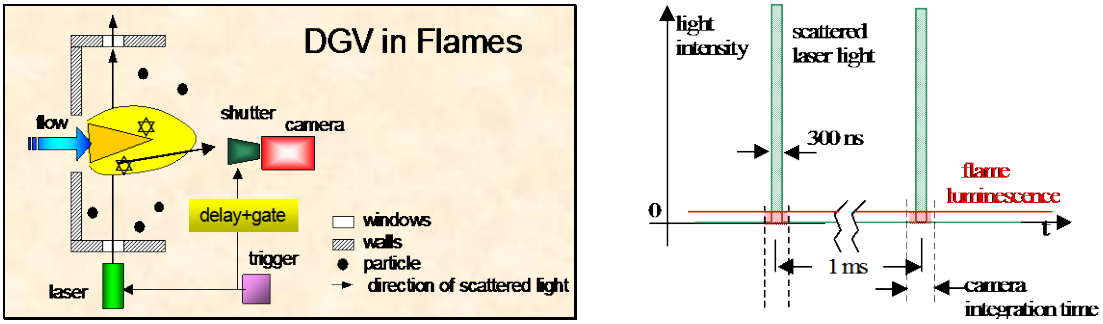

Figure 7: Principle of DGV in flames using pulsed lasers and shuttered cameras.

To achieve high measurement accuracy, it is advantageous, that the laser provides a narrow linewidth and is frequency stabilized. The laser frequency is tunable over several iodine lines of different flank-slope which can be used to optimize the measurement system for different velocity ranges. The long pulse lasers are optimized to emit a Gaussian ”single-mode” pulse with 300 ns pulsewidth (FWHM) to several microseconds corresponding to a nearly Fourier-limited linewidth (FWHM) of about 1.5 MHz at 532 nm. For non-steady (single pulse-) velocity measurements we acquired a so called macro pulse laser with a tunable long pulse length and 200 mJ pulse energy (Table 2).

Table 2: Comparison of two pulsed laser concepts available at DLR-AT

concept	f /Hz	pulse length /ns	resonator	pulse energy /mJ	single pulse measurement
long pulse	1000	300	long	1	no
tunable macro pulse	40	300-10000	no power resonator	200	yes

2.1.3.5 Experimental set-up for cw lasers and low power pulses

To generate the light sheet the laser beam is guided through a fibre to a light sheet box which contains the complete light sheet generation optics (Figure 8). The height of the light sheet and the distance of the waist can both be adjusted. The maximum height for a parallel light sheet is 140 mm. The distance of the waist from the light sheet box can be changed by the position of the collimating lens behind the fibre. The attainable diameter of the waist is a function of this setting and the diameter of the fibre. In the experiments described below, the fibre core diameter was 200 µm, the working distance was 1 m and the waist had a thickness of about 3.5 mm. The separation of laser and optics facilitates the alignment of the laser light sheet relative to the object of investigation.

The light sheet optics is also optimized for long exposure times. The light sheet has a flat top-hat intensity profile, generated by a scanning technique with a modulation frequency of 10 to 100 Hz. A top-hat profile minimizes the intensity dynamics in the measured images with positive influence on the measurement accuracy.

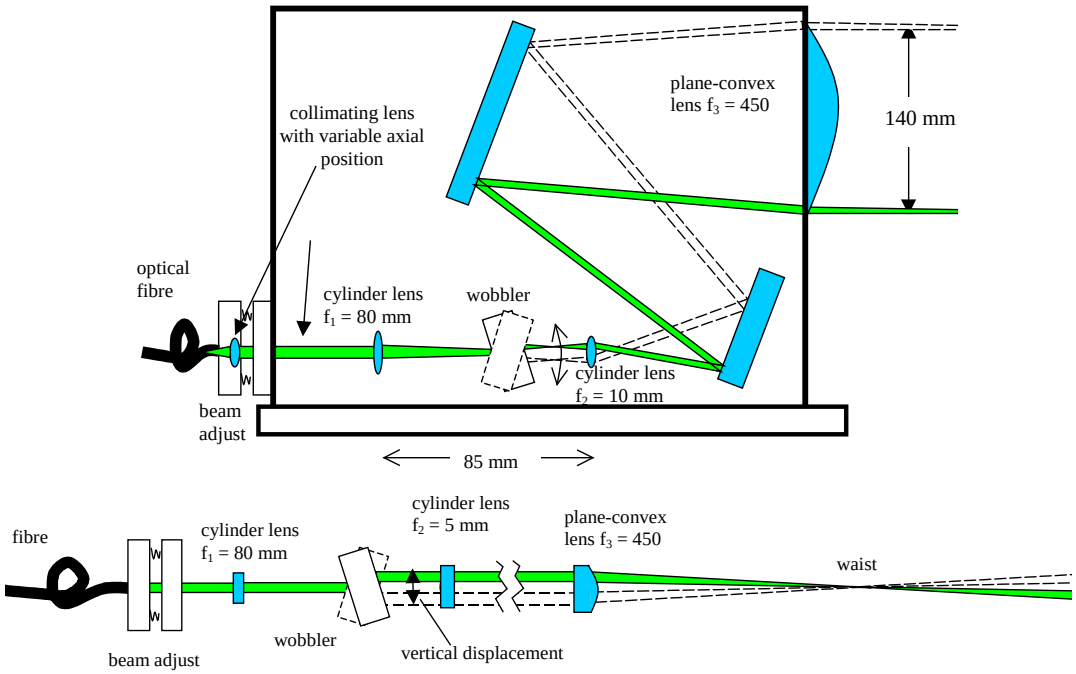

Figure 8: Generation of the scanning light sheet. Side view (top) and top view (bottom).

To prevent the appearance of stimulated Brillouin scattering (SBS) [25,26] and other non-linear optical effects in the fiber, a fiber with 200 µm core diameter was used. SBS reduces the transmitted intensity drastically for single-mode lasers if smaller core diameters are used (increase of power density). In pre-experiments fibers with different core diameters were tested. At, e.g., 50µm core diameter about 70% of the incident power was lost by back-scattering. Due to multiple SBS and four wave mixing (FWM) processes a “paling” of transmitted lines with line distances in the order of 34 GHz (bulk silica, 514.5 nm) can appear [25]. This can be excluded for our measurement for two reasons. Firstly, the transmitted intensity corresponded well to the fiber attenuation and secondly it would have been impossible to absorb the laser light by strong iodine lines because the coincidence of iodine line positions and additional laser lines would be randomly.

The arrangement of the light sheets relative to flame and cameras is shown in Figure 9. To facilitate the optical access a "nearly cubic" combustion chamber (about 100x100x113 mm^3) made of steel was designed. One wall was substituted by a glass window for the camera access. Rectangular window flanges with vertical slits in the combustion chamber wall for the light sheet passage were fitted to the chamber. The window flanges are air purged to protect the windows from particles. The tracer particles (SiO_2 , 0.8 µm diameter, Merck) were added to the air flow near to the air blust nozzle with co-rotating air swirls also shown in Figure 9. The dimensions of the sketch are not in scale but chosen for clearness of the representation. In reality the inner diameter of the nozzle is 7 mm.

The DGV camera system [24] uses one collecting lens which generates an intermediate image. This is transferred by a transfer lens to the chips of the two cameras. A non polarising beam splitter plate is used to reduce polarization influences. A laser line filter is used to reduce ambient light. The images are taken by a pair of intensified, 12-bit, cooled, slow scan CCD cameras (LaVision). Intensified cameras were needed, because they can be synchronised with the pulsed laser in the way that the image intensifier is only switched on during the laser pulse. In addition, these cameras can perform long exposures of several seconds without integrating too much dark current. Therefore, they are a good choice for a DGV system which is optimised for time averaged measurements.

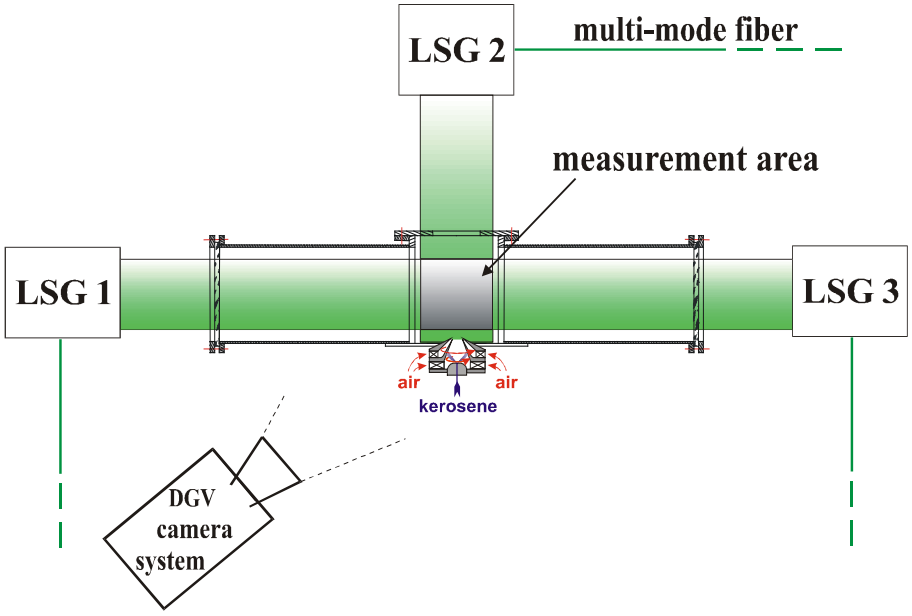

Figure 9: Experimental set-up on a laboratory burner showing the orientation between light sheets, camera and flow direction.

In order to get identical images from both cameras, the cameras are mounted on micro positioning devices to allow precise alignment. By an additional software correction the alignment can be further enhanced. The image processing is performed by using a program written in the language IDL. The steps of the post processing were described in [24]. This post processing only takes a few seconds and can be started immediately after the DGV pictures are taken. In this way the technique is nearly on-line.

The enlargement of the laser pulse build-up time by 1.4 µs as a consequence of multi-mode operation of the long pulse laser was used to simplify the DGV-data acquisition. We used cameras with gated image intensifiers providing the possibility to set the appearance of the light pulse near to the end of the amplification period. In multi-mode operation the light pulse appears after the gate period (width about

800 ns) and the corresponding flame-image is not intensified. In this way images are only measured in case of a correct frequency stabilized operation of the laser thus enabling correct averaging.
A similar set-up on a combustor facility is shown in Figure 10. Here the image was guided by a probe including an image guide [27]. In the "vertical DGV configuration", three divergent light sheets perpendicular to the main flow direction were used which entered the combustion chamber through windows. The light sheets were vertical to the floor and parallel to the combustion chamber exit. The dimension of the facility was comparable to the TMK facility. A bigger side window mounted at the entrance position of light sheet 1 was used for the OH* measurements described below. A cooled endoscope with flexible image fiber bundle (Figure 12) transferred the scattered light to the DGV camera system.
The flexible image fiber bundle used was from HINZE and has a cross section of 2x2 mm. The sharpness of the images was optimized with an eyeglass lens added to the standard entrance lens of this fiber bundle. The exit area was matched to the cross section of the image intensifier (respectively chip area) using a f = 50 mm objective in retro-orientation and a lens with 300 mm focal length as transfer optic. To suppress the flame background and broadband radiation from heated seed particles an interference filter (532 nm center wavelength) was used. First test runs were used to optimize the purge air channel arrangement until the entrance window stayed clean during the experiments.
For the tested "horizontal DGV configuration" an additional water cooled light sheet generating probe was developed to provide a divergent light sheet parallel to the main flow direction. Two further horizontal divergent light sheets entered through windows. The measurement area was then imaged through the top window by another fiber bundle with objective. Due to remaining intense light reflexes from the combustion walls the results were distorted and not presented in [27]. Further work on the correction of data acquired under such conditions is in progress.

For the application at high temperature a solid particle seeding generator was developed at DLR to provide sufficient seeding rates at high mass flows (Figure 11). The generator can be used for pressures up to 20 bar and the second development generation had a stirrer to prevent clustering of the particles, which have to be dry to prevent agglomeration. Actually we use a version with pin holes at the entrance and exit of the pressure container, without stirrer. Provided the pressure ratio before and after the hole is two or more we have a sonic flow with the same mass flow through entrance and exit pinhole and a constant seeding rate. The entrance pin hole prevents a too rapid pressure increase compressing the particle material and the exit pinhole substitutes the valve used before to destroy particle agglomerates.

In [27] the first successful application of phase resolved DGV measurements in a realistic gas turbine test combustor (Siemens test rig NDP1) is reported together with phase resolved OH* emission measurements. The measurements were performed under stationary flame conditions, with stable combustion oscillation and near to the oscillation limit at locations downstream of the burner exit and give information on the respective velocity field and heat release of the flame measured at a single burner atmospheric test rig. The DGV- and OH* measurement results presented improved our understanding of the processes of combustion oscillations and may contribute to the development of new solutions to suppress these intolerable combustion oscillations in gas turbine combustors. Especially the OH* emission might become a useful online monitor of the operation conditions of the combustor in order to get a pre-indicator for the detection of starting oscillations, which could be helpful in avoiding costly damages.

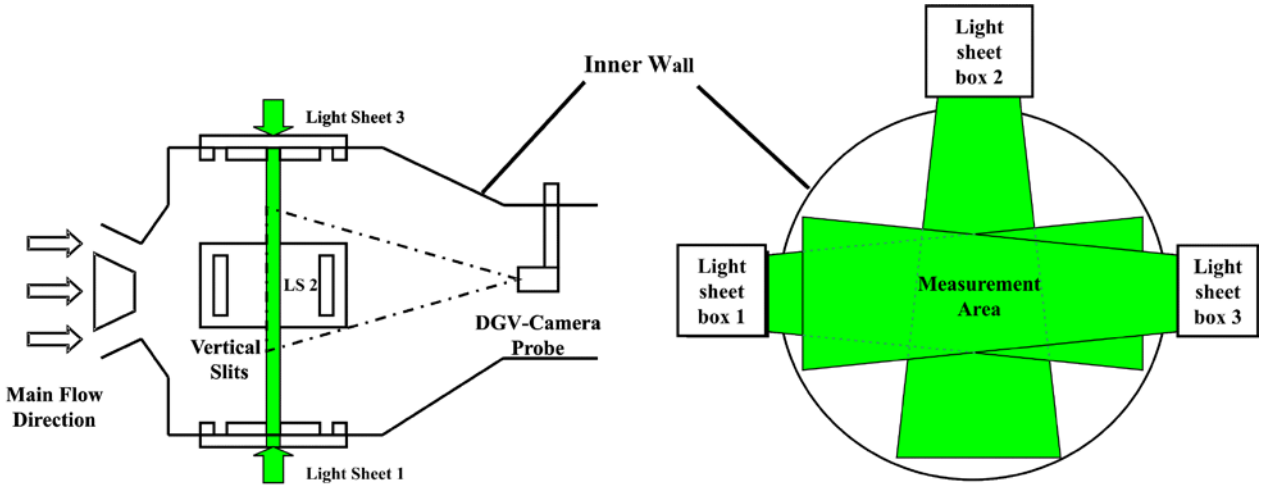

Figure 10: Top view and cross section of the DGV arrangement for the measurements of the vertical planes.

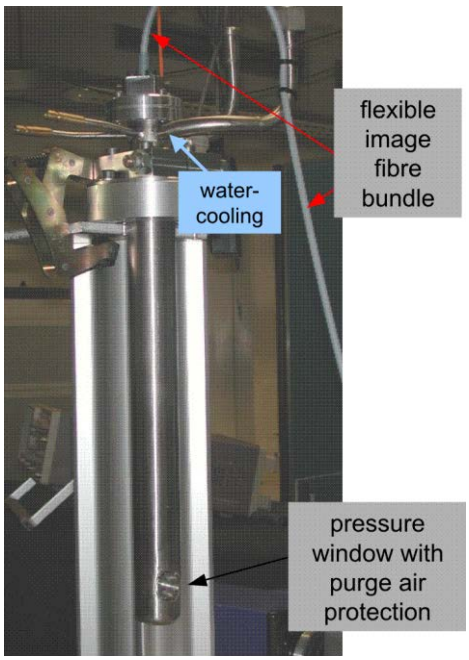

Figure 12: Water cooled endoscope with flexible image fibre bundle

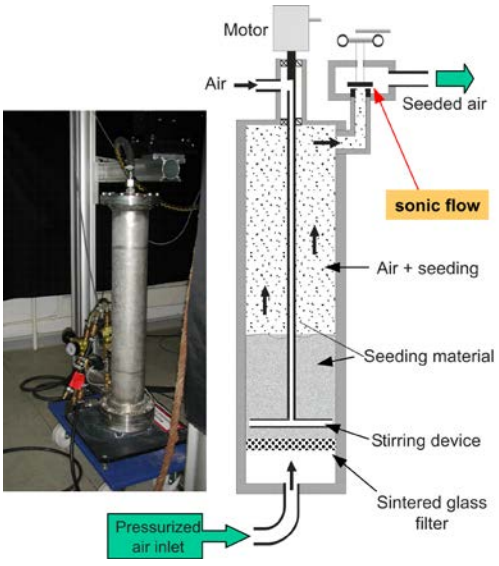

Figure 11: Solid particle seeding generator for pressures up to 20 bar

2.1.4 Filtered Rayleigh Scattering (FRS)

The temperature distribution is a key property in the analysis and optimization of modern combustors. Planar optical measurement techniques are capable to meet this demand in a cost effective manner. One of the limited planar techniques suitable to measure the temperature over the entire temperature range from room temperature over hot wall temperatures to highest combustion temperatures is Rayleigh scattering. Rayleigh scattering makes use of the fact that elastically scattered laser light from particles with diameters in the nanometer scale region, namely the elastic scattering from atoms and molecules, holds information on density, pressure, temperature and velocity inside the observed region of interest. It requires neither particle seeding nor a seeding of poisonous tracer gases (e.g. NO).

Point wise, spectrally resolved Rayleigh scattering was applied in multiple flow property measurements with sampling rates up to 10 kHz [28]. In combustion experiments, Rayleigh scattering thermometry was used as a temperature standard to calibrate a laminar premixed propane/air flame with an uncertainty of less than 1 % [29].

Frequency scanning filtered Rayleigh scattering (FRS), introduced in [14] was used in the application example presented in Chapter 2.2.3 to measure time-averaged temperature distributions in atmospheric laminar lean premixed CH_4/Air flames with different equivalence ratios.

Being several orders of magnitude weaker than other elastic scattering effects, such as geometric scattering from surfaces and windows or Mie scattering from larger particles such as dust or soot, the accuracy of Rayleigh scattering measurements strongly depends on background noise and stray light correction. The complexity of accurately determining the undesired but nonetheless omnipresent background signal becomes increasingly challenging when extending the technique to planar measurements. The avoidance of strong reflections from surfaces or windows is the first method of choice. The filtering of large particles from the measurement flow is performed in [30]. In [31] it is proposed to measure the background level by flooding the test section with helium, which has a Rayleigh scattering cross section of about 75 times less than e.g. nitrogen or oxygen. Since these methods require extensive procedures and are at best suitable under laboratory conditions, the alternative of filtered Rayleigh scattering [32] seems to be best suited for providing a Rayleigh signal without the presence of the strong elastic scattering from larger particles (Mie scattering) or surfaces.

In FRS the filtering is achieved with the absorption bands of atomic or molecular gases, which remove the strong elastic scattering components from the measured signal. Figure 13 illustrates the spectral response of a volume illuminated with narrow line width laser light. The scattering from particles in the Mie regime and the light scattered from surfaces have a similar narrow spectral bandwidth and frequency as the illuminating light source. In comparison the Rayleigh profile has a spectral bandwidth of several gigahertz based on broadening mechanisms related to the molecular motion [33]. By placing the iodine filter in front of the detector, the filter's transmission curve is superimposed on the spectral answer of the observed volume element. Spectral shares inside the blocking range are absorbed by the filter, including the Mie and geometric scattering, but also a considerable amount of the Rayleigh scattered light is attenuated. The remaining spectral contributions of the Rayleigh signal that pass the filter can be accumulated by a sensitive detector and comprise the FRS signal from which further information such as temperature can be deduced.

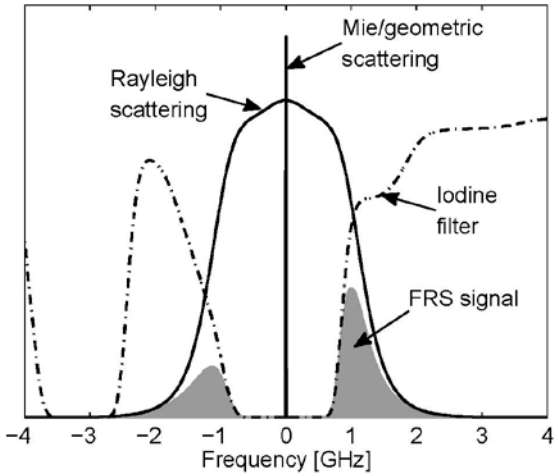

Figure 13: FRS working principle: the narrow bandwidth light scattered from large particles (Mie) or surfaces (geometric) is absorbed by the iodine filter, while parts of the Rayleigh scattering pass through.

In combustion diagnostics, most Rayleigh scattering and FRS systems reported in the literature use narrow linewidth pulsed laser sources (100 – 150 MHz) [34,35] to illuminate the measurement plane, allowing short camera exposure times and thus reducing background contributions from flame luminosity or blackbody radiation. While being advantageous in this respect, an insufficient suppression of laser induced background noise in FRS measurements is reported by a number of researchers using pulsed laser sources. In [14], a Lorentzian broadening of the spectral lineshape of the laser is indicated and a direct measurement of the laser induced background level by evacuating the test cell is proposed. A residual longitudinal mode competition in the laser's oscillator is reported in [36], resulting in a 5 – 10 % bias of the acquired signal.

The FRS implementation applied in chapter 2.2.3 follows a different approach by focusing on time-averaged measurement rather than providing instantaneous measurements. The FRS system is based on a continuous wave diode-pumped solid state frequency-doubled Nd:YVO_4 laser and a molecular iodine filter. The laser provides single frequency light at 532 nm with a spectral line width < 5 MHz. No background light induced by laser line broadening was observed using this light source.

In investigating steady phenomena or in obtaining mean values in unsteady flows, the frequency scanning FRS can be applied. In frequency scanning FRS, the laser's frequency is tuned along the absorption profile of the iodine filter, providing an n-tuple of grayscale intensities for each camera pixel, with n as the number of scanning frequencies. In contrast to the frequency scanning FRS system presented in [37], the scanning range is limited to frequencies were the optical density of the iodine filter is sufficient to totally suppress elastically scattered background light. Thus, provided that the gas composition, the pressure and the velocity are known, the measured intensity of every camera pixel is only a function of gas temperature. The described technique was calibrated comparing FRS and CARS results on a McKenna Burner.

The left side of Figure 14 shows the result for a single pixel element of a temperature analysis in a laminar lean premixed flame ($\Phi = 0.8$, $CH_4 = 1.1$ slpm, Air = 15.6 slpm) provided by Mc-Kenna type flat field (diffusion) burner. The model equation is fitted to the measured data of the frequency scan in a least squares sense, resulting in a temperature of 1635 K. On the right of Figure 14, the fitting algorithm was applied to each camera pixel, resulting in a temperature field of the burner flame. Beginning ~13 mm above the burner plate, in a height of 15 mm, the temperature of 1725 K corresponds to the point-wise results acquired by CARS within 2 %.

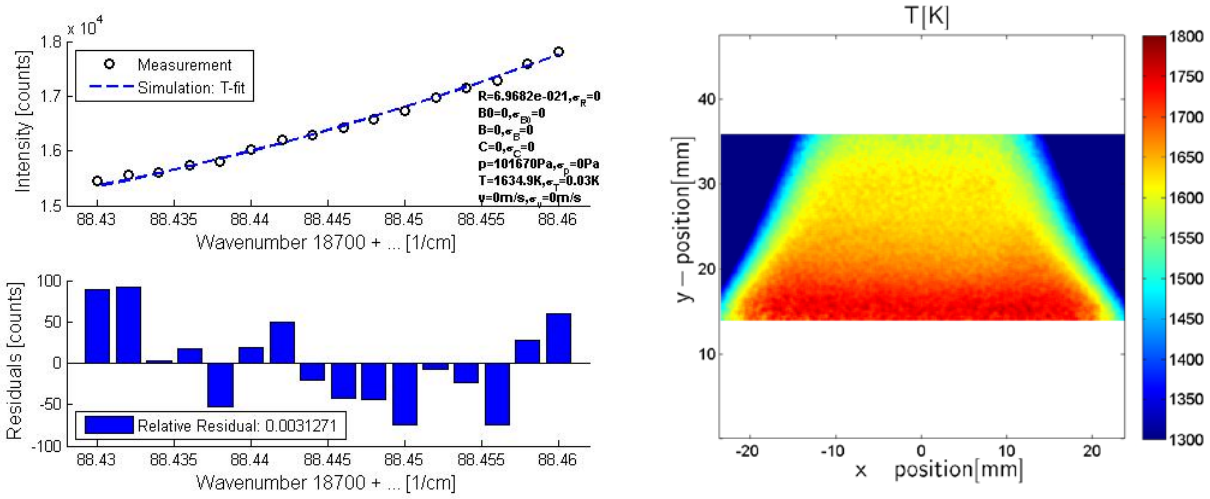

Figure 14: Left: A Levenberg-Marquardt algorithm [38] is used to determine the temperature by fitting the model equation (blue dashed line) to the measured data (black circles). Right: The fitting routine is applied to each camera pixel resulting in a temperature map of the burner flame.

2.2 Optical Diagnostic Methods for Reacting Flows

In Figure 15 the application regimes of various spectroscopic diagnostic methods are presented. The highlighted region (roughly 100 mbar to 1 bar) crossing green fields indicates that LIF, CARS and Rayleigh scattering are in the optimum range for an application. Whereas electron based techniques are difficult to apply.

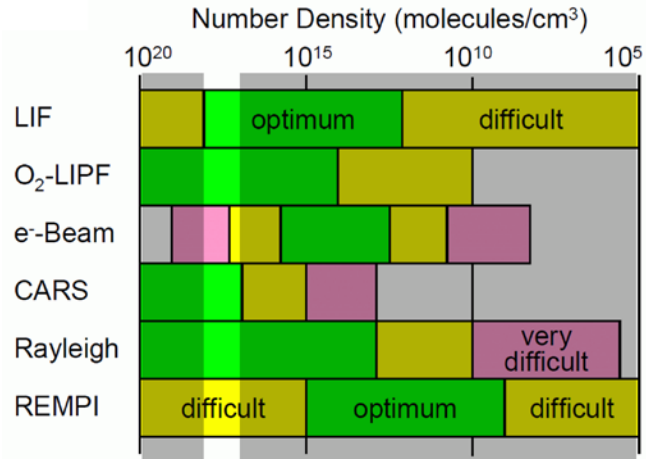

Figure 15: Application regimes of various spectroscopic diagnostic methods; the highlighted region roughly indicates pressure regime of 100 mbar to 1 bar (after J.W.L. Lewis, C. Dankert, R. Cattolica, W. Sellers, T. Niimi).

2.2.1 Chemiluminescence

From synchronously acquired DGV or PIV and 2D-OH* chemiluminescence images, the correlation between heat release and velocity field can be measured. Also information on the distance of chosen combustion parameters to unstable combustion conditions can be won.

For the indication of the reaction zone the radiation of electronically excited hydroxyl radicals OH* can be used. The electronically excited OH* is a product of the reaction:

$$HCO + O \rightarrow OH^* + CO$$

The formyl radical HCO is the most interesting intermediate of the hydrocarbon combustion. But at realistic combustion conditions optical measurement of HCO was not mentioned in literature up to 2004. In contrast to this, the narrow band structure of the OH* emission spectrum at 312 nm ± 7 nm enables a sensitive and selective detection of OH* chemiluminescence [39]. The variation of OH* chemiluminescence with the flow rate is linear, the slope varies very weakly as a function of the equivalence ratio. So OH* chemiluminescence provides an indirect, but easy measure of the formyl radical HCO, as a good indicator of heat release under steady and unsteady conditions and even near extinction.
From a measurement of the OH* chemiluminescence only the volumetric information of the heat release can be deduced. The intensity of an OH* image is always the integral of all contributions towards the camera view. On the additional assumption of axial symmetry it is in principal possible to deconvolute OH* images to deduce the spatially resolved heat release, provided we can simultaneously image the outer flame area containing no OH* signal [40].
If the field of view is smaller than the complete flame area, presented OH* distributions of the examined flames are typically not deconvoluted.
The integral OH* chemiluminescence intensity is usually imaged through a filter by an intensified CCD camera using a side window.
For phase resolved measurements the image acquisition is synchronized with the combustion oscillations to deduce a ‘movie’ of the OH* distribution during the combustion oscillations. In [27] the integration time was 100 µs for a single image. To discriminate the influence of the turbulent fluctuation, the periodic fluctuations were deduced from phase averaged images comprising 400 single shots. An application to high pressure Liquid Oxygen (LOX)/Methane coaxial injection and combustion is presented in [41].

2.2.2 Laser Induced Fluorescence (LIF)

For the investigation of the temperature field of the transonic hot plume spectroscopic methods relying on fluorescence of the hydroxyl molecule (OH) are particularly well suited since it is a by-product of the hot plume generation (methane or hydrogen combustion). While the 2-line OH-PLIF temperature measurement technique is already well established [42], an experimentally less complex, absorption corrected, 1-line OH-PLIF technique has been developed at AT-TM [43], [44] and has been the method of choice for the investigation of lean combustion [45], [46], [47], [48], [49], [50]. The technique exploits the fact that the OH equilibrium concentration grows exponentially with temperature but is nearly independent of the air-fuel ratio (λ) in lean combustion ($\lambda>1.1$). Highlights of this technique are an excellent signal-to-noise ratio and a high temperature sensitivity. Application examples on a generic combustor are given in Figure 16 and Figure 17.

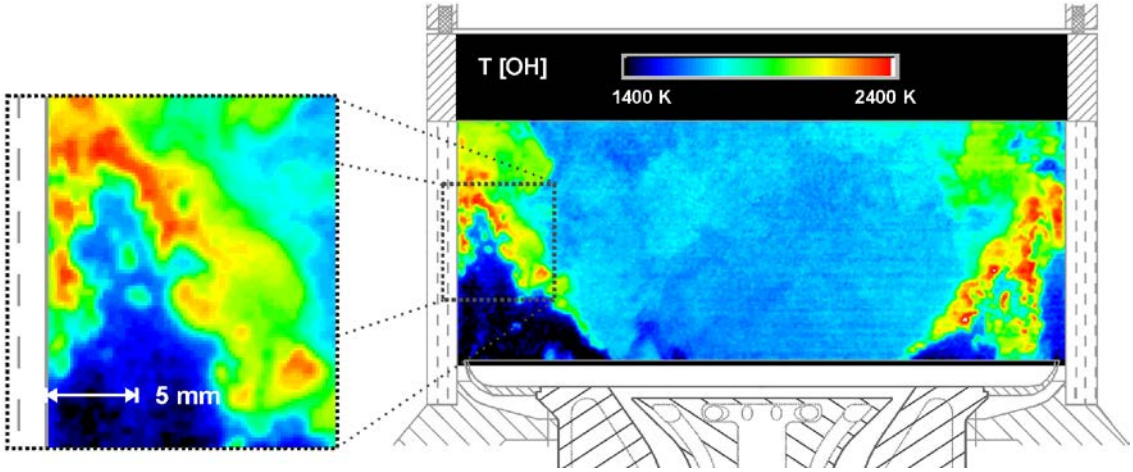

Figure 16: Instantaneous temperature inside a combustion chamber with swirl flow combustor determined using the OH-T-PLIF technique.

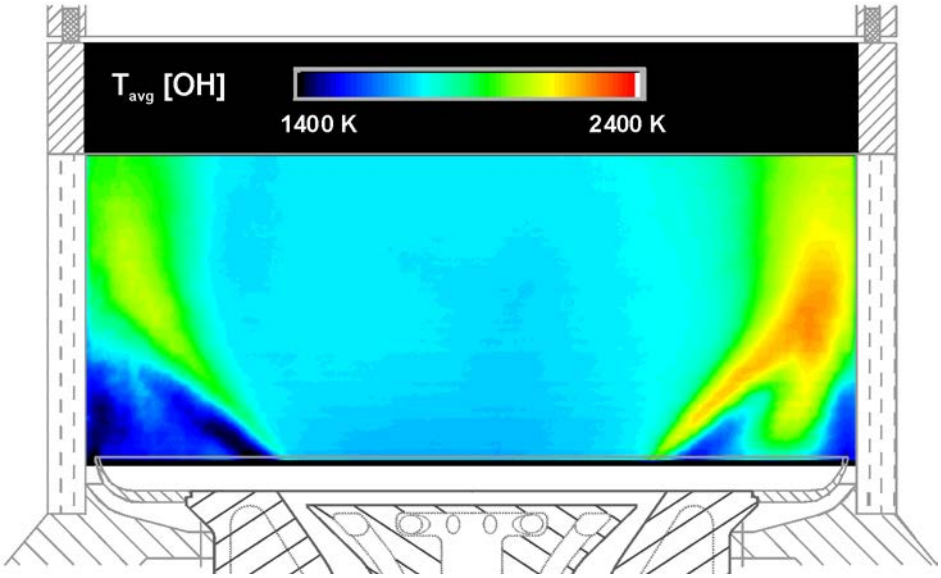

Figure 17: Average temperature field inside a combustion chamber with swirl flow combustor

2.2.3 Filtered Rayleigh Scattering (FRS)

The technique was described in Section 2.1.4. One drawback of FRS is the dependence of the scattering signal intensity on the relative weight of the different scattering molecular gases in the probe volume, that means on the gas composition. The highest accuracy will be reached in a known environment like air. The application of FRS in the external edge flow seems to be border crossing but for a low mixture with burned gases near to this condition. Other possible disturbers like particles or soot are expected to be less important because of the signal filtering.

An actual promising result is presented below (Figure 18) showing a first application near to a highly illuminating wall and a bright flame. The application example demonstrates for the first time the achieved spatial resolution during real generic combustor operation at 5 bar [51,52]. Even near to the highly illuminating flame zone (skipped white area) and in close vicinity to the cooling wall the flow

structure was resolved. And the incoming cooling air temperature of 450 K was measured correctly (dark blue Figure 18), as set by the thermocouple controlled loop.

Due to the diffraction index fluctuations under high pressure and stronger density gradients, the application is expected to be more difficult compared to the base flow measurements in the low temperature regime at lower pressure. In the here presented application hot combustor gases are in direct interaction with an effusive cooled wall.

The light sheet was arranged vertical to the effusive cooling plate of the burner housing. A combined image was taken consisting of several images with 16 x 16 mm dimension. A sensor resolution of 16 px/ mm corresponds to about 0.2 mm spatial resolution (3 px for one peak).

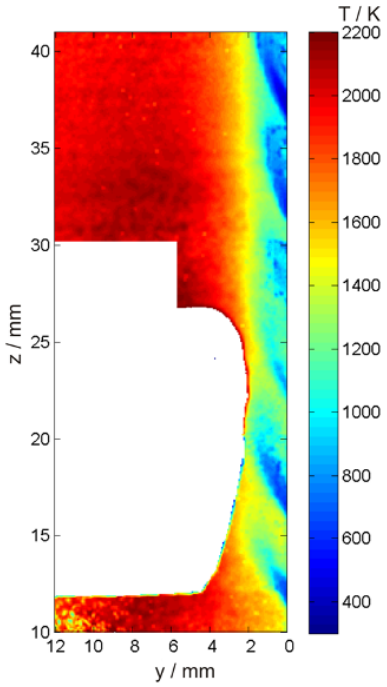

Figure 18: Temperature field measured with FRS and high spatial resolution [52].

As camera objective a Nikon macroplanar (f = 100 mm, F = 2) was used. The working distance (camera objective – Laser light sheet) was 340 mm. This fits well to the dimensions of the TMK facility (diameter 600 mm) and is also usable at the VMK facility.

The light sheet thickness was about 0.4 mm, the light sheet height 11 mm, the laser power 5 W at 532 nm. Nevertheless a 4s average measurement was taken. Therefore according to the expected run time of up to 10 s the scanning FRS approach cannot be used at HTF for non-steady measurements. To overcome this limitation the mentioned macro pulse laser should be tested, which is already available at DLR-AT.

To accomplish a sufficient background light suppression for FRS a bigger nozzle length of (typically 1.2 D) would be advantageous to enhance the distance to the combustion zone.

2.2.4 Coherent Anti-Stokes Raman Scattering (CARS)

2.2.4.1 CARS Set-up

A commercial broadband CARS system (SOPRA) is available at the Institute of Propulsion Technology which is optimized for time resolved flame measurements. The system is described in detail in [53]. Figure 19 shows a simplified sketch of the CARS set-up, which mainly consists of two stable units. The first consists of the CARS laser (Figure 20) and the second the spectrometer and the detector.

Typically CARS experiments are performed in a planar BOX-CARS beam arrangement [54] on nitrogen. This provides sufficient spatial resolution combined with easy access to the facility and simplified beam handling in one optical plane. The probe volume is formed by three crossing laser beams which interact with the medium and generate a blue shifted signal beam at $\nu_{CARS} = \nu_1+\nu_{RS}$. The two pump beams are at ν_1 with a wavelength of 532 nm and the dye laser beam at ν_2 (about 607 nm). ($\nu_{RS} = \nu_1-\nu_2$) is the Raman shift. Using an achromatic lens with a focal length of 500 mm to focus the laser beams, and 12 mm beam separation the corresponding probe volume, in which 95% of the CARS signal is generated, is shorter than 10 mm. The diameter of the probe volume is about 100 µm. For 300 mm focal length it the probe volume would be about 3 mm and for shorter focal lengths or bigger beam distances a spatial resolution in the sub-mm range can be achieved.

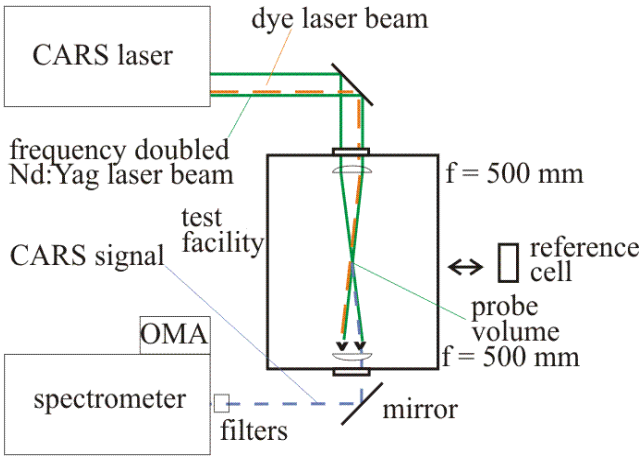

Figure 19: Schematic sketch of CARS set-up. View from the top for the planar BOX-CARS arrangement.

Figure 20: Photograph of the open CARS laser container, including the beam separation and polarization optics. IR cavity and two laser heads at the top, green laser beam at the center and on the right side, dye laser on the left. Laser exit in the lower right corner.

The laser system is based on a frequency stabilized, injection seeded, single mode Nd:Yag laser. The stable infrared resonator emits pulsed radiation with a near Gaussian intensity beam profile at a wavelength of 1064 nm. This laser beam is first amplified and then frequency doubled in a KTP-crystal resulting in the pump beam (ν_1) with a wavelength of 532 nm. The pump beam has a pulse length of 14 ns, a repetition rate of 10 Hz. A total pulse energy of 55 – 62 mJ is used for high temperature applications. To generate the broadband dye laser ("Stokes") beam Rhodamin 610 was used in the oscillator and amplifier cell of the dye laser. The dye laser is pumped transversely by a portion of the green laser beam and emits broadband radiation (ν_2) with a pulse energy of about 3.5 – 4 mJ. Width and spectral position of the broadband dye laser are optimized for the temperature range under

investigation. This is achieved by tuning the dye concentration and adjusting an intra-cavity Fabry-Perot etalon. For low pressures and for very high temperatures the polarisation of pump and Stokes beam is used parallel relative to each other to obtain maximum signal intensity. Estimations showed that the signal intensity would not be sufficient for other configurations. The absence of stimulated Raman effects, which can result in an excess vibrational population, was proved by measurements in a low pressure cell. As a consequence of the high CARS efficiency reached with the single mode laser system, even at the highest available laser powers we never found a population distortion due to such effects.

Reference spectra for the normalization of the spectral CARS gain profile are measured in an Ar flow cell directly before and after the experiments. The signals are guided by dielectric mirrors, coupled into the spectrometer, and finally imaged on the detector by a concave reflection grating (Jobin Yvon, 2100 lines/mm). Up to now a linear intensified photodiode array with 512 diodes (model 1420/HQ from EG&G with phosphorus P46) was used as detector. Spectrometer and laser can be located inside the test facility during the experiments and controlled from a neighbouring room.

2.2.4.2 CARS Data evaluation

An overview on the CARS theory is provided in several references, e.g. [55,56,57,58,59]. Temperatures were evaluated by a weighted fit of the measured single pulse spectra to precalculated theoretical spectra, stored in a spectra library. Data evaluation and data acquisition used here, were developed at the DLR Cologne and especially adapted for measurements at high temperature and pressure [60,61,62]. The CARS system was successfully applied in several applications, e.g. [53,63,64].

Due to the broadband operation of the dye laser with each laser pulse it is possible to record a complete nitrogen CARS spectrum, which can be evaluated giving a single pulse temperature. From measured ensembles temperature mean value, RMS(T) and some other statistical information are extracted.

For the evaluation of rotational and vibrational temperatures a two dimensional library is used. The fit is based on the assumption of independent Boltzmann distributions for the rotational and vibrational populations. In the weighting process the average spectral CARS gain profile, CARS specific noise, and detector properties are accounted for.

Due to the 10 Hz operation of the CARS system the number of acquired single pulse spectra is dominated by the facility run time (up to 10 seconds expected) and the working cycle of the facility.

To determine the accuracy of extracted rotational and vibrational temperatures laboratory experiments were performed, however, only up to about 3000 K [60,53,62] in flames and furnaces. Under test facility conditions with high signal intensities the typical accuracy of the mean temperatures is about 2 – 3 % for a one dimensional temperature fit and more than 4 % for the independent fit of T_{rot} and T_{vib}, for temperatures below 2000 K [53]. At, e.g., 1600 K the root mean square value of 1D- single pulse temperatures is less than 40 K. For the evaluation of non-equilibrium spectra the accuracy of the 2D-temperature results is at very high temperatures dominated by the small signal heights realized and by the chosen finite spectral range (increased scatter). For the temperature evaluation up to about 3000 K only Raman shifts from 2223.2 - 2512.4 cm^{-1} are used, which is the spectral range verified by the high temperature pre-experiments in furnaces mentioned [62]. Thereby at high temperatures the influence of highly excited molecular states on the results is minimized. If a thermal non-equilibrium is expected the experimental single pulse spectra are compared to a library containing up to about 1000 spectra with varying T_{rot}, and T_{vib}.

2.2.4.3 CARS Application example

In the frame of ESA's TRP project "AMOD" a test campaign was performed in DLR's arc heated facility L3K [65]. The test campaign was run in order to gather experimental data that can be used for the validation of thermo-chemical models that are applied in CFD simulation schemes for entry flow

problems (compare also [66]. In high enthalpy flows with complex non-equilibrium chemistry, like at entry conditions, the flow characterization is essential to estimate the aerodynamic behaviour and the Thermal Protection System (TPS) performance of entry capsules. Therefore, all tests were performed at high enthalpy flow conditions with a total enthalpy of 11.8 MJ/kg. Non-intrusive laser based measurement techniques are one of the key tools, which are necessary for the determination of the flow parameters. For this flow condition a large number of free stream measurements and measurements in the shock region of a model were performed. The CARS measurement technique was applied for free stream characterization and measurements of temperature profiles in the shock region [65].

"Freezing" of the vibrational temperature on a level higher than the translational temperature was expected in the free stream due to the strong expansion of the heated gas from the arc heater behind the nozzle throat and the long vibrational relaxation time of nitrogen. The interpretation of the results is eased by the fact that an air expansion is under investigation remaining mainly nitrogen in the flow. The CARS measurements on nitrogen were chosen because of the high thermal stability of molecular nitrogen, resulting in a mass fraction of still 76 % (air 78.09 %). This is in contrast to the thermal dissociation of oxygen (rest mass fraction 7×10^{-3}) in the free stream.

Additionally, the spectral simulation of nitrogen CARS spectra is well developed. Due to the high heat loads the test time is limited to less than a minute for safe operation of the facility. The NO-LIF technique [4] which is usually applied for the characterization of high enthalpy flow fields of the arc heated facilities is not applicable in the high temperature high pressure region in front of the body. Therefore CARS temperature measurements were performed to analyse the thermodynamic behaviour of the flow in front of a probe body with high temporal and spatial resolution. Thermal non-equilibrium was identified by single pulse measurements. A large number of measurements with a measurement rate of 10 measurements per second was taken in the free stream as well as in the shock layer. From each measurement spatially resolved rotational and vibrational temperature values and density values were obtained. The rotational and vibrational temperatures measured in the free stream at model location show a very homogeneous temperature distribution which confirms the conclusion from Pitot pressure and heat flux profiles.

Under free jet conditions the vibrational transitions always appear well separated, resulting in a better sensitivity for the 2D-temperature fit and a reduced temperature scatter. Because the broadening and shift of the spectral band contours is still characteristic for T_{rot} and T_{vib}. An experimental spectrum from the free stream region at the nominal position x = 9.5 mm is plotted in Figure 21 together with the simulated spectrum using a rotational

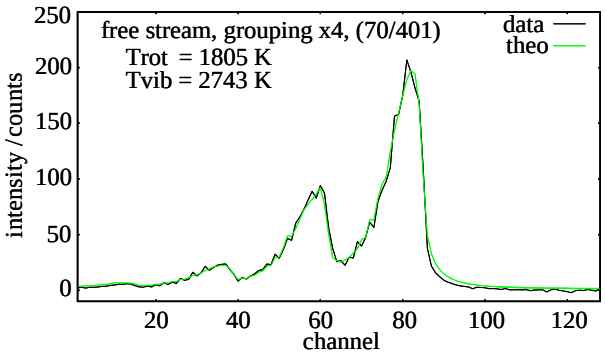

Figure 21: Experimental CARS spectrum measured in the free stream (probe body outside) and simulated spectrum with the rotational and vibrational temperatures.

temperature of 1805 K and a vibrational temperature of 2743 K. This temperature combination represents the values for the best agreement of theory and measured spectral data.

The spectra showed that (depending on temperature and vibrational transition) an intensity from about 25 (v = 2→3 free stream, Figure 21) to more than 200 cts/channel was realized, sufficient to analyze single pulse data. As expected the spectra presented show that the non-resonant signal contributions are very small under the given conditions.

An example of the CARS spectrum 1.5 mm in front of the model is given in Figure 22. This example shows the quality of the signals and the agreement with the simulated spectrum. The realized spatial resolution was more than a factor 2 smaller than the expected temperature plateau in front of probe body.

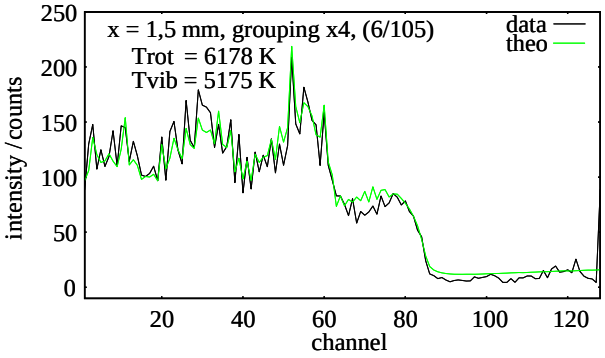

Figure 22: CARS spectrum 1.5 mm in front of the cylindrical model and simulated spectrum for the best agreement for rotational and vibrational temperatures.

A good spectral resolution in the experiments at low pressure and under atmospheric conditions is advantageous for the determination of the rotational temperature and simplifies the detection of a non-equilibrium excitation. But especially in the in high temperature range the experiments showed a clearly superior signal to noise ratio using a grouping of four detector diodes, corresponding to 1,44 cm^{-1}/channel resolution and a slit width of 60 µm. For lowest signal levels in the free stream the CARS dependent temperature scatter dominates the total temperature scatter RMS(T), which is in the order of 200 K. For the high temperature range at 5800 K the temperature scatter is increased.

Because of the extended temperature range to be measured in the actual experiments, the parameter set used for the nitrogen CARS spectra simulation was extrapolated to higher quantum numbers ($v \leq 10$, $J \leq 150$) to achieve a Boltzmann-distribution for the rotational and vibrational population and the spectra simulation covers an extended spectral range (1850-2450 cm^{-1}).

It can be expected that the CARS single pulse accuracy dominates the scatter of the measured temperature data. This is especially valid for the result with probe body showing very high rotational and vibrational temperatures at the same time. Here intensity fractions originating from highly excited vibrations superpose with intensities from rotational transitions belonging to the ground state transition (v = 0→1). The temperature sensitivity is reduced and the 2D-temperature scatter will therefore increase under these conditions. The mean value $T_{rot} = T_{vib}$ is even at low signal levels still assignable because the value is mainly dominated by the center of gravity shift of the intensity distribution.

Strong non equilibrium concerning rotational and vibrational temperatures was measured in the free stream and in the bow shock region. The free stream rotational temperature is good agreement with the numerical simulation. However the measured vibrational temperature is considerable lower compared to the simulated.

Measurements with CARS in the shock layer at different distances to the model surface provided an almost constant temperature level along the stagnation point stream line until the edge of the boundary layer. In addition, the good spatial resolution allowed to extract the position of the bow shock from the

profiles and to estimate the shock shape and the shock's stand-off distance. The stand-off distance was found be 7.5 mm for the high enthalpy condition. With the new nozzle designed for extremely high heat flux rates the broadband CARS was successfully applied for the first time to qualify measurements on a high enthalpy, hypersonic flow field.

3 Comparison of the most suitable measurement techniques

Comparison of DGV to PIV

Pros and cons of DGV:

+ insensitive to beam steering (less important at low pressure)
+ usage of image guides possible (for PIV not recommended, see chapter 4)

- background sensitivity of DGV (see chapter 4)
- for DGV a higher seeding level is required compared to PIV

Although optical access from three sides seems to be possible in general at TMK and VMK, an optical set-up with endoscope (compare chapter 2.1.3) is not favoured at the hot plum test facility, also because of the probe position in the hypersonic flow and the high heat load resulting from H_2/O_2 combustion. More arguments against a probe application are given in chapter 4. Also laser coupling to the set-up by fibres with high core diameter is not recommended, because this results in too thick light sheets (some mm). Because of the high power density of the laser pulses glass fibres with smaller core diameters (<< 200 µm) cannot be used for DGV. Additionally, during the analysis of the external edge flow, the light sheets can illuminate the model structure, which is counterproductively for the application of DGV (compare recommendation in chapter 4) .
These basic arguments are also valid for single pulse DGV, using image guides coupled to one camera, and a pulsed laser [20,18], but with the optical arrangement recommended in chapter 4 the laser background due to reflexions would be reduced.

We would prefer the application of PIV because of actual progress in combustion applications, the low pressure level (< 1 bar) and the reduced seeding needs.

LIF compared to CARS and FRS

OH-LIF is most promising for the hot flow. In contrast to CARS, LIF offers spatially correlated 2D-results on a single shot basis. This is the important feature for the analysis of combustion oscillations; especially with regard to the limited facility run time. The expected realizable spatial resolution is better for LIF, because imaging techniques are in general less sensitive to beam distortions, compared to focusing measurement techniques. Moreover the CARS signal declines quadratically with probe volume length and molecular density. Furthermore CARS on the main combustion product H_2O is no standard technique for temperatures of 3000 K and more. However DLR-AT has one of the few groups with experience in water spectra simulation and CARS measurements on water in H_2/air and H_2/O_2 combustion. Inside the edge flow CARS could be applied on N_2, but it is still a point measurement method.

Because of the low temperatures probably it would be more promising to measure the temperature inside the edge flow field using FRS, as border crossing application. But FRS was not tested near to a bright hydrogen–oxygen combustion up to now. Additionally only limited experiences exist for the high temperature range [67]. But depending on the flow interaction FRS can be attractive because OH-LIF applied to the edge flow could suffer from low OH concentrations. Especially the absorption correction for single line OH-LIF could be critical at low OH densities. In this case 2 line LIF would be necessary.

Fortunately for the hot flow it can be stated, that in a hydrogen-oxygen combustion the OH concentration is much higher compared to the combustion of natural gas with air.

4 Recommendations for Facility Design

Regardless of the type of optical diagnostics employed the HTF will require adequate optical access to the regions of interest, in particular the base flow area. Figure 23 outlines a possible configuration in which the test section has optical access from all four sides. For most of the proposed planar optical measurement techniques three optical access windows would be sufficient to image a light sheet plane with a camera placed normal to the light sheet. The ability to have the light sheet exit the facility on the opposite side is a prerequisite for diagnostics that rely on absorption calibration (e.g. OH-T-PLIF). At the same time the passage of the light sheet reduces laser flare within the test section because the light is not scattered by the opposite wall.

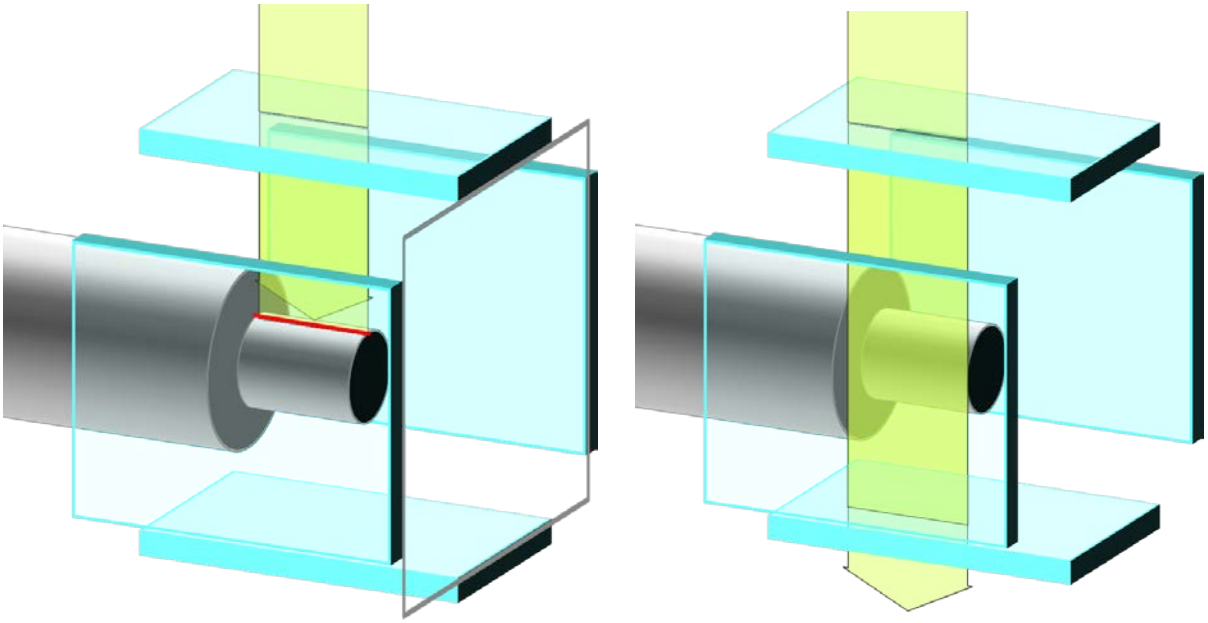

Figure 23: Possible light sheet arrangements for imaging the base flow region. Note that the light sheet in the left configuration hits the ejector creating laser flare (red line) that may saturate the imaging device (camera).

The availability of an additional window in the line of sight has two advantages: First, the background will be less susceptible to light scattered within the test section, which improves contrast for the velocimetry techniques (e.g. PIV) and reduces signal degradation for the techniques relying on quantitative intensity measurements (e.g. LIF). The second advantage is that the additional window allows the simultaneous application of line of sight methods (e.g. schlieren imaging) in parallel with the light sheet imaging methods. This allows for time- and space-correlated measurements of different quantities.

A possible alternative to direct optical access though windows is the use of endoscopes or boroscopes. Within the area of high pressure combustion research this is generally the only feasible way to obtain measurement data and generally requires less modifications to the test rig itself. Unfortunately there are two drawbacks with endoscope based methods the mainly concern the imaging aspects: the light sensitivity of the endoscope in comparison the conventional typically is reduced by an order of magnitude, due to the small size of the entrance pupil and losses in the imaging system. The second shortcoming the greatly reduced spatial resolution in comparison to direct imaging. The spatial

resolution of endoscopes is insufficient to adequately image submicron particles that are necessary for PIV in trans- and supersonic flows. While optical methods such as LIF can still operate at reduced spatial resolution, since they are intensity based, they do require the transmission of UV light for which very few commercial solutions are currently available. Light transmission efficiency and optical resolution of the currently available endoscopes is poor in comparison to direct imaging. To address this technology gap dedicated research projects at DLR are underway to enable endoscopic UV imaging on high pressure combustion facilities (DLR Project EndoKoDi, AG-Turbo 2.3.4). Spin-offs from this research can be of future benefit to application of optical diagnostics in the HTF.

While endoscopic imaging is a less favored choice for the HTF, the delivery of laser light via borescope (*Spiegelrohr*) may be a viable choice because it forgoes at least one optical window and allows the placement of the light sheet in positions that are not available via window access. Borescope light sheet delivery has been used quite extensively for PIV in turbomachinery [68,69,70] as well as for PIV measurements in transonic and supersonic flows within blow-down facilities [71,72,73].

4.1 LIF

There are basically two different approaches to derive temperature information from a LIF measurement, which were described in [43]: One way is to probe the thermal population distribution of molecular states. This method has the advantage that the concentration of the indicator molecule needs not to be known; the only requirement is that the internal degrees of freedom are in thermal equilibrium. The disadvantage is that the relative populations of at least two molecular states need to be probed simultaneously, which requires usually a high experimental expenditure for excitation of two molecular transitions with different wavelengths. Even if only a temporally averaged temperature field is desired, subsequent excitation of two lines using the same laser will inevitably lead to a systematic bias towards higher temperature, because of the nonlinear dependence of both state population and the number density of indicator radicals on temperature. The second method is based on the measurement of a temperature dependent concentration of the indicator molecule. This method, based on OH radicals as test species, will be discussed in our paper. It has the advantage of considerably less experimental effort and time for set-up of the experiment, because it requires just one laser for excitation of a molecular line. The nearly exponential growth of the OH concentration with respect to temperature enables the high temperature sensitivity of this measurement technique. Its main drawback results from the usually ambiguous dependence of the OH concentration on both temperature and stoichiometry Φ. This restricts the application to scenarios with lean mixtures, because at sufficiently low equivalence ratios the OH equilibrium concentrations depend only weakly on Φ and mainly on temperature. A second requirement is that the OH concentrations need to be in chemical equilibrium, because high non-equilibrium concentrations at or near flame fronts will feign higher temperatures. The decay rate of chemical superequilibrium increases with pressure; consequently, high pressures are favourable for the application of this method [43].

A new set-up for synchronous single line OH-LIF and PIV measurements with high spatial resolution is presented in Figure 24.

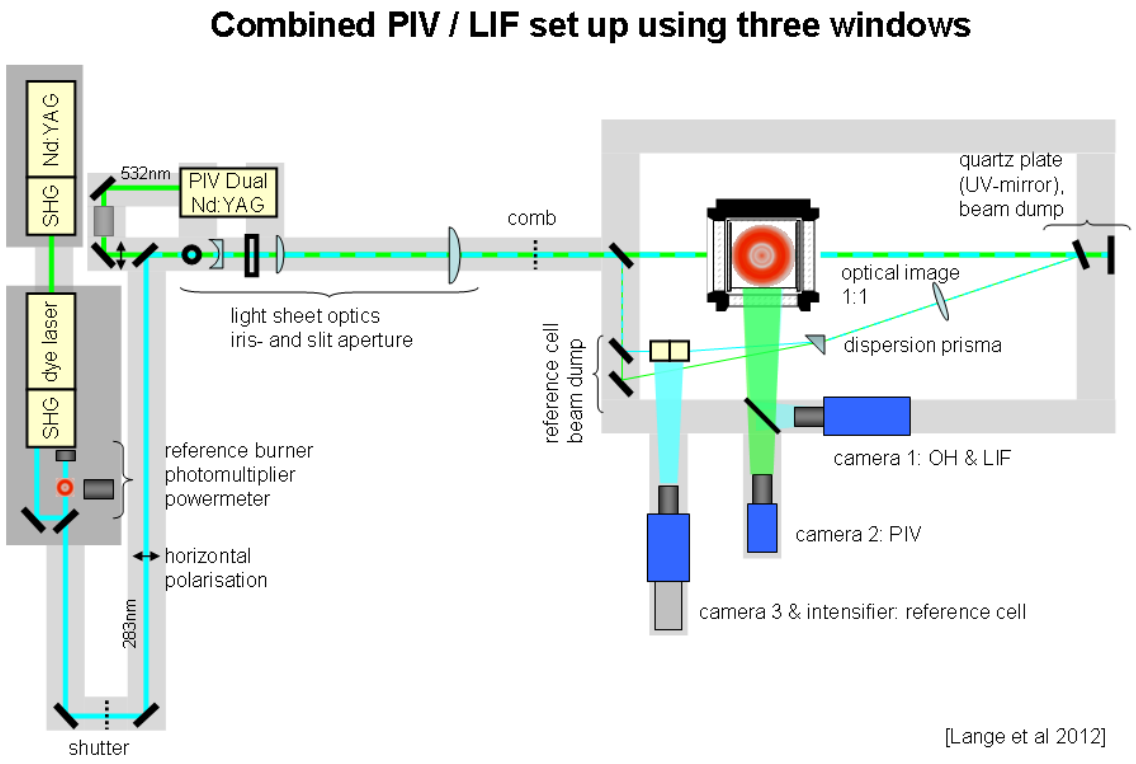

Figure 24: Combined PIV/single line LIF set-up using three facility windows [12].

At the HTF, for example the top and bottom windows could be used for the light sheets and the window perpendicular for the cameras. With f = 50 mm at 400 mm working distance or f = 800 mm at 800 mm working distance a 17 cm field of view is far bigger than the 3 – 4 cm dimension under discussion. The complete exit flow would be visible. The required distances to the laser light sheets are actually somewhat more than 170 mm at VMK and bigger than about 300 mm at TMK.

An application example demonstrating the achieved spatial resolution during generic combustor operation at 5 bar is shown in Figure 25 [12,13]. A camera objective f = 100 mm was used at a working distance of about 300 mm, which is the same distance as the half actual TMK diameter. The UV- light sheet height was 48 mm, with a thickness less than 0.15 mm. A spatial resolution of about 0.2 mm was achieved.

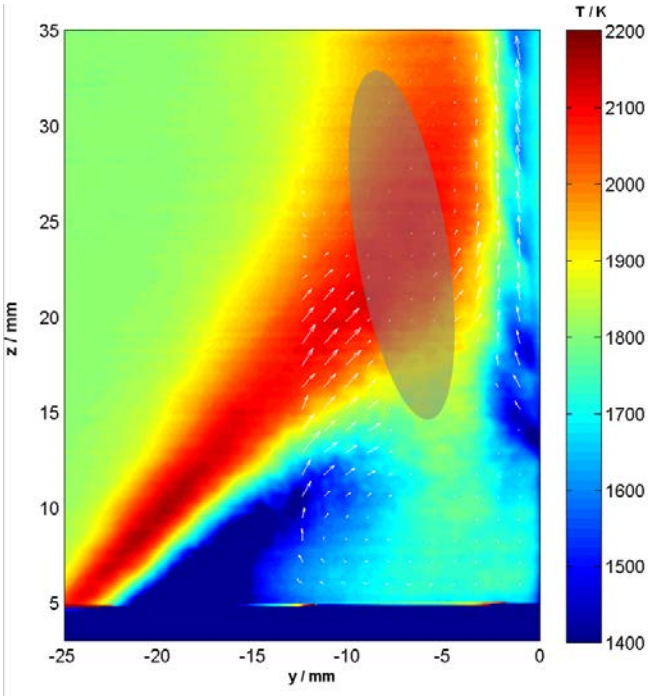

Figure 25: Correlated temperature and velocity field from synchronous LIF and PIV measurements on a generic combustor with effusive cooled wall (right side) [12]. LIF image area shown**:** 35 x 25 mm. The dark blue zones on the right indicate cooling air and the dimension of the cooling film. See also the PIV vectors nearly parallel to the wall.

It is recommended to try the less complex single line approach with absorption correction first under the conditions of HTF. If necessary the 2 line LIF set-up with a second UV Laser can be installed. This laser will be adjusted on the same light sheet direction shown in Figure 24.

The OH concentration inside the external edge flow is unknown. Depending on the nozzle expansion and flow interaction, the eddy under investigation consists mainly of air. A successful OH concentration measurement requires an OH concentration in the order of $0.1 – 2x10^{16}$ molecules/cm^3 [12].

In [43] the OH equilibrium concentration as function of temperature T and equivalence ratio Φ, was calculated for a methane/air flame at 6 bar. On page 15 of the HTF proposal the OH mass fraction is given due to a numerical analysis of a planar nozzle provided with a H_2 film injector (0 - 0.01).

4.2 PIV

In Figure 26 and Figure 27 possible set-ups for PIV are shown. Big windows as presented in Figure 23 are advantageous and the light sheet can be arranged as shown in Figure 23.

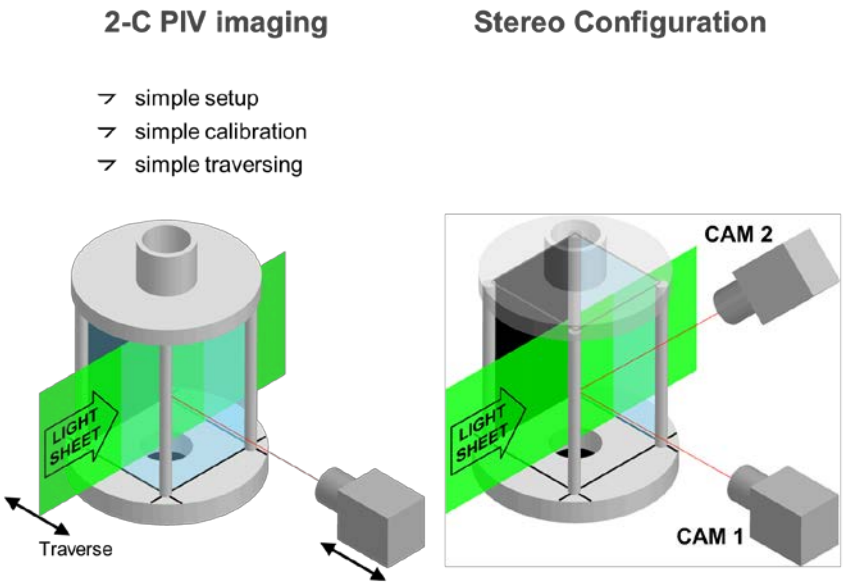

Figure 26: Camera position relative to light sheet for 2-C PIV and Stereo PIV.

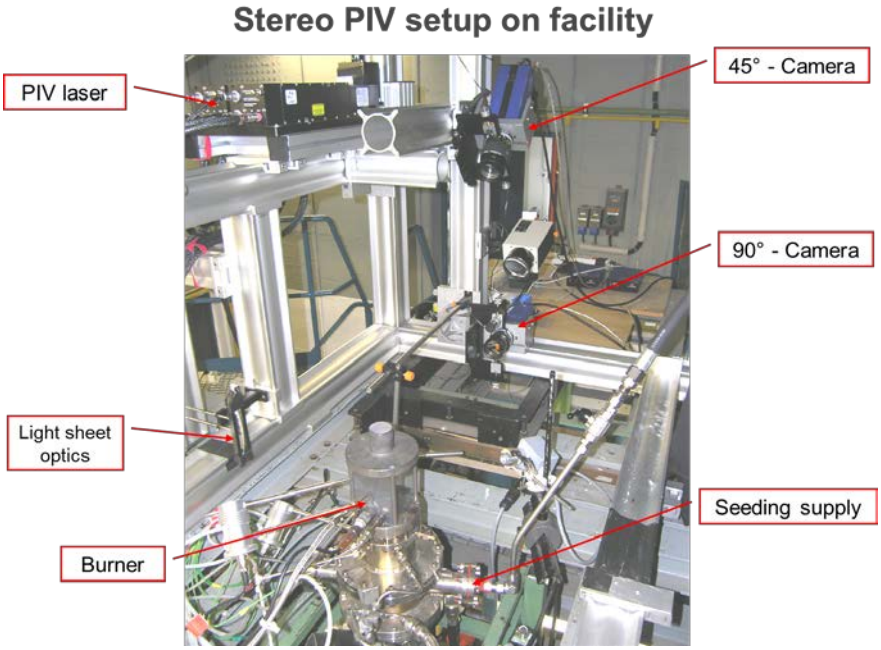

Figure 27: Example for a Stereo PIV set-up on a burner.

The stereoscopic approach is described in detail in [6] and [74]. In [6] it was stated, that since the measurement precision of the out-of-plane component increases as the opening angle between the two

cameras reaches 90°, it is not always possible to mount the camera pair on a common base, when using large observation distances, and much less to provide a symmetric arrangement. Therefore a general description for asymmetric recording and associated calibration has been developed [6]. Another problem that arises through the use of large focal length imaging lenses: their limited angular aperture restricts the distance between the lenses in a translation imaging approach.
Designed for use with a fixed format sensor centered on the optical axis of the lens, most lenses are not only limited in their optical aperture but also characterized by a strong decrease in the modulation transfer function (MTF) towards the edges of the field of view. To adequately image small particles a good MTF at small f numbers is a stringent requirement. Since lens systems with an oblique principal axis are practically nonexistent, a departure from the translation imaging method is unavoidable. As the best MTF is generally present near the lens principal axis, the alternative angular displacement method aligns the lens with the principal viewing direction.
The additional requirement for small f-numbers is associated with a very small depth of field which only can be accommodated by additionally tilting the back plane according to the Scheimpflug criterion in which the image plane, lens plane and object plane for each of the cameras intersect in a common line. The oblique view of the scene is associated with a perspective distortion that is further increased by the Scheimpflug imaging arrangement. In essence, the perspective distortion results in a magnification factor that is no longer constant across the field of view and requires an additional means of calibration to be described [6].

List of Abbreviations

BOS	background oriented schlieren
BOSS	Big Optical Single Sector (large single sector test rig at DLR-KP)
CARS	coherent anti-Stokes Raman scattering
CFD	computational fluid dynamics
DFWM	degenerate four wave mixing
DGV	Doppler global velocimetry
DLR	Deutsches Zentrum für Luft- und Raumfahrt (German Aerospace Center)
DLR-AT	Institut für Antriebstechnik (DLR-Köln)
DLR-RA	Institut für Raumfahrt-Antriebe (DLR-Lampoldshausen)
DLR-VT	Institut für Verbrennungstechnik (DLR-Stuttgart)
FRS	filtered Rayleigh scattering
L2F	laser-2-focus velocimetry (also LTA)
LDA	laser Doppler anemometry
LIF	laser induced fluorescence
LuFo	Luftfahrt-Forschungsprogramm (Aeronautic Research Programme of Germany)
Mie	Mie light scattering on particle
N_2	molecular nitrogen
OH	hydroxyl radical
OH*	hydroxyl radical, electronically excited
PDA	phase Doppler anemometry
PDF	probability density function (synonymous with *histogram*)
PIV	particle image velocimetry
PLIF	planar laser induced fluorescence
PS	polarisation spectroscopy
QLS	quantitative light sheet (mixture ratio via Mie scattering)
Raman	Raman scattering (inelastic scattering of light)
Rayleigh	Rayleigh scattering (elastic scattering of light off molecules)
RQL	rich quench lean (aero-engine combustion concept)
SSC	Single Sector Combustor (optical combustor test rig at DLR-KP)
TDL	tuneable diode laser
TGS	transient grating spectroscopy
UV	ultra violet (light)

5 List of References

[1] ESA-ITT, "Statement of Work, Launcher stage separation and plume interaction validation," ESA Directorate of Technical and Quality Management, Tech. rep. April 2010.

[2] S.N.B. Murthy and J.R. Osborn, "Base flow phenomena with and without injection: experimental results, theories, and bibliography," in *Aerodynamics of Base Combustion, Progress in Astronautics and Aeronautics*, 2nd ed., S.N.B. Murthy, Ed.: American Institute of Aeronautics and Astronautics, New York, 1976, vol. 40, pp. 7-210.

[3] F. Bos et al., "Feasibility Study of a Hot Plume Test Facility," , vol. 487, feb 2001, p. 639.

[4] V. Zapryagaev et al., "Experimental Investigation of Base Pressure with Hot Supersonic Jet for External Supersonic Flow," , vol. 487, feb 2002, p. 579.

[5] Ronald J. Adrian and Jerry Westerweel, *Particle image velocimetry*.: Cambridge Univ. Press, New York, USA, 2011.

[6] Markus Raffel, Christian E. Willert, Steve T. Wereley, and J\", *Particle Image Velocimetry - A practical guide*, 2nd ed. Berlin Heidelberg New~York: Springer, 2007.

[7] Andreas Schröder and Christian Willert, *Particle Image Velocimetry "New Developments and Recent Applications"*, Claus E. Ascheron and Adelheid H. Duhm, Eds.: Springer Berlin, Heidelberg, New York, 2008, vol. 112.

[8] Christian Willert et al.,.: Springer Verlag, January 2008, vol. 112, pp. 283-309. [Online]. http://elib.dlr.de/55160/

[9] C. Willert and M. Jarius, "Planar flow field measurements in atmospheric and pressurized combustion chambers," *Experiments in Fluids*, vol. 33, no. 6, pp. 931-939, 2002, LIDO-Berichtsjahr=2003. [Online]. http://elib.dlr.de/1152/

[10] Christian Willert et al., "Combined PIV and DGV applied to a pressurized gas turbine combustion facility," *Measurement Science and Technology*, vol. 17, no. 7, pp. 1670-1679, June 2006. [Online]. http://elib.dlr.de/43827/

[11] Olaf Diers, Denis Schneider, Melanie Voges, Peter Weigand, and Christoph Hassa, "Investigation of Combustion Oscillations in a lean Gas Turbine Model Combustor ," , May 2007. [Online]. http://elib.dlr.de/48930/

[12] Lena Lange, Michael Schroll, Johannes Heinze, and et al, "to be published:. combined LIF and PIV measurements.," *16th International Symposium on Applications of Laser Techniques to Fluid Mechanics, 09-12 July 2012, Lisbon, Portugal*, 2012.

[13] Lena Lange, "LIF and PIV.," Ruhr Universität Bochum, Ph.D. dissertation.

[14] J. Forkey, "Development and Demonstration of Filtered Rayleigh Scattering: a Laser Based Flow Diagnostic for Planar Measurement of Velocity, Temperature and Pressure," Princeton University, Ph.D. dissertation 1996.

[15] R.L. McKenzie, "Measurement capabilities of planar Doppler velocimetry using pulsed lasers," *Applied Optics*, vol. 35, 1996.

[16] M. Fischer, J. Heinze, K. Matthias, and I. Röhle, "Doppler Global Velocimetry in flames using a newly developed, frequency stabilized, tunable, long pulse Nd:Yag laser," *10th International Symposium on Applications of Laser Techniques to Fluid Mechanics, Session 35, Lisbon, Portugal*, 2000.

[17] C. Willert, E. Blümcke, M. Beversdorff, and W. Unger, "Application of Phase-Averaging Doppler Global Velocimetry to Engine Exhaust Flows," *International Symposium on Applications of Laser Techniques to Fluid Mechanics, Lisbon , Portugal, July 10-13*, 2000.

[18] Tom O. H., David S. Nobes, and Ralph P. Tatam, "Investigation into the selection of viewing configurations for three-component planar Doppler velocimetry measurements," *Applied Optics*, vol. 46, pp. 4102-4116, 2007.

[19] Christian Schäfer, "Entwicklung einer zeitaufgelösten Doppler Global Velocimetry Messtechnik mit einem kontinuierlichen Laser," Diplomarbeit, Fachbereich Informatik und Naturwissenschaften Fachhochschule Südwestfalen, Durchgeführt am Deutschen Zentrum für Luft- und Raumfahrt e.V. (DLR), Institut für Antriebstechnik, Abteilung Triebwerksmesstechnik, Linder Höhe, 51147 Köln, Master's thesis 2007.

[20] Tobias Strehlau, "Entwicklung eines kombinativen Messverfahrens auf Basis spektraler Filterung von Laserstreulicht zur simultanen Bestimmung von Geschwindigkeiten und Temperaturen," Diplomarbeit in Physik, Institut für Antriebstechnik des Deutschen Zentrums für Luft- und Raumfahrt, Mathematisch-Naturwissenschaftliche Fakultät der Rheinischen Friedrich-Wilhelms-Universität Bonn, Master's thesis 2010.

[21] Komine, "System for measuring velocity field of fluid utilising a laser-Doppler spectral image converter," *US Patent 4 919 536*, 1990.

[22] T.J. Beutner and G.E.A. Mosedale, "Doppler Global velocimetry Applications in Large Scale Facilities," *20th Advanced Measurement and Ground Testing Technology Conference, Albuquerque, AIAA-98-2608*, 1998.

[23] J.F. Meyers, "Evaluation of Doppler Global Velocimetry Data Processing," *8th international symposium on applications of laser techniques to fluid mechanics, Lisbon, Proceedings, Paper 11.1*, 1996.

[24] I. Röhle, "Doppler Global Velocimetry, Principle and Application," *RTO-Lecture Series 217 on: Planar OpticalMeasurement Methods for Gas Turbine Components, RTO-EN-6, AC/322(AVT)TP/20, Cleaveland Ohio and Cranfield UK, September 1999*, 1999.

[25] P. Labudde, P. Anliker, and H.P. Weber, "Transmission of narrow band high power laser radiation through optical Fibers," *Optics Communications*, vol. 32, pp. 385-390, 1980.

[26] G.P. Agrawal, *Nonlinear Fiber Optics*, 2nd ed.: Academic Press, 1995.

[27] M. Fischer et al., "Development of Doppler Global Velocimetry (DGV) devices and combined application of DGV and OH*-chemiluminescence imaging to gas turbine combustor," *Proceedings, 12th Intern.Symp.on Applications of Laser Techniques to Fluid Mechanics,12-15 July,2004,Lisbon,Portugal*, 2004. [Online]. http://elib.dlr.de/1285/

[28] A. Mielke and K. Elam, "Dynamic measurement of temperature, velocity, and density in hot jets using Rayleigh scattering," *Experiments in fluids*, vol. 47, pp. 673-688, 2009.

[29] G. Sutton, A. Levick, G. Edwards, and D. Greenhalgh, "A combustion temperature and species standard for the calibration of laser diagnostic techniques," *Combustion and Flame*, vol. 147, pp.

39-48, 2006.

[30] J. Panda and R.G. Seaseholtz, *Velocity and Temperature Measurement in Supersonic Free Jets Using Spectrally Resolved Rayleigh Scattering*.: Technical report, NASA, 2004.

[31] D. Fourguette, R. Zurni, and M. Long, "Two-dimensional Rayleigh thermometry in a turbulent nonpremixed methane-hydrogen flame," *Combustion science and technology*, vol. 44, pp. 307-317, 1986.

[32] R. Miles and W. Lempert, "Two-dimensional measurement of density, velocity, and temperature in turbulent high-speed air flows by UV rayleigh scattering," *Applied Physics B: Lasers and Optics*, vol. 51, pp. 1-7, 1990.

[33] R.B. Miles, W.R. Lempert, and J.N. Forkey, "Laser Rayleigh scattering," *Measurement Science and Technology*, vol. 12, p. R33, 2001.

[34] D. Most and A. Leipertz, "Simultaneous Two-Dimensional Flow Velocity and Gas Temperature Measurements by use of a Combined Particle Image Velocimetry and Filtered Rayleigh Scattering Technique," *Appl. Opt.*, vol. 40, pp. 5379-5387, 2001.

[35] J. Zetterberg, "Development of Laser-Spectroscopic Techniques for New Detection Schemes in Combustion Diagnostics," Lund University., Ph.D. dissertation 2008.

[36] S.P. Kearney, R.W. Schefer, S.J. Beresh, and T.W. Grasser, "Temperature imaging in nonpremixed flames by joint filtered Rayleigh and Raman scattering," *Appl. Opt.*, vol. 44, pp. 1548-1558, 2005.

[37] M. Boguszko and G. Elliott, "On the use of filtered Rayleigh scattering for measurements in compressible flows and thermal fields," *Experiments in Fluids*, vol. 38, pp. 33-49, 2005.

[38] W. Vetterling, B. Flannery, W. Press, and S. Teukolski, *Numerical Recipes in Fortran-The art of scientific computing.*, 1992.

[39] L. Haber, U. Vandsburger, W. Saunders, and V. Khanna, "An examination of the relationship between chemiluminescent light emissions and heat release rate under non adiabatic conditions," *ASME- GT-0121*, 2000.

[40] C. J. Dasch, "One-dimensional tomography: a comparison of Abel, onion-peeling, and filtered backprojection methods," *Applied Optics*, vol. 31, No.8, pp. 1146-1152, 1992.

[41] Johannes Lux and Oskar Haidn, "Effect of recess in high pressure Liquid Oxygen (LOX)/Methane coaxial injection and combustion," *Journal of Propulsion and Power*, vol. 25, no. 1, pp. 24-32, 2009. [Online]. http://elib.dlr.de/54327/

[42] Jay B. Kohse-Höinghaus, *Applied Combustion Diagnostics*, Norman Chigier, Ed.: Taylor and Francis, New York, 2002. [Online]. http://www.routledge.com/books/details/9781560329138/

[43] Johannes Heinze et al., "PLIF thermometry based on measurements of absolute concentrations of the OH radical," *Zeitschrift für Physikalische Chemie*, vol. 225, no. 11-12, pp. 1315-1341, 2011. [Online]. http://elib.dlr.de/73536/

[44] Rajesh Sadanandan, Wolfgang Meier, and Johannes Heinze, "Experimental study of signal trapping of OH laser induced fluorescence and chemiluminescence in flames," *Applied Physics B*, 2011. [Online]. http://elib.dlr.de/71077/

[45] M. Carl et al., "Experimental and Numerical Investigation of a Planar Combustor Sector at Realistic Operating Conditions," *Transactions of the ASME - A - Engineering for Gas Turbines and Power*, vol. 123, no. 4, pp. 810-816, 2001, LIDO-Berichtsjahr=2001. [Online]. http://elib.dlr.de/3086/

[46] T. Behrendt, J. Heinze, and Ch. Hassa, "Experimental investigation of a new LPP injector concept for aero engines at elevated pressures," , 2003, LIDO-Berichtsjahr=2003. [Online]. http://elib.dlr.de/1160/

[47] Robert Giezendanner-Thoben, Ulrich Meier, Wolfgang Meier, Johannes Heinze, and Manfred Aigner, "Phase-Locked Two-Line OH-PLIF Thermometry in a Pulsating Gas Turbine Model Combustor at Atmospheric Pressure ," *Applied Optics*, no. 44, pp. 6565-6577, 2005. [Online]. http://elib.dlr.de/19932/

[48] Johannes Heinze, Olaf Diers, Eggert Magens, and Ulrich Meier, "Phase-resolved 2D diagnostics of self-excited combustion oscillations in a gas turbine model combustor," , August 2009. [Online]. http://elib.dlr.de/63633/

[49] Ulrich Meier, Johannes Heinze, and Christoph Hassa, "Response of Spray and Heat Release to Forced Air Flow Fluctuations in a Gas Turbine Combustor at Elevated Pressure ," , May 2007. [Online]. http://elib.dlr.de/49065/

[50] Christoph Hassa, Johanes Heinze, Leif Rackwitz, and Thomas Dörr, "Validation methodology for the development of low emission fuel injectors for aero-engines," , September 2006, pp. 8.10.5.1--8.10.5.12. [Online]. http://elib.dlr.de/44691/

[51] Ulrich Doll, "Filtered Rayleigh Scattering., to be published," Ruhr Universität Bochum, Ph.D. dissertation.

[52] Ulrich Doll, Michael Fischer, Guido Stockhausen, and Christian E. Willert, "Fundamentals of Filtered Rayleigh Scattering," *16th International Symposium on Applications of Laser Techniques to Fluid Mechanics, 09-12 July 2012, Lisbon, Portugal*, 2012.

[53] Michael Fischer, Eggert Magens, Hedwig Weisgerber, Adi Winandy, and Sebastian Cordes, "Coherent Anti-Stokes Raman Scattering Temperature Measurements on an Air Breathing Ramjet Model," *AIAA Journal*, vol. 37, no. 6, pp. 744-750, 1999. [Online]. http://elib.dlr.de/48786/

[54] A.C. Eckbreth, "BOXCARS: Crossed-Beam Phase-Matched CARS Generation in Gases," *Applied Physics Letters*, vol. 32, pp. 421-423, 1978.

[55] D.A. Greenhalgh, *Quantitative CARS Spectroscopy, Chapter 5 of Advances in non-linear spectroscopy*, R.J.H. Clarke \&, Ed.: John Wiley \& Sons Ltd, 1987.

[56] A.C. Eckbreth, *Laser Diagnostics for Combustion Temperature and Species*.: Abacus Press, Cambridge Mass., ISBN 0-85626-344-3, 1988.

[57] J.W. Nibler and G.V. Knighten, *Coherent Anti Stokes Raman Spectroscopy*, A. Weber, Ed.: Springer Verlag, Topics in Current Physics 11: Raman Spectroscopy of Gases and Liquids, 1979.

[58] S.A. Druet and J.P. Taran, *Prog. Quant. Electr.*, vol. 7, 1, 1981.

[59] E. Magens, *CARS software documentation for the CARS data evaluation*.: E. Magens, Institute of Propulsion Technology, DLR, 1998.

[60] M. Fischer, E. Magens, and A. Winandy, "Single-Shot Broadband Nitrogen CARS Measurements with Temperatures up to 3200 K: Comparison of Different Data Evaluation Schemes," *Proceedings of the XI'th European CARS Workshop, Florence, March 23-25, 1992, published in "Coherent Raman Spectroscopy: Applications and New Developments", World Scientific Publishing Co. Pte. Ltd., Singapore*, pp. 165-170, 1993.

[61] M. Fischer, E. Magens, and A. Winandy, "N2 and H2O Thermometry at High Pressure and Temperature," *poster presentation at the XIV European CARS Workshop, El Escorial, Spain*, 1995.

[62] M. Fischer, "Untersuchungen zur Einsatzfähigkeit der N2- und H2O-CARS-Thermometrie und H2O-CARS-Konzentrationsmessung bei der Analyse von H2-Staustrahltriebwerken," Technische Universität Berlin, Ph.D. dissertation 2006.

[63] J. Koopman, M. Fischer, E. Magens, A. Winandy, and B. Meislitzer, "Non-intrusive Measurements," *Potential Use of Hydrogen in Propulsion, European Community report, EC Contract no. 5077-92-11 EL ISP D, EQHHPP Phase III.0-3, Subtask: Non-intrusive Measurements, Institute of Propulsion Technology, German Aerospace Center (DLR)*, Jan. 1996.

[64] P. Griebel et al., "Experimental Investigation of an Atmospheric Rectangular Rich Quench Lean Combustor Sector for Aeroengines," *ASME 97-GT-146, Orlando, Florida*, 1997.

[65] Michael Fischer et al., "Single Pulse Broadband Nitrogen CARS Measurements in the High Enthalpy, Hypersonic Flow Field of L3K at Temperatures up to 5800 K," *7th European Symposium on Aerothermodynamics for Space Vehicles, May 9-12 2011, Brugge, Belgium, Paper 2138374*, 2011. [Online]. http://elib.dlr.de/74297/

[66] F. Grisch et al., "Coherent Anti-Stokes Raman Scattering Measurements and Computational Modeling of Nonequilibrium Flow," *AIAA Journal*, vol. 38, p. 1669, 2000.

[67] S. P. Kearney, S. J. Beresh, R. W. Schefer, and T. W. Grasser, *Filtered Rayleigh Scattering Diagnostic for Multi-Parameter Thermal-Fluids.*: SANDIA REPORT, SAND2004-0158, 2004.

[68] Melanie Voges, Christian Willert, Reinhard Mönig, Martin Müller, and Heinz-Peter Schiffer, "The challenge of stereo PIV measurements in the tip gap of a transonic compressor rotor with casing treatment," *Experiments in Fluids*, vol. 52, pp. 581-590, 2012, 10.1007/s00348-011-1061-y. [Online]. http://dx.doi.org/10.1007/s00348-011-1061-y

[69] Melanie Voges, Manfred Beversdorff, Chris Willert, and Hartmut Krain, "Application of particle image velocimetry to a transonic centrifugal compressor," *Experiments in Fluids*, vol. 43, pp. 371-384, 2007, 10.1007/s00348-007-0279-1. [Online]. http://dx.doi.org/10.1007/s00348-007-0279-1

[70] M. Voges et al., "Investigation of Blade Tip Interaction With Casing Treatment in a Transonic Compressor---Part I: Particle Image Velocimetry," *Journal of Turbomachinery*, vol. 133, no. 1, p. 011007, 2011. [Online]. http://link.aip.org/link/?JTM/133/011007/1

[71] F. Schrijer, F. Scarano, and B. van Oudheusden, "Application of PIV in a Mach 7 double-ramp flow," *Experiments in Fluids*, vol. 41, pp. 353-363, 2006, 10.1007/s00348-006-0140-y. [Online]. http://dx.doi.org/10.1007/s00348-006-0140-y

[72] D. Ragni, F. Schrijer, B. van Oudheusden, and F. Scarano, "Particle tracer response across shocks measured by PIV," *Experiments in Fluids*, vol. 50, pp. 53-64, 2011, 10.1007/s00348-010-0892-2. [Online]. http://dx.doi.org/10.1007/s00348-010-0892-2

[73] F. Scarano, B. W. van, W. J. Bannink, and M. Bsibsi, "Experimental Investigation of Supersonic Base Flow Plume Interaction by Means of Particle Image Velocimetry," , vol. 563, feb 2005, p. 601. [Online]. http://adsabs.harvard.edu//abs/2005ESASP.563.601S

[74] A. K. Prasad, "Stereoscopic particle image velocimetry," *Experiments in Fluids*, vol. 29, pp. 103-116, 2000.

[75] Joshua J. Smith, Gerald Schneider, Dmitry Suslov, Michael Oschwald, and Oskar Haidn, "Steady-state high pressure LOx/H2 rocket engine combustion," *Aerospace Science and Technology*, vol. 11, no. 1, pp. 39-47, 2007, Propellant combustion phenomena. [Online]. http://www.sciencedirect.com/science/article/pii/S1270963806001398

[76] Johannes Lux and Oskar Haidn, "Flame Stabilization in High-Pressure Liquid Oxygen/Methane Rocket Engine Combustion," *Journal of Propulsion and Power*, vol. 25, no. 1, pp. 15-23, 2009. [Online]. http://doi.aiaa.org/10.2514/1.36852

[77] Melanie Voges, Joachim Klinner, Chris Willert, Manfred Beversdorff, and Richard Schodl, "Assessment of Powder-based Seeding Materials for PIV Applications in Transonic, Supersonic and Reacting Flows," , May 2007. [Online]. http://elib.dlr.de/48597/

[78] Melanie Voges, Joachim Klinner, Chris Willert, and Erich Blümcke, "PIV Messungen In interagierenden Überschall-Freistrahlen In druckbelasteter Umgebung," , April 2007. [Online]. http://elib.dlr.de/48599/

[79] F. Scarano and B. W. , "Planar velocity measurements of a two-dimensional compressible wake," *Experiments in Fluids*, vol. 34, pp. 430-441, 2003, 10.1007/s00348-002-0581-x. [Online]. http://dx.doi.org/10.1007/s00348-002-0581-x

[80] M. Havermann, J. Haertig, C. Rey, and A. George, "PIV Measurements in Shock Tunnels and Shock Tubes," in *Particle Image Velocimetry*.: Springer Berlin / Heidelberg, 2008, vol. 112, pp. 429-443, 10.1007/978-3-540-73528-1_23. [Online]. http://dx.doi.org/10.1007/978-3-540-73528-1_23

[81] J. Haertig, M. Havermann, C. Rey, and A. George, "Particle Image Velocimetry in Mach 3.5 and 4.5 Shock-Tunnel Flows," *AIAA Journal*, vol. 40, pp. 1056-1060, 2002.

[82] Martin Bitter, Sven Scharnowski, Rainer Hain, and Christian Kaehler, "High-repetition-rate PIV investigations on a generic rocket model in sub- and supersonic flows," *Experiments in Fluids*, vol. 50, pp. 1019-1030, 2011, 10.1007/s00348-010-0988-8. [Online]. http://dx.doi.org/10.1007/s00348-010-0988-8

[83] H. Weisgerber et al., "Experimental and Numerical Analysis of an Expansion Flow in Chemical and Thermal Nonequilibrium," *Fourteenth International Symposium on Air Breathing Engines, XIV ISABE, Florence, Italy, 5-10 September*, 1999. [Online]. http://elib.dlr.de/1412/

[84] H. Weisgerber et al., "Experimental Analysis of Exhaust Gas in a Hypersonic Nozzle," , vol. AIAA-98-1600, 1998, LIDO-Berichtsjahr=2000. [Online]. http://elib.dlr.de/969/

[85] R. Schodl et al., "Optical Diagnostic Techniques in Turbomachinery," *22nd AIAA Aerodynamic Measurement Technology and Ground Testing Conference, St. Louis, Missouri, USA, June 24-27, 2002, AIAA-2002-3038*, 2002. [Online]. http://elib.dlr.de/1149/

[86] R. Schodl et al., "Doppler Global Velocimetry for the analysis of combustor flow," *Aerospace Science and Technology*, vol. 6, no. 7, pp. 481-493, 2002. [Online]. http://elib.dlr.de/1151/

[87] R. Schodl et al., "Doppler Global Velocimetry for the analysis of combustor flow," *Aerospace Science and Technology*, vol. 6, no. 7, pp. 481-493, 2002. [Online]. http://elib.dlr.de/1151/

[88] I. Roehle and C. Willert, "Extension of Doppler global velocimetry to periodic flows," *Meas. Sci. Technol.*, vol. 12, pp. 1-12, 2001.

[89] Lord Rayleigh, "The explanation of certain acoustical phenomena," *Nature*, vol. 18, 1878.

[90] J.F. Meyers, "Identification and minimization of errors in Doppler global velocimetry measurements," *10th Int. Symp. of Laser Techniques to fluid Mechanics, Lisbon, Portugal*, 2000.

[91] Johannes Koopman et al., "Modelling of Low Emissions Combustors using Large Eddy Simulations. Work Package 4: Reacting Flow, Temperature and Species Data.," unpublished January 2005. [Online]. http://elib.dlr.de/21582/

[92] W. Koechner, *Solid State Laser Engineering*, 3rd ed.: Springer Series in Optical Sciences, 1992.

[93] Christoph Hassa et al., "Nonintrusive Flowfield, Temperature and Species Measurements on a Generic Aeroengine Combustor at Elevated Pressures ," *Proceedings-CD, ASME Turbo Expo 2006: Power for Land, Sea and Air, GT 2006-90213*, 2006. [Online]. http://elib.dlr.de/43953/

[94] S.A. Greenwood, "Combustion drive pressure oscillations (humming) - a low emission design problem," *Global Gas Turbine News*, vol. 41, pp. 12-15, 2001.

[95] Michael Fischer, Johannes Heinze, Martin Müller, Olaf Diers, and Dennis Schneider, "Optical diagnostics on a catalytic burner," , May 2008. [Online]. http://elib.dlr.de/55167/

[96] M. Fischer et al., "Single Pulse Broadband Nitrogen CARS Measurements on a High Enthalpy, Hypersonic Flow Field at Temperatures up to 5800 K," , Book of abstracts ECONOS 2010, ,Jacobs University, 9th European Conference on Nonlinear Optical Spectroscopy (ECONOS) / 29th European CARS workshop, 21.-23.06.2010, Bremen. [Online]. http://elib.dlr.de/67732/

[97] Olaf Diers et al., "Characterization of a real size retrofittable catalytic combustion system," *Proceedings of ASME Turbo Expo 2008: Power for Land, Sea and Air, GT2008-50516*, June 2008. [Online]. http://elib.dlr.de/57162/

[98] O. Diers, J. Koopman, M. Fischer, and C. Hassa, "Investigation of two advanced cooling mixing concepts for a rich quench lean combustor.," *ASME Turbo Expo 2001, New Orleans, USA, June 4-8, 2001, 2001-GT-85*, 2001. [Online]. http://elib.dlr.de/1100/

[99] J.J. Degnan, "Theory of the optimally coupled q-switched laser," *IEEE Journal of Quantum Electronics*, vol. 25, pp. 214-220, 1989.

[100] S.M. Correa, "A Review of NOx Formation under Gas-Turbine Combustion Conditions," *Combustion Science and Technology*, vol. 87, pp. 329-362, 1993.

[101] "DESIRE project proposal (project No. NNE5/388/2001)," Tech. rep. 2001.

6 Appendix

6.1 Scientific Background of Authors

At the Institute of Propulsion Technology the Dept of Engine Measurement Techniques (AT-TM) has long term experience in the application of combustion diagnostics for industrial scale test facilities for aero-propulsion and gas turbine combustion in the context of numerous national and international projects conducted both at the institute and its partners. The emphasis of the department's activities is on the development and application of image and laser based optical techniques to provide validation data from component test rigs such as compressors, turbines, combustion chambers, cascade wind tunnels, engine intakes and similar. Given that these facilities are generally operated at flight-relevant operating conditions, that is, at elevated pressures, high temperatures, high Reynolds numbers, etc, considerable expertise is available in bringing a wide variety of optical diagnostic techniques to fruition (see e.g [45], [11], [47], [50], [48] [49], Table 3). Because of this expertise the Dept. of Engine Measurement Techniques also has a long history of involvement in projects beyond its core activities related to aero-propulsion research. For example a numerous optical flow velocimetry techniques have been applied in trans-, super- and hypersonic wind tunnels, as well as in-flight and in automotive applications.

Table 3: Involvement of the Dept. of Engine Measurement Techniques (AT-TM) in recent EU projects. Not mentionend are nationally funded Projects such as those in the frameworks of AG-Turbo, LuFo 3 and LuFo 4 (e.g.COOREFF, FetMaTec, EffMaTec, LemCoTec, and others)

EU Project		**Time**	**Methods**	**Object**	**Comments**
MOLECULES	FP4	2003 – 2004	PIV, DGV, OH-PLIF, CARS	Swirled gas combustor	Full 3-D characterization
FUELCHIEF	FP5	2006 - 2007	OH-PLIF, OH*, CH*, DGV, PIV	Gasturbine combustors	Also using endoscopic imaging, phase-resolved
CATHLEAN	FP5	2006	OH*, CARS	Catalytic combustor	
TLC	FP6	2005-2007	OH-PLIF		Development PLIF Temperature Meas.Techniques based on OH radical
TLC	FP6	2008	OH-PLIF	Premixed Kerosene Burner	
TIMECOP A.E.	FP6	2008-2009	OH*, Kero-PLIF, OH-T PLIF, Mie-scattering	Pre-evaporated Kerosene combustion	Phase-resolved
INTELLECT D.M.	FP6	2008-2009	Mie-scattering, Kero-PLIF, OH*, OH-T-PLIF	Unscaled jet-engine swirl burner	Industrial scale burners, up to 12 bar
NEWAC	FP6	2010-2011	Mie-scattering, Kero-PLIF, OH*, OH-T-	Unscaled jet-engine swirl burner	Industrial scale burners, up to 12 bar

			PLIF, PIV		
AMOD (ESA's TRP project)		2010/2011	CARS	DLR's arc heated facility L3K with a newly designed nozzle, which will allow to apply severe heat loads in excess of 10 MJ/m2 to models placed in the flow field.	heat shields non equilibrium flow free stream at 64 mbar and in the vicinity front of a probe body at app. 1 bar first CARS temperature measurements at 5800 K

Deutsches Zentrum
für Luft- und Raumfahrt e.V.

TN2441

Design Trade-Off and Cost Analysis

May 24, 2013

Ali Gülhan
Dominik Saile
Andreas Henckels

Institute of Aerodynamics
and Flow Technology
Supersonic and Hypersonic
Technology Department

DLR **Deutsches Zentrum**
für Luft- und Raumfahrt e.V.
in der Helmholtz-Gemeinschaft

ESA STUDY CONTRACT REPORT

No ESA Study Contract Report will be accepted unless this sheet is inserted after the coverpage of each volume of the Report.

ESA CONTRACT No.: AO/1-6731/ 11/NL/SFe	SUBJECT Hot Testing Facility for ELV Propulsion Characterization		CONTRACTOR DLR
* ESA CR( )No	* STAR CODE	No of TN 2441	

ABSTRACT:

This report presents the results from the design trade-off and the cost analysis in the framework of the ESA technology research project "Hot Testing Facilities for ELV Propulsion Characterization". Three main options are discussed, which are the upgrade of the Vertical Facility VMK in Cologne, the upgrade of the Trisonic Facility TMK in Cologne and the establishment of a new facility. With respect to the latter, a distinction is made for that option between the establishment of a TMK-like facility in Cologne and a completely new facility somewhere else. The different options are checked against the main cost drivers. The trade-off analysis shows that and upgrade of the existing VMK and TMK with two complementary set-ups for hot plume testing is financially and technically favorable.

The work described in this report was done under ESA contract. Responsibility for the contents resides in the author or organization that prepared it.

Name of author: A. Gülhan, D. Saile, A. Henckels (DLR, Cologne, Germany)

** NAME OF ESA STUDY MANAGER	** ESA BUDGET HEADING
N. Murray DIV: TEC-MPA DIRECTORATE: D\TEC	

* Sections to be completed by ESA

** Information to be provided by ESA Study Manager

8 Design Trade-Off and Cost Analysis - TN2441

A detailed cost analysis was sent to ESA before and is attached below. In the following, a short overview to the considerations are given.

Three different options for the hot testing facility were investigated, which are

- Option I: Upgrading the Vertical Facility VMK in Cologne.
- Option II: Upgrading the Trisonic Windtunnel TMK in Cologne.
- Option IIIa: Establishment of a new TMK facility in Cologne.
- Option IIIb: Establishment of a completely new facility.

Then, the main cost items were identified. These are

- design of the facility and test model,
- procurement/manufacturing of facility components,
- procurement/manufacturing of the model,
- development and procurement of the instrumentation,
- facility infrastructure,
- building infrastructure,
- integration and assembly,
- commissioning and calibration of the facility,
- facility maintenance costs per year,
- facility maintenance costs over 20 years.

As concluding remarks, it can be stated that

- the establishment of a completely new facility (Option IIIb) is very expensive and cannot be justified.
- the stablishment of a copy of the TMK facility in Cologne only for hot plume testing is less feasible, since the expected work load cannot compensate the investement and operation costs.

- upgrading the VMK facility with some modifications to the facility and establishment of a new test set-up for hot plume testing is financially attractive and technicaly acceptable.
- upgrading the TMK facility with some modifications to the facility and establishment of a new test set-up for hot plume testing is financially attractive and technically acceptable.
- upgrading the VMK and TMK facilities with two complementary test set-ups for hot plume testing is financially and technically favourable.

CONTENT

1 Intention of ESA and facility requirements

ESA's invitation to tender [1] is motivated by discrepancies between the wind tunnel simulations with cold jet-on conditions and actual in-flight measurements on the ARIANE 5. Therefore, the present objective is to provide accurate and flight representative wind tunnel data concerning the underestimated base pressure and the interrelated base drag, the heat loads, and the fluctuating loads on the nozzle.

By simulating the hot nozzle plume inside the wind tunnel facility, reliable data should support a better understanding of the ELV flow physics and particularly be used for the validation of CFD computations. The desired facility must allow the simulation of a single plume like VEGA first stage and multiple plumes like ARIANE 4 and 5 first stages. In a supplementary documentation ESA outlines more detailed requirements for this new „Hot Testing Facilities for ELV Propulsion Characterization" [2].

2 DLR approach for ELV propulsion characterization

2.1 Overview

Based on ESA's requirements, DLR suggests the combined upgrading of both, VMK and TMK facility, leading into a joined realization of its options I and II [3]. Succeeding tests at these facilities will focus on different physical effects as well as different conditions along the ascent trajectory (Tab. 1). Gained data will provide detailed physical insight from overlapping simulation capabilities by synergetic effects.

2.2 Upgrade of VMK

In order to accommodate "single and multiple nozzle" scaled wind tunnel models at VMK, the facility needs to be equipped with a new nozzle of about 600 mm exit diameter, i.e. comparable to TMK nozzle exit. Depending on the test configurations, an improved optical access will be necessary. Further on, the infrastructure for hot plume tests with gaseous or liquid combustors has to be upgraded and adapted to recent safety standards.

For the support of the rocket model, two different configurations will be realized: Additionally to a lateral strut supported model, a second model will be supported by an axial strut integrated and fixed upstream the nozzle throat. (Fig. 1a). In contrast to commonly lateral supported configurations, no disturbances generated by struts perturb the base flow. Also choking effects by tunnel blockage as well as reflections will be reduced significantly. Investigations on the influence of plume interactions are possible by attaching boosters to the central body (Fig. 1b). The hot gas for the single or multiple plumes will be generated either by solid propellants or hydrogen/oxygen combustion.

Table 1: DLR approach for ELV propulsion characterization.

Facility:	Vertical Wind Tunnel Cologne (VMK)	Trisonic Wind Tunnel Cologne (TMK)
Addressed flight regime:	Mach 0.5 ÷ 0.95 at low altitude.	Mach 0.6 ÷ 2.0 (optional up to 5.7), altitude variation above Mach 1.5.
Test section:	Free jet	Transonic (perforated walls) and supersonic test sections
Model support:	Model with upstream (Fig. 1a, b) and strut (Fig. 2a, b) support.	Only model with strut support (Fig. 2a, b).
Model size	Core stage: base diameter of 160 mm	Core stage: base diameter of 67 mm
Plume generation:	Single and multiple plumes with solid propellants and H_2/O_2-combustion.	Single plume with solid propellants and H_2/O_2-combustion. Multiple plumes only with solid propellants.
Focused effects:	Influence of fuel mixture ratio, variation of total temperature, thermal analysis, strut influence.	Altitude variation, variation of angles of attack, dynamic pressure response, thermal analysis.
Costs:	~ 620.000 € for facility upgrade ~ 220.000 € for maintenance per year ~ 75.000 € for standard test campaign	~ 990.000 € for facility upgrade ~ 400.000 € for maintenance per year ~ 150.000 € for standard test campaign

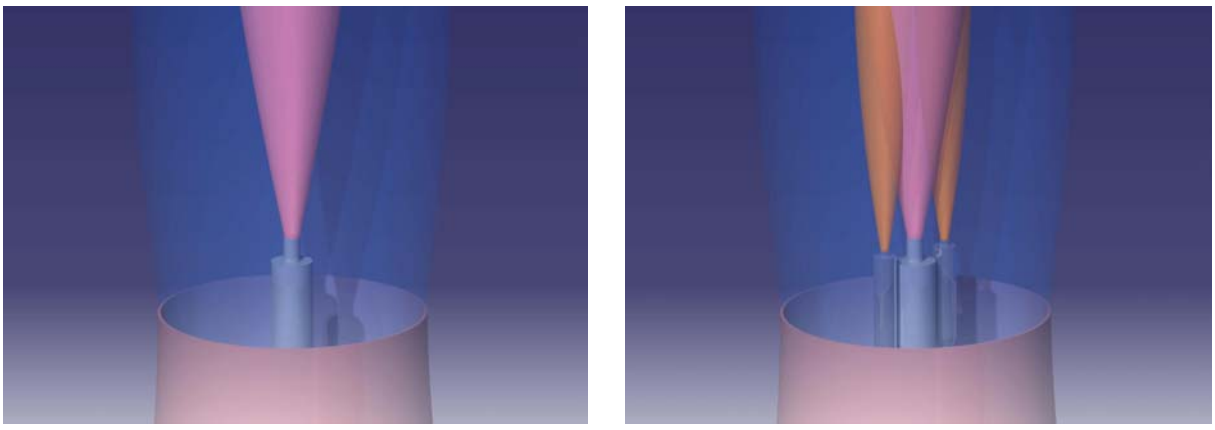

Fig. 1a and b: A wind tunnel model, fixed by an integrated strut far upstream the nozzle will allow studies on an undisturbed base flow with single or multiple plumes.

2.3 Upgrade of TMK

To generate hot plumes at the TMK solid propellants as well as hydrogen/oxygen combustion will be used. Also at this facility, a main upgrade issue is the safe operation of the facility. To ensure recent standards, a new reliable flushing system has to be developed and integrated. At TMK, an upstream supported model will be not feasible, i.e. blockage aspects of a lateral sting have to be examined carefully (Fig. 2a). So, tests of multiple stage plumes may only be carried out by using small solid propellants (Fig. 2b).

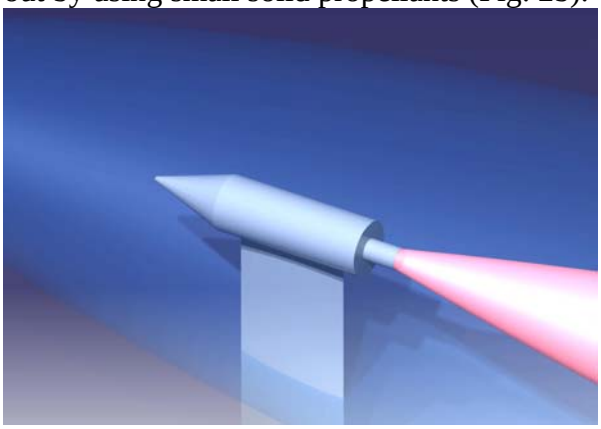

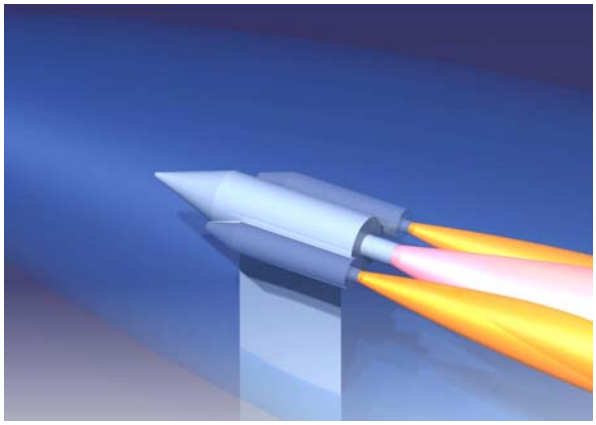

Fig. 2a and b: Rocket model fixed by a lateral strut without and with boosters.

2.4 Expected achievements and added values

These two measures will allow performing relevant testing on models with scaling ratios of about 1/55 for ARIANE 4, of about 1/80 for ARIANE 5, and of about 1/45 for VEGA. Mainly identical measurement techniques will be applied to provide reliable flow data from both facilities. Overall dynamic flow field diagnostics will be carried out by high speed Schlieren techniques locally supported by unsteady surface pressure measurements. Data of resulting velocity fields are generated from PIV measurements. Gas concentrations and temperatures will be measured by OH LIF. Based on IR-thermography thermal analyses will be performed.

By conducting experiments in both facilities it is possible to validate the results by crosschecking, and also, to take into account the influence of the TMK walls or the VMK free shear layers. The main difference between plumes, generated by solid propellants and oxygen/hydrogen combustion is the molar mass and the ratio of specific heats inside the resulting flow field. Thus, a detailed study of the differences will reveal the sensitivities of these parameters. Last, a comparison of the two wind tunnel model support configurations will provide insight into the influence of a strut. This may help to find correction methods also for data gained during past tests.

3 New transonic wind tunnel

3.1 Overview

The DLR proposal [3] additionally considers the establishment of new facility. Two options are taken into account: Option IIIa is a copy of TMK in Cologne, option IIIb represents a scaled version of TMK. An overview to the different options is given in Tab. 2.

Table 2: Overview to option IIIa and IIIb.

Facility:	Option IIIa: Copy of TMK in Cologne	Option IIIb: New large scale transonic wind tunnel
Addressed flight regime:	Mach 0.5 ÷ 1.3.	Mach 0.5 ÷ 1.3.
Test section:	Transonic (perforated walls)	Transonic (perforated walls)
Model support:	Only model with strut support (Fig. 2a, b).	Only model with strut support (Fig. 2a, b).
Model size:	Core stage: base diameter of 67 mm	Core stage: base diameter of about 160 mm Booster stage: base diameter of 90 mm
Plume generation:	Single plume with solid propellants and H_2/O_2-combustion. Multiple plumes only with solid propellants.	Single and multiple plumes with solid propellants and H_2/O_2-combustion.
Focused effects:	Altitude variation, variation of angles of attack, dynamic pressure response, thermal analysis.	Altitude variation, variation of angles of attack, dynamic pressure response, thermal analysis.
Costs:	~ 6.545.000 € for facility establishment ~ 450.000 € for maintenance per year ~ 185.000 € for standard test campaign	~ 20.075.000 € for facility establishment ~ 900.000 € for maintenance per year ~ 280.000 for standard test campaign€

3.2 Option IIIa: Copy of TMK in Cologne

This new facility is equipped with a transonic test section, and is explicitly intended for transonic testing. The test section is permanently installed, thus, in opposition to TMK, no integration time for transonic testing is necessary. The wind tunnel models are identical to the strut supported models shown in Fig. 2a and 2b. Tab. 2 depicts the main characteristics of option IIIa.

3.3 Option IIIb: New large transonic wind tunnel

The proposed large wind tunnel facility is a scaled version of TMK with the objective to perform multiple plume stage testing with H_2/O_2-combustion for the core and also for the booster stages on larger wind tunnel models. The new test section is gearing to a cross section of about 2 m by 2m, which is approximately 3.3 times the lateral length of TMK. Correspondingly, the wind tunnel model can equally be scaled. For a design shown in Fig. 2a and 2b, investigations of a core stage with two boosters with a diameter of about 160 mm and 90 mm, respectively, are possible.

3.4 Expected achievements and added values

The advantage of option IIIa concerns the exclusive usage for transonic wind tunnel testing. On the other side, it has to be taken into account that a facility like this is not as versatile as TMK and cannot be used for investigations above the transonic regime, which is possibly essential as a reference point for the validation of the measurement techniques. And, although the technology is based on the existing TMK facility, costs for the facility establishment, maintenance and the preliminary lead time needed for the realization still persist and are significant (Tab. 2).
The large transonic wind tunnel, option IIIb, with a larger cross section is advantageous with respect to the possibility of testing a complete core stage-booster configuration with H_2/O_2-combustion. A lateral width of 3.3 times higher than TMK results in a cross section, which is about 11 times higher, meaning the mass flow increases with the same factor. The mass flow can be considered as the dominant measure for the infrastructure and the wind tunnel itself. For instant, the new large transonic wind tunnel facility must be capable to provide 11 times the mass flow of the existing TMK facility. Consequently, costs for the facility establishment, maintenance and the preliminary lead time needed for the realization are massive compared to the combined approach of DLR with VMK and TMK (see in Tab. 1 and Tab. 2). The added value in comparison to the DLR approach is limited if model size and inherent opportunities to study base flow effects are considered.

4 References

[1] “ESA ITT, A0/1-6731/11/NL/SFe, Hot Testing Facilities for ELV Propulsion Characterization”, pp. 1-3, 2011.

[2] “ESA ITT, Statement of Work, Hot Testing Facilities for ELV Propulsion Characterization, Appendix 1 to A0/1-6731/11/NL/SFe,” vol. T418-303MP, pp. 1-13, 2011.

[3] A. Gülhan, K. Hannemann, C. Willert, A. Henckels, and D. Saile, “DLR Proposal-No.: 3005921/Hot Testing Facilities for ELV Propulsion Characterization,” 2011.

Bibliography

[1] (2002). High Speed Wind Tunnel and Test Systems Design Handbook. Publication number: AER-EIR-13552-E:1–72.

[2] (2003). Flight 157 - Ariane 5 ECA, Press Conference, Paris - January 7, 2003.

[3] (2011a). ESA ITT, A0/1-6791/11/NL/SFe, Hot Testing Facilities for ELV Propulsion Characterization. pages 1–3.

[4] (2011b). ESA ITT, Statement of Work, Hot Testing Facilities for ELV Propulsion Characterization, Appendix 1 to A0/1-6791/11/NL/SFe. vol. T418-303MP:1–13.

[5] Babuk, V., Glebov, A., Dolotkazin, I., DeLuca, L. T., D'Andrea, B., Vorozhtsov, A., and Klyakin, G. (2005). New Generation of Cheap and Ecologically Safe Solid Propellants for Space Applications. *EUCASS - European Conference for Aerospace Sciences, Moscow, Russia, 2005.*

[6] Baik, D. S. and Zumwalt, G. W. (2002). Analytical Model of the Base Flow Between a Subsonic and Supersonic Flow. *Journal of Propulsion and Power*, 18-1:35–43.

[7] Banuti, D. (2012). TN2200 Scaling Issues. pages 1–20.

[8] David, C. and Radulovic, S. (2005). Prediction of Buffet Loads on the Ariane 5 Afterbody. *6th International Symposium on Launcher Technologies.*

[9] DeLuca, L. T., Tomasi, D., Signoriello, D., Levi, S., Cianfanelli, S., Sinditskii, V. P., Babuk, V. A., Klyakin, G. F., and Vorozhtsov, A. B. (2006). Dual-Oxidizer Metallized Solid Propellants for Low-Cost Space Access. *International Astronautical Congress, Valencia, Spain, 2-6 October 2006.*

[10] Douglass, H. W., Schmidt, H. W., Levinson, L., and Zehetner, H. C. (1972). Liquid Propellant Gas Generators. *NASA SP-8081*, pages 1–103.

[11] Esch, H. (1986). Die 0,6-m x 0,6-m-Trisonische Messstrecke (TMK) der DFVLR in Koeln-Porz. DFVLR-Mitt. 86-21:1–79.

[12] Foust, M. J., Deshpande, M., S. Pal, T. N., Merkle, C. L., and Santoro, R. J. (1996). Experimental and Analytical Characterization of a Shear Coaxial Combusting GO2/GH2 flowfield. *AIAA 34th Aerospace Sciences Meeting and Exhibit, Reno, NV, Jan. 15-18 1996.*

[13] Frey, M. (2001). *Dissertation zur Behandlung von Stroemungsproblemen in Raketendusen bei Ueberexpansion.*

[14] Goethert, B. H. (1961). *Transonic Wind Tunnel Testing.*

[15] Guelhan, A., Hannemann, K., Willert, C., Henckels, A., and Saile, D. (2011). DLR Proposal-No.: 3005921/Hot Testing Facilities for ELV Propulsion Characterization.

[16] Isakowitz, S. J. and Jr., J. H. (2004). *International Reference Guide to Space Launch Systems*.

[17] J. M. Locke, S. Pal, R. D. W. and Santoro, R. J. (2009). Toward Time-Resovled Measurements in a Gaseous Hydrogen/Oxygen Rocket. *45th AIAA/ASNE/SAE/ASEE Joint Propulsion Conference and Exhibit, 2-5 August 2009m Denver, Colorado, USA*.

[18] J. M. Locke, S. Pal, R. D. W. and Santoro, R. J. (2011). Diode Laser Absorption Spectroscopy Measurements in a Gaseous Hydrogen/Oxygen Rocket. *49th AIAA Aerospace Sciences Meeting including the New Horizons Forum and Aerospcae Exposition, 4-7 January 2011, Orlando, Florida, USA*.

[19] Kaufmann, J. and Pinard, D. (2010). ESA's Next Generation Launcher Status Of FLPP Launch System Concept Investigations. *1st International Astronautical Congress, Prague, Czech Republic, 2010*, 6:5030–5038.

[20] Leroux, P. (2011). Ariane 5 - Data relating to Flight 202. *Astrium*.

[21] M. D. Moser, S. P. and Santoro, R. (1995). Laser Light Scattering Measurements in a GO2/GH2 Uni-Element Rocket Chamber. *AIAA 95-0137, 33rd AIAA Aerospace Sciences Meeting, Reno, NV, Jan. 9-12 1995*.

[22] M. J. Foust, S. P. and Santoro, R. J. (1996). Gaseous Propellant Rocket Studies using Raman Spectroscopy. *AIAA 96-2766, 32nd AIAA/ASME/SEA/ASEE Joing Propulsion COnference and Exhibit, FL, U.S.A, July 1-3 1996 Lake Buena Vista*.

[23] M. Lehman, S. P. and Santoro, R. (1997). Summary of GH2/GO2 Raman Sepctroscopy Experiments for a Shear Coaxial Injector. *Chemical and Physical Processes in Combustion, Fall Technical Meeting, The Eastern States Section, 1997*, pages 119–122.

[24] Marshall, W. M., Pal, S., Woodward, R. D., and Santoro, R. J. (2005). Benchmark Wall Heat Flux Data for a GO2/GH2 Single Element Combustor. *41st AIAA/ASME/SAE/ASEE Joint Propulsion Conference and Exhibit, AIAA 2005-3572, 10-13 July 2005, Tucson, Arizona, U.S.A.*

[25] Merenich, J. J., Moser, M. D., Pal, S., and Santoro, R. (1993). Velocity Field Measurements in a Gaseous Hydrogen/Oxygen Rocket. *Technical Meeting. The Eastern States Section of the Combustion Institute, Princeton, New Jersey, Oct. 25-27 1993*.

[26] Moser, M. D., Merenich, J. J., Pal, S., and Santoro, R. (1993). OH-Radical Imaging and Velocity Field Measurements in a Gaseous Hydrogen/Oxygen Rocket. *AIAA 93-2036, 29th AIAA/ASME/SAE/ASEE Joint Propulsion Conference and Exhibit, Monterey, CA, June 28-30 1993.*

[27] Murthy, S. N. B. and Osborn, J. R. (1976). *Base flow phenomenon with and without Injection: Experimental results, Theories and Bibliography.*

[28] Ponomarenko, A. (2009-2012). RPA Rocket Propulsion Analysis - http://www.propulsion-analysis.com/.

[29] S. Pal, W. Marshall, R. W. and Santoro, R. (2006). Wall Heat Flux Measurements in a Uni-Element GO2/GH2 Shear Coaxial Injector. *3rd International Workshop on Rocket Combustion Modeling, Vernon, France.*

[30] Saile, D., Guelhan, A., and Henckels, A. (2012). Design Trade-Off (preliminary). pages 1–7.

[31] Schoones, M. M. J. and Bannink, W. J. (1998). Base Flow and Exhaust Plume Interaction. Part 1: Experimental Study.

[32] Simmons, F. S. (2000). Rocket Exhaust Plume Phenomenology. *The Aerospace Press and American Insitute of Aeronautics and Astronautics.*

[33] Stahl, B., Emunds, H., and Guelhan, A. (2009). Experimental investigation of hot and cold side jet interaction with a supersonic cross-flow. *Aerospace Science and Technology*, 13:488 – 496.

[34] Stahl, B., Siebe, F., and Guelhan, A. (2010). Hot-Gas Side Jet in a Supersonic Freestream. *Journal of Spacecraft and Rockets*, 47:957 – 965.

[35] Sutton, G. P. and Biblarz, O. (2001). *Rocket Propulsion Elements.*

[36] Triesch, K. and Krohn, E.-O. (1986). Die Vertikale Messstrecke (VMK) der DFVLR in Koeln-Porz. DFVLR-Mitt. 86-22:1–97.

[37] Tucker, P. K., Menon, S., Merkle, C. L., Oefelein, J. C., and Yang, V. (2008). Validation of High-Fidelity CFD Simulations for Rocket Injector Design. *AIAA 2008-5226, 44th Joing Propulsion Conference and Exhibit, Hardford, CT, July 21-23 2008.*

[38] Wong, H., Meijer, J., and Schwane, R. (2005). Theoretical and and Experimental Investigation of Base-Flow Buffeting on Ariane 5 Launch Vehicles. *5th European Symposium on Aerothermodynamics for Space Vehicles, November 2005, Cologne, Germany.*

[39] Zapryagaev, V. I., Lokotko, A. V., Nikiforov, S. V., Pavlov, A. A., Tchernyshev, A. V., Bannink, W. J., Ottens, H., and Muylaert, J. (2002). Experimental Investigation of Base Pressure with Hot Supersonic Jet for External Supersonic Flow. *4th Symposium on Aerothermodynamics for Space Applications, Capua, Italy, 2001.*